ESA SP- 1233(1)
July 1999

Reports for Mission Selection
THE FOUR CANDIDATE EARTH EXPLORER CORE MISSIONS

Gravity Field and Steady-State Ocean Circulation Mission

ESA SP-1233 (1) - The Four Candidate Earth Explorer Core Missions -
GRAVITY FIELD AND STEADY-STATE OCEAN CIRCULATION

Report prepared by: Earth Sciences Division
Scientific Co-ordinator: Johnny A. Johannessen

Earth Observation Preparatory Programme
Technical Co-ordinator: Miguel Aguirre-Martinez

Cover: Richard Francis &

Published by: ESA Publications Division
c/o ESTEC, Noordwijk, The Netherlands
Editor: Bruce Battrick

Copyright: © 1999 European Space Agency
ISBN

CONTENTS

1 INTRODUCTION 5

2 BACKGROUND AND SCIENTIFIC JUSTIFICATION 9

2.1 SCIENCE CASE 9
2.2 STATE-OF-THE-ART OF GRAVITY FIELD DETERMINATION 13
2.3 HIGH-RESOLUTION GRAVITY FIELD DETERMINATION FROM SPACE 18
2.4 GOCE MISSION RATIONALE 22
2.5 COMPLEMENTARY SPACE MISSIONS AND AIRBORNE PROJECTS 24
2.6 SUMMARY 27

3 RESEARCH OBJECTIVES 31

3.1 INTRODUCTION 31
3.2 SOLID EARTH 32
3.3 ABSOLUTE OCEAN CIRCULATION 45
3.4 ICE SHEETS 64
3.5 GEODESY 65
3.6 GLOBAL SEA-LEVEL CHANGE 69
3.7 SUMMARY 74

4 OBSERVATION REQUIREMENTS 79

4.1 GRAVITY FIELD REQUIREMENTS FOR SCIENCE 79
4.2 OVERVIEW OF SIMULATION TECHNIQUES 81
4.3 SIMULATION AND COMPARISON OF NORMALISED MISSIONS 83
4.4 MISSION SIMULATIONS AND DETERMINATION OF GOCE BASELINE PARAMETERS 86
4.5 SUMMARY 89

5 MISSION ELEMENTS – OVERVIEW 91

5.1 SPACE SEGMENT 93
5.2 GROUND SEGMENT 94
5.3 GROUND OBSERVATIONS 94
5.4 CONTRIBUTIONS FROM OTHER MISSIONS 95
5.5 MISSION PERFORMANCES 95

6 SYSTEM CONCEPT 97

6.1 FROM MISSION TO SYSTEM REQUIREMENTS 97
6.2 MISSION DESIGN AND OPERATIONS 99
6.3 THE INSTRUMENTS 109
6.4 THE SATELLITE 125
6.5 THE LAUNCHER 154
6.6 THE GROUND SEGMENT 156
6.7 TECHNICAL CONCEPT SUMMARY 159

7 DATA PROCESSING 161

7.1 INTRODUCTION 161
7.2 PRE-PROCESSING (LEVEL 0 AND LEVEL 1 PROCESSING) 163
7.3 LEVEL 2 PROCESSING 167
7.4 VALIDATION 170
7.5 SUMMARY 171

8 MISSION PERFORMANCE AND MISSION REQUIREMENTS 173

8.1 ERROR ANALYSIS AND END-TO-END SIMULATOR 173
8.2 EXPECTED GOCE PERFORMANCE 181
8.3 SUMMARY OF EXPECTED SCIENCE PERFORMANCE 185

9 PROGRAMMATICS 191

9.1 DEVELOPMENT APPROACH 191
9.2 HERITAGE, CRITICAL AREAS AND RISKS 193
9.3 RELATED MISSIONS, INTERNATIONAL CO-OPERATION POSSIBILITIES AND TIMELINESS 194
9.4 ENHANCEMENT OF CAPABILITIES AND APPLICATIONS POTENTIAL 197

ANNEX: GRAVITY FIELD QUANTITIES/TERMINOLOGY 199

REFERENCES 203

GLOSSARY 213

ACKNOWLEDGEMENTS 217

1 Introduction

The Living Planet Programme document (ESA SP-1227, 1998) describes the plans for the Agency's new strategy for Earth Observation in the post-2000 time frame. It marks a new era for European Earth Observation based on smaller more focused missions and a programme that is user driven, covering the whole spectrum of interests ranging from scientific research-driven Earth Explorer missions through to application-driven Earth Watch missions. The user community is therefore now able to look forward to a programme of more frequent, but very specific missions directed at the fundamental problems of Earth system science.

Out of the nine Earth Explorer Core Missions identified in ESA SP-1196 (1-9), four Core Missions were selected for Phase-A studies, which began in June 1998, namely: the Land-Surface Processes and Interactions Mission; the Earth Radiation Mission; the Gravity Field and Steady-State Ocean Circulation Mission; and the Atmospheric Dynamics Mission. The Phase-A studies were all completed in June 1999 and, drawing on the findings emerging from this work and complementary scientific and technical support studies, Reports for Mission Selection have been written for all four.

This Report for Mission Selection for the Gravity Field and Steady-State Ocean Circulation Explorer (GOCE) was prepared by a Core Mission Drafting Team consisting of four members of the GOCE Mission Advisory Group (MAG); G. Balmino, R. Rummel, P. Visser and P. Woodworth. They were supported by the other MAG members, including C. Le Provost, R. Sabadini, H. Sünkel, and C.C. Tscherning. The technical content of the report (notably Chapter 6) has been compiled by the Executive based on inputs provided by the industrial Phase-A contractors. Others who, in various ways, have contributed to the report are listed in the Acknowledgements.

The primary aim of the GOCE Mission is to provide unique models of the Earth's gravity field and of its equipotential reference surface, as represented by the geoid, on a global scale with high-spatial-resolution and to very high accuracy. Such an advance in the knowledge of the Earth's gravity field and its geoid will help to develop a much deeper understanding of how the Earth's interior system works as schematically illustrated in Figure 1.1.

New and fundamental insight is therefore expected into a wide range of research and application areas, including Solid Earth Physics, Oceanography and Geodesy. The GOCE Mission therefore addresses all the areas discussed under Theme 1 of the Living Planet Programme (ESA SP-1227, 1998), except those directly related to magnetometry. To reach the measurement goal and meet the scientific objectives, the payload consists of an electrostatic gradiometer and a combined GPS/GLONASS precise positioning system.

The Report for Mission Selection for GOCE, together with those for the other three Earth Explorer Core Missions, is being circulated within the Earth Observation research community in preparation for The Four Candidate Earth Explorer Core Missions ConsultativeWorkshop in Granada (Spain) in October 1999.

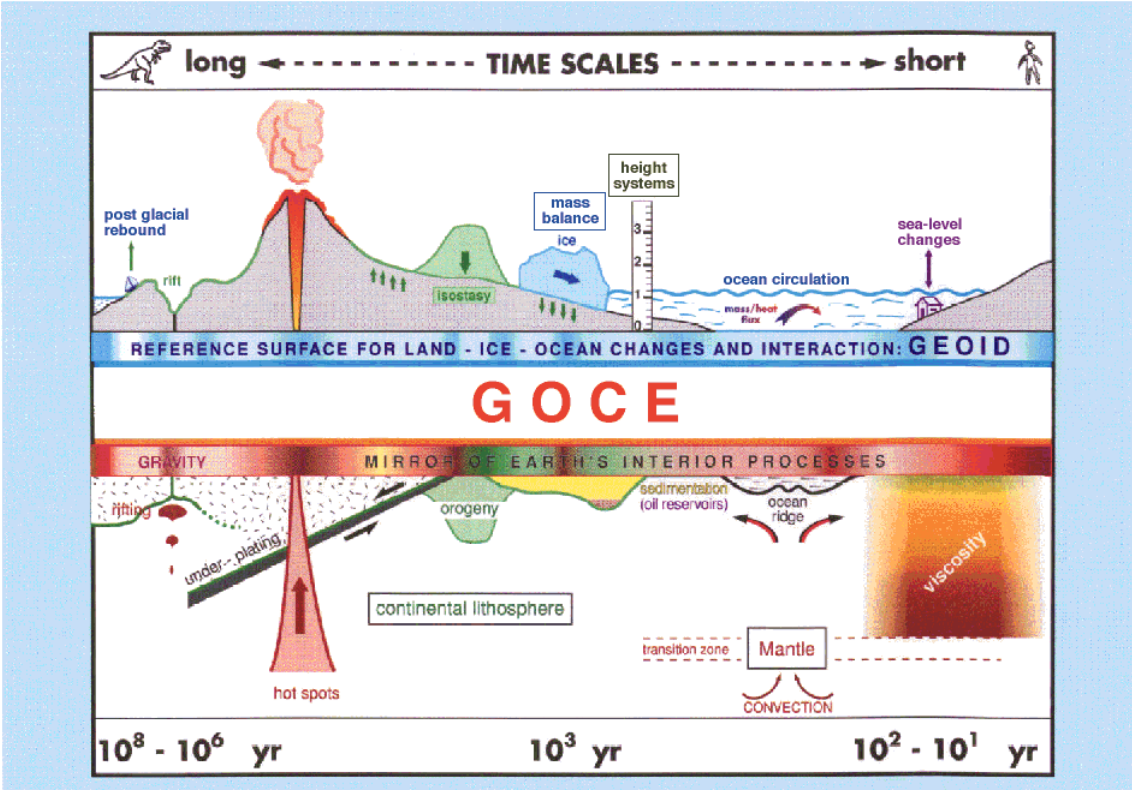

Figure 1.1. *The gravity field as derived by the GOCE mission has a twofold role in Earth sciences: the geoid as hypothetical ocean surface at rest (ocean circulation, sea-level, height systems) and gravity as a mirror of Earth's interior processes (rifting, sedimentation, mass readjustment).*

Following this introduction, the report is divided into eight chapters:

– Chapter 2 addresses the background and scientific justification for the mission in the context of issues of concern and the associated need to advance current scientific understanding. It also includes the rationale that stems from the scientific needs through to the gravity gradiometer selection, obtained in view of other planned gravity field missions. In so doing, it provides a clear identification of the potential 'delta' in new and advanced understanding and knowledge that would be gained from the mission.

– Drawing on these arguments, Chapter 3 discusses the importance of the research objectives and the technical maturity of the mission. Its quantitative usefulness and application potential within the specific multidisciplinary research fields are also clearly demonstrated in this chapter.

– Chapter 4 addresses the mission goal and its specific objectives in the context of the observation requirements and their transfer to geophysical parameters and associated data products. In this respect, it confirms that the GOCE mission, with its outstanding measuring capabilities, would be unique in obtaining new quantitative knowledge of the Earth's gravity field and its geoid reference surface.

– Chapter 5 provides a short overview of the various mission elements such as: the space and ground segments, the necessity for ground observations, the contribution from other satellite missions, and mission performances.

– Chapter 6 provides a complete summary description of the proposed technical system concept (space and ground segments). The technical maturity is, in particular, emphasised in the context of meeting the observation requirements addressed in Chapter 4.

– Chapter 7 continues with a discussion of data processing including a description of techniques and algorithms. The overall scheme in the processing chain is described and it clearly demonstrates the feasibility of transforming the raw data via calibration and validation to geophysical data products.

– The comparison of expected mission performance versus performance requirements is provided in Chapter 8. This draws on the main findings of the previous chapters, and uses dedicated error analysis and end-to-end simulation tools. The expected instrument performance is then converted to expected science performance, demonstrating that the key specific objectives (discussed in Chapter 3) within solid Earth physics, absolute ocean circulation, ice sheets, and geodesy can indeed be achieved.

– Programme implementation, including development schedule, risks and international collaboration, is discussed in Chapter 9. In particular, drawing on the previous chapters, Chapter 9 discusses GOCE in the context of other related missions, concluding that the proposed launch in 2004 would be very timely to the scientific community.

2 Background and Scientific Justification

Current knowledge of the Earth's gravity field and its geoid, as derived from various observing techniques and sources, is incomplete. Within a reasonable time, substantial improvement can only come by exploiting new approaches based on satellite gravity observation methods. The purpose of this chapter is to provide an overview of the rationale that leads from the science case to the proposed mission concept underlying GOCE.

2.1 Science Case

For a better understanding of the physics of the interior of the Earth, of the dynamics of the oceans and of the interaction of continents, ice and ocean in sea-level studies (as well as for better orbits and height systems in science and engineering), it is necessary to significantly improve our knowledge of the gravity field of the Earth, both in terms of accuracy and spatial resolution. This need has been emphasised over the years by various international bodies and in particular by the International Union of Geodesy and Geophysics (IUGG), and two of its associations, the International Association of Geodesy (IAG) and the International Association for the Physical Sciences of the Oceans (IAPSO).

Only by means of satellites can this be achieved globally, homogeneously and within a reasonable time period. However, in order to meet the accuracy and resolution requirements for the gravity field by means of a space mission, one has to deal with the attenuation of the gravity field at satellite altitude. The Earth Explorer Gravity Field and Steady-State Ocean Circulation Core Mission (GOCE) will achieve this by employing, for the first time in space, the concept of gradiometry, i.e. the measurement by a satellite instrument of the second derivatives of the Earth's gravitational potential (see Annex).

The gravity field plays a peculiar dual role in Earth sciences. On the one hand, by comparing the actual field with that of an idealised Earth body (e.g. an idealised Earth in hydrostatic equilibrium) deviations, called gravity anomalies, can be derived. These indicate the state of mass imbalance in the Earth's interior and provide important insights into the dynamics of the planet. Gravity anomalies are one of only three means available to look into the structure of the Earth's interior, the other two being the analysis of the propagation of seismic waves and magnetometry. In this sense, the gravity field provides a mirror into the Earth's interior (see lower part of Fig. 1.1).

On the other hand, the geoid (i.e. the equipotential surface at mean sea-level of a hypothetical ocean at rest) serves as the reference surface for all topographic features, whether they belong to land, ice or ocean (see upper part of Fig. 1.1). The geoid is defined purely by the Earth's gravity field and its accuracy will benefit from any improvement in the latter's precision and spatial resolution. When mountain

topography is measured (e.g. by remote sensing) the accuracy with which the geoid is determined plays no significant role. However, in all cases involving small height differences, such as in engineering and geodesy, or in studies of ice motion, sea-level changes or ocean circulation, requirements for an accurate knowledge of the geoid, in terms of precision and resolution, are extremely high.

Three brief examples are used below to demonstrate the expected impact of the GOCE mission on studies of the interior structure of the Earth, absolute ocean circulation and the unification of height systems.

Solid-Earth Physics

Assume a gravity anomaly model of the Alps derived from terrestrial measurements (Fig. 2.1 upper panel). Then, given a Digital Terrain Model (DTM) of the Alps and an appropriate model of rock densities, one can calculate the terrain's gravity effect and subtract it from the given anomaly model (Fig. 2.1, panels of the second row). This is like generating a gravity-anomaly field map for the Earth without topography. Surprisingly, the remaining field (Fig. 2.1 lower panel) is only slightly smoother and it is even larger in amplitude than the original anomaly field. The well-known explanation of this observation is isostasy, i.e. the concept of dynamic support or static compensation of all visible topography and of the mass deficit of the oceans.

The remaining anomaly field is an expression of the state of mass imbalance and ultimately of the density anomaly structure in the Earth's lithosphere and mantle. It is directly related to a large variety of solid-Earth processes, currently not well understood. However, the translation of the gravity anomaly to the density anomaly field is an inverse problem. Nowadays seismic tomography is providing excellent three-dimensional views of the seismic velocity anomaly field in the Earth's mantle and in the lithosphere in some selected regions. Again, there is no easy way to translate the anomalous velocity into the corresponding anomalous density structure (see Ricard and Froidevaux, 1990).

The combination of the two, i.e. of the residual gravity anomaly field and three-dimensional seismic tomography, supported by information from deformation and displacement measurements made at the Earth's surface, by laboratory research on the physical/chemical properties of mantle material and of magnetic anomalies in the crust and lithosphere, is of tremendous promise. It will significantly improve our understanding, in particular, of the continental lithosphere and of the interaction on the upper mantle with the lithosphere (see section 3.2). The key objective is not the gravity anomaly field itself, but the anomalous density structure derived from it.

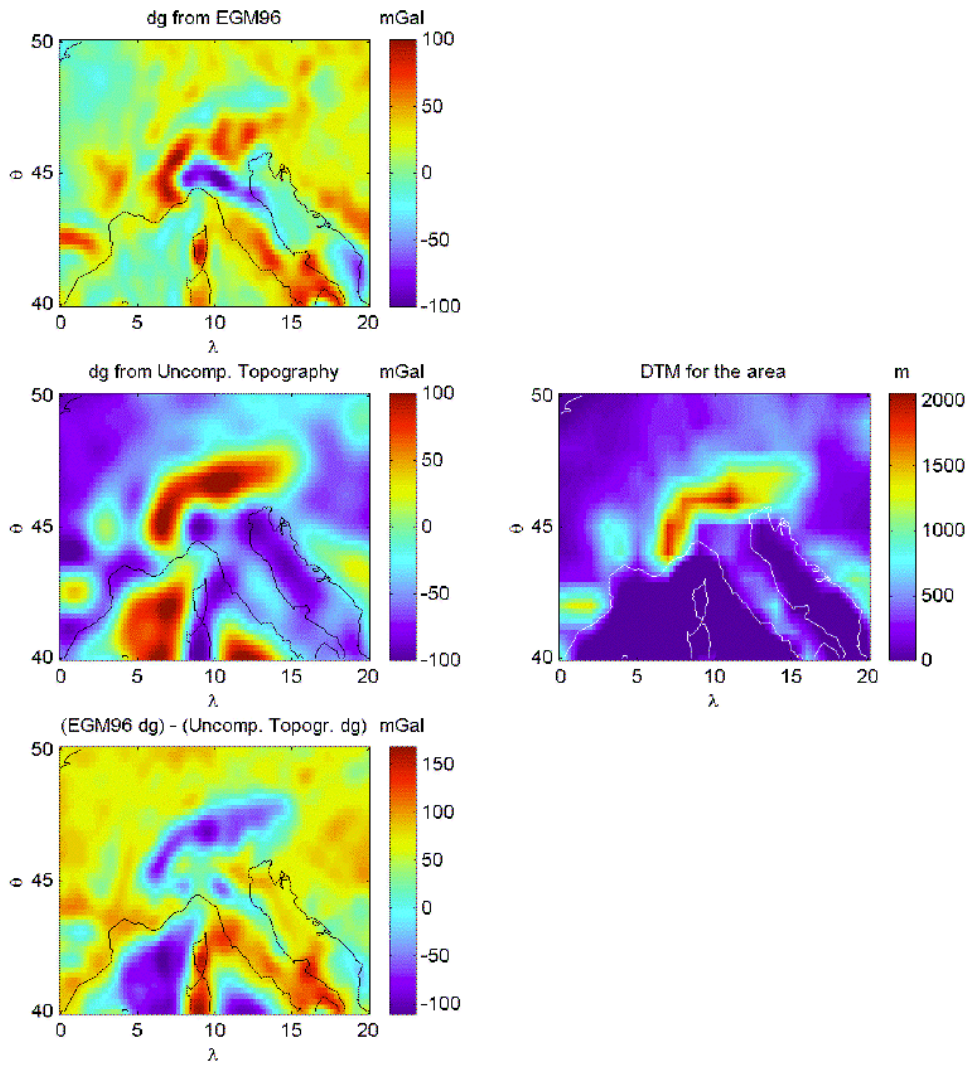

Figure 2.1. *Observed anomalous gravity field of the Alps (upper panel), terrain model of the same region (middle panel, right), synthetic anomalous gravity field as derived from the terrain model (middle panel, left); difference between observed and synthetic gravity field reveals inhomogeneous density structure in the lithosphere (lower panel).*

Absolute Ocean Circulation

Given the observations for GOCE in terms of gravity field determination, the shape of the marine geoid in radial direction can be determined with cm precision down to length scales of 100 to 200 km (see Chapters 3 and 4). Satellite radar altimetry is determining the actual ocean surface with approximately the same precision. The deviation of this mean ocean surface, as obtained from altimetry, from the geoid is the ocean steady-state dynamic topography. As most ocean currents on long time scales

are in geostrophic balance, dynamic ocean topography can be directly translated into ocean surface circulation. The principle is briefly illustrated in Figure 2.2.

With data from past, present and future satellite altimetry missions, this method is able to provide long-term global determinations of absolute ocean surface circulation. Furthermore, as explained in section 3.3, ocean surface circulation determines the mean transport of heat and mass by the ocean. Despite the fact that these are currently not properly quantified, they are recognised to be important elements of climate.

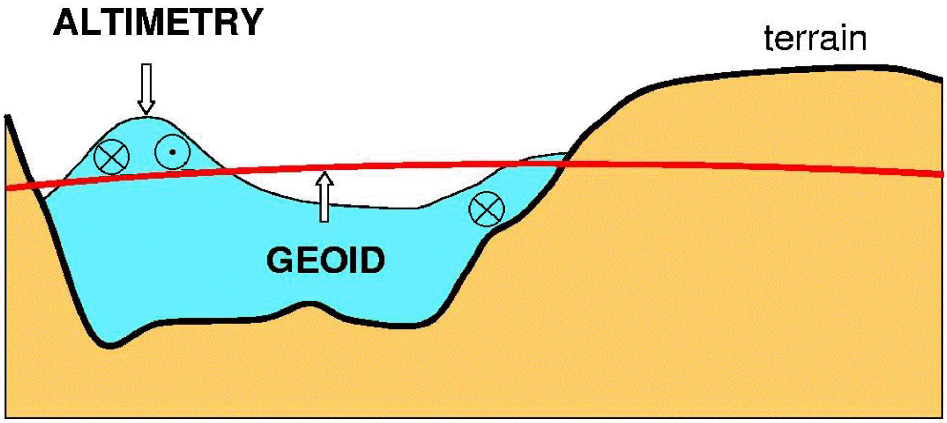

Figure 2.2. *The geoid defines the idealised ocean surface at rest. Its deviation from the actual mean ocean surface as derived from altimetry is the dynamic* ocean surface topography.

Geodesy

On land and ice sheets, the difference between ellipsoidal heights (as measured by the Global Positioning System (GPS)) and the geoid obtained from GOCE gives 'pseudo-levelled' or orthometric heights. This differentiation opens the prospect of an extremely efficient and accurate method of height determination for science, mapping and engineering. In addition, all existing height systems could be transferred to one global reference level. This, as well as the additional benefits of a global, accurate and detailed knowledge of the Earth's gravity field, e.g. for orbit determination and inertial navigation, is discussed in section 3.5.

2.2 State-of-the-Art of Gravity Field Determination

2.2.1 Theoretical Foundation

Gravitational acceleration as expressed by Newton's fundamental law of gravitation is a three-dimensional vector field. Its dominating feature reflects the almost spherical shape of the Earth, the well known 9.8 m/s^2. The main deviations from a spherical field reflects the Earth's rotation and oblateness. Here in this section the focus of interest is in the important effect of much smaller deviations due to the gravitational attractions of a wide range of mass inhomogeneities at the Earth's surface and in its interior.

For global gravity field analysis, the Earth's gravitational potential is represented by a spherical harmonic series, cf. (Heiskanen and Moritz, 1967):

$$\begin{aligned} V(r,\theta,\lambda) &= \frac{GM}{R}\sum_{l=0}^{\infty}\left(\frac{R}{r}\right)^{l+1}\sum_{m=0}^{l}\overline{P}_{lm}(\sin\theta)(\overline{C}_{lm}\cos m\lambda + \overline{S}_{lm}\sin m\lambda) = \\ &\frac{GM}{R}\sum_{l=0}^{\infty}\left(\frac{R}{r}\right)^{l+1}\sum_{m=-l}^{l}K_{lm}Y_{lm}(\theta,\lambda) \end{aligned} \tag{2.2.1}$$

with $\overline{P}_{lm}$ and Y_{lm} the real and complex valued spherical harmonics of degree and order m, respectively, GM the gravitational constant (G) times mass (M) of the Earth and R the Earth's mean radius. In satellite applications, $\{r, \theta, \lambda\}$ are the spherical co-ordinates of the spacecraft. With $r = R + h$ and h the altitude of the satellite, the factor $(R/r)^{l+1}$ describes the field attenuation with altitude. The series coefficients $\overline{C}_{lm}$ and $\overline{S}_{lm}$ (or in complex form K_{lm}) are to be determined. They are the fundamental gravity field unknowns. The infinite series is usually truncated at the maximum resolvable degree $l = L$, which can be translated into a corresponding spatial-scale (half wavelength given in km) D with

$$D = 20000/L \tag{2.2.2}$$

The series coefficients allow the determination of geoid heights (measured in metres above an adopted reference ellipsoid) with:

$$N(\theta,\lambda) = R\sum_{l=2}^{L}\sum_{m=0}^{l}\overline{P}_{lm}(\sin\theta)\left[\overline{C}_{lm}\cos m\lambda + \overline{S}_{lm}\sin m\lambda\right] \tag{2.2.3}$$

and of gravity anomalies (measured in mgal) by

$$\Delta g(\theta,\lambda) = \gamma\sum_{l=2}^{L}(l-1)\sum_{m=0}^{l}\overline{P}_{lm}(\sin\theta)\left[\overline{C}_{lm}\cos m\lambda + \overline{S}_{lm}\sin m\lambda\right] \tag{2.2.4}$$

where γ is mean gravity (see also Annex).

Alternatively, the gravitational potential can be expressed in a system of orbit elements (for a circular orbit) as

$$V(r,u,\Lambda) = \frac{GM}{R}\sum_{l=0}^{L}\left(\frac{R}{r}\right)^{l+1}\sum_{m=-l}^{+l}\sum_{k=-l}^{+l}K_{lm}F_{lmk}(I)\exp[i(ku+m\Lambda)] \qquad (2.2.5)$$

with F_{lmk} being the inclination functions (Kaula, 1966), I the orbit inclination, $\Lambda = \Omega - \theta_G$ the difference in longitude between the Greenwich meridian and the longitude of the ascending node, and u the argument of latitude of the satellite in the orbit plane.

From the gravitational potential, any other gravity function can be deduced quite easily. This includes geoid heights (eq. 2.2.3), gravity anomalies (eq. 2.2.4) and the gravitational acceleration vector. For gradiometry, second-order derivatives (with respect to the three spatial directions), the so-called gravitational gradients, are of particular interest. The nine second-order derivatives form a symmetric 3×3 matrix where the trace (diagonal) is zero in empty space. The radial component of the gravitational gradient can be expressed as:

$$V_{zz} = \frac{\partial^2 V}{\partial z^2} = \frac{GM}{R}\sum_{l=0}^{L}\frac{(l+1)(l+2)}{R^2}\left(\frac{R}{r}\right)^{l+3}\sum_{m=-l}^{+l}\sum_{k=-l}^{+l}K_{lm}F_{lmk}(I)\exp[i(ku+m\Lambda)] \qquad (2.2.6)$$

In this expression it is important to note that the 'differentiation factor' $(l+1)(l+2)$ can counteract the attenuation factor $(R/r)^{l+3}$. The corresponding expressions for orbit perturbations Δx, Δy and Δz in the along-track, cross-track and radial directions for all second derivatives of the gravitational potential are summarised in Table 2.1.

In the case of Δy, V_{xy} *and* V_{yz} a modified inclination function has to be used (Sneeuw, 1994). The parameter $\beta = k\dot{u} + m\dot{\Lambda}/n$ is the normalised orbit frequency, with n the mean orbit frequency.

Δx	$i\dfrac{2(l+1)\beta - k(\beta^2+3)}{\beta^2(\beta^2-1)n^2R}$	$\left(\dfrac{R}{r}\right)^{l+2}$		
Δy	$\dfrac{1}{(1-\beta^2)n^2R}$	$\left(\dfrac{R}{r}\right)^{l+2}$		
Δz	$\dfrac{(l+1)\beta - 2k}{\beta(\beta^2-1)n^2R}$	$\left(\dfrac{R}{r}\right)^{l+2}$		
V_{xx}	$\dfrac{-(k^2+l+1)}{R^2}$	$\left(\dfrac{R}{r}\right)^{l+3}$	-1400	3/8
V_{yy}	$\dfrac{k^2-(l+1)^2}{R^2}$	$\left(\dfrac{R}{r}\right)^{l+3}$	-1400	3/8
V_{zz}	$\dfrac{(l+1)(l+2)}{R^2}$	$\left(\dfrac{R}{r}\right)^{l+3}$	+2800	1
V_{xy}	$\dfrac{-ik}{R^2}$	$\left(\dfrac{R}{r}\right)^{l+3}$	Small	1/8
V_{xz}	$\dfrac{-ik(l+2)}{R^2}$	$\left(\dfrac{R}{r}\right)^{l+3}$	≈10	1/2
V_{yz}	$\dfrac{l+2}{R^2}$	$\left(\dfrac{R}{r}\right)^{l+3}$	small	1/2

Table 2.1. *Sensitivity coefficients that relate observable orbit perturbations and gradiometric components to the unknown spherical harmonic coefficients (e.g. compare to eq. 2.2.6). The expressions are given for the along-track, cross-track and radical perturbations, Δx, Δy and Δz, respectively, that can be measured by SST, and for the second derivatives V_{xx} ,V_{yy} ,V_{zz} , V_{xy}, V_{xz} ,V_{yz} , measurable by satellite gradiometry. Each of these quantities exhibits a characteristic 'view' on the Earth's gravitational field. Also shown (in the two right columns) are the order of magnitudes of the gradiometer components, i.e. the average size (DC value in Eötvös) of each of the components and the average ratio of the individual signal spectral powers with respect to that of the dominant radial component V_{zz}.*

In gravity field studies the average signal strength (i.e. the power spectral density (PSD)), is expressed in terms of degree variances c_l, where

$$c_l = \sum_{m=0}^{l}\left[\bar{C}_{lm}^2 + \bar{S}_{lm}^2\right] = \sum_{m=-l}^{l}\left|K_{lm}\right|^2 \tag{2.2.7}$$

or in terms of their square roots, the root-mean-square (RMS) value per degree. It can be shown that on the Earth's surface the degree variances follow the rule of thumb, according to Kaula (1966):

$$c_l = 1.6\frac{10^{-10}}{l^3} \quad \text{(dimensionless)} \tag{2.2.8}$$

i.e. the field strength tapers off with $1/l^3$. At satellite altitude, this attenuation effect is increased by the $(R/r)^{l+1}$ term. For high-resolution gravity field determination by satellite the main goal is to counteract this attenuation term.

2.2.2 Available Gravity Data

Presently three gravity data sources are available.

a) *Mean gravity anomalies*, taken typically over areas of 100 x 100 km^2 or 50 x 50 km^2, are derived from terrestrial gravimetry in combination with height measurements and from ship-borne gravimetry. Their accuracy depends on data density and the precision of the height and gravity measurements. Before the late 1980s, mean values of acceptable accuracy were available only for North America, Western Europe and Australia. In recent years, due to an enormous effort to encourage data exchange, the situation has significantly improved.

The Bureau Gravimétrique International (BGI) and the National Imaging and Mapping Agency (NIMA) are collecting, screening and editing gravity material on a worldwide basis. Airborne gravimetry has been applied with success to some selected areas such as parts of Antarctica and Greenland (e.g. Brozena and Peters, 1994). However, due in particular to the sparseness of data in some large continental areas and the generally poor quality of older sea gravimetry data, severe inconsistencies remain and the geoid precision does not drop much below approximately 50 to 80 cm in most parts of the World. A global map of currently available mean gravity anomalies is shown in Figure 2.3.

b) In ocean areas, *satellite altimetry* can in some sense be regarded as a direct geoid measuring technique. However, after removing time-varying effects, such as tides, by averaging repeated measurements, the resulting stationary sea-surface still deviates from the geoid due to dynamic ocean topography. In fact, this difference, the mean-sea-surface topography, will be seen to be of key importance in oceanography.

For geophysical investigations, the distinction between mean-sea-surface and the geoid is for many applications of minor importance. As a result, altimetry has been applied to the study of the oceanic lithosphere with enormous

success. However, the distinction is essential for oceanography and sea-level studies. In these investigations, a geoid determined completely independently of altimetry is essential.

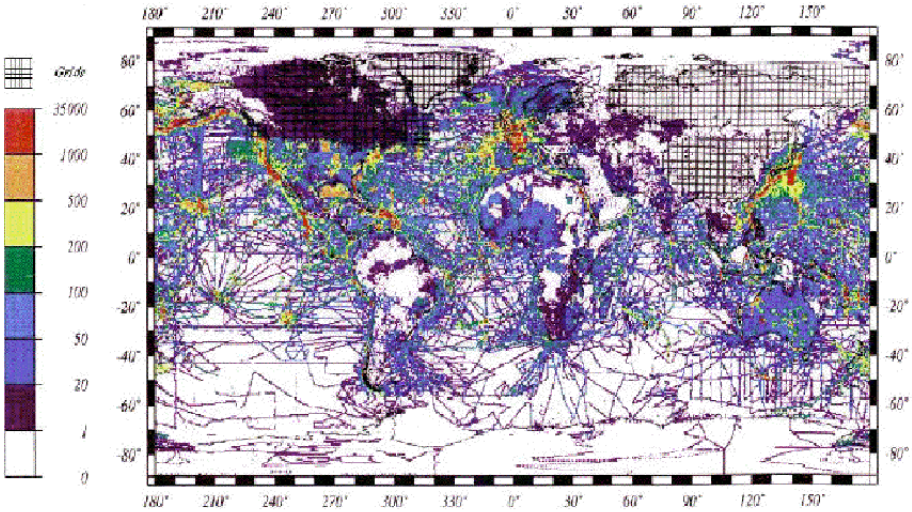

Figure 2.3. *Distribution of presently available gravity measurements in the database of the Bureau Gravimétrique International spanning the last half century. Over some areas, only grid values are available (i.e. no detailed survey data). Greenland was recently mapped by airborne gravimetry.*

c) For more than three decades now, several institutions have determined geopotential models from *satellite orbit analysis*. These are derived from the combined analysis of orbits of a large number of mostly non-geodetic satellites with different orbit elements. They exploit a variety of tracking techniques but primarily laser and Doppler measurements. These models are presented as sets of coefficients $\overline{C}_{lm}$ and $\overline{S}_{lm}$ of a spherical harmonic expansion of the field and they provide information on the long wavelength part of the spectrum only. A representative example of one of the best currently available geopotential models, based purely on satellite orbit analysis (no altimetry, no terrestrial surface gravity), is the GRIM-4S gravity field model (Schwintzer et al., 1997). It is complete to degree = 72 and order m = 72. This corresponds to a spatial half wavelength of D = 300 km.

A ‘stabilisation technique’ has had to be employed to obtain a solution for the complete set of coefficients. However, for some groups of coefficients from this model, the error estimates approach 100% of the expected size of the terms, particularly above degree 36 (or for half wavelength *D* = 560 km). Intrinsic limitations prohibit further significant improvements in resolution by

this approach. A better de-correlation of the individual coefficients is feasible in the future by employing new tracking concepts such as DORIS and, in particular, space-borne GPS that allow (almost) uninterrupted tracking.

Combined models of these three data sources exist, of which the best is the EGM96 (Lemoine et al., 1998). Neither of the above three data sources nor their combination can meet the requirements from solid-Earth physics, oceanography and geodesy, not even to a limited extent. This is why one can say with good reason that "… the gravity field over land areas on Earth is less well known than is that of Venus" (McKenzie, 1994). The solution must therefore come from dedicated gravity field mapping by satellite.

2.3 High-Resolution Gravity Field Determination from Space

As explained above, the traditional techniques of gravity field determination have reached their intrinsic limits. Any advances must rely on space techniques because only they provide global, regular and dense data sets of high and homogeneous quality. It may seem almost paradoxical to obtain the measurements from several hundreds of kilometres up in space, away from the attracting mass anomalies, which one would like to identify and discriminate. This point will be returned to later.

If it is decided to deduce gravity from space, the question is why not extend the traditional method of orbit analysis (see section 2.2). In that technique the satellite, in its orbital motion around the Earth, is considered as a test mass in free fall in the Earth's gravitational field and from this motion the gravitational field is deduced. However, there are two limitations in the method. The first arises because satellites can be tracked from the ground only over short intervals and, as a consequence, the gravity signal 'printed onto the orbit' can only be extracted where it produces an orbit signal of large size such as at or close to orbit resonances. The second occurs because satellite motion is not determined by gravitation alone but disturbed by several types of surface forces of non-gravitational origin. These disturbances corrupt our present gravity models. From an appreciation of these two limitations, three fundamental criteria for any future dedicated satellite gravity mission arise:

Uninterrupted tracking in three spatial dimensions.

Measurement or compensation of the effect of non-gravitational forces.

Orbital altitude as low as possible.

All three criteria can be met by exploiting the concept of satellite-to-satellite tracking in the high-low mode (SST-hl). Thereby a Low Earth Orbiter (LEO) is equipped with a receiver of the U.S. Global Positioning System (GPS) and the Russian counterpart (GLONASS) and with a three-axis accelerometer (see Fig. 2.4a). The receiver 'sees' twelve or more GPS and GLONASS satellites at any time. Their ephemerides are determined very accurately by the large network of ground stations that participate in the International GPS Service (IGS). Taking their orbits and the GPS/GLONASS measurements of the LEO (pseudo-range and carrier phase), the orbit of the LEO can be monitored to cm-precision without interruption and in three dimensions.

In addition, the accelerometer, placed at the satellites' centre of mass measures the non-gravitational forces. The effect of the latter can then be taken into account computationally, or can be compensated for by a drag-free control mechanism. A first satellite of this type (without drag-free control) will be the German CHAMP (Reigber et al., 1996) that will be launched early 2000.

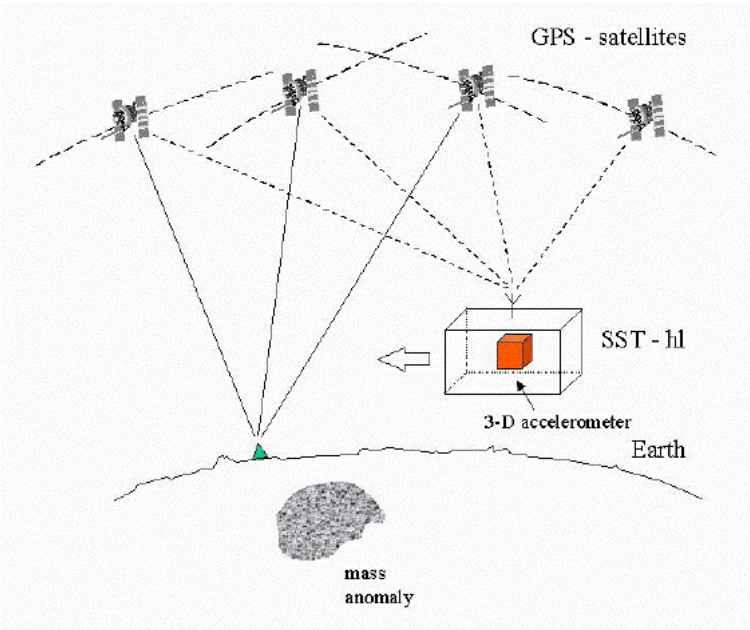

Figure 2.4a. *Concept of satellite-to-satellite tracking in the high-low mode (SST-hl). A low Earth orbiter is tracked by the high orbiting GPS and GLONASS satellites, relative to a net of ground stations. Non-gravitational forces on the low orbiter are measured by accelerometry.*

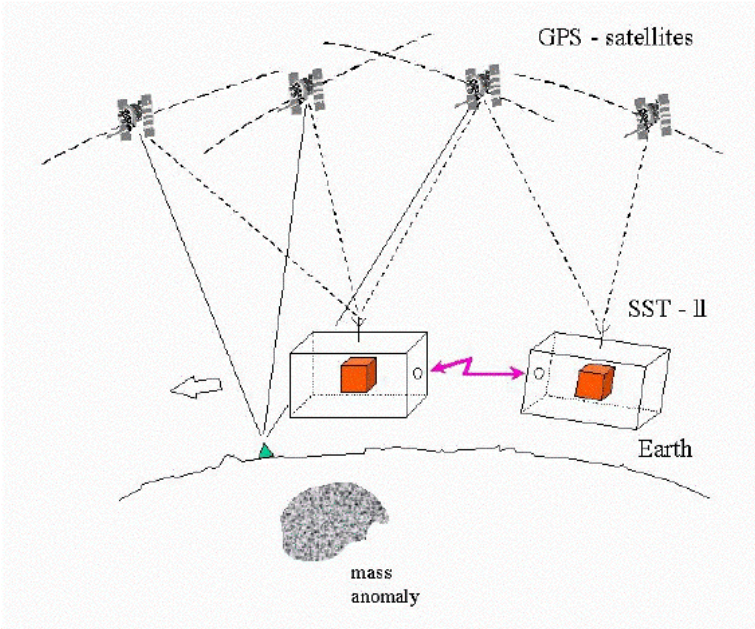

Figure 2.4b. *Concept of satellite-to-satellite tracking in the low-low mode (SST-ll) combined with SST-hl. The relative motion between two low orbiters following each other in the same orbit at a distance of few hundred kilometres is measured by an inter-satellite link.*

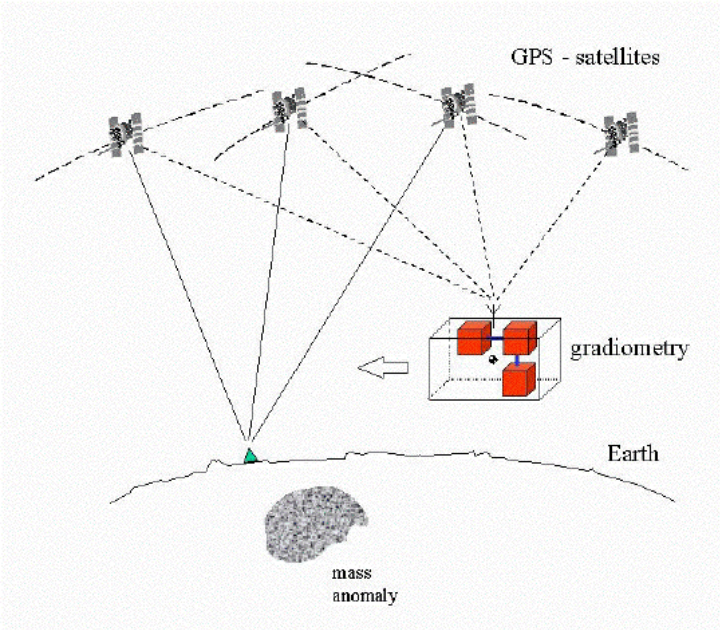

Figure 2.4c. *Concept of satellite gradiometry combined with SST-hl. The second-order derivative of the gravitational potential of the Earth is measured in a low orbiting satellite by differential accelerometry.*

However, even with this configuration and with an altitude as low as 300 or 400 km, the problem of gravity field attenuation prohibits the attainment of really high-spatial-resolution. Thus, a fourth criteria enters:

Counteract gravity field attenuation at altitude.

The classical approach of highlighting the effect of small-scale features in physics is differentiation. Two alternative concepts of differentiation can be conceived. Either one applies satellite-to-satellite tracking in the low-low mode (SST-ll) or satellite gradiometry; both still combined with SST-hl. In the case of SST-ll (see Fig. 2.4b), two spacecraft in essentially the same orbit and a distance of somewhere between 100 and 400 km apart, 'chase each other'. The relative motion between the two satellites is measured with the highest possible precision. Again the effect of non-gravitational forces on the two spacecraft can either be compensated for or be measured. The quantity of interest is the relative motion of the centres of mass of the two satellites, which has to be derived from the inter-satellite link together with the measured acceleration and attitude data. The first experiment of this type will be the US-German mission GRACE, (GRACE, 1998).

The alternative to SST-ll is to apply satellite gradiometry as proposed for GOCE. Satellite gradiometry is the measurement of acceleration differences, ideally in all three spatial directions, between the test-masses of an ensemble of accelerometers inside one satellite (see Fig. 2.4c). The measured signal is the difference in gravitational acceleration at the test-mass locations inside the spacecraft, where of course the gravitational signal stems from all the attracting masses of the Earth, ranging from mountains and valleys, via ocean ridges, subduction zones, mantle inhomogeneities down to the core-mantle-boundary topography. The technique can resolve all these features as they appear in the gravity field. The measured signals correspond to the gradients of the component of gravity acceleration or, in other words, to the second derivatives of the gravitational potential. Non-gravitational acceleration of the spacecraft (for example due to air drag) affects all accelerometers inside the satellite in the same manner and ideally drops out when taking the differences. Rotational motion of the satellite does affect the measured differences, but can be separated from the gravitational signal by separating the measured 3×3 matrix of second derivatives into a symmetric and an anti-symmetric part. Again, a low orbit implies relatively high signals.

Generally speaking, one can now argue that the basic observable in the three cases discussed in section 2.3 (namely SST-hl, SST-ll and satellite gravity gradiometry (SGG)) is gravitational acceleration. With the orbits of the high-orbiting GPS and GLONASS satellite assumed to be known with high accuracy, the case of SST-hl corresponds to an 'in-situ' 3-D position, velocity or acceleration determination of a LEO. For SST-ll, the principle corresponds to the line-of-sight measurement of the range, range rate or acceleration difference between the two low-orbiting satellites.

Finally, in the case of satellite gradiometry, the measurement is of acceleration differences in 3-D over the short baseline of the gradiometer instrument. In short, therefore the principles are:

SST-hl: 3-D accelerometry corresponds to gravity acceleration

SST-ll: inter-satellite link corresponds to acceleration differences between two LEOs

SGG: gradient of gravity components corresponds to the acceleration gradient.

Thus in a mathematical sense it is the transition from the first derivative of the gravitational potential (SST-hl), via the difference of first derivatives over a long baseline (SST-ll) to the second derivative (gradiometry). The guiding parameter that determines sensitivity with respect to spatial-scales of the Earth's gravity field is the distance between the test masses, being almost infinity for SST-hl and almost zero for gradiometry.

The mathematical concept is illustrated by the spectral scheme of Fig. 2.5. The sensitivity parameters (eigenvalues) connecting orbit acceleration $\Delta\ddot{x}$, velocity $\Delta\dot{x}$ and position perturbation Δx describe orbit perturbation theory (n being orbit mean angular velocity, k running from 0 to L). The fundamental problem of any satellite gravity mission is the amplification of the errors by the factor $(r/R)^{l+1}$ when transferring the measured 'signal + noise' from satellite altitude to the Earth's surface. This effect is minimised by:

- flying the test mass as low as possible, and
- not just measuring V or its gradient (= SST-hl), but rather its second order derivatives (= gradiometry).

More details are provided by Rummel (1997).

2.4 GOCE Mission Rationale

GOCE will be the first gravity gradiometry satellite mission. It is specifically designed for the determination of the stationary gravity field – geoid and gravity anomalies – to high accuracy and spatial resolution. It is the only means capable of meeting all of the fundamental criteria described in section 2.3, namely:

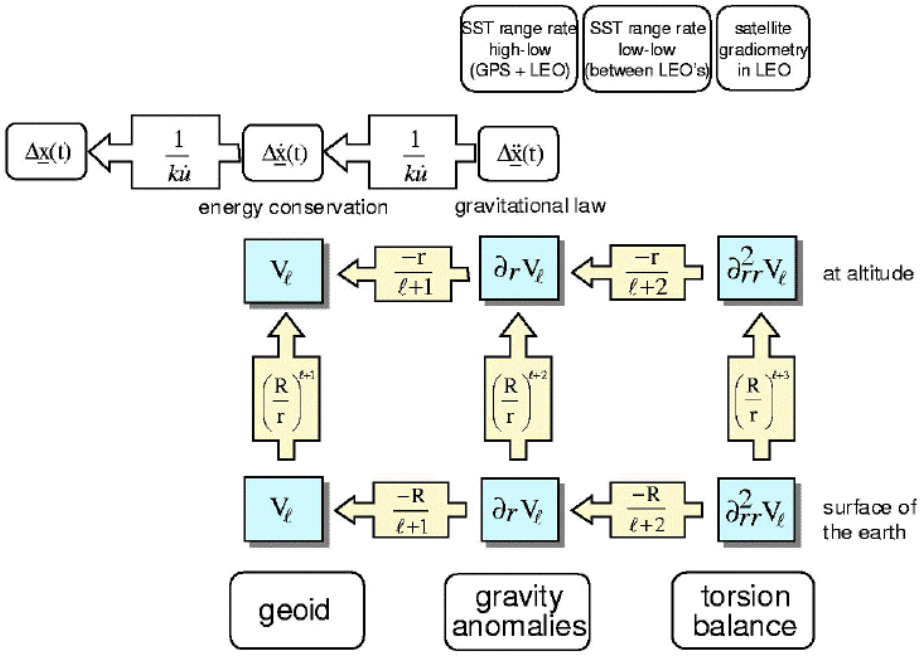

Figure 2.5. *The three fundamental gravity quantities are the potential (geoid), and its first (gravity anomaly) and second derivatives (corresponding to torsion balance measurements), here as a function of spherical harmonic degree* $V_l, \partial V_l/\partial r, \partial^2 V_l/\partial r^2$. *These three quantities are damped by a factor* $(R/r)^l$ *at satellite altitude. Measuring gravity gradients balances the attenuation by the factor* $(l+1)(l+2)$.

- It will be continuously tracked in three dimensions by the systems of GPS and GLONASS satellites, relative to the dense ground network of IGS stations.

- It will control drag forces and eliminate remaining residual effects by differential measurement, the so-called common mode rejection (CMR) principle. Rotational motion will also be controlled, and remaining rotational effects will be determined by a novel combination of measured off-diagonal gradient components and star sensors (Aguirre-Martinez, 1999).
- It will fly in an extremely low and almost polar orbit (Sun-synchronous).
- It will efficiently overcome the problem of attenuation of the gravity field at altitude by the principle of gradiometry.

In addition, gradiometry has the unique and important ability of being able to measure the gravity field in three spatial dimensions independently and without any preferred direction. It therefore permits observations of the gravitational field of the Earth in

three complementary ‘illuminations’ with no directional bias (Fig. 2.6). This indeed suggests that to avoid aliasing of any component of the gravity field into another component, the main components need to be measured individually as can be obtained with GOCE.

2.5 Complementary Space Missions and Airborne Projects

In this section a comparison of the GOCE mission capabilities with other spaceborne gravity field missions and airborne gravity observations is first provided, followed by a brief review of the complementarity of information from other satellite missions.

The expected performances of CHAMP, GRACE and GOCE are compared in Figure 2.7 (further details of this comparison are reported by Balmino et al., 1998). The figure shows the signal degree RMS values according to Kaula’s rule (eq. 2.2.8) and the noise degree RMS of the best available satellite gravity model. Signal and noise line intersect somewhere between $l = 20$ and $l = 30$ ($D \approx$ 1000-660 km).

CHAMP is to be seen as a proof-of-concept mission, as it will be the first time that uninterrupted three-dimensional high-low tracking has been combined with 3-D accelerometry. This technique will not improve our available gravity field models much in terms of accuracy and spatial resolution (see line SST-hl in Fig. 2.7), but it will de-correlate the spherical harmonic coefficients $\bar{C}_{lm}$ and $\bar{S}_{lm}$ significantly and therefore make current models much more reliable.

GRACE will be the first SST-ll mission. It will improve the accuracy of the spherical harmonic coefficients at long and medium spatial-scales by up to three orders of magnitude. This will allow the measurement of the temporal variations in the gravity field, such as those due to bottom-pressure variations, seasonal and annual variations in groundwater and soil-moisture levels, changes in the masses of the Antarctic and Greenland ice sheets or atmospheric pressure changes (see NRC, 1997). One could refer to this as a ‘spyglass effect’. The high slope of the noise line of GRACE (Fig. 2.7) suggests that any decrease or increase of mission performance has little effect on its spatial resolution, but a large effect on its ability to resolve temporal variations.

The noise line of *GOCE*, on the other hand, is much flatter, leading to a much higher spatial resolution. One could refer to it as ‘extended spectral window effect’ (Fig. 2.7). By employing gradiometry, the noise line is roughly decreased by a factor ‘l -squared’ as compared to the case of SST-hl. Here an increase in mission performance has only a minor effect in terms of temporal resolution, but a large effect on its ability to resolve spatial variations. One can expect that gravity signatures as short as 65 km will be resolved with GOCE. Thus it is concluded that the two missions, GRACE and GOCE, are complementary, with GRACE focusing in particular on the temporal variations of the gravity field and GOCE on attaining maximum spatial resolution.

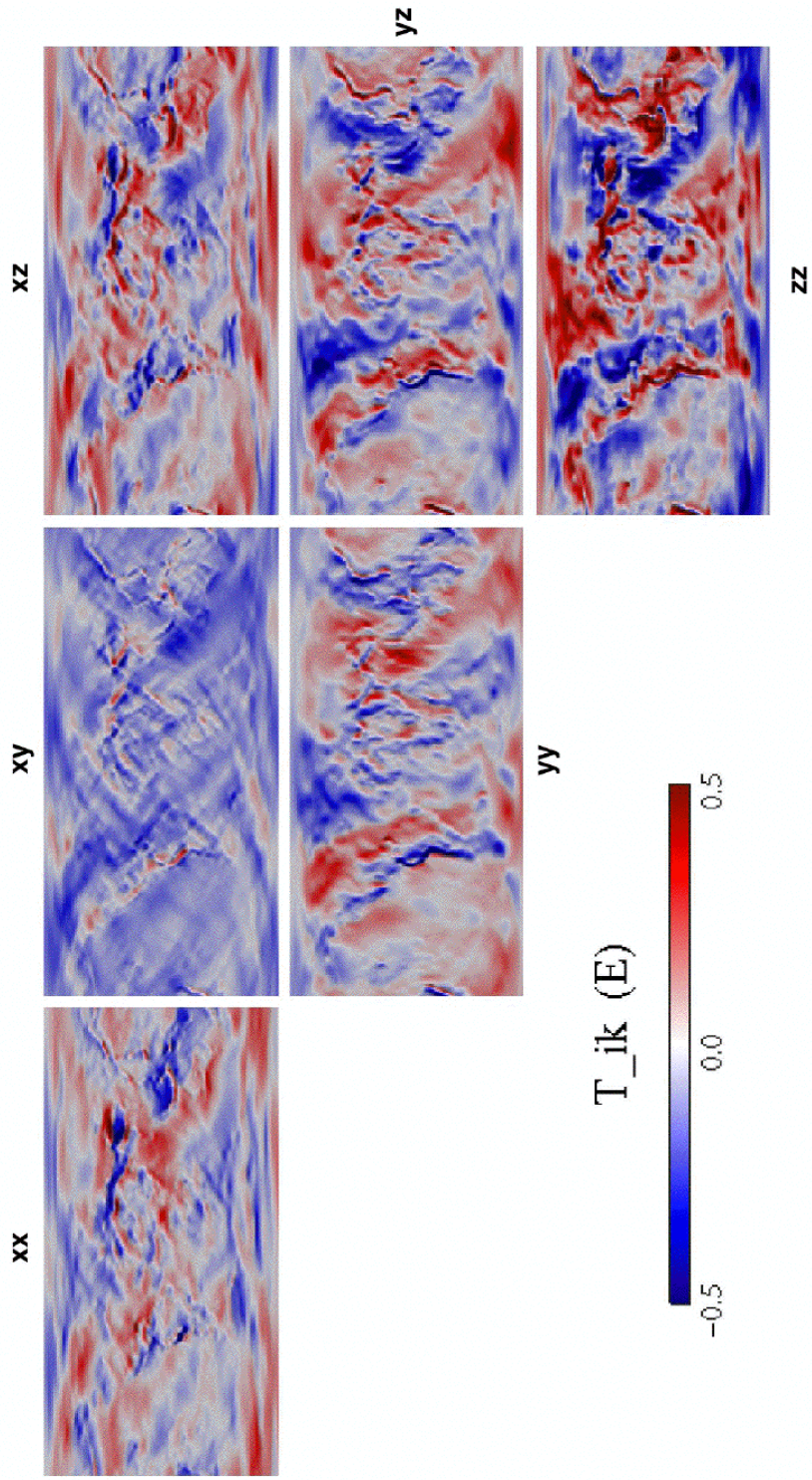

Figure 2.6. *View of the Earth's gravity field, broken down into the major components and its cross-components. Note that the yx, zx, and zy components (not shown) equal the xy, xz and yz components respectively, and that the sum along the diagonal is zero.*

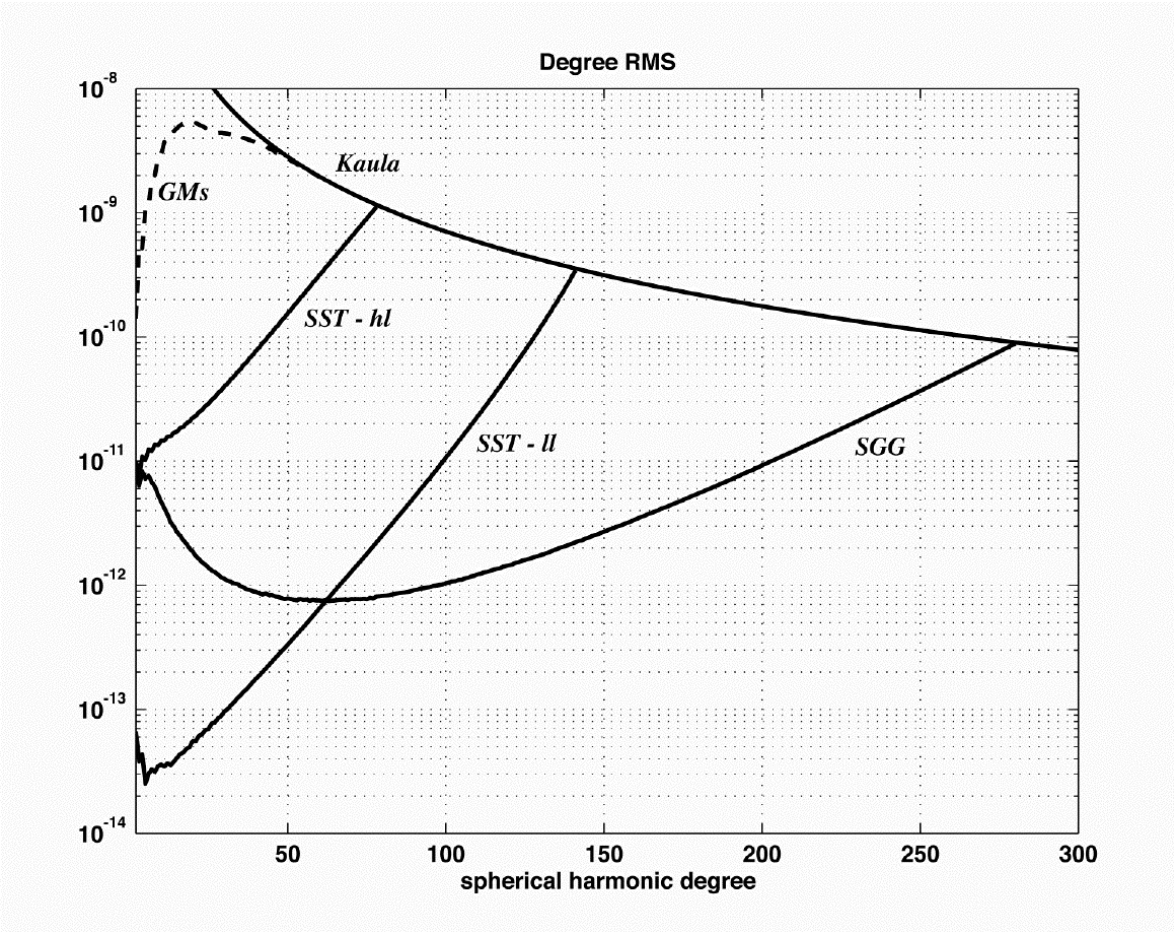

Figure 2.7. *Representative error degree variance spectra (see Annex) of the gravity mission concepts SST-hl, SST-ll and satellite gradiometry in comparison with one of the best currently available satellite gravity models (GMs) and with the signal degree variances of the gravity field (Kaula). The high precision of SST-ll at long and medium length scales and the high-spatial-resolution of gradiometry are apparent here.*

These various complementary satellite gravity field concepts as well as those from other satellite mission and airborne observations are summarised in Table 2.2. An airborne gravimetric sensor, for instance, measures the sum of gravity and aircraft acceleration. However, by exploiting differential GPS, aircraft acceleration can be determined and separated from the gravity signal. Thus, although still affected by various systematic error sources, airborne gravimetry has been shown to be able to produce very useful results. Projects at present concentrate on the polar regions, where satellite gravity missions may leave small gaps due to their non-polar inclinations (Brozena, Peters and Salman, 1997 or Wei and Schwarz, 1997).

Past, present and future altimeter missions, such as GEOSAT, TOPEX/ POSEIDON, ERS-1 and ERS-2, in the near future Envisat, Jason and the planned ice altimeter missions ICESAT and CRYOSAT as well as SAR interferometry (INSAR) are all

important complements to GOCE for its application to oceanography and ice-sheet research. In ocean areas, the difference between the quasi-stationary ocean surface (freed from all time-varying effects) and the geoid yields steady-state ocean circulation. Over ice sheets, taking an approach similar to that applied to the determination of sea-floor bathymetry from altimetry, the combination of ice-sheet topography (or elevation) and the measured gravity anomaly field would permit better determination of bedrock topography and, therefore, provide important new input to the study of the dynamics of continental ice sheets.

Complementary Data	
Proof-of-concept of SST-hl combined with 3-D accelerometry	CHAMP
Temporal variations of Earth gravity field	Available models (tides, atmospheric pressure, ocean variability) and results from GRACE
Gravity field at polar caps and small-scale gravity information in some regions	Available and planned airborne and terrestrial gravimetry data
Solid-Earth physics	Topographic models (DTMs) and seismic tomography as primary data sets, lithospheric magnetic field from ØERSTED and CHAMP and planned magnetometry satellite missions
Oceanography	Data sets from past, current and future ocean altimetry (GEOSAT, T/P, ERS-1 & 2, Envisat, Jason etc.)
Ice research	Ice altimetry (ICESAT, CRYOSAT) and INSAR
Geodesy	Current and future global satellite positioning and navigation systems (SLR, VLBI, DORIS, GPS, GLONASS, GNSS-2)
Sea-level	Global tide-gauge network (GLOSS), GPS/DORIS, satellite ocean and ice altimetry and GPS

***Table 2.2**. Overview of the complementary space and in-situ data to be used in combination with GOCE data.*

2.6 Summary

Insufficient knowledge of the Earth's global gravity field is presently the weak link in the realisation of a global integrated geodetic/geodynamic observing system, which combines the three components:

– geometry and surface deformation (GPS, differential INSAR, ocean and ice altimetry),

– the Earth rotation (VLBI, satellite and lunar laser ranging, GPS, DORIS), and
– the Earth's gravity field.

Once all three components have attained the same level of accuracy and spatial/temporal resolution, their combination will allow the monitoring and modelling of a series of geodynamic, ice and ocean processes as well as their interactions. The connections between these three components and the link to geophysical processes are shown in Fig. 2.8 (see also ESA SP-1227, 1998; pp. 82-83). GOCE will make this observing system complete.

In summary, the GOCE Mission is clearly timely and well justified in the context of the current scientific understanding, ongoing and planned international activities and the potential delta that it would provide. The latter is clearly documented in Chapters 3, 4 and 8. In particular

– GOCE provides unique data of relevance to Theme 1 of 'The Living Planet Programme' (ESA SP-1227, 1998) except for in the context of the magnetic field.
– GOCE will address science objectives associated with the determination of the gravity anomaly field and the geoid, the importance of which have long been emphasised in the strategic programme and in the literature (e.g. Williamstown Report, 1969; ESA, 1978; NASA, 1987; Mueller and Zerbini, 1989; ESA, 1986; ESA, 1991; ESA, 1994; Balzer et al., 1996), in resolutions by scientific unions and their associations (IUGG, IAG, IAPSO), and international programmes such as WCRP, WOCE and CLIVAR.
– The extremely high accuracy and spatial resolution of gravity field and geoid recovery that are possible with GOCE are achieved by employing the principle of gravity gradiometry, for the first time, in a satellite.

Experience from past and on-going studies suggests the importance of combining European skills in orbit mechanics, aerospace engineering, numerical mathematics and gravity field analysis with the aim of producing the best possible global geoid and gravity anomaly field model products.

The signal and noise behaviour of the complete system has been analysed by means of a comprehensive closed loop simulation,. Whereas in an open loop, end-to-end simulation, system parameters and spectral representations have been propagated to global gravity field and geoid performance. These important issues are fully addressed in Chapters 4 and 8. Moreover, in a series of studies the impact of such potential data sets has been quantified in great detail for solid Earth physics, absolute ocean circulation, ice sheet and geodesy. The results are further presented in Chapters 3 and 8.

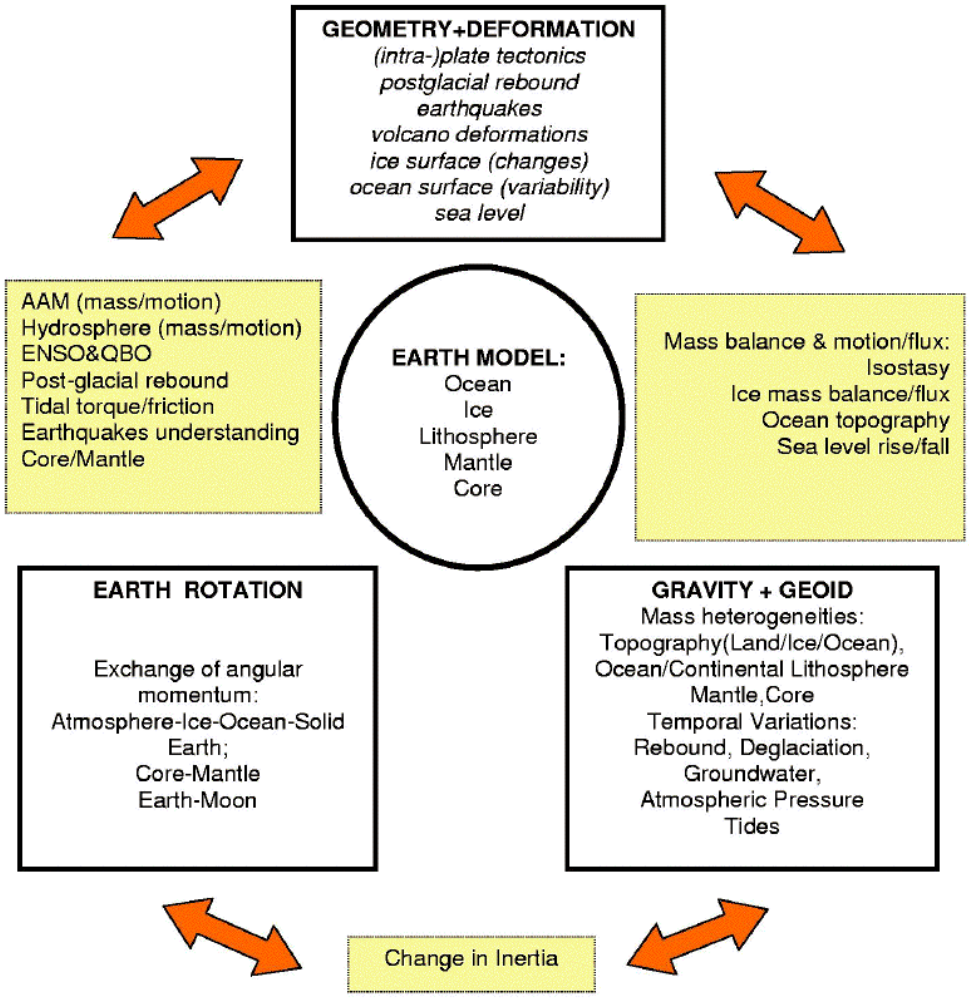

Figure 2.8. *Earth processes and their observability in an integrated geodetic/ geodynamic observing system with the components of geometry, Earth rotation and gravity field/geoid.*

3 Research Objectives

3.1 Introduction

The Earth's geological evolution has resulted in it possessing a shaped gravity field which departs significantly from the ellipsoid (a sphere flattened at the poles) one would expect for a rotating radially-symmetric planet. The difference between the real, measured values of gravity and those that would be produced by the idealised body is denoted as the 'gravity anomaly'. Anomalies range typically between ± 300 mgal (or $\pm 3 \times 10^{-4}$ g), with higher magnitudes in active tectonic areas. Gravity anomalies are a measure of the imbalance in mass between that of the surface topography and the corresponding density contrasts beneath. They can be related to density anomalies in the solid Earth and ultimately to internal stresses and motions. A precise, high-resolution measurement of the shape of the gravity field describes a set of 'fingerprints' of past and on-going geological processes which have to be understood if the planet's overall geo-biosphere, including man's influence upon it, is to be properly monitored and protected.

The 'geoid' (a 'level surface' the average radial distance of which from the centre of the Earth is the same as that of the mean-sea-surface, or MSS, and which would correspond to sea-level if no currents were flowing) departs from the Earth's ideal 'ellipsoidal figure of equilibrium' by ± 100 m as a consequence of the same density inhomogeneities in the structure of the lithosphere and mantle that result in the gravity anomalies. The special significance of the geoid is that its shape defines the local horizontal and on land provides the reference surface for 'topography'.

On short length scales, the geoid is almost a plane, so that we can tell immediately from the orientation of another surface whether or not it is 'sloping'. At larger scales, we need to know the detailed shape of the geoid to determine whether objects (such as water or ice masses or even the 'solid' Earth over long time scales) will fall or roll or flow 'downhill' if unobstructed, by moving towards a lower gravitational potential. In other words, moving to another surface of constant gravitational potential nearer to the centre of the Earth and approximately parallel to the geoid. For example, the water surface in the open ocean, which for some reason does not happen to have a shape corresponding to that of the geoid, will attempt to restore itself to that surface by flowing.

The single most important piece of information required to address questions about the dynamics of ocean circulation is the difference between the shape of the sea-surface and that of the geoid. This difference is known as the 'dynamic topography' and varies typically within the range ± 1 m in most parts of the ocean. Elevation above the geoid, or 'orthometric height', also plays an important, if not always the major, role in determining ice-sheet flows. Dynamic topography and orthometric height can be measured on a near-global basis only by observing 'geocentric height' (heights relative to the centre of the Earth) by means of satellite radar altimetry (plus precise orbital

analysis), the Global Positioning System and other advanced geodetic techniques, and by subtracting geoid heights determined from a gravity mission. The former is now technically straightforward and routine; the provision of a precise geoid model is the main subject of this proposal.

This chapter highlights the importance of precise, high-spatial-resolution information on the shape of the geoid to a wide range of research into processes in the solid Earth, oceans and ice sheets and for advanced geodetic applications. The importance stems from the considerable interest (within the scientific community and the general public) in research into climate change and anthropogenic influences on the World's environment, into understanding of earthquake mechanisms, and into the shortage of natural resources.

The scientific objectives of the GOCE Mission are based on the unique capability of a gravity gradiometer to provide an accurate and detailed global model of the Earth's gravity field and geoid. This model will, in turn, serve the following multi-disciplinary scientific objectives:

- to provide new understanding of the physics of the Earth's interior including geodynamics associated with the lithosphere, mantle composition and rheology, uplifting and subduction processes
- to provide, for the first time, a precise estimate of the marine geoid, needed for the quantitative determination, in combination with satellite altimetry, of absolute ocean currents and their transport of heat and other properties
- to provide estimates of the thickness of the polar ice sheets through the combination of bedrock topography derived from space gravity and ice-sheet surface topography
- to provide a better global height reference system for datum connection, which can serve as a reference surface for the study of topographic processes, including the evolution of ice-sheets and land-surface topography.

Advances in each of these areas of research will benefit developments in others. This is further demonstrated towards the end of this chapter in the context of a discussion of global sea-level change, a topic of considerable interest and concern to a large fraction of Europe's and the World's population.

3.2 Solid Earth

3.2.1 Overview

As in the case of other planets, the gravity field of the Earth is an essential quantity for probing its interior structure and for modelling of its dynamical behaviour under various circumstances, such as heating from the interior, redistribution of masses

between solid and fluid parts, and loading of its surface. The investigation is essentially an inverse problem which has no unique solution but, in the Earth's case, it is greatly supplemented by information coming from seismology.

Figure 3.1 provides a simplified picture of an interior section through the centre of the Earth, inferred from geophysical studies. This is intended to help introduce the terminology that will be used to indicate the various layers in the context of the major geodynamical processes that will be discussed and whose physical understanding will gain from a high-resolution gravity mission. The mechanically stiff outer layer is called the lithosphere, which is, in turn, subdivided into an oceanic and a continental part. The major geodynamical processes that involve the oceanic lithosphere are spreading at the ocean ridges and subduction at active continental margins as indicated in the picture. The cold, dense oceanic lithosphere enters the mantle at subduction zones, interacting with the overriding lithosphere, where complicated geodynamical processes, such as back arc opening and volcanism occur. The arrow at the subduction zone indicates the velocity of the plate with respect to the mantle, controlled by the downward pull exerted by the cold subducted plate, the push at the ocean ridge and the basal viscous drag.

One of the major issues relating to the dynamics of ocean plates is the structure and evolution of the region where an ocean plate bends to initiate subduction at an ocean trench. Opening of the back arc basin, volcanism (represented by the volcanic line in the region called back arc in the figure), and rates of subsidence in the trench (indicated by the arrow) are in fact ultimately controlled by the dynamic interaction between the ocean plates and the overriding plates and by the rheological properties of the mantle. Ocean ridges are the locations where the oceanic lithosphere is generated by means of spreading, as shown by the horizontal arrows; subduction and spreading are major plate-tectonics processes.

The continental lithosphere is the location of the periodic glaciation and deglaciation events, at least during the last million years. The last deglaciation ended about 7000 years ago, and the planet is still recovering its isostatic equilibrium after the unloading of the lithosphere due to the melting of the ice-sheets. The response of the planet to these events (stresses) and the associated gravity anomalies depends on crustal and mantle rheologies and lithosphere thickness. This process is called Post-Glacial Rebound (PGR), and will be discussed in the following sections. A major issue related to the structure of the continental lithosphere is the possible existence of deep roots beneath the continents. Deformation of the continental lithosphere under the influence of extensional forces is visible as elongated depressions called rifts that are present in a variety of tectonic environments.

Rheology studies are also important for improving our comprehension of mechanisms that involve the mantle, the portion of the planet beneath the lithosphere down to the core mantle boundary. Mantle convection, depicted by the arrows, is certainly one of these, involving the circulation of mantle material on geologic time-scales. The

dynamics of fast upwelling plumes in the mantle that are responsible for the appearance of hot spots in the lithosphere is also important for these studies.

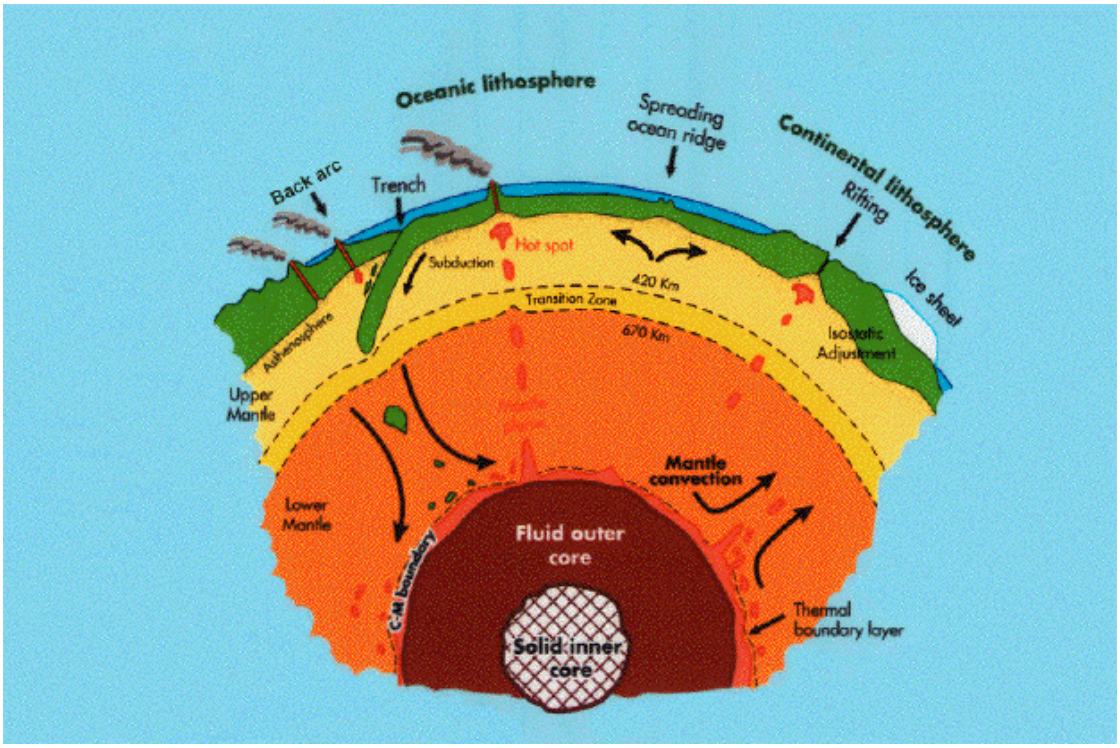

Figure 3.1. *The major dynamic processes of plate tectonics and the layers in which the Earth is differentiated (not to scale). From the outer lithosphere, divided into the ocean and continental parts, the upper mantle, the transition zone and the lower mantle are shown. The fluid outer core and solid inner core are also portrayed. From left to right, subduction and related back arc opening, hot spots and a spreading ocean ridge are shown. For the continental lithosphere, isostatic adjustment following post-glacial rebound is suggested.*

The mantle is subdivided into an upper and a lower mantle by a transition zone, between 420 and 670 km deep, depicted in the figure by the dotted strip. The transition zone plays a major role in the style of convection within the mantle. It is not known today whether there are separate convection regimes in the upper and lower mantles, or interpenetrating convections as numerical simulation suggests. The low-viscosity region beneath the lithosphere and the uppermost part of the upper mantle is called the ‘asthenosphere’, represented by the shaded area above the transition zone in Figure 3.1. Typical length scales for phenomena seen at the surface are 50 to 400 km, depending on their type and mean depth.

What geophysicists are lacking most today is a picture of the gravity field over the continents which could match the information that satellite altimetry has brought over

the oceans (cf. section 2.2), in terms of new information for many unsurveyed areas, homogeneity of data quality and improved resolution. The situation has changed dramatically from what it was about two decades ago when gravity was better (although often poorly) known over the continents with little (or difficult to use) information over oceanic areas. Clearly, considering the difficulties involved in improving the coverage of gravity field surface measurements (even using air-borne techniques), the cost and time associated with the use of classical techniques, only a global, space mission can now bridge the gap within a reasonable time frame. Over areas that are already densely surveyed, it will provide the necessary reference to bring all existing data sets into a homogeneous system, the lack of which today is a serious problem hampering the proper use of many data in global, or even regional models.

What must be recognised is that regional studies provide the framework within which more detailed local studies fit. With an accurate homogeneous gravity field, it will become possible to constrain the more local problems. For instance, a study of regional dynamic interactions between mantle convection and the lithosphere provides constraints on lithospheric strength and stress fields that are critical in understanding sedimentary basin evolution.

Although the resolution to be obtained cannot truly compete with the few kilometre resolution grids coming from satellite altimetry, a gravity mission will yield information over large areas which cannot all be predicted, though some of it, concerning the continental lithospheric structure, upper-mantle convection under the continents and the interaction between mantle convection and lithospheric deformation, has been awaited for a long time.

Last but not least, the quality of the satellite-altimetry-derived gravity field in oceanic areas should not be over-estimated. The present solutions assume that the sea-surface has been properly corrected for dynamical phenomena whereas it is clear that this cannot be done today, especially considering the eddies that translate into artefacts in the gravity field at scales of tens to hundred kilometres (they cannot be completely filtered out by averaging the instantaneous sea-surface, due to their proper motion). This means that the marine gravity field will also be improved by a mission like GOCE, enabling the refinement of many studies and present models of the oceanic lithosphere. Requirements for doing so are 0.5-1 mgal precision at 100-200 km resolution approximately.

3.2.2 Joint Use of Gravity and Seismic Data

The combined use of the three fundamental data sources: seismic records, gravity anomalies and magnetic anomalies, aided by information about the physical behaviour of the Earth’s interior (coming from laboratory studies) and by topographic data sets, are the way to a detailed picture into the dynamics of lithosphere and mantle.

Studies of the joint inversion of gravity and seismic tomographic data (Zerbini et al., 1992) have shown that the combined use of these two data sets (which reduces the mathematical instabilities characterising the inversion procedure) improves significantly the images of the interior of the Earth based on the inversion of tomographic images alone.

Figure 3.2 is an example of a simulation over the lithosphere and upper mantle, for a subduction zone for which the structure is sought in terms of slowness anomalies (anomalies in the inverse of the P-wave velocities, a quantity approximately proportional to the square root of the density). The study performed consists of numerical experiments based on a 2D-model, representing a vertical cross-section of the upper-mantle. The region is partitioned into a set of 150 km $\times$ 60 km cells. The basic slowness field is assumed to be vertically stratified, consistent with the seismic model PREM (Dziewonski and Anderson, 1981). The slab-like structure, reasonably similar to the one that probably exists in the Hellenic arc area, is responsible for negative slowness anomalies in the range -1% to -3% and to the local variation of gravity anomalies (50 to 100 mgals over distances of 100 to 300 km). The results, with and without gravity gradient observables at satellite altitude, demonstrate the impact of the gravity field information on the quality of the inversion process. By varying the parameters of such simulations to determine the sensitivity to gravity field knowledge, the required accuracy and resolution are found to be 1 to 2 mgal and 100 km, respectively.

The derivation of density anomaly models by such methods will be made possible by GOCE and the results will be essential for most studies of the continental lithosphere.

3.2.3 The Continental Lithosphere

Although the continental lithosphere appears passive when compared with the dynamically active oceanic one, which is pushed at ocean ridges and pulled at subduction zones, it is nevertheless the locus of important geodynamical processes, due to collisions with other continental and oceanic plates and to interactions with the asthenosphere and upper mantle. This coupling with the asthenosphere and mantle is due to thermal processes, such as hot spots, diapirs or small-scale convection instabilities, responsible for the formation of sedimentary basins and continental rifting. The continental lithosphere is also subject to tectonic forcings which in many places impact sea-level changes as much as, for example, glacial isostatic adjustment following the Pleistocene de-glaciation.

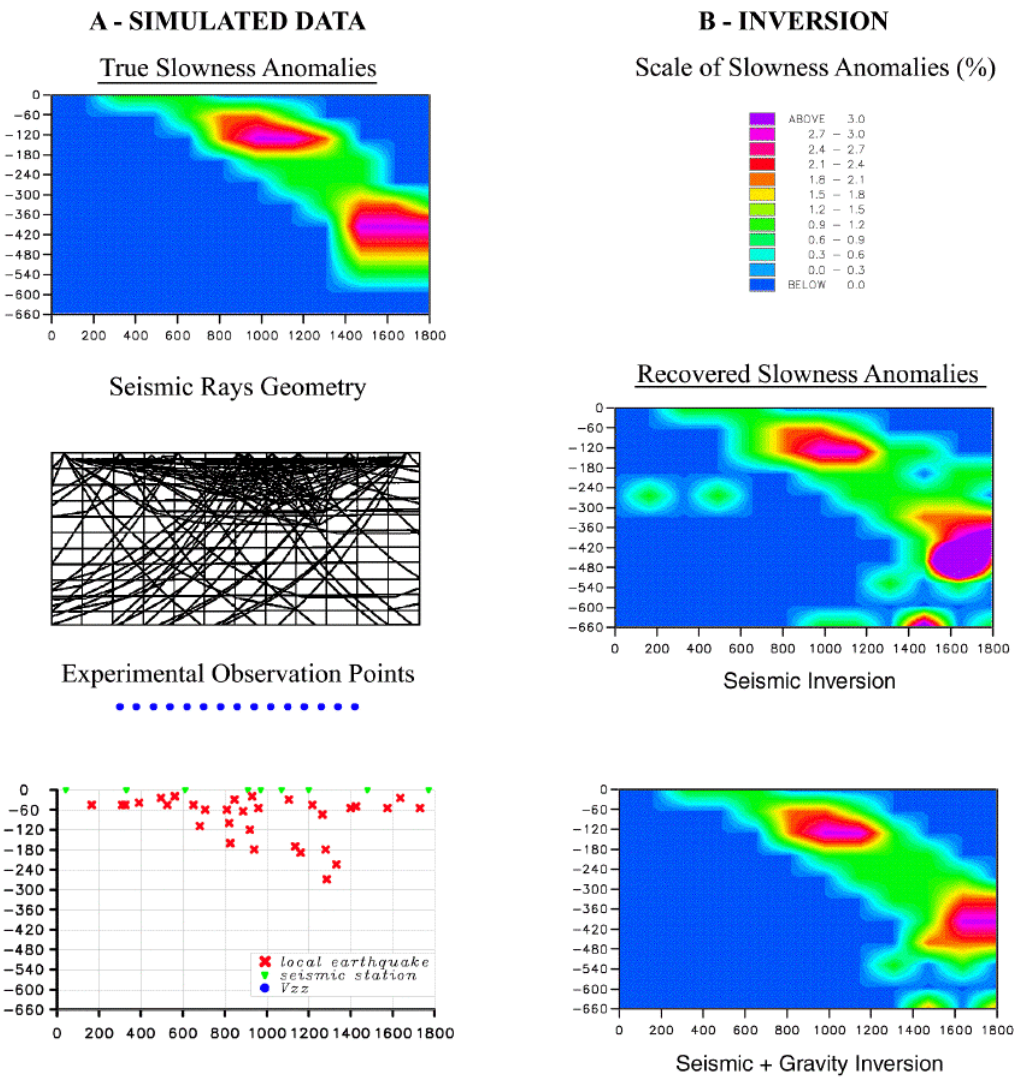

Figure. 3.2. *Simultaneous inversion of gravity and seismic tomographic data. The left panel (A) gives the parameters of the simulation; (upper): generated slowness anomalies (equivalent to density anomalies); (middle): seismic observables (300 P-wave travel times and seismic rays, observed from 9 surface seismic stations; the rays are radiated by the local earthquakes as well as by rays coming from 5 teleseismic earthquakes which occurred outside the region but were detected by the seismic stations considered; (lower): location of seismic stations (green), of 32 local earthquakes (red), and of 15 measurements of gravity gradients at GOCE altitude (blue). The right panel (B) shows the anomalies recovered by using seismic data only (upper), and by using both seismic and gravity data (lower). Seismic travel times have a 5% noise level and gradiometric data a 5 mE noise level. The image of the slab is drastically deteriorated when using seismic data alone, while the inclusion of the GOCE data improves the quality of the image of the slab in both the upper and lower mantle.*

(a) Sedimentary basins

In continental areas, tectonics occur away from the direct influence of plate-margin processes. Sedimentary basins are the signatures of the response of the continental lithosphere to extensional and bending forces and thermal instabilities in the asthenosphere or upper mantle. The GOCE mission can play a crucial role in understanding the formation of these basins, because the thermal instabilities will be visible, through the associated density anomalies, in the measured gravity field, provided that the accuracy and resolution are 1-2 mgal, 50-100 km respectively. Besides the scientific importance of the studies of sedimentary basin formation, there is an economic interest in strategic resources located in the basins, such as oil fields.

(b) Rifts

Another important tectonic process that occurs in the continental lithosphere is rifting, associated with elongated depressions where the entire thickness of the lithosphere is deformed by extensional forces. Rifts are common tectonic features because the strength of the continental lithosphere is least under extension, and can be found in a variety of tectonic settings. Rifts are often associated with upwelling of hot material from the mantle, visible in the gravity field because of its negative density with respect to the normal mantle.

Numerical modelling of continental rift zones and rifted continental margins with their gravity characteristics (typical signals of 10-30 mgals extending over 20 to 200 km) demonstrate that residual anomalies are sensitive indicators of the state of flexure at an extensional basin, which also controls the shape of the basin (Fig. 3.3). Such modelling also requires knowledge of the topography, typically with 10 m precision over areas of 5×5 km^2.

An improved gravity field over continental rift areas, determined with an accuracy of 1 to 2 mgal and a resolution of 20 to 100 km, would enhance knowledge of the major geodynamical causes of rift formation and evolution.

(c) Tectonic motions and sea-level change

Tectonic processes that result in vertical motion impact sea-level trends along continental margins. Tectonic motions can be due to active convergence between plates and density anomalies embedded in the upper mantle. For example, in the Adriatic region, modelling of the tectonic motions (Di Donato et al., 1999), show that they are responsible for a sea-level signal superimposed on the eustatic and isostatic ones due to Pleistocene deglaciation (Fig. 3.4a). In this study, the tectonic model is characterised by a realistic geometry of the Apenninic chain, overthrusting onto the Adriatic domain and by an upper mantle density structure inferred from seismic tomography. A substantial improvement in the density structure at the lithospheric and upper mantle level is expected from GOCE, on the basis of a simultaneous inversion of gravity and seismic tomography data, as shown in section 3.2.2.

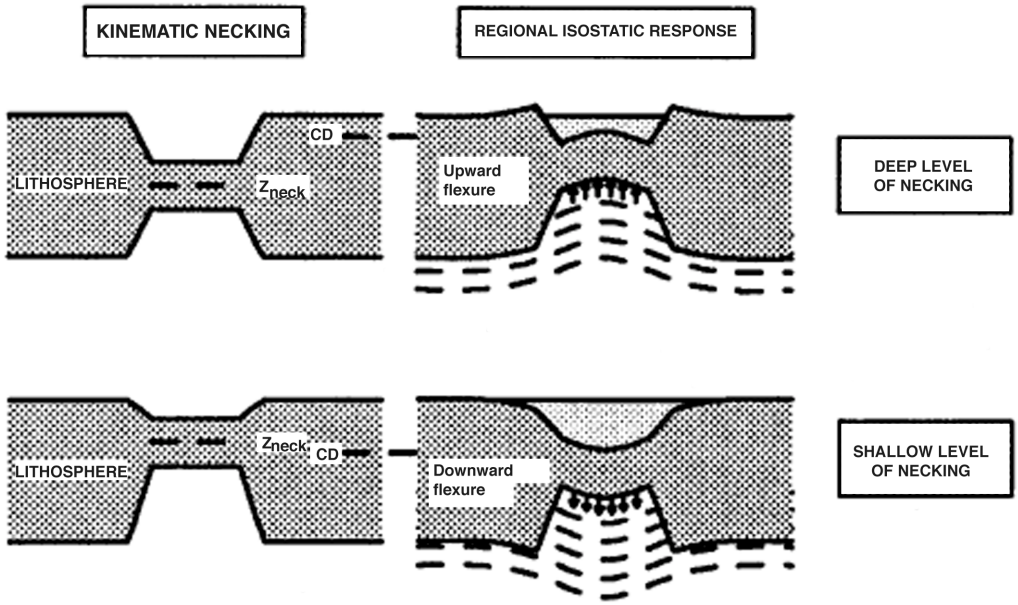

Figure. 3.3. *Schematic of the concept of lithosphere necking with a finite flexural rigidity. The level of necking* z_{neck} *is defined as the level of no vertical motion in the absence of gravity or isostasy (left figures). For necking levels that create a surface depression deeper than compensated depth CD (locally compensated basin depth), an upward load acts on the lithosphere and an upward state of flexure results, with flexurally supported rift shoulders (upper figures). Conversely, for relatively shallow levels of necking (lower figures), a downward load acts on the lithosphere and a downward state of flexure results, with flexurally downwarped basin flanks (from Kooi et al., 1992).*

The push of the African continent is indicated by the thick arrows directed roughly to the north (Fig. 3.4b), in agreement with a recent VLBI solution. The Tyrrhenian subduction is portrayed by the deep lithospheric structure beneath the Calabrian Arc, with geometric characteristics in agreement with seismic tomography. The glacial isostatic adjustment (GIA) model is based on an analytical, viscoelastic, hydrostatically pre-stressed, self-gravitating, stratified, spherical Earth model and in the ICE-3G model for Pleistocene ice melt of Tushingham and Peltier (1991). The glacially induced sea-level variations in the area arise from various coupled processes including the loading associated with Pleistocene meltwater filling the Mediterranean basin, the rebound in Fennoscandia (that drives mantle flow from the Mediterranean region to the uplifting area centred in the Gulf of Bothnia), and the long-wavelength motion of the water away from the Mediterranean towards subsiding regions at the periphery of previously glaciated areas.

The observed sea-level variations come from historical artefacts such as Roman ruins. Providing the sea-level changes averaged over the last few thousand years. Present day sea-level changes might differ because of recent changes in Greenland and Antarctic ice volume, glacier melt and global warming during the past few hundred years. Present day ice-mass changes and global warming were not modelled in the study.

Figure 3.4c accounts only for the effects of density anomalies at upper-mantle level (of the order of 100 kg/m^3) and for plate horizontal motions. It clearly indicates that active tectonics alone cannot explain archaeologically inferred sea-level records within the Adriatic. In Aquileia and the Istria promontory the tectonic model provides at most 0.1-0.2 mm/yr, which is at least 0.3 mm/yr lower than the observed trend in this region. The highest predicted sea-level rise in the Adriatic Sea due to active tectonics is 0.4-0.5 mm/yr, occurring in the Po delta plain (in Ravenna). However, even in this case, the model predictions are significantly below the sea-level rise of 1.1 ±0.2 mm/yr recorded at this site.

These results demonstrate the importance of density anomalies at lithospheric and upper-mantle level on predictions of sea-level change. Here such anomalies are responsible for gravity field variations of about 10 mgal over distances of 100 km or more. These conclusions can easily be generalised to the areas of the World where the lithosphere and upper mantle are varying laterally in their density structure due to active tectonics.

Figure 3.4d shows the effects of GIA alone. The most noticeable effect of the water load is a long-wavelength sea-level rise in the Adriatic Sea, increasing from 0.3-0.4 mm/yr in the northern part of the basin and along the coasts of Albania and Croatia, to 0.5-0.6 mm/yr in Apulia. Except in Apulia, where the GIA model correctly predicts the sea-level rise (in Egnatiae) suggesting that GIA is the dominant mechanism for sea-level change over the last thousand years at this site, GIA alone cannot, in general, entirely explain the observations.

Figure 3.4e, in which the model combines sea-level effects of active tectonics and GIA, gives better agreement with archaeological data (e.g. in Aquileia and, to a lesser extent, in the Istria promontory).

Comparison of tectonic and GIA results shows that the anomalous density structure at the lithospheric and upper-mantle level and relative plate motion are responsible for the appearance of short-wavelength features in sea-level changes which are of importance for a correct interpretation of sea-level data. A detailed knowledge of the density structure from GOCE will thus allow the risk of sea-level change in coastal areas to be estimated. It will also allow the sea-level changes due to climate changes and anthropogenic activities to be quantified using the residual between the observed data and the modelled effects of tectonics and GIA.

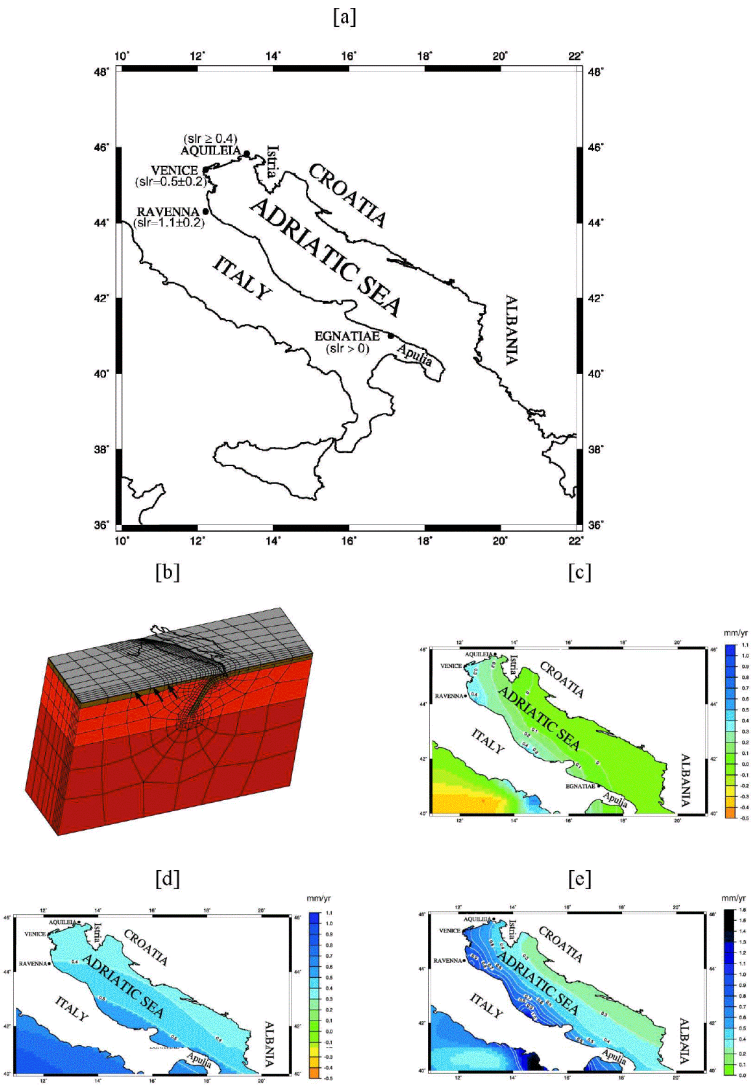

Figure. 3.4. *Tectonic motions and sea-level changes in the Adriatic region based on observations and modelling. [a] Site locations, observed sea-level rates, slr, (in mm/yr), error bars for Venice and Ravenna are shown; [b] Mesh of the finite-element tectonic model: the brown, light and dark reds indicate the lithosphere, upper and lower mantle respectively; the brown dipping plate is the subducted oceanic lithosphere beneath the Calabrian Arc in the southern part of peninsular Italy; the coastlines of Italy are drawn on top with the thick curve, with the finer mesh indicating the decoupling zone of the Apennines with respect to the Adriatic plate on the right; the horizontal arrows indicate the push of Africa; slab pull is activated in the subducted lithosphere; the elastic structure is constrained by the seismic model PREM and the Earth model has a 120 km thick elastic lithosphere; viscosity is* 10^{21} *Pa.s in the upper mantle and increases in the lower mantle by a factor 30 (in agreement with long-wavelength geoid modelling). [c], [d], and [e] are the present-day rates of sea-level change due to active tectonics, glacial isostatic adjustment and the sum of both effects, respectively.*

Seismic Hazards

Earthquakes can be characterised on at least two time scales: a short one associated with rupture of a fault and the propagation of elastic waves, and a long one associated with the slow build up of stress due to geodynamic processes and stress relaxation due to visco-elastic flow of crust and mantle. Although earthquake data are widely exploited on the basis of the aforementioned short time scale, studies on the slow build up of stress due to tectonic loading are still largely lacking. In order to emphasise the impact of the GOCE mission on the recovery of the density structure at the upper-mantle level, which is crucial to the modern approach to seismic hazard studies, the accumulation of deviatoric stress in central Italy, recently affected by the Umbria-Marche seismic crisis, was simulated (largest circles in Figure 3.5a). Details of the simulation can be found in Negredo et al., 1999.

A 2D viscoelastic dynamic model allows the stress distribution, due to the geodynamic processes likely to be active in this region, to be quantified: near North-South convergence between Africa and Eurasia, upwelling of hot asthenosphere underneath Tuscany and underthrusting/subduction of the Adriatic lithosphere under the Apennines. Model results are compared with the earthquake distribution and seismotectonic observations. The modelled section (Fig. 3.5b) includes the lithosphere and the sublithospheric upper-mantle and has a horizontal extent of 1250 km and a depth of 670 km.

The geometry of the central shallow part of the model is constrained by earthquake distribution, tomographic images and seismic data. Density anomalies are derived from seismic tomography and petrological data, though, in general, with poor accuracy.

Three model simulations are presented here, in which density anomalies are progressively added. In Run 1 only the velocity boundary condition simulating the effects of the Africa-Europa convergence is applied. In Run 2 a negative density anomaly of 100 kg/m^3 simulating the asthenospheric upwelling underneath Tuscany is introduced. The unloaded slab of Runs 1 and 2 is conceptually equivalent to a detached slab. In Run 3 the slab is loaded with a positive density anomaly of $80\,kg/m^3$, reproducing gravitational sinking.

The adopted density anomaly value accounts for the eclogitization of the subducting lower crust and for a temperature-related density anomaly within the slab. The GOCE mission will allow the density structure to be constrained in detail: the assumed density anomalies correspond to gravity variations of 5 to 10 mgals over distances of 100 km typically, and the mission should yield a precision about ten times better at such resolution.

Figure 3.6 displays the model-predicted distributions of the equivalent von Mises (deviatoric) stress that correlates with the distribution of earthquakes.

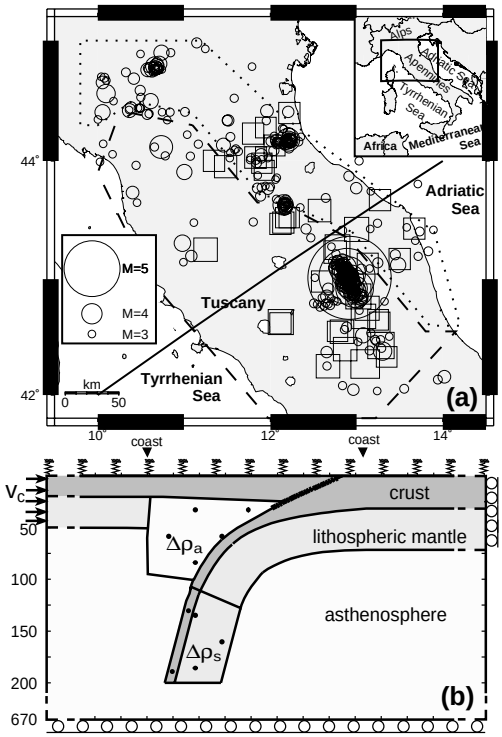

Figure 3.5. *(a) Location of the modelled profile. Circles represent earthquakes which occurred from January 1988 to September 1997. Their size increases with magnitude. The solid and dashed lines indicate the areas characterised by prevalent tensional and compressive stress field, respectively. (b) Model geometry and boundary conditions.* V_c *denotes the velocity boundary condition (to account for the eastward extrusion of the Tyrrhenian domain caused by the African indentation), circles denote free slip condition. The bottom is fixed in the vertical direction whereas a buoyant restoring force (denoted by springs) proportional to the vertical motion and to the density contrast is applied to the upper surface. Different grey shadings indicate different materials and overprinted dots indicate regions with density anomalies. Close to the surface, the subduction fault is locked (barbed portion). At deeper levels, it is unlocked, allowing for continuous aseismic slip.*

If convergence is the only active mechanism (Run 1; Fig. 3.6a), the stress is concentrated in the crust, in disagreement with the occurrence of earthquakes deeper than 25 km. The activation of upwelling of hot asthenospheric material (Run 2; Fig. 3.6b) generates bending stresses down to 80 km in the Adriatic plate as it deepens under the Apennines. The resulting pattern of von Mises stress is compatible with the occurrence of subcrustal earthquakes. When the deep density anomaly in the slab (Run 3; Fig. 3.6c) is also activated, an increase in the bending stresses in the knee of the slab is obtained (however, the stress distribution at depths shallower than 90 km is

similar to Run 2, and the sole comparison with the earthquake distribution does not make it possible to discriminate between them).

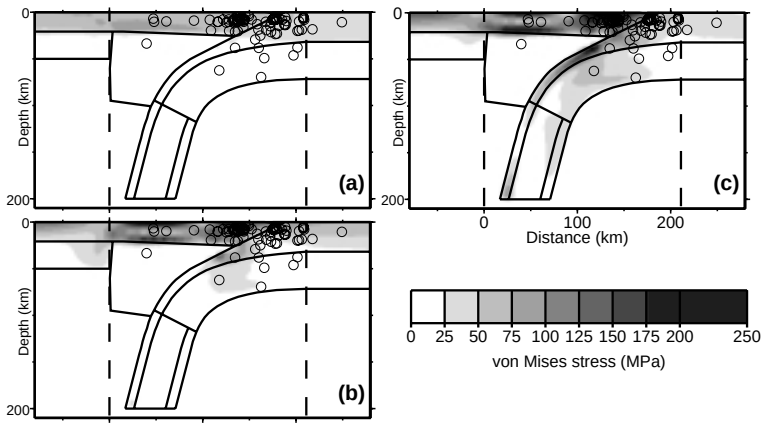

Figure 3.6. *Von Mises stress distribution obtained for model simulations 1 (a), 2 (b) and 3 (c) (see text). The earthquakes located in a 40 km band centred on the modelled profile are projected on the section.*

These results indicate the major impact of lateral variations, in the density structure of the lithosphere and upper mantle, in controlling the stress pattern in an earthquake prone area. It is well known that statistical approaches based on historical records of seismicity are insufficient to mitigate seismic risk, as the slow time scales of earthquakes due to tectonic loading can be several thousands of years, beyond the scope of historical seismic records. A new appraisal in the field of seismic hazard prediction can be gained by modelling the slow build up of stress due to tectonic loading and by comparison with the predicted deformation pattern obtained from GPS surveying.

Such modelling requires knowledge of the density anomalies in the lithosphere and upper mantle, which petrology and seismic tomography alone cannot provide (section 3.1.2). Only from the inversion of the gravity data from GOCE, will it be possible to derive the worldwide pattern of the density structures in the uppermost portion of the planet with sufficient accuracy and spatial resolution. These data in turn will advance understanding of their impact, together with the relative motions of the plates and the rheology of the crust, in controlling earthquake nucleation in seismogenic regions.

3.3 Absolute Ocean Circulation

3.3.1 Introduction

Knowledge of the ocean's central role in modifying climate, through its large heat capacity and transports and the complexity of its interactions with the atmosphere and cryosphere, has long been insufficient for the accurate prediction of climate change, whether due to natural or anthropogenic forcings. For example, it is known qualitatively that half or more of the excess energy input (the incoming solar radiation minus the infrared radiation to space) in tropical areas is carried by the oceans towards the poles, the other half being transported by the atmosphere. However, quantitative estimates are coarse, and predictions of how such fluxes would be modified by 'enhanced greenhouse forcing' are even coarser.

Such uncertainties associated with ocean circulation resulted in the formation a decade ago of the World Ocean Circulation Experiment (WOCE) by the World Climate Research Programme (WCRP). The extensive WOCE 'field phase', including its Hydrographic Programme, has now been completed, with an 'analysis phase' continuing into the next century. Some strategic in-situ measurements, such as those of the global tide-gauge network, remain as part of the WCRP CLIVAR (Climate Variability and Predictability) programme and the IOC/WMO Global Ocean Observing System (GOOS). In addition, monitoring of the global ocean continues to rely heavily on the availability of remote-sensing information, and in particular on satellite radar altimetry. The initiation and start of WOCE was timed to coincide with the availability of altimeter data, such as has been provided by the TOPEX/Poseidon and ERS-1/2 missions, and future ocean monitoring will depend upon the data available from Jason-1, Envisat and other missions.

Altimeter satellites allow the measurement of very precise, regular and quasi-global sea-surface heights. As most changes in ocean surface currents, on time scales of a few days or longer, result in geostrophic balance, gradients of the sea-surface pressure (or the 'dynamic ocean topography' i.e. the sea-level above the geoid) can be employed almost directly as proxy-current information. Unlike in-situ measurements, altimetry data are global and can be collected repeatedly for many years. Unlike other surface quantities measured from space, they can be related to ocean processes and currents within the whole water column. They are also relatively simple oceanographic quantities which can be assimilated directly into ocean and climate numerical models.

While variations in the sea-level and thus in the ocean currents can be derived directly from satellite altimeter data, assessment of the absolute value of the ocean dynamic topography (and hence the absolute surface circulation) requires the independent determination of what would be the elevation of an ocean at rest, i.e. the geoid. The latter is not known at present with sufficient precision. Indeed, it will be seen that the typical elevation scale of the dynamic topography is of the order of 0.1 to 1 m, while

the precision of present geoid models is also multi-decimetric on the scale of many ocean-circulation features.

With current altimetric missions providing such effective measurements of ocean circulation variability, and with future missions likely to continue these measurements well into the next century, it is reasonable to ask why oceanographers need to know the mean circulation itself in such spatial detail. There are several reasons.

Firstly, it will be demonstrated clearly below that both modelled and real oceans undoubtedly contain short-spatial-scale components of mean flows. It is important to be able to measure the locations and magnitudes of such short-scale features by means of altimetry and gravity, to compare them to information from conventional hydrography, to understand their relationships to bathymetry and other controlling factors and to assess their importance for oceanic-mass and heat-flux estimation. It is through mean flows, as well as variabilities (e.g. eddies), that the ocean transports its heat, fresh water and dissolved species. Hence, the aggregated short-scale mean flows could well prove to be of importance to climate.

Secondly, it is through instabilities in the mean flows that the ocean generates eddies and it is possible to generate different degrees of variability in different numerical models depending on the mean flows programmed into them and on the way in which the factors controlling the means are parameterised (e.g. interactions with bathymetry). In particular, the variability can act as a brake on or stimulant to the mean flows by means of internal stresses (Fig. 3.7). Consequently, in dealing with non-linear processes and in studying transient perturbations of the system, it is essential to start from as good a description as possible. This was essentially the motivation underlying the WOCE ‘decadal snapshot’ of the ocean, namely to provide a data set on which models with potential for predictive capability might be based.

Thirdly, it is clear that data assimilation schemes for ‘ocean forecasting’ have reached a stage of development where the optimal use of altimetric variability information can be achieved as long as the mean ocean state (i.e. the absolute ocean circulation) can be properly parameterised. In this case, the dynamic topography obtained from MSS minus geoid, acts as a powerful model constraint on the assimilation of (inevitably) noisy altimeter variability information, providing a window on ocean processes at depth.

Fourthly, it will be shown that knowledge of the short-spatial-scale geoid will be essential to computations of fluxes through basin-size oceanic sections, again by providing model constraints to the assimilation of other information (altimetry, hydrography), each of which will contain measurement uncertainties.

Therefore, it is clear that understanding the mean and understanding the variability of the ocean circulation must go hand-in-hand, particularly with regard to the construction

of the next generation of numerical ocean models with the potential for a better description of the role of the ocean in the global climate system.

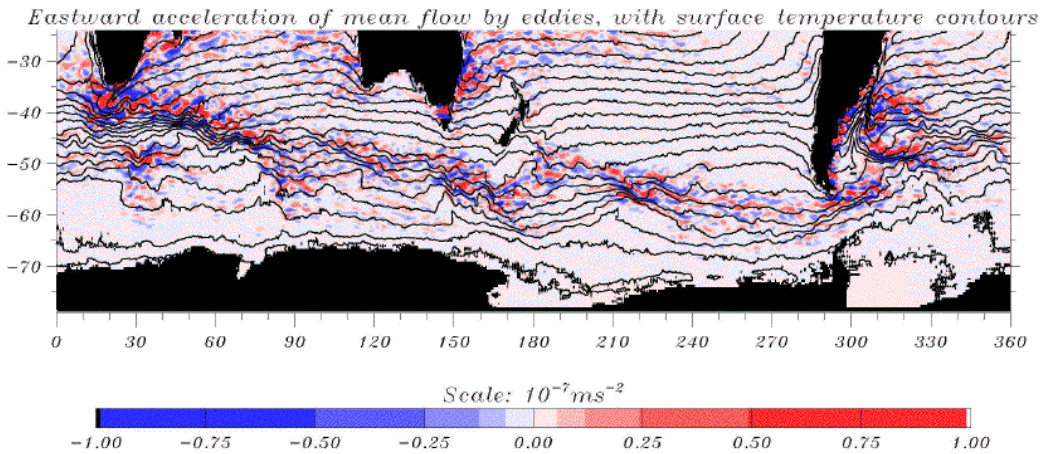

***Figure 3.7**. Eastward force exerted by eddies on the zonal mean flow of the Antarctic Circumpolar Current obtained from T/P and ERS-1 satellite altimeter data together with sea-surface temperature contours (Hughes and Ash, 1999). Temperature contours are shown with 1.5 degree spacing.*

3.3.2 Requirements for Short-Spatial-Scales

For many years, the oceanographic community has been requesting a space gravity mission which would provide a precise, high-spatial-resolution description of the Earth's gravity field and geoid independent of the quasi-geoid information provided by altimetry. Studies, dating from at least Wunsch and Gaposhkin (1980), have been made of optimal methods for the separation of the oceanic dynamic topography from the geoid in order to determine the global ocean circulation (some detailed studies were conducted even prior to the altimetry era; see for example NASA, 1970). Currently this separation can already be performed adequately at the basin-scale wavelengths (e.g. Fig. 3.8) but cannot be performed at present for degree larger than about 20 (or half-wavelengths less than about 1000 km) as, at that spatial-scale, geoid model error becomes larger than the dynamic topography signals (Fig. 3.9). The application of imprecise geoid models to the determination of dynamic topography at shorter spatial-scales can consequently result in the computation of false multi-decimetric topographic signals which will correspond to false transport calculations of several 10's of Sv

(where 1 Sv = 10^6 m^3/s) which is of significance in climate studies (Wunsch and Stammer, 1998).

In fact, both the deep-ocean and coastal circulation do contain important features with short-spatial-scales, which are at present hidden by the geoid inaccuracies. However, it is necessary to resolve the short-scales for a proper understanding of ocean dynamics, for constraining ocean-circulation models in terms of data assimilation and for computation of mass and heat fluxes. One way of demonstrating these features is by the use of ocean models. Major progress has been made recently in ocean-circulation modelling, largely as a consequence of the significant improvement in grid resolution to below 10 km. These models still do not provide a full representation of the real ocean, but many important short-spatial-scale, realistic-looking features can be represented.

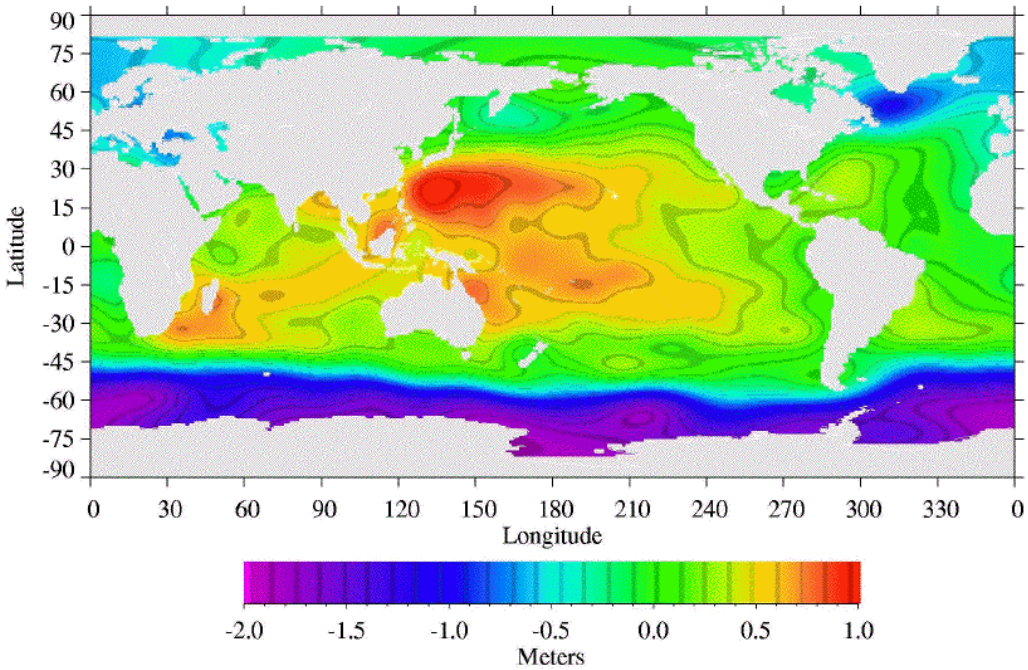

Figure 3.8. *The large-scale ocean dynamic topography obtained by differencing the mean-sea-surface obtained from a combination of T/P and ERS-1 data (over a 2 year period 1993-1994) and the EGM-96 geoid model up to degree 20 (Lemoine et al.,1998).*

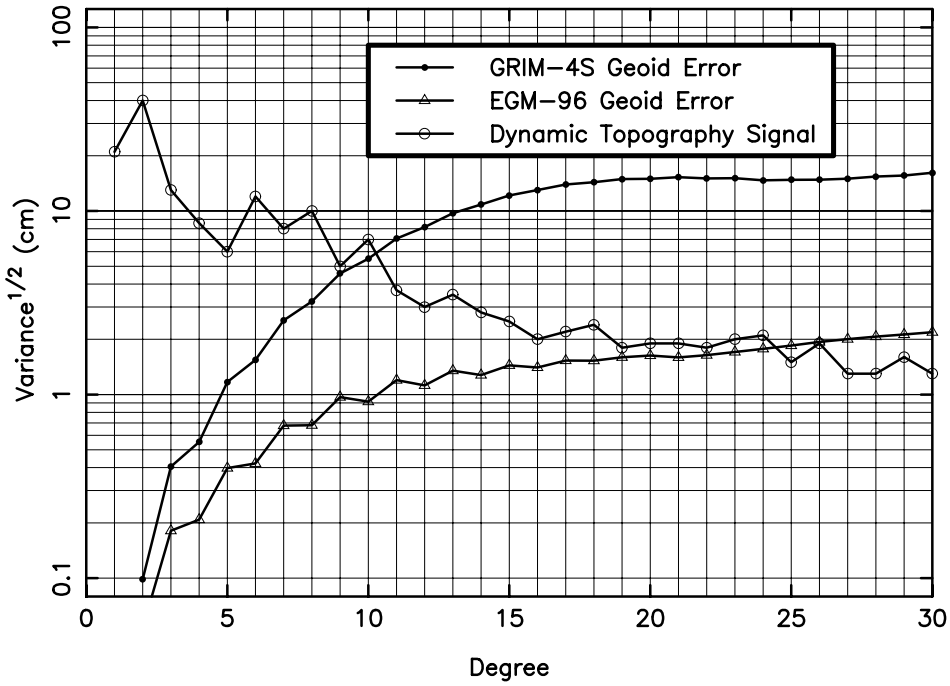

Figure 3.9. *Power spectrum of the ocean dynamic topography (computed by Nerem et al., 1994) compared to estimated errors from the EGM-96 model of the geoid. The crossover of the two curves can be seen at about degree 20. Note that the EGM-96 solution is based partly on altimeter as well as satellite-tracking information which makes it less of an 'independent geoid' for ocean studies than models based on tracking data alone (e.g. GRIM-4S). However, the latter have considerably larger uncertainties, even at basin scales. Most ocean applications at present make use of models such as EGM-96.*

For example, Figure 3.10 shows ocean topographies obtained using the 1/12˚ resolution MICOM ocean model of the North Atlantic (Paiva et al., 1999; Chassignet et al., 1999). Figure 3.10a indicates the complete topography over all spatial-scales, Figure 3.10b the topography for scales with half-wavelength larger than 1000 km, and Figure 3.10c,d,e the parts of the topography with spatial-scales shorter than 1000, 250 and 100 km half-wavelength, respectively (i.e. approximately degree 20, 80 and 200, respectively).

Figure 3.10b can be seen to correspond essentially to the present situation in which geoid model uncertainties result in the MSS being separable from the geoid surface to approximately degree 20 only. Figure 3.10c simulates that part of the topography which is unresolved with present data sets, and which will remain unresolved without a gravity mission. Figure 3.10d indicates schematically that part of the topography which will remain unresolved even after a medium-resolution gravity mission such as GRACE is flown; many interesting features, such as the fronts associated with the Azores Current and western boundary currents will remain to be explored. Finally,

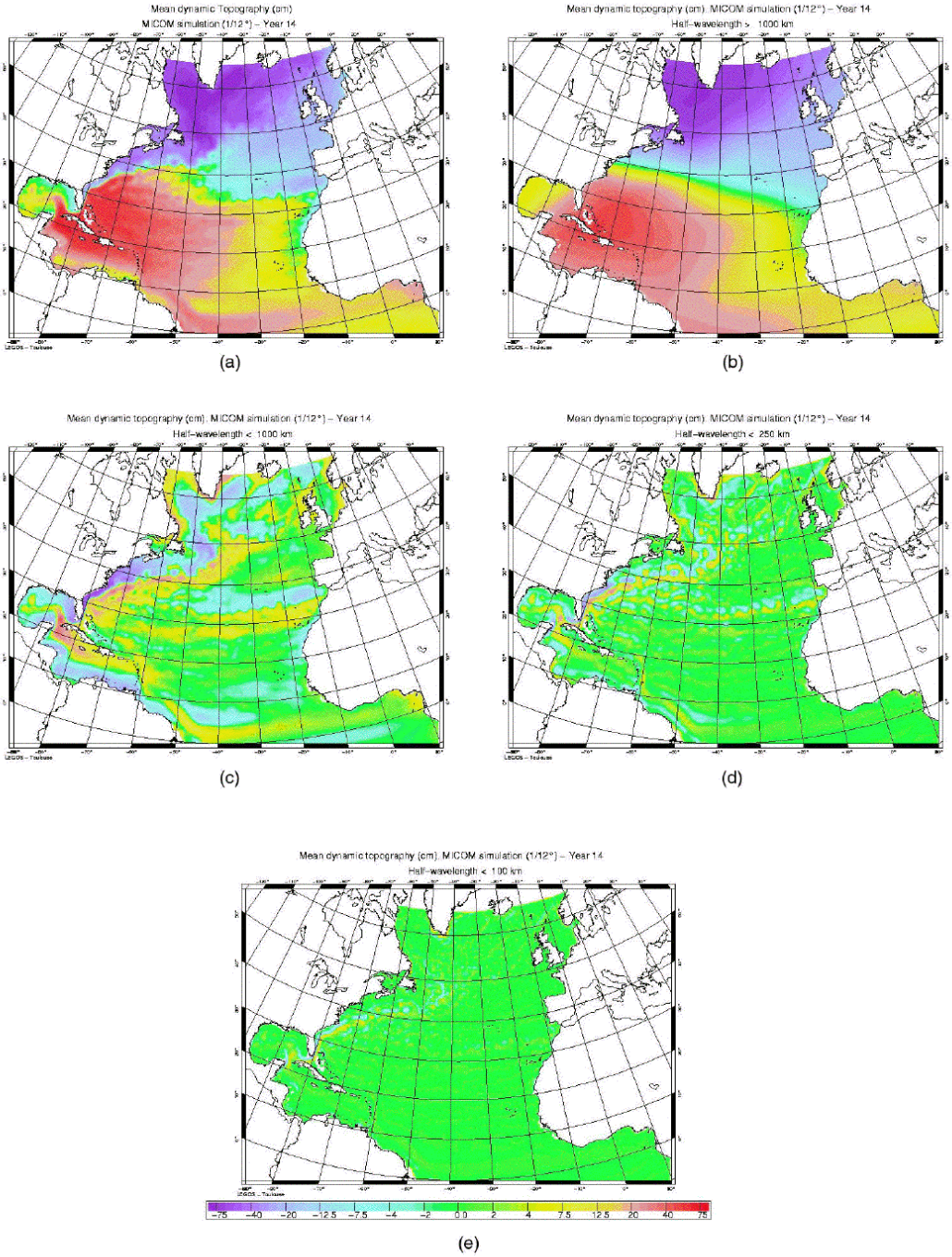

Figure 3.10. *(a) Ocean topography over all spatial-scales obtained using the 1/12 degree resolution MICOM ocean model of the North Atlantic; (b) the same topography, but for scales with half-wavelength larger than 1000 km; (c,d,e) the same*

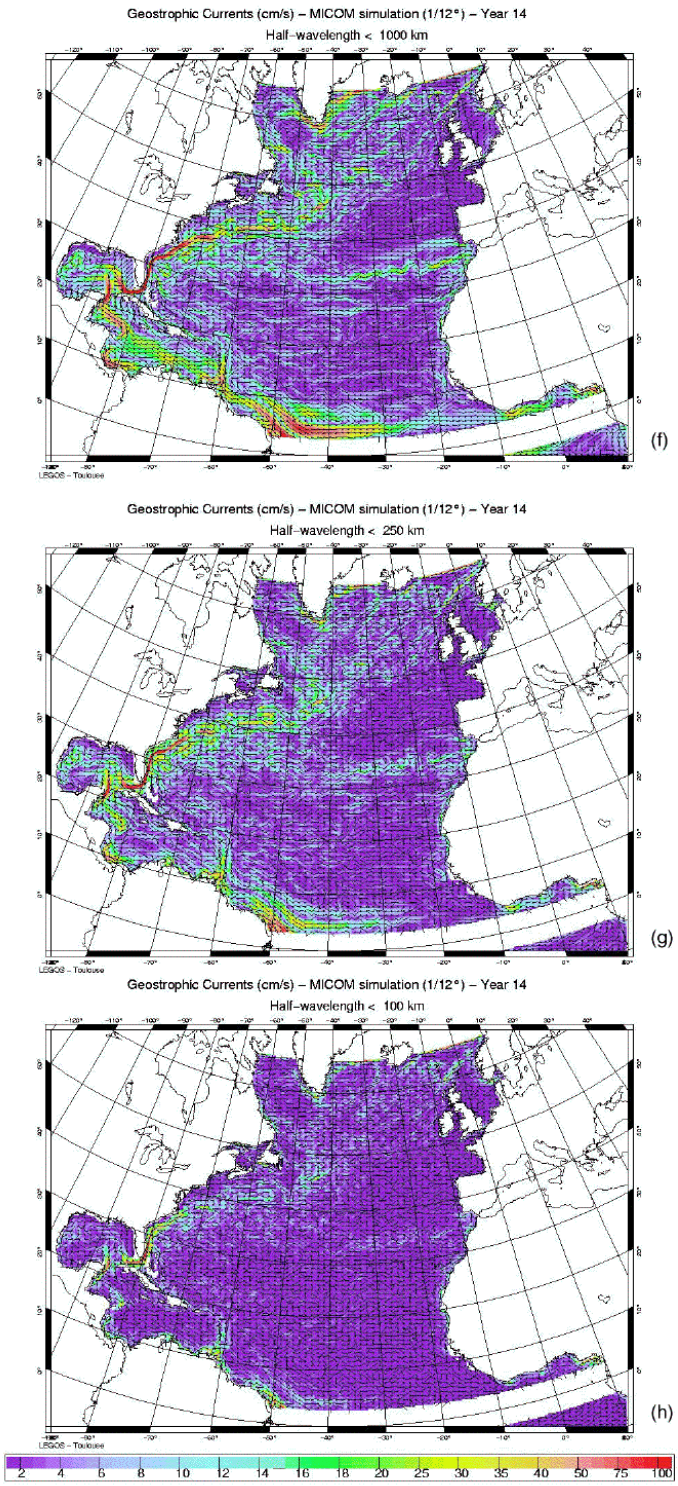

topography, but for spatial-scales shorter than 1000, 250 and 100 km half-wavelength respectively; (f,g,h) geostrophic surface currents corresponding to spatial-scales of the topography with half-wavelengths less than 1000, 250 and 100 km, respectively.

Figure 3.10e indicates that part of the dynamic ocean topography at the shortest scales which will remain unresolved to satisfactory precision after GOCE; it can be seen that most of the features in Figure 3.10d no longer remain in Figure 3.10e, with the exception of decimetric signals associated with the intense and short-scale Florida Current and Gulf Stream front.

Figures 3.10f,g,h present the geostrophic surface currents derived from the high-pass-filtered topographies of Figures 3.10 c,d,e corresponding to half-wavelengths of 1000, 250 and 100 km respectively. It can be seen that many of the features in the current field are unresolved with present-day geoid data sets (Fig. 3.10f), and that many features will remain unresolved even after a medium-resolution mission such as GRACE (Fig. 3.10g). After GOCE, on the other hand, most of the current field will be determined (Fig. 3.10h).

Figure 3.11 presents a similar set of figures, but for the global ocean making use of data from the 1/8˚ resolution OCCAM model (Webb et al., 1997), indicating in Figure 3.11a the complete topography over all spatial-scales, and in Figures 3.11b,c that part of the topography with spatial-scales shorter than 1000 and 250 km half-wavelength respectively (i.e. approximately degree 20 and 80, respectively) which are unresolved with the use of present-day geoid models and which would remain unresolved after a medium-resolution gravity mission. The two latter figures demonstrate that much remains to be understood about the global ocean topography.

There are clearly many short spatial features which must be resolved and understood: frontal signatures of the major currents; definition of narrower and smaller boundary currents; Antarctic Circumpolar Current (ACC) jet banding; zonal equatorial signals. Spectra obtained from across the major current systems in the models confirm that mesoscale energy in the height fields is centred in the 100-250 km half-wavelength band, as also observed in the real ocean from altimetry.

Geostrophic surface currents derived from the OCCAM topography for spatial-scales shorter than 1000, 250 and 100 km are shown in Figures 3.11d,e,f respectively. Again, it can be seen that many features of the current field are unresolved with present knowledge (Fig. 3.11d), and will remain unresolved even after a mission such as GRACE (Fig. 3.11e), whereas after GOCE very few signals in the current field will remain to be resolved (Fig. 3.11f).

The proper understanding of the short-spatial-scale dynamical processes shown above is as important to the study of ocean circulation and its heat and mass transport as measurements at the largest (gyre, basin) scales, which are just about possible today (Fig. 3.9). For example, it is important to know if the real oceanic current systems such as the ACC consist of a number of narrow jets of high velocity (and therefore bands of large sea-surface gradient) rather than of continuous flow across their complete widths. Evidence for such jet banding, which requires a high-resolution gravity mission to

resolve, is evident in Figures 3.11d,e, from analysis of other ocean models carried out by the authors of the report and from the modelling studies of other authors (e.g. Maltrud et al., 1998; Best et al., 1999).

The 100 km half-wavelength cut off-of-interest suggested by the relatively few remaining signals of interest in Figures 3.10e,h and Figure 3.11f is consistent with requirements for improved geoid models suggested in previous studies in terms of the Rossby radius of deformation, a dimension that characterises a spatial-scale boundary. At scales larger than this, the ocean circulation is largely described in terms of geostrophic balance in response to applied forcings (e.g. wind stress) and is, therefore, accessible to measurement by observations of sea-surface height. At scales shorter than this, the circulation tends to have the character of turbulent cascades which are not in geostrophic balance (Gill, 1982). At mid-latitudes, the radius associated with the first baroclinic vertical mode (most currents at these latitudes have primarily baroclinic components) is 40 km, increasing towards the equator. This translates into a requirement for centimetric knowledge of the geoid down to half-wavelengths of 120 km.

An additional example of the need for high-spatial-resolution, but using real rather than model data, is shown in Figure 3.7, which plots the force exerted by eddies on zonal flows of the ACC obtained from combined T/P and ERS-1 satellite altimeter data (Hughes and Ash, 1999). The eddies can be seen to exert either strong positive or negative eastward forces, varying within small ranges of latitude across the ACC. Knowledge of the eddy statistics of the real ocean from altimetry, together with knowledge of the precise positions of the ocean jets from altimetry plus gravity (rather than from the assumption of frontal positions by means of sea-surface temperature or hydrographic information at present), will enable the determination of the role played by the eddies in maintaining the jet components of the circulation.

As a further example, again using real data, Figure 3.12 shows the sea-surface temperature gradients in the Southern Ocean from ERS ATSR information (Hughes and Ash, 1999). These demonstrate the locations and typical scales of many of the ACC's sharp frontal areas, most of which will have decimetric signals in the absolute ocean topography, and which it is intended to localise precisely and measure by means of GOCE.

From Figures 3.7 and 3.10-3.12 it is clear that not only modelled oceans, but also the real ocean,, contain short-wavelength features of importance and that it is essential that their precise positions and amplitudes be measured as accurately as possible. At the short-spatial-scales of order several 100 km, MSS minus geoid signals will be decimetric, requiring a geoid determination of order 1-2 cm if these shorter scale signals are to be measured to within 10 % or better locally. Information of order 5 cm accuracy may even be of potential application to short-spatial-scale (30-50 km) coastal studies. With a proper understanding of the role of the positions, strengths and dynamics of the short-spatial-scale fronts and jets in controlling the ocean circulation,

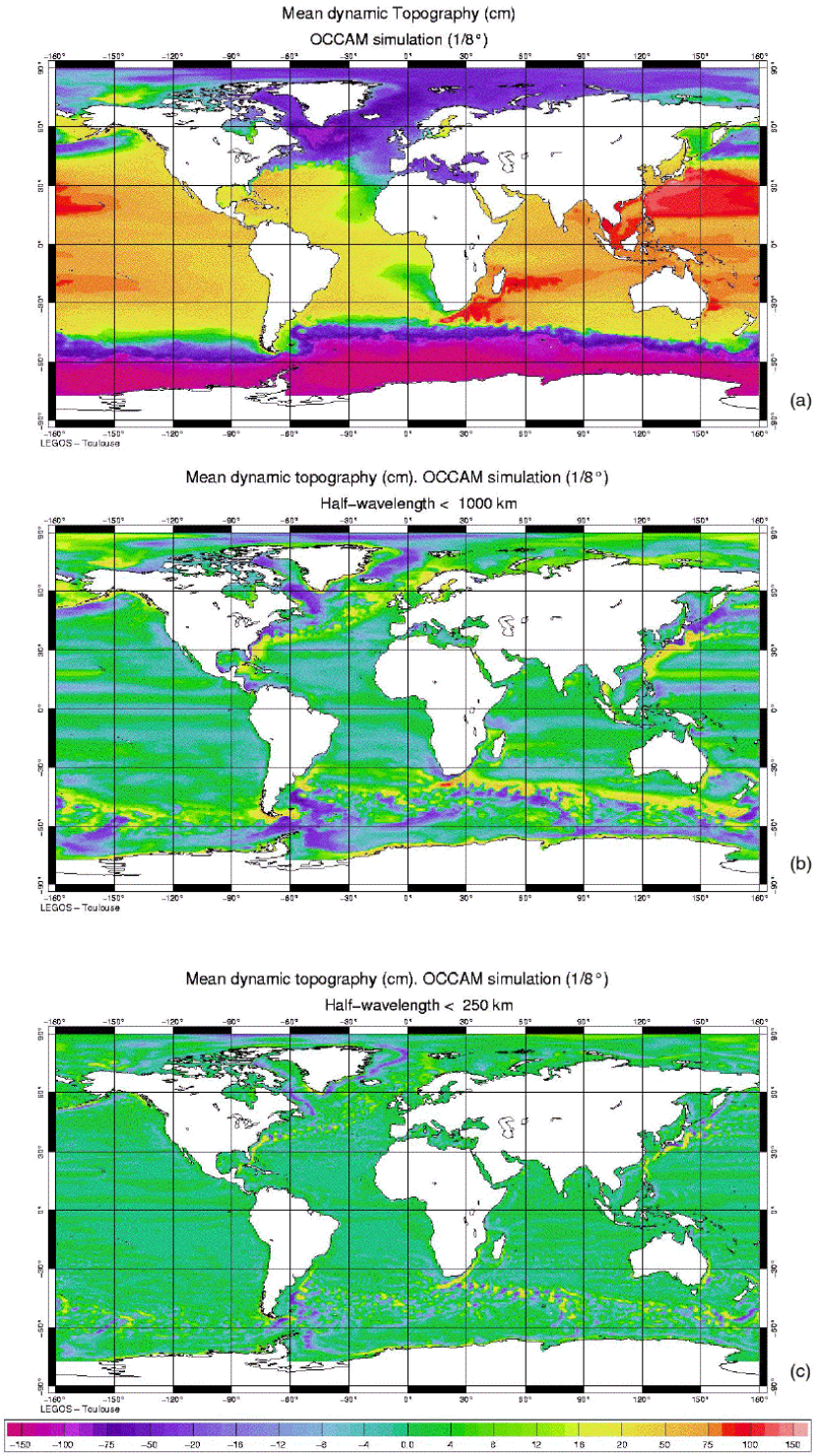

Figure 3.11. *(a) Ocean topography over all spatial-scales obtained using the 1/8-degree-resolution OCCAM global model; (b,c) the same topography but for spatial-scales shorter than 1000 and 250 km half-wavelength, respectively;*

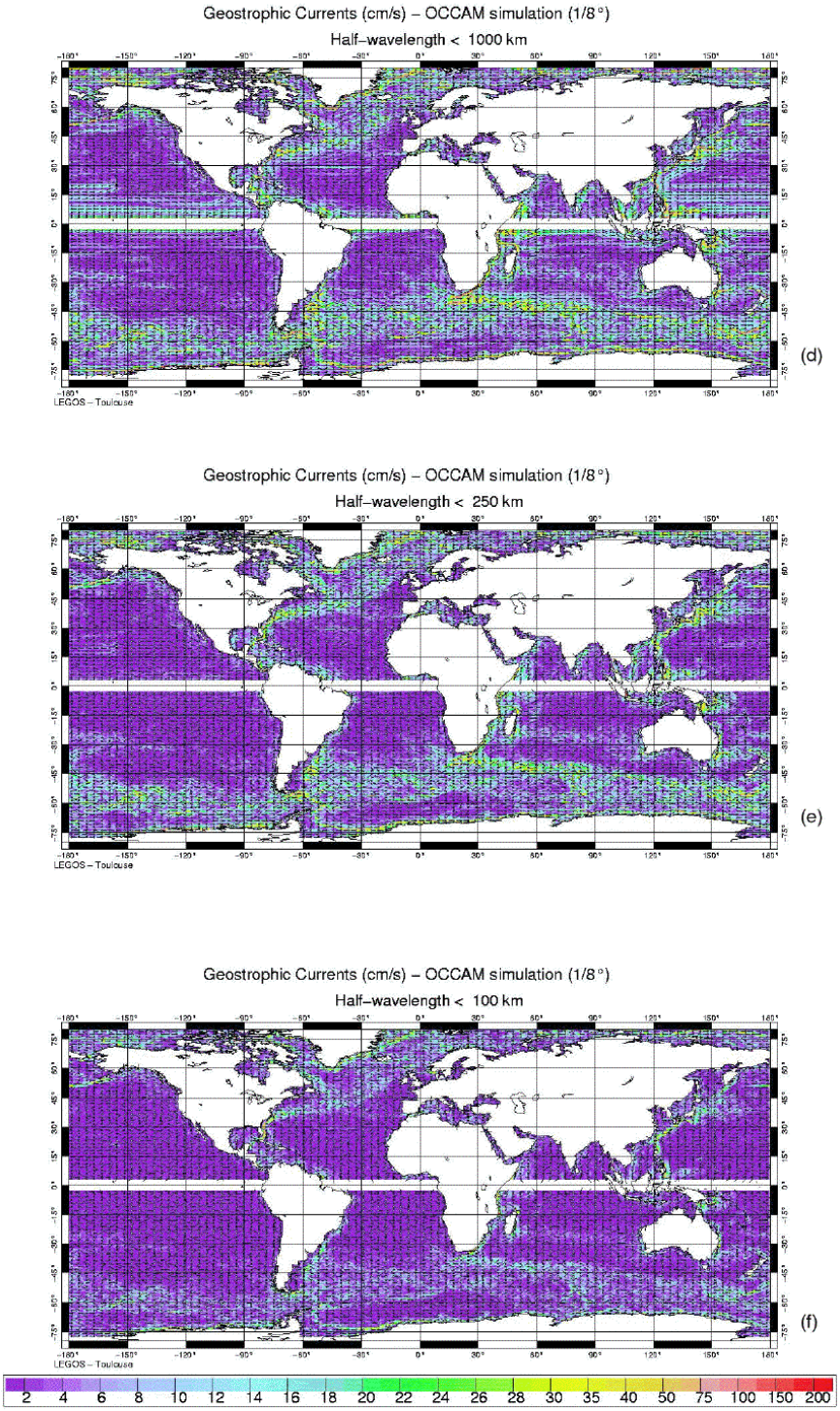

(d,e,f) geostrophic surface currents corresponding to spatial-scales of the topography with half-wavelengths less than 1000, 250 and 100 km, respectively.

greater confidence will be attached to the construction of the next generation of ocean and climate models.

3.3.3 Benefits of Short-Scale Geoid to Ocean Forecasting

The potential benefits of a precise, high-spatial-resolution geoid to ocean data assimilation and 'ocean forecasting' (which may one day be routine for all parts of the ocean through programmes such as GODAE and its successors), has been demonstrated for an area of eastern North Atlantic. In this area, a 3-D data assimilation scheme (SOPRANE) is already operational for the forecasting of the regional eddy field. In this feasibility study (Dombrowsky et al., 1999), fields from the high-resolution POP model (Smith et al., 1999) were employed as 'sea truth' and to provide simulated altimeter mean dynamic topography (MDT) and residuals (with respect to the MDT) for assimilation into the similar resolution (1/10˚) quasi-geostrophic SOPRANE model. The MDT, or the absolute ocean circulation, in the model acts as a constraint on the regional eddy field arising through the instabilities in the circulation. In the case of real data assimilation, of course, the dynamic topography parameterisation used in the model contains errors from the altimetric MDT and geoid models employed. The latter were simulated in the present study by using the ideal MDT derived from POP, but excluding scales below 100 km half wavelength (MDT-1) or 250 km (MDT-2).

The conclusion of this study highlights the potential benefit of GOCE. The range of the average departure of the one-week forecast of the total circulation (mean and eddy field) from a perfect prediction (using the full POP MDT) is a factor of 2 smaller using MDT-1 rather than MDT-2 (1.8 Sv rather than 4 Sv standard deviation in the upper 200 metres). Also, the predictive skill of SOPRANE was shown to make two-week forecasts feasible with MDT-1 to the same level of precision as one-week forecasts with MDT-2. This improvement is in addition to that in the knowledge of the mean circulation itself, i.e. in the spatial resolution of the absolute value of the velocity field.

3.3.4 Implied Accuracies Required for the Basin Scale

It will be seen in Chapter 4 that the observational requirements at shorter scales for the GOCE mission automatically satisfy requirements at the basin scale. The requirement at the basin scale can be set by reference to the present accuracy of computing the MSS from satellite altimetry. Clearly, to determine the dynamic topography, the geoid must be determined at least as accurately as the MSS. At large spatial-scales, MSS accuracy will be determined primarily by systematic residual errors in orbits (section 3.5) and environmental altimetric corrections, which are at present centimetric but which may eventually become sub-centimetric for missions such as Jason-1. If full advantage is to be taken of the extraordinary precision now available from altimetry, it is necessary to attempt to measure the geoid to order 0.1 cm over similar spatial-scales.

It is a characteristic of geostrophic balance that the error in computing volume flux through an ocean section will not depend on the actual width of the section, but only upon the height error across the section, where the latter may stem from either MSS or geoid uncertainties, assuming barotropic (uniform) flow through the section. For example, an integrated error of 1 cm in geoid height-difference across a North Atlantic zonal section at 30 N with 5000 m depth will result in a (assumed barotropic) transport error of 7 Sv and approximately 10^{14} W in meridional heat transport (ESA, 1996). These are large numbers, but measurements to this accuracy would represent significant improvements compared to present uncertainties where oceanic fluxes may be uncertain to first order (typically 10^{15} W or larger). The 7 Sv can be compared to estimated formal baroclinic volume transport errors of approximately 2 Sv based on hydrographic sections (Macdonald, 1995; Wunsch and Stammer, 1998). Although the uncertainties from the hydrography are considered to be underestimated by a factor of 2 or 3 (ESA, 1996), it points to the need for altimetric and geoid measurements to aim at considerably better than 1 cm precision and to have errors comparable to (or smaller than) other complementary oceanographic information at these scales.

Similar geoid accuracy requirements can be obtained from a consideration of coastal tide-gauge data. For example, tide gauges (together with GPS in future) are being used to monitor a number of the World's straits as part of WOCE and CLIVAR. Such straits include the Drake Passage, the Amsterdam-Kerguelen, Australian 'choke points' of the Antarctic Circumpolar Current (ACC), the Bermuda-Charleston and Caribbean island 'choke points' of the Gulf Stream and the Straits of Gibraltar. In future, it is to be hoped that the many narrow straits of the Indonesian Through-Flow region, which are of great climatological importance, will also be instrumented. Where the distance across the strait is short, and where extensive local gravity information exists, then regional geoid models can be constructed enabling the geoid-difference across the strait to be computed to good accuracy and to be employed together with geocentric sea-surface height difference to determine absolute sea-level gradients. The Straits of Dover are one example.

However, as the distance increases, especially in areas where present gravity information is sparse, then geoid-difference becomes an imprecisely determined quantity. The ACC provides a good example in this case. Distances across it are of the order of 1000-2000 km. ACC transport through the Drake Passage is considered to be approximately 130 Sv with a meridional change in dynamic topography of approximately 120 cm across the current. It has an rms variability in the Drake Passage (mostly barotropic) of around 10 Sv on weekly time scales and longer, which translates into cross-passage sea-level variability of order 5 cm. This has been monitored by coastal and deep sea tide gauges for several years and more recently by altimetry. If it is asserted that there is a need for knowing the mean transport as well as its rms variability (e.g. to within 5 Sv), then there is a requirement to know the geoid-difference to better than centimetric accuracy.

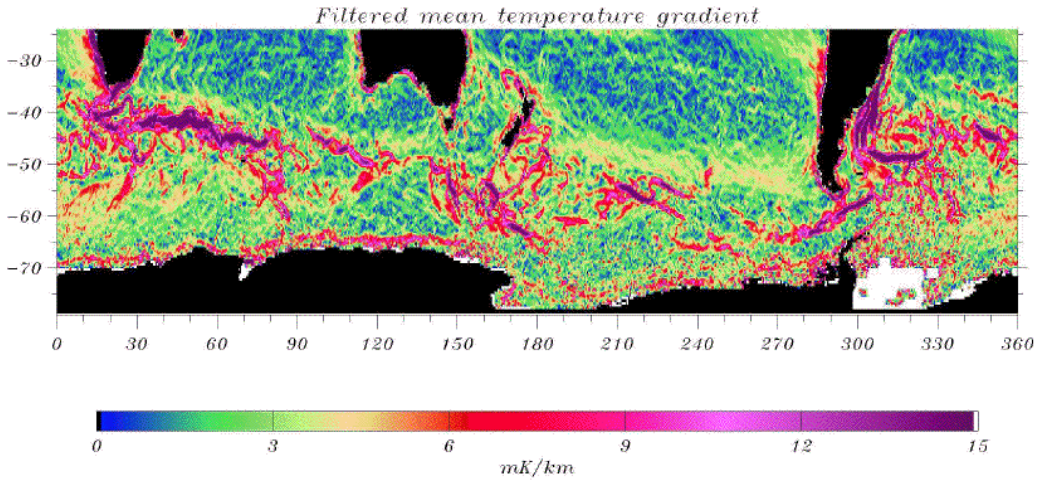

Figure 3.12. *Filtered mean-sea-surface-temperature gradients in the Southern Ocean obtained from the ERS/ATSR indicating the presence of many short-spatial-scale features (Hughes and Ash, 1999).*

3.3.5 Simulation Studies of Improvement in Flux Estimates

Developments for merging the gravity information, which will be obtained by GOCE and other gravity missions, into ocean models have recently been discussed by Ganachaud et al. (1997), Wunsch and Stammer (1998), Woodworth et al. (1998) and Le Grand and Minster (1999). Figure 3.13 shows the dynamic topography of the South Atlantic Ocean obtained from classical hydrographic data, indicating in particular the subtropical gyre in the north and the many fronts associated with the Antarctic Circumpolar Current in the south. Superimposed on the map are a number of sections through which have been studied the potential improvements in volume flux estimates obtained using a 1˚ inverse ocean model after assimilation of an altimeter-derived MSS (with uncertainty set to 2 cm as an estimate of the precision of altimetric measurements at the time of GOCE), hydrographic data and either the current EGM-96 or potential GOCE geoid model fields (see Chapter 4 for a full discussion of the latter; in this assimilation GOCE error fields up to degree 180 only were employed).

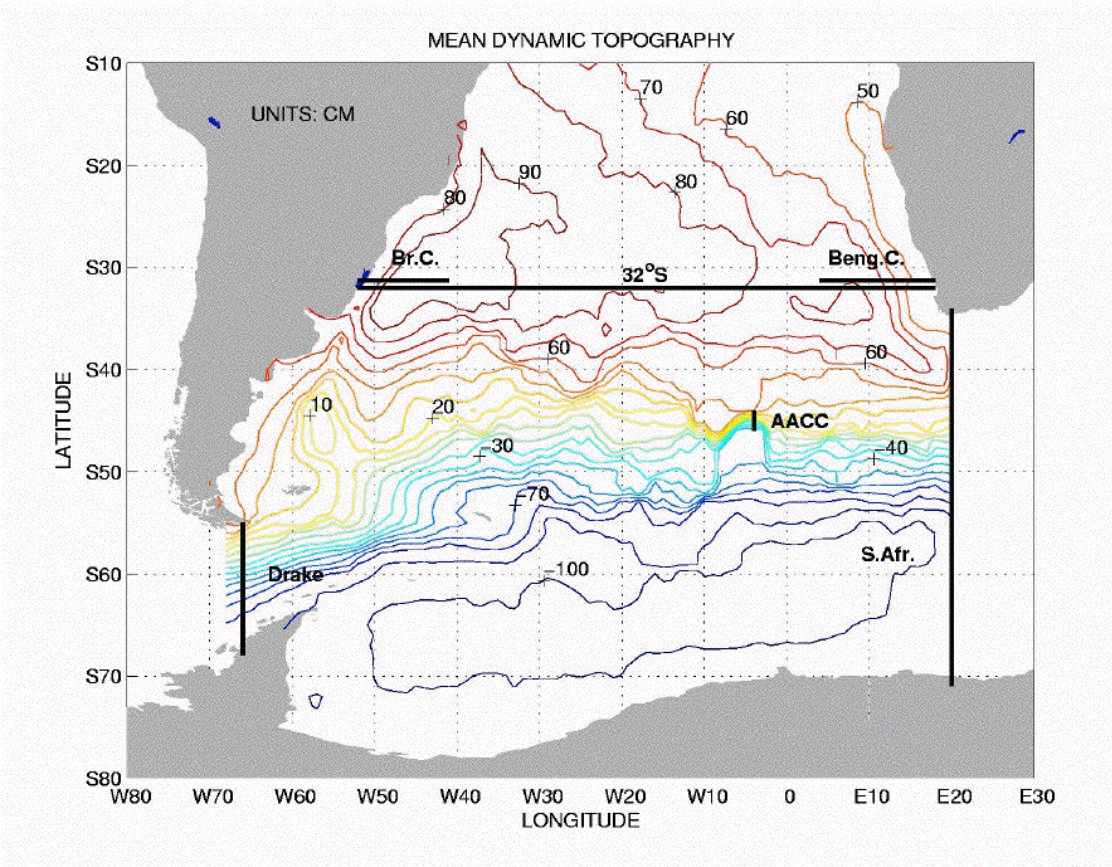

Figure 3.13. *Mean dynamic topography of the South Atlantic Ocean determined from hydrographic data, upon which sections discussed in the text are superimposed.*

Sections across the South Atlantic have been chosen to represent flows through the Drake Passage (a zonal section at 32˚ S between Africa and South America) through the widest part of the sub-tropical gyre, a short section through a sharp front in the ACC close to the Greenwich meridian (labelled 'AACC'), the South African ACC 'choke point', a section across the Brazil Current and a section across the Benguela Current. Figure 3.14 indicates the reduction in uncertainty of transports through each of the sections when using the anticipated GOCE error spectrum compared to that currently available from EGM-96. For each section, the reductions for the entire water column, for surface waters and at depth are shown. The transports estimated in the reference EGM-96 calculation and the associated uncertainties are indicated in parentheses.

The layers considered in this study have been chosen to represent the various dynamical regimes present in the ocean. For example, transports in the entire water column correspond to inter-basin exchanges of volume. Transports in the upper 100 m of the water column roughly correspond to the layer where Ekman transports (direct wind-driven surface flows) take place. The uncertainties in these Ekman transports are

larger than the uncertainties in the geostrophic transports (which are of the order of 1 Sv) obtained with the current EGM-96 error budget (indicated by the errors of the transports obtained by the model using EGM-96 shown in parenthesis in Figure 3.15), and limit the impact of the determination of the latter. However, the Ekman transport uncertainties can be expected to be greatly reduced in the future, as more precise wind scatterometer observations become available. Certainly, the calculations provide good indications of the impact of GOCE in the thicker layers (from the surface to a few hundred metres depth).

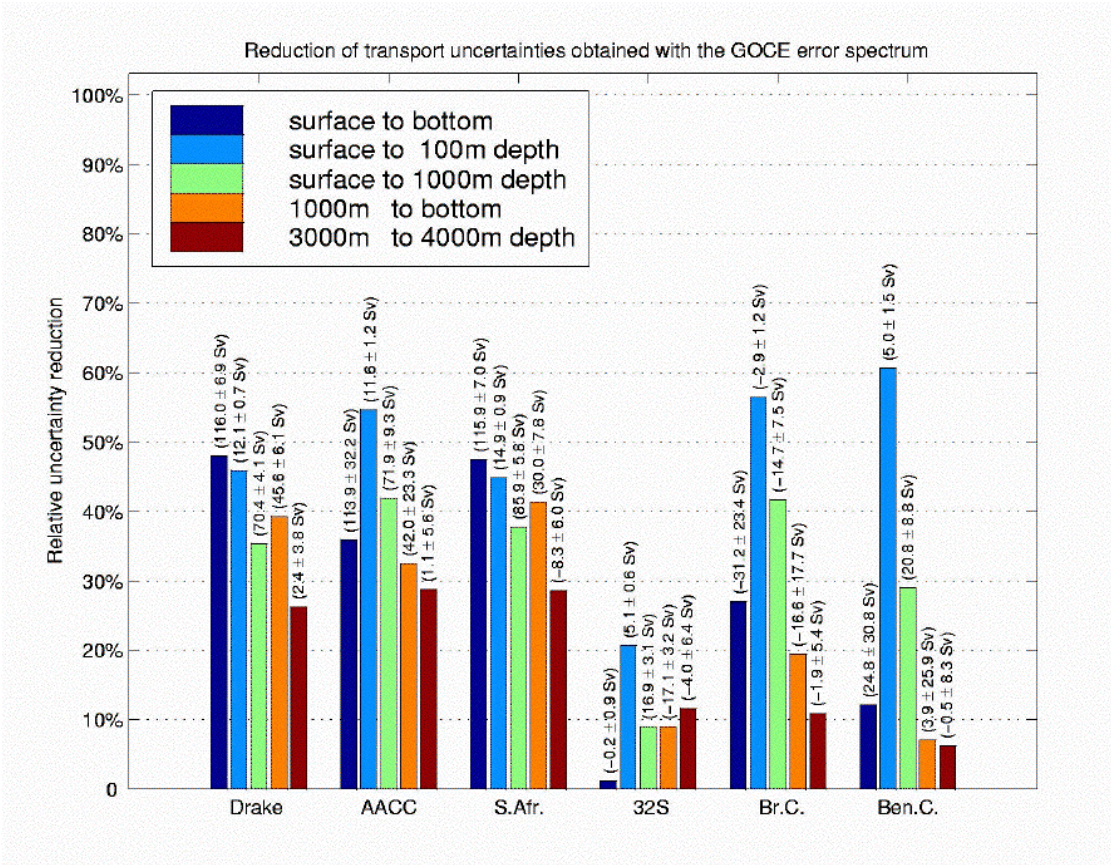

Figure 3.14. *Reductions in uncertainty of volume transports within an inverse ocean model when estimated GOCE errors are employed instead of those of EGM-96 for the Drake Passage, the short section across the ACC near to the Greenwich Meridian (AACC), the South African 'choke point', the 32° S African-South American gyre section, the Brazil Current section and the Benguela Current section. Numbers in parentheses show the transports obtained by the model using the present-day EGM-96 model, together with their uncertainties.*

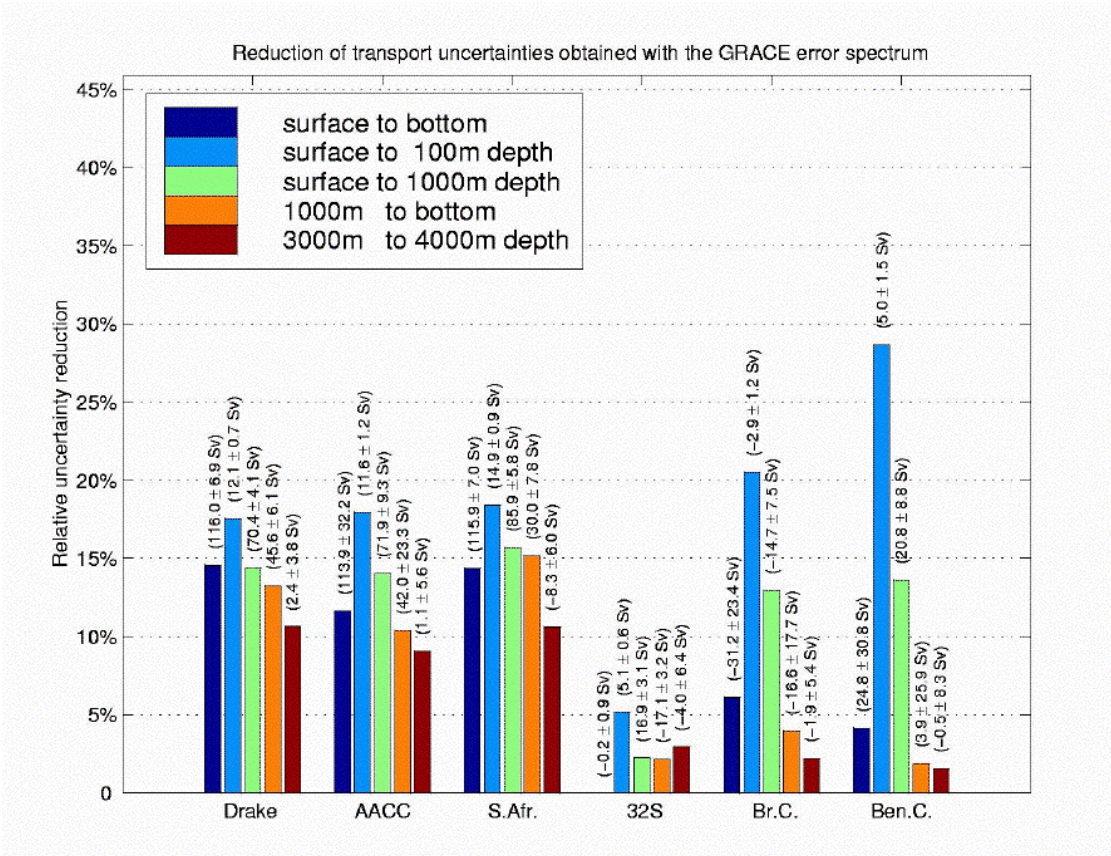

Figure 3.15. *As for Figure 3.14, but with estimated errors for the GRACE gravity mission.*

Transports in the upper kilometre of the water column correspond to the upper branch of the thermohaline circulation. Transports below 1 km depth correspond to the lower branch of this circulation. The present estimate of the uncertainties in these transports is approximately 10%. Consequently, the thermohaline transports are already fairly well known. However, the remaining uncertainties are still large in terms of our knowledge of the climate system and, perhaps more importantly, in terms of detection of potential climates changes. Indeed, a climate change of the order of the present-day uncertainties is likely to have a large effect on the environment because the transports of heat associated to the thermohaline circulation are huge (typically 1 Sv of volume transport corresponds to a heat transport of 5×10^{13} W). Therefore, the reduction of these uncertainties by means of data from a gravity mission is of great importance.

Transports in the deep layers of the ocean between 3000 and 4000 m depth correspond to the transports associated with the so-called ‘reference level’ velocities. These velocities cannot be determined by hydrography alone and must be determined from physical constraints, such as mass conservation, or from direct current measurements.

The largest reduction in transport uncertainty occurs in the upper-ocean, which is not surprising because reduced geoid errors will directly provide precise constraints on upper-ocean velocities. The overall reductions are very significant, being over 50% for the top 100 m of the short AACC section and up to 40% for the top kilometre. In the deep-ocean, the relative impact of GOCE is also significant, with a 30% transport uncertainty reduction in the Circumpolar Current. Such reductions follow from the major improvements in geoid model accuracy to be expected for remote areas of the ocean and will be of major importance to climate modelling. The impact on surface-to-bottom transports is also large for the three sections located in the Circumpolar Current, reflecting its barotropic character.

The impact on uncertainties in transports across the South Atlantic gyre at 32° S is smaller than the impact in other sections. The impact on uncertainties in surface-to-bottom transports is negligible because this transport is constrained by mass conservation to be zero within small error bars, and cannot be further reduced. The impact on surface transports is larger, but it is still much smaller than the corresponding impact found in the ACC sections. On the other hand, the impact on the shorter sections at 32° S across the Brazil Current and the Benguela Current is much larger. The transport uncertainty reduction reaches 60% in the upper 100 m and 40% in the upper kilometre, which is similar to the impact found in the Circumpolar Current. This result shows that the impact of gravity missions cannot be measured by looking at trans-oceanic sections only, especially in the case of a high-resolution mission like GOCE. The impact on transport uncertainties in the deep layers and the impact on transport uncertainties in the whole water column, however, are smaller in the Brazil Current and in the Benguela Current sections than in the ACC sections, thereby reflecting the fact that the ocean circulation is more baroclinic in these two regions.

That the largest absolute impact (about 10 Sv) is associated to the short section in the AACC and that the largest relative impact is associated to the sections across intense oceanic jets like the Brazil Current and the Benguela Current, is consistent with the idea that the GOCE mission will have a larger impact on narrow and intense currents because of its high-resolution.

The reduction of uncertainties in upper-ocean transports in the Brazil Current and in the Benguela Current would help oceanographers to identify the path used by surface waters to enter the Atlantic. The first path, usually referred to as the ‘warm water path’ (Gordon, 1986), attributes the origin of these surface waters to the Indian Ocean. The second path, the ‘cold water path’ (Rintoul, 1991), assigns their origin to the Circumpolar Current through the Drake Passage. The answer to this question has important implications in terms of the heat transport and its impact on the climate system. Indeed, the surface waters that enter the Atlantic replace cold waters leaving this ocean in the deep layers. Therefore, the net heat flux into the Atlantic depends on how warm the surface waters are, the warm water path corresponding to a larger northward heat flux than the cold water path because it is associated with a larger temperature contrast between the upper and the lower ocean. The path used by surface

waters is still a matter of debate among oceanographers because of the general lack of data from the Southern Ocean. GOCE, by reducing existing uncertainties in the upper-layer transport estimates of the Benguela Current by a factor of two, would greatly improve our knowledge of the upper-ocean circulation in this region.

An estimate of the impact of GRACE obtained with the same assumptions used for GOCE is presented in Figure 3.15 with the use of an error spectrum estimate to degree 150, which is the limit of information currently available for GRACE. An expansion to degree 180, as used for GOCE, would be more consistent with the resolution of the inverse model. Using an expansion to degree 150 is equivalent to assuming that the uncertainties in the GRACE geoid model will not be different at degree 150 and degree 180. This assumption, which is not justified in reality, is very favourable to GRACE. Hence, as expected, the amplitude of the impact of GRACE is less than half that of GOCE, while the distribution of the impact of GRACE on the various layers of the ocean and on the various sections is similar to the distribution of the impact of GOCE. This suggests that the propagation of the information on surface velocities provided by the combination of a geoid model and altimetric data is set by the characteristics of the ocean's in-situ fields. Despite the use of assumptions that are favourable to GRACE, the overall results show the importance of having an accurate and high-resolution mission like GOCE designed to measure the gravity field at the small scales that characterise the ocean circulation.

3.3.6 Improvements to Bathymetric Information

A major constraint on the construction of advanced deep-ocean and shelf models of ocean tides and circulation is the inadequacy of presently available bathymetric information. Attempts have been made to employ recently available high-spatial-resolution altimetric mean-sea-surface information (i.e. effectively the geoid at short-scales), constrained by bathymetric ship track data, to provide improved models of ocean depth (Smith and Sandwell, 1994, 1997; Knudsen and Andersen, 1996; Ramillien and Cazenave, 1997; Berge-Nguyen et al., 1999).

Bathymetry can be straightforwardly related to spatial gravity variations for half-wavelengths of approximately 10-500 km, with non-topographic gravity signals arising from sub-surface density changes contributing errors in the determination. At larger spatial-scales, dynamic effects become significant and the correlation between bathymetry and gravity disappears. Consequently, the method cannot be applied and bathymetric models have to rely on conventional data from ship measurements.

Although it is difficult to quantify the benefit of GOCE to such studies, the mission should be capable of improving bathymetric determinations, as a consequence of the overall gravity field improvement for half-wavelengths shorter than the 500 km.

3.4 Ice Sheets

A proper understanding of the mechanisms controlling ice-sheet mass balance has been shown to be essential to studies of long-term changes in sea-level and ocean circulation. For example, the Intergovernmental Panel on Climate Change (IPCC) Second Scientific Assessment (1995) made clear that the lack of knowledge of the mass balance of the Greenland and Antarctic ice sheets is a major uncertainty in accounting for past, observed global sea-level changes and in predicting future changes.

A precise gravity field over Greenland and Antarctica, together with greater amounts of information on ice thickness from in-situ surveys, will result in improved knowledge of ice sheet mass fluxes and associated dynamical behaviour, and thereby sea-level change over long time scales. Gravity data will reflect the shape of the bedrock that underlies the ice sheets. For the maritime Antarctic and North Greenland ice sheets, bedrock geometry is a control (some think the major control) on fluctuations of ice-sheet mass. For example, arguments connected with the stability of the West Antarctic ice sheet revolve around the relative importance of the geometry and rheology of the bed at the ice sheet margins (Thomas et al., 1979; Hughes, 1981; MacAyeal, 1992).

ERS altimetry and SAR interferometry are now providing detailed observations of the surface velocity of the Greenland and Antarctic ice sheets. They are also providing the short-spatial-scale topography of the marginal regions of the ice sheets. These data provide complete surface boundary conditions for the modelling of ice flows. However, lack of information on ice thickness precludes attempts to use these data to estimate calving fluxes, especially in Antarctica. The high-spatial-resolution provided by GOCE will provide the first possibility (through gravity inversion) of estimating bed geometry for many important ice streams, enabling the first case studies of century-time-scale fluctuations of many of the largest ice streams. The relatively more copious ice-thickness data from Greenland compiled by the Danish Geodetic Institute and other groups will enable partial validation of GOCE information prior to application to Antarctica. Simulations show that the rock-ice interface may be determined with a standard error of less than 10 m for features typically 80 km and larger, enabling an improved determination of, amongst other features, the total volume of the ice sheets.

The accurate geoid provided by GOCE will be important in two further respects. Firstly, as for the ocean, the geoid provides the reference surface for the gravity-driven ice flow. This is driven by pressure gradients parallel to the geoid. This is of particular importance to ice-shelf dynamics. Presently, the geoid is too poorly known to allow the determination of the driving stresses from altimetry. Secondly, it will make it possible to convert earlier obtained levelled heights to ellipsoidal heights, which may be compared to modern GPS-determined ellipsoidal heights (Roman et al., 1997 and section 3.5).

Furthermore, ongoing monitoring of the ice sheets by means of ERS, Envisat and future high-latitude altimetry (e.g. ICESAT, CRYOSAT) will be a major beneficiary of improvement in orbital accuracy provided by a gravity mission.

3.5 Geodesy

Geodesy is concerned with the measurement of the Earth's shape and the mapping of its regions. Its products are used extensively in all branches of the Earth sciences. In addition, they are applied to many areas of civil engineering, exploration, mapping and cadastral work and are the basis of all geo-information systems. Whereas positioning on the Earth's surface in two- or three-dimensional co-ordinates is based on purely geometric techniques, height determination requires knowledge of the Earth's gravity field. Only through knowledge of differences in gravity potential is it possible to decide on the direction of the flow of water or the direction of 'up' and 'down'. The traditional, very cumbersome and slow, technique of height determination is by means of geodetic levelling in combination with gravimetry. All developed countries have an ongoing programme of maintenance of large and dense systems of benchmarks with height values produced in this manner for scientific and applied users. Geodetic levelling attains mm-precision over smaller distances, but is subject to systematic distortions on continental scales. It is this latter weakness that severely limits the comparison and connection of height systems used in neighbouring countries or, for example, of tide gauges located on distant coasts. Separation of land areas by sea inevitably leads to large discontinuities between height systems.

A global geoid of 1 cm accuracy at about 100 km spatial resolution and a gravity field model with 1-2 mgal precision accuracy and the same spatial resolution would serve four major objectives in geodesy:

- control or replacement of traditional levelling by 'levelling with GPS'
- unification of height systems worldwide so as to refer to one height datum which will allow, for example, comparison of sea-level and sea-level changes in the North Sea with those in the Mediterranean
- separation of gravity acceleration from vehicle acceleration in inertial navigation
- elimination of gravitational uncertainty from satellite orbit trajectories.

Levelling by GPS: In a similar way as ocean altimetry combined with the geoid determines dynamic ocean topography, the combination of GPS and geoid determines land topography and topographic heights (Schwarz and Sideris, 1987 or Rummel, 1992). In other words, with the aid of geoid heights above an adopted ellipsoid, geometric heights above this ellipsoid, as determined by GPS or any follow-on system, are convertible to heights above sea-level. The latter are denoted 'orthometric

Figure 3.16. *Concept of 'levelling by GPS': Differential GPS provides ellipsoidal heights at terrain points (GPS heights); with precise geoid heights above the same adopted reference ellipsoid, GPS heights can be converted to orthometric heights (levelled heights).*

Unification of height systems: There are still a large number of unconnected height systems around the World. Each system refers to a reference point, usually a benchmark close to the sea and connected by levelling to mean sea-level obtained by a

tide gauge. The discontinuity in height systems is of no importance as long as there is no requirement to compare height values from the various systems. In the past, discontinuities had to be accepted whenever different geographical areas (with their individual height system) are separated by sea.
With the geoid precision to be achieved by GOCE, it will be possible to connect all height systems with cm-precision, provided at least one benchmark in each height system is equipped with precision space positioning such as GPS (see e.g. Heck and Rummel, 1990, Xu and Rummel, 1991, Khafid, 1998, and Arabelos and Tscherning, 1999). Therefore, GOCE will, for example, (1) bring all sea-level recordings into one system, (2) eliminate height discontinuities between adjacent islands, and (3) allow the removal of existing biases in terrestrial-gravity-anomaly data sets.

Separation of inertia and gravity in inertial navigation: The core sensors of any inertial measuring unit (IMU) for performing inertial navigation are a set of gyroscopes and accelerometers. These two units are either mounted on a space-stable (or levelled) platform or rigidly fixed to the vehicle to be navigated. IMUs are employed in land vehicles, for aircraft or missile guidance, in submarine navigation, pipeline maintenance and bore-hole control. The principle is quite simple: the accelerometers measure vehicle motion and single and double integration yields velocity and position differences, respectively. Changes in the orientation of the accelerometer triad are taken into account by the gyros.

However, one fundamental source of error is that the accelerometers measure not only vehicle motion, but the sum of vehicle and gravity acceleration. At present, the gravity part has been taken into account via a simple ellipsoidal gravity model. As a result, all deviations of the actual from an ellipsoidal gravity field are interpreted erroneously as vehicle accelerations. Precise knowledge of the gravity field, as provided by GOCE, will serve to drastically reduce this source of error and either allow an increase in the time intervals between which velocity or positioning updates are required or simply improve overall accuracy (see Schwarz, 1981, Forsberg, 1985).

Orbit determination: In addition to a further enhancement of past and future altimetric data sets for applications in oceanography and climatology as outlined in section 3.3, a high-accuracy gravity field model will provide a significant improvement in orbit computations for Earth-orbiting satellites. It will lead to a better understanding of the physics behind orbit perturbations. Especially for low-orbiting satellites, such a model will enable the separation of perturbations due to the static gravity field and those due to other perturbing forces. The latter will not only include non-conservative forces caused by atmospheric drag and solar radiation, but also perturbations caused by the solid Earth and ocean tides. It is foreseen that improvements can be made in modelling these perturbations.

This in turn will contribute to a further reduction in orbit-determination errors for Earth-orbiting satellites. Thus, for example, not only will the gravity field induced radial orbit error be reduced for altimetric satellites, but also the orbit error resulting

from inaccuracies in modelling other perturbations, non-conservative forces in particular. The latter inaccuracies may be aliased into existing models and are of the order of several centimetres for many of the altimetric satellites. These satellites include GEOSAT, ERS-1 and -2, and Envisat. Improved re-analysis of the old altimetric data sets will be possible. In addition, orbits will be improved in the flight direction and in the direction perpendicular to the orbital plane. This will significantly simplify and facilitate the use of, for example, SAR images taken by the ERS and Envisat satellites for many applications. Finally, improvements in modelling orbit perturbations will lead to more accurate orbit predictions, enabling the near real-time operational use of altimeter observations for oceanographic applications and of satellites carrying a GPS or GPS/GLONASS receiver for atmospheric sounding in weather-prediction models.

Accurate gravity field modelling will reduce the geographically correlated orbit error for altimetric satellites from a few cm with state-of-the-art models to less than a few mm. Table 3.1 contains estimates of the globally averaged geographically correlated orbit errors for different altimetric satellites. Values are included for the EGM-96 model based on its calibrated covariance and based on the expected performance of GOCE. For the past GEOSAT mission, the error will be reduced from 2.5 cm to about 1 mm. This reduction is required to estimate sea-level change with mm/year accuracy using historic altimetric data. Figure 3.17 displays the geographically correlated orbit error for the ERS and Envisat satellites using the EGM-96 model. It can be seen that the error varies over the globe and is always at the few-cm level, resulting in sea-level-change estimates that will have different errors for different regional areas. Thus improved gravity field modelling will not only result in improved global sea-level-change estimates, but it will also enable reliable estimation of regional sea-level change (see section 3.5).

Satellites	**EGM-96**	**GOCE Prediction**
ERS-1/2 and Envisat	2.36 cm	0.08 cm
GEOSAT and GFO	2.51 cm	0.14 cm
TOPEX and Jason	0.67 cm	0.08 cm

Table 3.1. *Geographically correlated orbit error.*

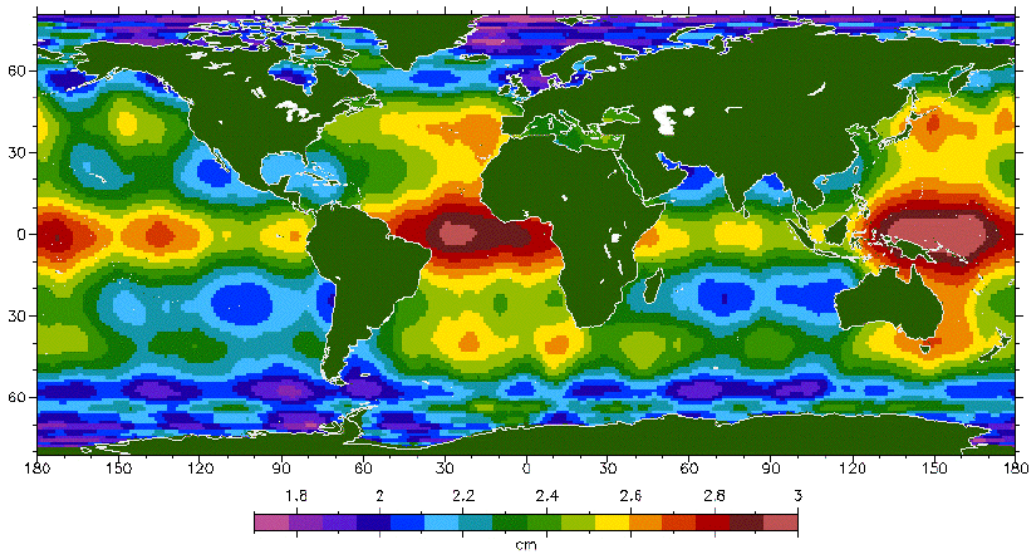

Figure 3.17. *Geographically correlated orbit error for the ERS and Envisat satellites based on the EGM-96 calibrated covariance.*

3.6 Global Sea-Level Change

Sea-level change is one of the most important components of global climate research to which GOCE will contribute. Global-averaged sea-levels are considered to have risen by between 10 and 25 cm during the past century, and are predicted to rise by the order of half a metre in the next century (Warrick et al., 1996). This will have important consequences for the 50-70% of the World's population which lives within coastal zones, which depend on the agricultural and industrial productivity of coastal regions ,or which have to be protected from coastal flooding (Bijlsma et al., 1996). Possible impacts on low-elevation coral islands (e.g. Maldives) and river deltas (e.g. Bangladesh) are obvious and have been well documented. Less well known is the fact that a rise of 50 cm along the East coast of England and other parts of the European Atlantic coast will increase the probability of flooding by an order of magnitude (Coles and Tawn, 1990).

It is essential that we attempt to understand the various components of sea-level change at the coast (e.g. section 3.2), rather than simply observe the combined effect with networks of tide gauges, if accurate predictions are to become possible. In addition, it is clear from inspection of the historical tide-gauge data set (Fig. 3.18), and from study of currently-available models (Figures 3.19 and 3.20), that future sea-level changes resulting from the various climate and geological processes will be anything but globally uniform. It is most important, therefore, to provide coastal planners with the information that will be of greatest utility in their particular areas.

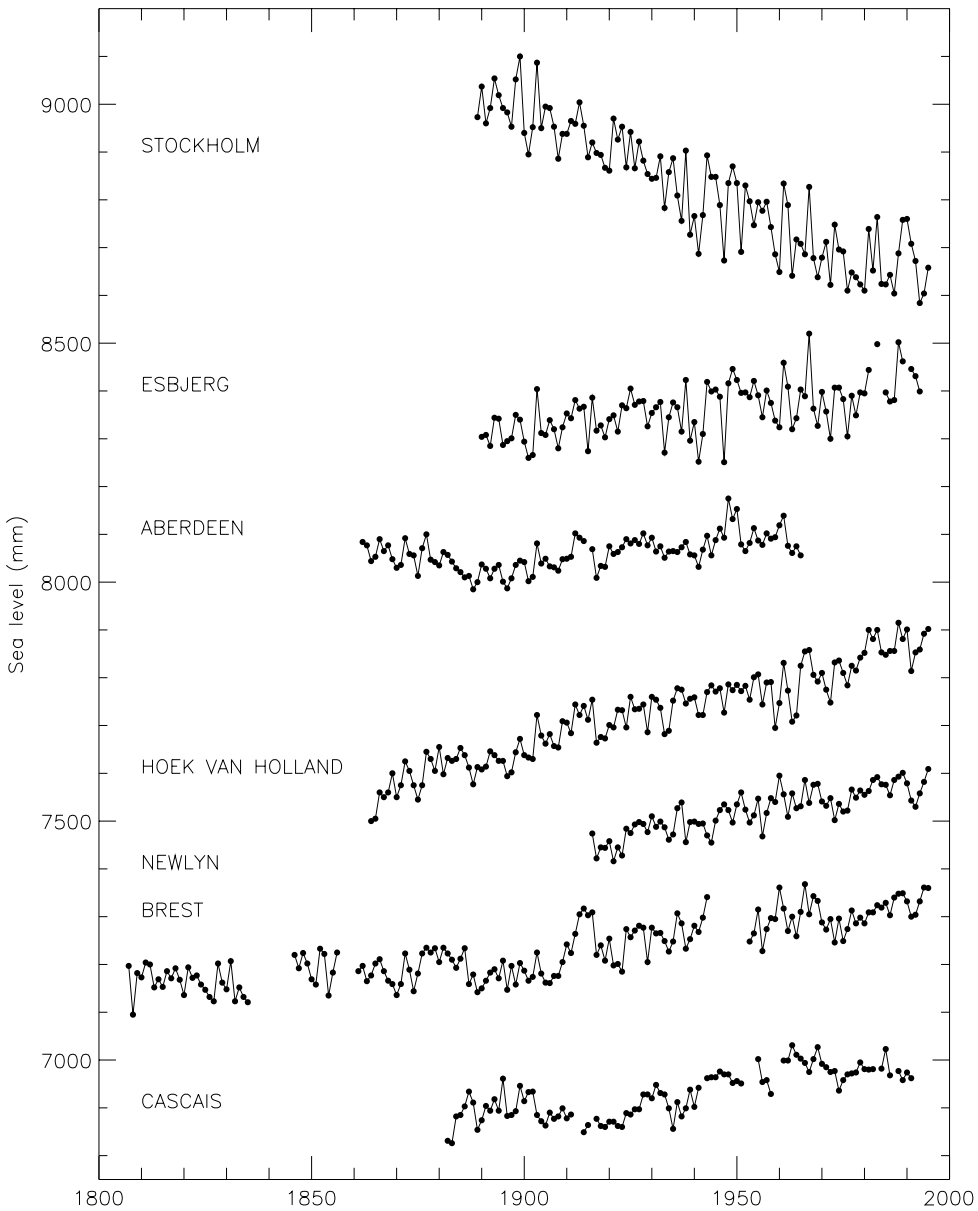

Figure 3.18. *Long sea-level records from selected sites north to south in Western Europe. Each record has been offset vertically for presentation purposes. The apparent fall in sea-level at Stockholm of order 40 cm/century is due to post-glacial rebound of the land. The positive secular trends at stations further south are comparable to the global average of between 10 and 25 cm/century.*

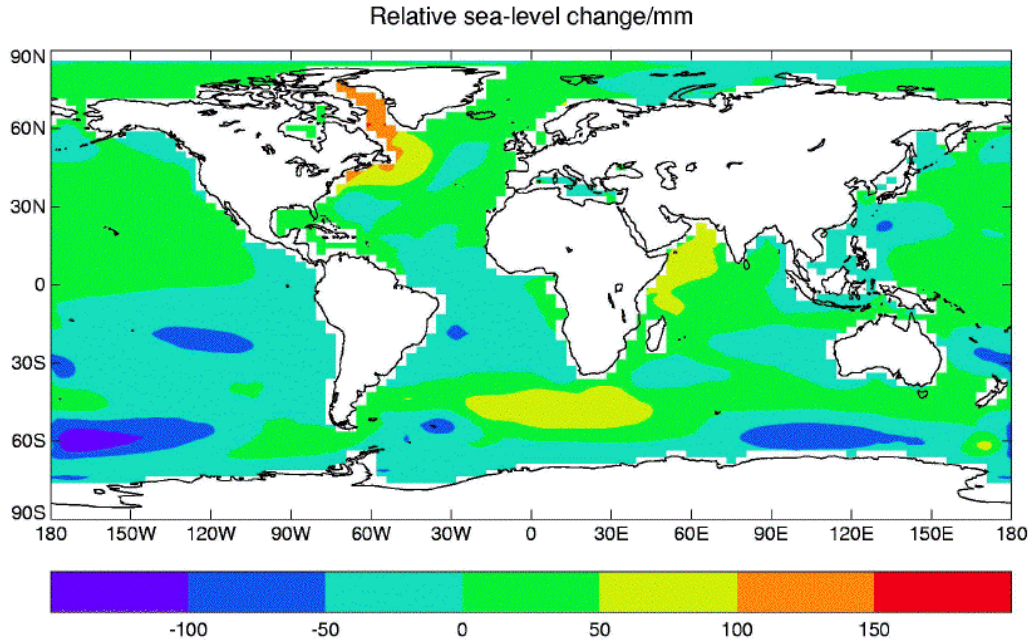

Figure 3.19. *Spatial variations in global sea-level change due to oceanic thermal expansion approximately 70 years from the present from a GCM model run. Note that a global mean rise of 10.2 cm is removed and hence the changes are relative to this mean (from Warrick et al., 1996).*

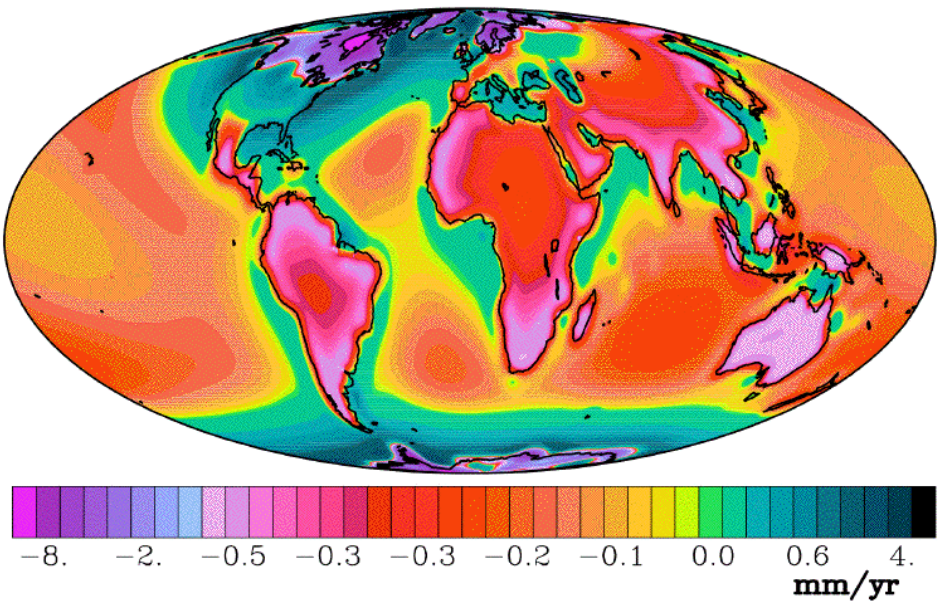

Figure 3.20. *Spatial variations in global relative sea-level change due to post-glacial rebound as predicted by model ICE4G-VM2 (Peltier, 1998).*

GOCE can improve our understanding of past sea-level changes, and thereby improve predictions of future changes, in at least five ways:

(1) A GOCE-derived oceanographic geoid will result in more reliable determinations of ocean heat and volume fluxes for use in General Circulation Models (GCMs) employed to model sea-level change due to thermal expansion, which is expected to cause most of the change in the next century. Figure 3.21, which summarises the mid-range predictions for future global-average change from the Second Assessment Report (1995) of the Intergovernmental Panel on Climate Change (IPCC), demonstrates the relative importance of the thermal expansion component of the predictions and shows clearly the necessity of being able to model such processes satisfactorily. Several studies suggest an even larger than average rate of rise of sea-level in the North Atlantic as a consequence of modification of the rate of bottom water formation (e.g. Bryan, 1996). A 49 cm rise implies an order of magnitude increase in the frequency of storm surge over-topping in many areas.

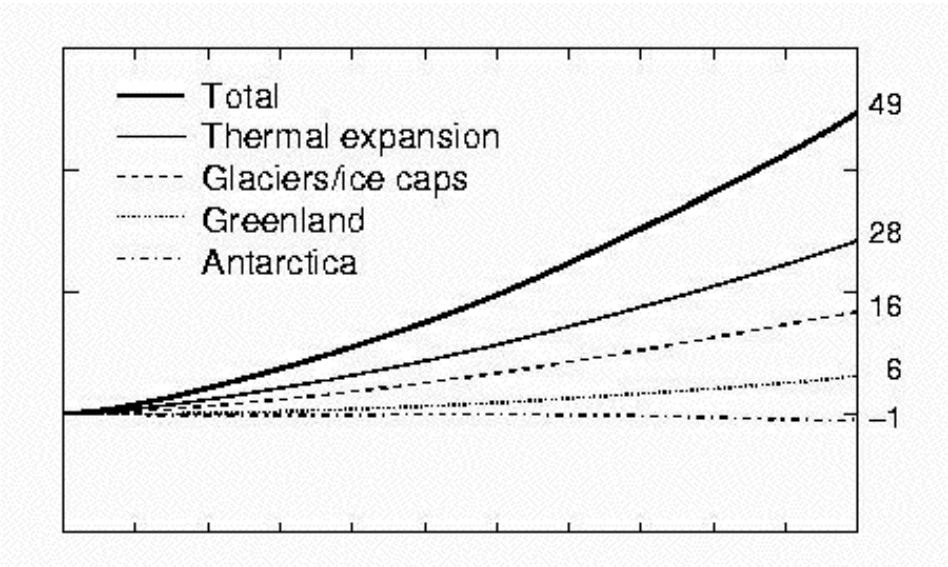

Figure 3.21. *Best-estimate projected individual contributions to global sea-level change 1990-2100 from the IPCC Second Assessment Report (Warrick et al., 1996).*

(2) Similarly, a precise geoid over the Greenland and Antarctic ice sheets will provide information on bedrock topography and, with altimetry, ice thickness and surface gradients essential to studies of mass balance (section 3.4).

(3) Time series of sea-level changes observed by tide gauges during the last century contain two major components. The first results from real changes in ocean volume (and redistribution of this volume) due to the changing ocean circulation as a result of a range of oceanographic, glaciological, hydrological and meteorological forcings. In principle, these should be capable of being

understood with reasonable accuracy, as long as an adequate set of climate models can eventually be constructed. The second component results from changes in the levels of the land upon which the gauges are located as a result of a number of geological processes.

Inspection of the global tide-gauge data set demonstrates that the global effects of Post Glacial Rebound (PGR) can be clearly identified in the records (e.g. Fig. 3.18), along with signals of a more local nature such as those due to earthquakes or mining subsidence (Emery and Aubrey, 1991). Most analysts of the data set have attempted to isolate the 'real' (i.e. climate) signal of sea-level change by employing a geodynamic model of PGR and by selective geographical filtering of the tide-gauge records in order to reject those most obviously located in tectonic or anthropogenically-influenced areas where PGR cannot be considered the main geological process (e.g. Douglas, 1997).

More accurate models of PGR (e.g. Peltier, 1998) and of local tectonics (section 3.2) than those currently available will result in more precise estimates of the rates of 'real' global- and regional-average sea-level change during the past century by reanalysis of the historical tide-gauge records. This will provide tighter constraints within which to assess the quality of hindcasted sea-level trends from the climate models.

The models will also allow more accurate predictions of future changes at sites along the coast without tide gauges. Although the use of Global Positioning System (GPS) receivers will probably become routine at gauge sites and many other locations (Neilan et al., 1998), thereby providing data on local rates of vertical land movement, there will never be complete coverage by means of this technique. Where rates of vertical land movement have to be modelled rather than measured, the availability of precise PGR models will be essential.

(4) As a result of improvements in reliability of 'GPS minus geoid levelling' between sites (section 3.5), it will be more feasible to combine sets of short historical tide-gauge records (dispersed through a region) into regional composites. Such composites can already be constructed using short records from sites relatively close together (e.g. in the same port area) and employing conventional geodetic levelling.

(5) The improved knowledge of the longer-wavelength components of the gravity field from GOCE and other missions will lead to a significant improvement in radial orbit accuracy for previous (GEOSAT, ERS) and future (Envisat, GEOSAT Follow Ons) altimeter satellites which are operated at altitudes lower than those of TOPEX/Poseidon and Jason-1. The result will be a reduction in geographically-correlated orbit errors in multi-decadal time series of sea-level anomalies for studies of dynamic topography (section 3.5), low-frequency ocean circulation variability and long-term quasi-global sea-level change. It will

also enable the direct use of altimeter data from any repeat or non-repeat orbital cycle by the provision of a common, precise reference surface. By 2010, it should be possible to obtain a global, fully calibrated altimetric data set almost three decades long, which should provide the information on global sea-level trends and accelerations required for comparison to the geological-, archaeological and tide-gauge-derived sea-level data sets acquired over previous epochs.

3.7 Summary

The research objectives discussed in this chapter will be addressed in the context of observation requirements in Chapter 4. However, the likely scheme in which the gravity field and geoid data would be applied (in combination with other data and models), will first be summarised here in association with studies of solid-Earth physics, ocean mass transport and heat fluxes, ice sheet dynamics and geodesy.

The diagram in Figure 3.22 summarises how GOCE, together with other data, will contribute to a better knowledge of the most important solid Earth phenomena, especially those concerning the continental lithosphere.

The density plays a central role and this is the parameter that is best constrained by the precise knowledge of the gravity field that would be provided by GOCE, aided by regional and local seismic data wherever available, as shown in section 3.2.2.

The most demanding requirements on the quality of the recovered gravity field, in terms of precision and resolution, are associated with the phenomena and structures that require the most detailed insight (e.g. sedimentary basins and rifts) and are of the order of 1-2 mgal at 50-100 km. These numbers, if met, will satisfy the other modelling needs that require coarser resolution, namely from one hundred to several hundreds of kilometres.

The accurate and high-resolution marine geoid, as derived from GOCE, will in combination with precise satellite altimetry enable new estimates to be made of the absolute ocean topography (Fig. 3.23). In combination with in-situ data and ocean models, this will, in turn, act as an important constraint for calculations of oceanic mass transport and heat fluxes.

In a way, this scheme was used (indirectly) when the reduction in transport uncertainties was estimated for the selected sections in the Southern Ocean (section 3.3, Fig. 3.14).

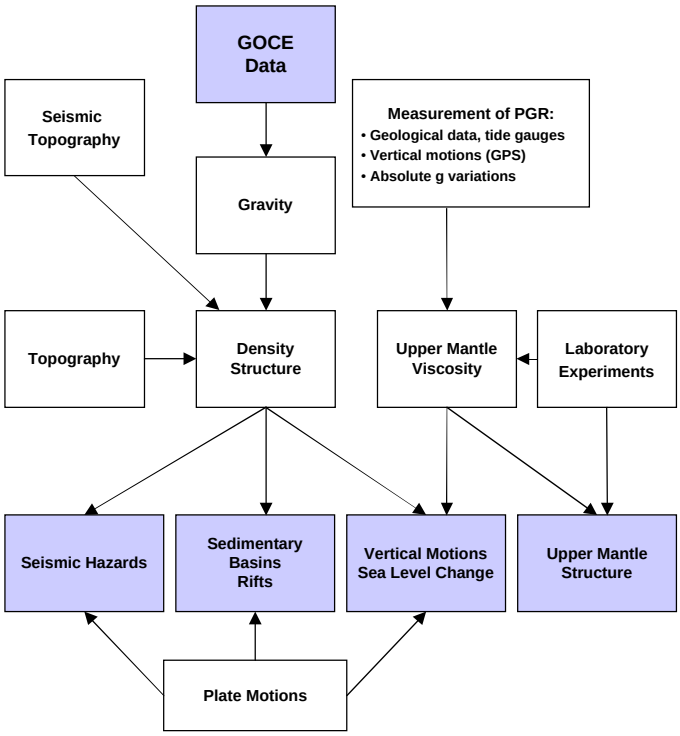

Figure. 3.22. *Schematic of how GOCE observations, together with other data, will contribute to a better knowledge of the solid-Earth phenomena.*

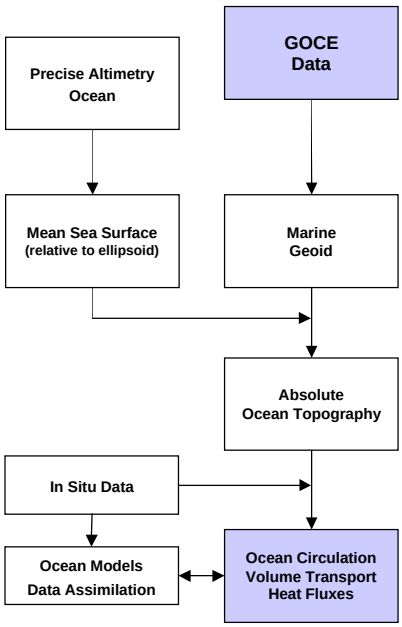

Figure 3.23. *Schematic of the improvement in absolute ocean circulation studies from combination of the GOCE-produced marine geoid with precision altimetry.*

Moreover, the accurate and high-resolution gravity anomaly field, as derived from GOCE, will in combination with precise satellite altimetry, enable new quantitative understanding to be obtained of the bedrock topography as suggested in Figure 3.24. In combination with in-situ data and ice sheet models, this will, moreover provide better constraints for studies of ice sheet dynamics and volume changes.

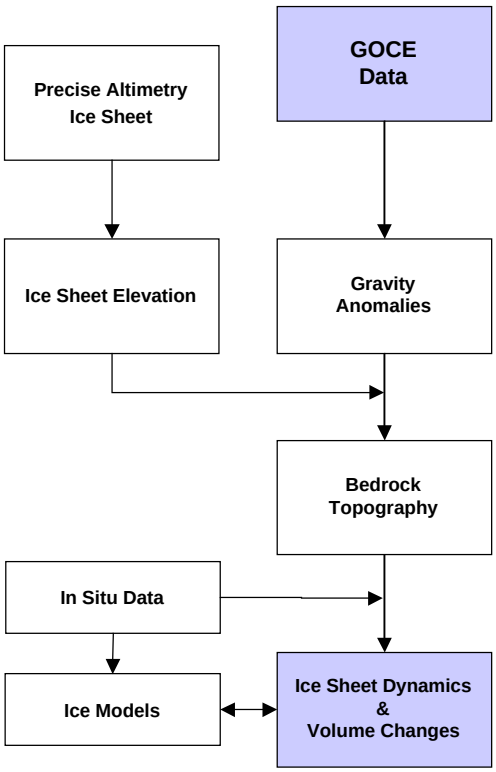

Figure 3.24. *Schematic of the improvement in studies of ice-sheet dynamics from combination of the GOCE-derived gravity anomalies with ice-sheet elevation from precision altimetry.*

Similarly the flowchart in Figure 3.25 summarises how the GOCE data can be used in combinations with other sources of information yielding new and important opportunities in geodesy; both scientific research and practical applications.

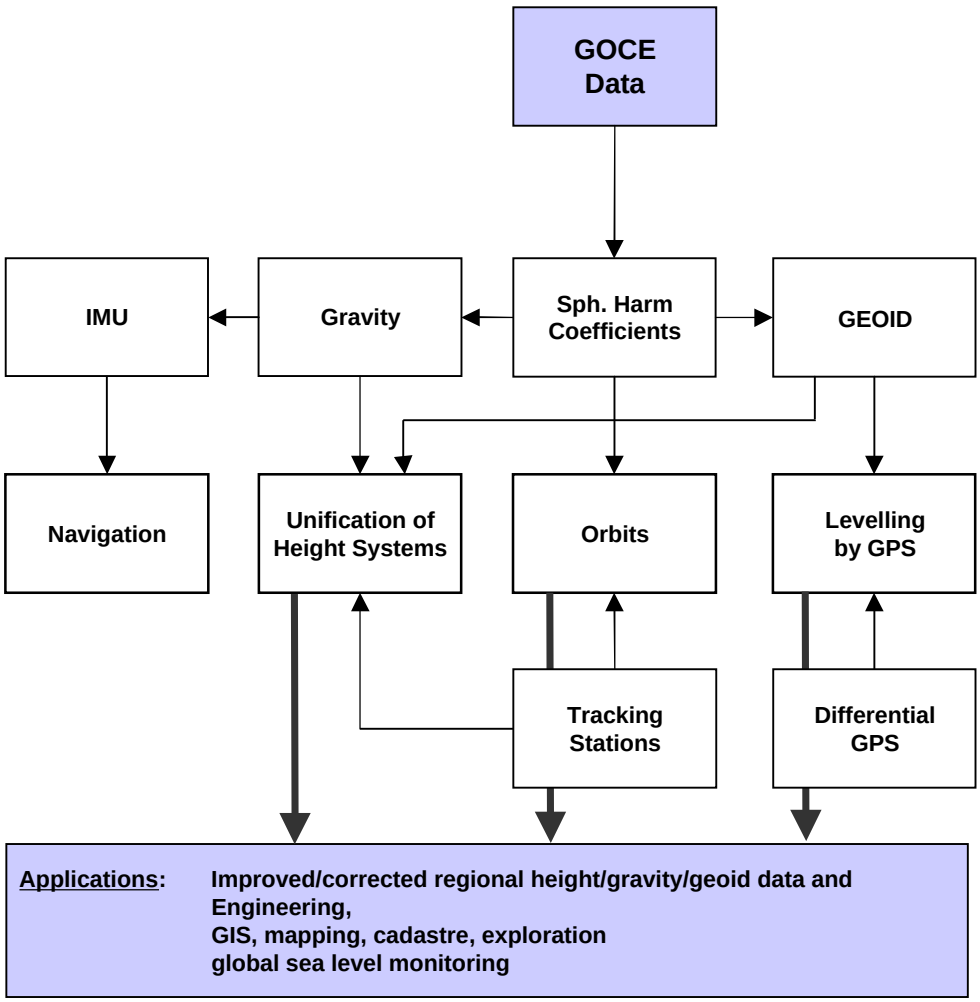

Figure 3.25. *GOCE data and their use for navigation, the unification of height systems, precise orbits and 'levelling by GPS', with a wide range of applications in practice and science.*

4 Observation Requirements

It has been shown in the previous chapters that there is a real need for a global, accurate, high-spatial-resolution model of the static part of the Earth's gravity field and its related geoid heights. The purpose of this chapter is to explain why the GOCE mission concept was selected and to provide the corresponding observation requirements. This draws on the results of several technical studies. The chapter will therefore:

- summarise gravity field requirements for science. The science objectives described in Chapter 3 are associated with requirements for the resolution and accuracy with which the gravity field parameters must be determined
- discuss the conversion of the science goals into observational requirements using the special mathematical tools and techniques introduced in Chapter 2.

The GOCE mission has been conceived and designed taking into account these scientific requirements and technological solutions, to provide the most accurate, global and high-resolution map of the gravity field and its corresponding geoid surface. It will combine the satellite gradiometry and satellite-to-satellite high-low tracking (SST-hl) techniques that have been found to be optimum for providing the required high-quality, high-resolution static gravity field. To ensure the global completeness of the derived gravity model, which also impacts on its accuracy, a quasi-polar orbit must be chosen.

4.1 Gravity Field Requirements for Science

The quantitative requirements for the different scientific goals are derived from the arguments developed in Chapters 2 and 3. They are expressed in terms of geoid-height and gravity-anomaly accuracies as shown in Table 4.1, linked to the corresponding spatial resolution to which they apply (expressed in half-wavelengths). Specifically, in the context of meeting the scientific objectives addressed under solid-Earth physics, oceanography and geodesy, the key requirements are:

- to measure the Earth's gravity anomaly field with an accuracy of better than 1 to 2 mgal (or 10^{-5} m/s^2)
- to determine (from the measured gravity anomaly field) the geoid with an accuracy better than 1 cm radially, and
- to achieve these measurements at a length scale of 100 km or less.

The requirements should be understood in the sense of most likely values, i.e. equal to standard deviations assuming a normal distribution of errors. Taking advantage of

numerous previous studies, the report focuses only on those science items for which the accuracy and resolution lie within the capability of the GOCE Mission.

APPLICATION	ACCURACY		SPATIAL RESOLUTION (half wavelength – D in km)
	Geoid (cm)	Gravity (mgal)	
SOLID EARTH			
Lithosphere and upper-mantle density structure		1-2	100
Continental lithosphere:			
• sedimentary basins		1-2	50-100
• rifts		1-2	20-100
• tectonic motions		1-2	100-500
Seismic hazards		1	100
Ocean lithosphere and interaction with asthenosphere		0.5-1	100-200
OCEANOGRAPHY			
– Short-scale	1-2		100
	0.2		200
– Basin scale	~ 0.1		1000
ICE SHEETS			
– Rock basement		1-5	50-100
– Ice vertical movements	2		100-1000
GEODESY			
– Levelling by GPS	1		100-1000
– Unification of worldwide height systems	1		100-20 000
– Inertial Navigation System		~1-5	100-1000
– Orbits *		~1-3	100-1000
SEA-LEVEL CHANGE	Many of the above applications, with their specific requirements, are relevant to studies of sea-level change.		

Table 4.1. *The requirement (developed in Chapters 2 and 3) expressed in terms of geoid height and gravity anomaly accuracies. (Orbits*: 1 cm radial orbit error for altimetric satellites).*

4.2 Overview of Simulation Techniques

It is now necessary to convert the scientific goals and requirements into observational requirements for the instrument and satellite systems. This has been done in steps, using various techniques, by different groups who have worked in this area for many years. The results and requirements given below are the outcome of the most recent simulations. They have been completely validated.

The mission goals may be stated in terms of error estimates for each of the coefficients of the series of a spherical harmonic expansion (gravity model) or of the derived surface mean gravity or geoid values. The relationship between the observations and the estimated quantities is obtained by error propagation from the known observation error characteristics, taking advantage of the fact that, to a very good approximation, both measured and derived quantities are linear functions of the gravitational potential. In principle, the potential, expressed in spherical harmonics, has an infinite number of components, so some boundary conditions have to be imposed to derive the final geophysical quantities from the observations. Since the data are obtained high above the Earth's surface, and the results are needed at the Earth's surface, errors are magnified (when going down). This may be controlled by imposing restrictions on the magnitude of the result (called 'norm minimalisation' or 'regularisation'). The observations may also have systematic errors. These may be accounted for by simulation, as it has been shown that such errors can be removed by taking advantage of the fact that there are areas at the Earth's surface where gravity is known precisely. In addition, the very-long-wavelength part of current global models (or of those to be obtained from missions like CHAMP and GRACE) can be taken as a reference comparison.

Different simulation studies have differed mainly in terms of the regularisation method used, or in the quantities for which the error estimates are expressed. They may use data at different altitudes and for different mission durations. A tremendous amount of work in this area has been accomplished between 1989 and 1996 by a consortium of European teams with the support of ESA (see for instance: CIGAR III, 1993 and 1995; CIGAR IV, 1996). Further efforts have been made since then to cross-validate different simulation approaches and results (Balmino et al., 1998), and also to address the different stages in the transformation of instrument outputs into tractable quantities (see Chapter 7). In the meantime, these simulation techniques have become international standards.

In simulating GOCE and other missions different approaches have been taken. They are justified by the different mathematical techniques for transforming GOCE observations into the gravity field parameters. They are needed to guarantee the precision of the derived models and hence the performance of the proposed mission. The methods and developed software will be the basis of all future activities aimed at retrieving global or regional gravity field information from satellite data.

(a) Dynamic Simulations (time-wise approach)

The measurable gravity gradients are considered as time series over the whole mission length along the spacecraft trajectories. The series coefficients are linearly related to the coefficients of a spherical harmonic expansion of maximum degree L. Then the result may be expressed as the standard deviation of $(L+1)^2$ coefficients. From these error estimates, errors on other quantities may be derived by linear error propagation. Several such studies have been carried out, for instance by Colombo (1989), Schema (1991), Balmino and Perosanz (1994), Rummel et al. (1995) and Balmino et al. (1999).

(b) Boundary Value Approach (space-wise approach)

If the observations are interpolated to form a dense grid on a surface at satellite altitude, then there exist, for different data types, simple relationships between the coefficients of the spherical harmonic expansion of the data and that of the gravitational potential. Typically the coefficients must be multiplied by the degree l for an SST type measurement and by l^2 for an SGG measurement (see section 2.5.). There is then a simple relationship between an idealised data set, and the coefficient errors, which is well suited to study the variation of errors as a function of altitude (see for instance Rummel et al., 1993; Albertella et al., 1999).

(c) Regional Recovery

Numerical and statistical approximation methods may both be used to work directly from the data (without gridding) to results at the Earth's surface. However, they generally assume that systems of equations with full matrices are to be solved and they have therefore primarily been used for regional simulations (see Arabelos and Tscherning, 1995). These studies have the advantage that the error may be directly propagated from the observations and that the actual gravity field variation (for instance inferred from the topography) may be taken into account.

4.2.1 Chosen Approach

The results presented here have been obtained by using the global time-wise approach. They have been verified by the space-wise approach. In order to explain the reasons underlying the chosen concept for the GOCE mission, so-called normalised missions have been simulated, each of them corresponding to one of the concepts described in section 2.3. It will be seen that the characteristics of the recovered gravity field errors for these idealised scenarios will determine the choice of the GOCE solution for the best possible static gravity field model. Finally, simulations of the baseline GOCE mission have been performed showing how well the scientific goals will be fulfilled.

A covariance propagation analysis approach has been used. This method allows the spherical harmonic coefficients of the gravitational potential (V) to be recovered by either inversion of the orbital perturbations in position (as monitored by SST-hl),

relative perturbations in position or velocity (as is the case in SST-ll), gravity gradient measurements in the SGG case, or some combination of these.

To simplify matters and to optimise the computational effort (for instance, about 90000 coefficients must be estimated for a model truncated at degree 300), a linear model is assumed. The mean orbit of the low satellite(s) is taken as circular and its plane is assumed to precess regularly around the Earth's rotation axis so that, measurements being taken at fixed step intervals, the resulting coverage is uniform. In the linear model, the transfer functions between the harmonics of the potential and the orbital perturbations in the three directions, i.e. along-track Δx, cross-track Δy, and radial Δz. The gravity gradient components (V_{xx}, V_{xy} , etc.) carry the key to the determination of these harmonics.

The expected a-posteriori error variances of the harmonic coefficients are estimated by a least squares scheme from an a-priori error model of the observations. Band-limited instruments and coloured noise have been introduced. In general, the resulting system of equations may be unstable or even singular (i.e. certain groups of coefficients cannot be determined). In such cases, it is necessary to introduce some a-priori or complementary information that permits a unique and stable determination of the solution. In some of the simulations reported below, a regularised solution is obtained by taking account of the error variances of the coefficients for which good estimates are available (from a current long-wavelength model), and/or signal variances as derived from a general model (Kaula's rule) for those coefficients for which no reasonable prior knowledge exists.

4.3 Simulation and Comparison of Normalised Missions

Missions based on different concepts may have characteristics so different that it may be impossible to clearly assess their contribution to gravity field knowledge. Therefore, it was necessary to perform a set of simulations of so-called conceptual and 'normalised' missions (e.g. all with polar orbit) which would use only one of the following techniques at a time: satellite-to-satellite tracking in the high-low mode (SST-hl), satellite-to-satellite tracking in the low-low mode (SST-ll), or satellite gravity gradiometry (SGG).

For a comparison of these concepts, the following baseline parameters are adopted (Table 4.2). To avoid misunderstanding, this is not a comparison of actual mission parameters, but of normalised missions.

Mission	Obs.	$\sqrt{(\text{PSD})}$	I [deg]	h [km]	T	L	ρ_0 [km]
SGG-*n*	V_{xx}, V_{yy}, V_{zz}	$5\,\text{mE}/\sqrt{\text{Hz}}$	90	250	30 d	240	—
SST *ll-n*	$\Delta\dot{\rho}$	$1\,\mu\text{m/s}/\sqrt{\text{Hz}}$	90	350	30 d	175	300
SST *hl-n*	$\Delta\,\underline{x}$	$1\,\text{cm}/\sqrt{\text{Hz}}$	90	350	30 d	100	—

Table 4.2. *Normalised mission concepts comparison. PSD = power spectral density (includes satellite and system errors), I = inclination, h = satellite altitude, T = mission duration, L = highest spherical harmonic degree in adjustment process,* ρ_0 *= inter-satellite distance, 1mE = 1 milli-Eötvös where 1 Eötvös =* $10^{-9}\,\text{s}^{-2}$*. The suffix '-n' denotes 'normalised' (idealised) missions.*

SGG-*n* represents a normalised gradiometric mission. Drag-free compensation (at an altitude of 250 km) is assumed (see Chapters 6 and 7) and only the three diagonal terms of the gravity gradient tensor are employed for gravity analysis. SST *ll-n* represents a normalised low-low satellite-to-satellite tracking mission; the measurement here assumed is range-rate $(\Delta\dot{\rho})$. An orbital height of 350 km is chosen, as the satellites are assumed not to fly drag-free. 350 km is rather a low altitude but highest sensitivities are attained. The inter-satellite distance of 300 km is chosen such that no 'common-mode' attenuation effects occur.

SST *hl-n* represents a normalised high-low satellite-to-satellite tracking mission. This can also be viewed as orbitography, i.e. the observable is the 3-D orbit perturbation of the low-altitude orbiter as tracked by GPS. No regularisation (i.e. no stabilisation of the final system of equations to be inverted) is applied. In addition, SST *ll-n* and SGG-*n* are not aided by GPS in these simulations (as will be seen, SGG benefits very much from GPS in the very low degrees). The given power spectral density (PSD) numbers of the sensors should represent the noise behaviour of present systems.

The results of the error simulations are presented in Figures 4.1a, b and c. Figure 4.1a shows the degree root mean square (RMS) values of the expected error of the spherical harmonic coefficients for the three mission concepts of Table 4.2. The curve 'Kaula' represents the expected signal degree RMS values and allows the definition of spectral (also spatial) resolution. Figure 4.1b expresses the same results, but translated into the cumulative expected geoid error: the very low plateau for SGG up to degrees 100 would decrease to an even lower value with the inclusion of GPS (see next section). Similarly, Figure 4.1c shows the cumulative expected error on the global gravity anomaly field.

[a]

[b]

[c]

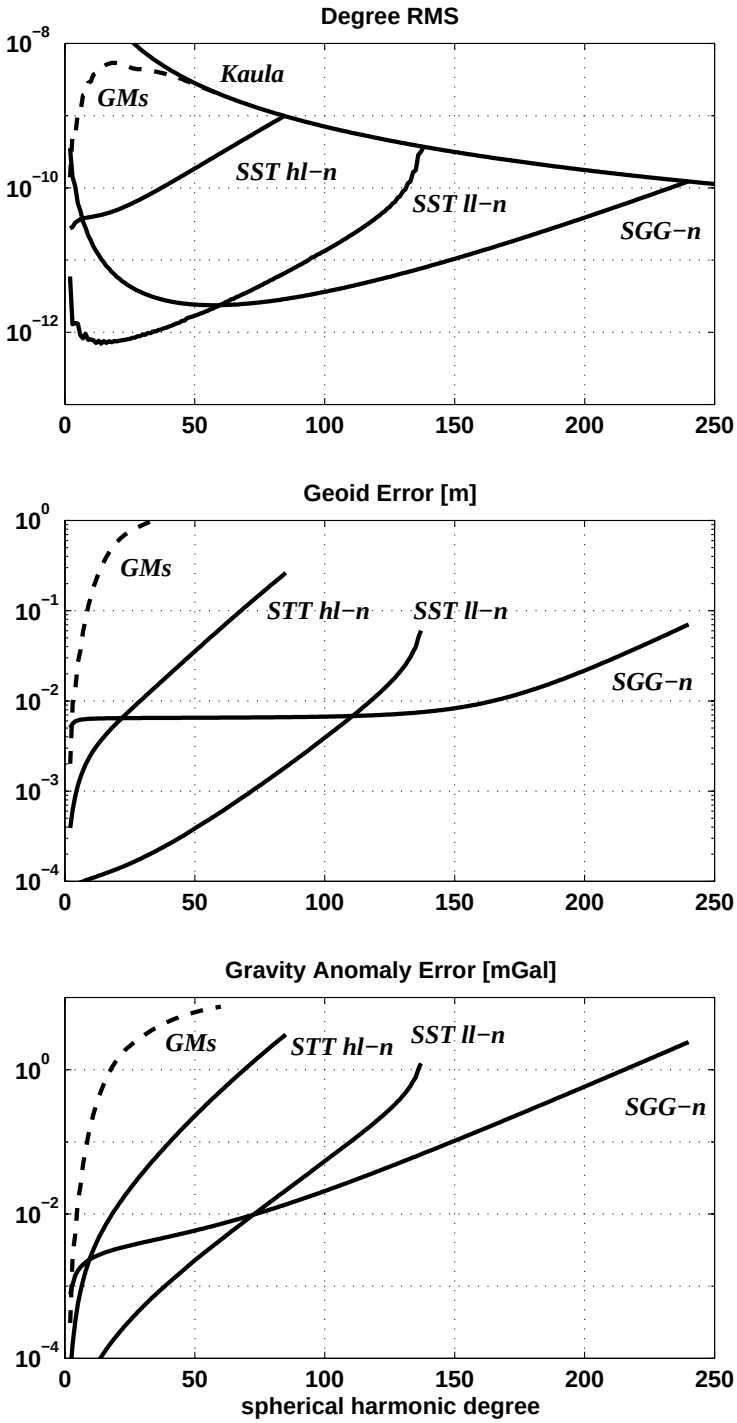

Figure 4.1. *Principal character of the normalised gravity satellite mission concepts. Also included are errors per degree of one of the best available gravity potential models (GMs) based purely on orbit information. The average signal behaviour in [a] is indicated by the 'Kaula' curve. The crossing between signal and error curve defines the maximum resolution. SST ll is for SST low-low, SST hl for SST high-low, SGG for gradiometry. The suffix '-n' stands for 'normalised' (idealised) missions.*

The results confirm earlier studies. In particular they show that SST with the employed sensor performance is superior in the lower harmonics and that the low-low mode is optimally suited for studying time-varying gravity effects, provided the mission is long enough (that is several years). Gradiometry, on the other hand, is superior for obtaining high-spatial-resolution and for such a purpose it does not require a long mission duration. As a general rule, it should be noted that an increase of measurement precision or decrease in altitude corresponds essentially to a shift in the error spectrum curve along the vertical axis in Figure 4.1. Due to the steep slope of the curve in the case of SST *ll*, the corresponding increase in spatial resolution is rather moderate.

The gradiometry curve, in contrast, is much flatter (especially on the geoid error), and therefore the gain in spatial resolution is very high in this case. Only if SST *ll* is flown at a very low altitude, necessitating a drag-free approach, would it be able to attain similar resolution to SGG. The SST *hl* curve shows that a space-borne GPS receiver achieves a gravity-field improvement of, say, one order of magnitude over current knowledge for low spherical harmonic degree.

It is then clear that, since most scientific objectives considered here (see Table 4.1) require a high-resolution, below 200 km half-wavelength in many cases (that is above degree 100), an SGG mission is essential. It is also obvious that, by combining it with SST high-low, the quality of recovery of the long-wavelength features will be significantly improved, while retaining the advantage of a single spacecraft and benefiting from existing satellite systems in high-altitude orbits.

4.4 Mission Simulations and Determination of GOCE Baseline Parameters

The mission and system parameters used here result partly from numerous simulation studies performed by combining and varying characteristics of the assumed SGG and SST high-low measurement systems, and partly from the present instrument design (Touboul et al., 1999), taking into account technical, operational and cost constraints revealed by several years of study.

In the preparation of the mission, simulation facilities have been developed, which allow the realistic simulation of the environment, the satellite orbit and attitude, the instruments, down to the production of the pure gravitational gradients that are used, together with the SST data, for the recovery of gravity model parameters. Closed-loop and end-to-end simulations have been performed (Oberndorfer et al., 1999) which guarantee the precision of the spacecraft position recovered from SST, of the gradients to be obtained, and subsequently of the gravity model that will be derived under the present mission and instrument-characteristic assumptions (see also Chapter 7).

The reference GOCE orbit is a dawn-dusk Sun-synchronous orbit at a design altitude of 250 km. The mission lifetime is 20 months for a total measurement duration of 12

months. There is no need for a repeat orbit. Actually what is required is a constantly drifting ground track that ensures a uniform coverage. With the chosen baseline mean altitude, a regular pattern with inter-ground track distances not larger than 85 km at the equator can be obtained after 30 days, which may be 'densified' with time depending on the altitude window selected. The smallest recoverable wavelength (as shown by the simulation) requires a measurement sampling interval of 4 seconds. A one-second sampling time is recommended, which is not demanding on the overall system. Drag compensation, which is essential to enhance the mission capabilities, is assumed. It does not lead to excessive complications and it enhances the mission capabilities.

Table 4.3 summarises the mission and measuring-system characteristics.

Measurement duration	12 months	
Orbit	almost circular, 250 km, 96.5°(Sun-synchronous)	
Position errors in monitoring the SST high-low	Δx (along-track) Δy (cross-track) Δz (radial)	2 cm/Hz$^{1/2}$ 1 cm/Hz$^{1/2}$ 3 cm/Hz$^{1/2}$
Gravity gradiometer error spectrum	full diagonal instrument $\left(V_{xx}, V_{yy}, V_{zz}\right)$ frequency $f < 10^{-3}\,\mathrm{Hz} : 1/f$ coloured noise $5*10^{-3}$ Hz$< f < 10^{-1}$ Hz, white noise $< 5*10^{-3}$ E/Hz$^{1/2}$ (spectrum as seen in Figure 8.2)	
Measurement sampling time	1 second	

Table 4.3. *Baseline mission and instrument characteristics. The errors in position are obtained by including errors of real GPS phase measurements, of propagation and of the IGS orbits (DEOS, Delft-private communication). The noise characteristics of the accelerometer take account of most recent instrumentl studies and developments (Touboul et al., 1999) for spacecraft (attitude, self gravity) and system error sources (Aguirre-Martinez and Cesare, 1999).*

The spherical harmonic coefficients and geoid and gravity anomaly error spectra have been derived using covariance propagation analysis as explained above. The regularisation has made use of error degree variances of a recent global model (satellite only solution) and signal degree variances of Kaula's rule. For comparison, a number of variants of the baseline simulation were carried out, such as changing the instrument configuration and noise characteristics of the gradiometer or of the SST-hl measurements, or changing the altitude and inclination, or the mission duration. The main findings are summarised below:

- The mission altitude is critical to performance and increases exponentially with decreasing altitude. The higher degrees especially (and consequently the resolution) benefit from reduced altitude.
- Coefficients close to order zero are less well determined, an effect caused by the gaps in polar coverage of a Sun-synchronous orbit (without the high-low SST this effect would be even more pronounced). However, on the Earth's surface this effect is minor and mapped back onto the polar areas entirely (see section 8.2).
- As a rough rule, an extension of mission length results in improvements in the performance level: error results are inversely proportional to the square root of the mission duration (this rule holds outside the regularisation regime).

The results, presented in condensed form in Figure 4.2, are those of the baseline mission. To be precise, in Figure 4.2a, the normal (median) per degree is taken which equals, loosely speaking, the degree RMS if the orbit had been polar. In this way the spectral distortion due to the polar gap is eliminated. However, the numbers are representative of the global field outside the polar gaps. The geoid and gravity anomaly error curves (Fig. 4.2b,c) are also computed in this way.

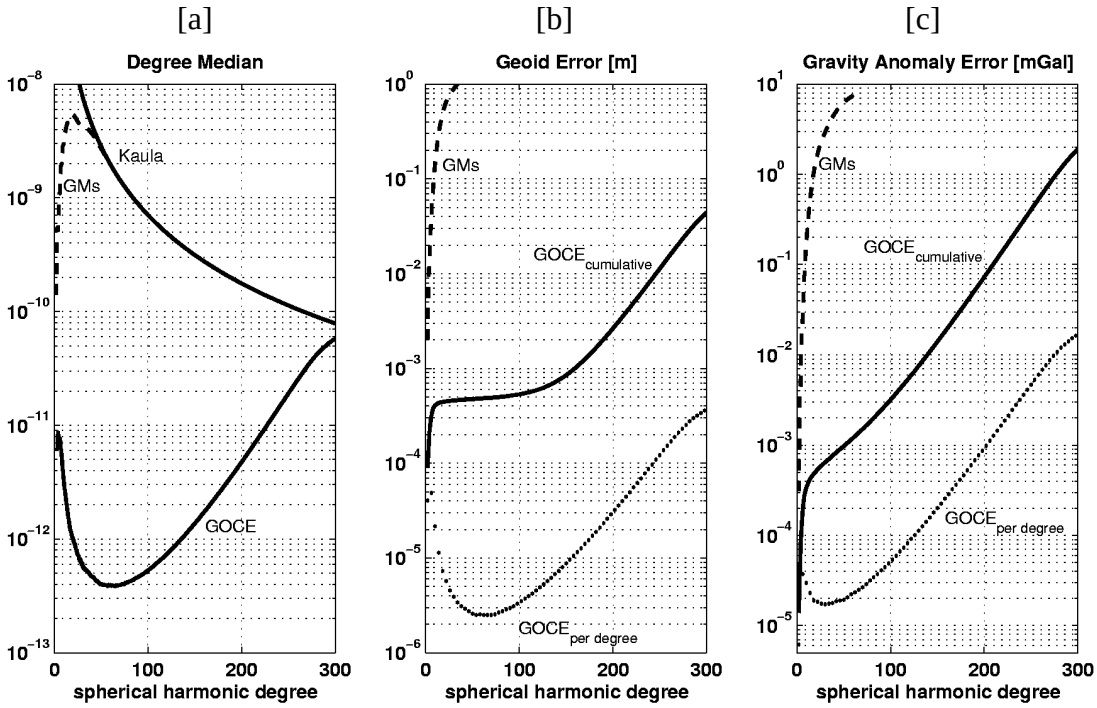

Figure 4.2. *Spectral error results of the GOCE baseline mission: [a] dimensionless degree RMS (median) curve, compared to current global satellite model (GMs) and a-priori (Kaula); [b] cumulative (plain line) and non-cumulative geoid error (dotted line); [c] cumulative (plain line) and non-cumulative (dotted line) gravity anomaly error. The GMs curves in [b] and [c] show current cumulative errors.*

The ultimate resolution that can be reached by the GOCE mission, as defined in Figure 4.2a where the estimated error reaches the signal magnitude, is therefore between degree 250 and 300. This corresponds to a resolution of about 65 km (the assumed time-space sampling is compatible with this).

In Figure 4.2b,c, cumulative errors (up to a certain degree *l* for increasing *l*) as well as non-cumulative errors (for a given degree *l*) are shown. The latter are relevant when discussing the ability of the mission to provide information at a specified length scale, whereas the cumulative errors must be considered when the interest lies in the absolute value of the geoid height or gravity anomaly at any point on Earth.

4.5 Summary

The results presented in Table 4.3 and Figure 4.3 confirm that the GOCE baseline mission would be unique (as compared to CHAMP and GRACE). The gradiometer, with its outstanding capabilities (section 2.4), notably

- continuous high-resolution measurements of the gravity field in three dimensions
- control of drag forces and rotational motion, and
- effective compensation of the attenuation of the gravity field at altitude,

would fulfil the requirements listed in Table 4.1 in the context of retrieving the Earth's gravity field and its geoid to an accuracy of 1-2 mgal and 1-2 cm at a spatial resolution of about 100 km.

The way this improved quantitative knowledge of the Earth's gravity field and its geoid will impact on the scientific studies to be performed downstream is discussed in Chapter 8 for the different areas of scientific research addressed in Chapter 3. In particular, this impact is emphasised in association with the new quantitative research capabilities within geodynamic and tectonic studies, absolute ocean circulation and different scientific research and application areas of geodesy.

5 Mission Elements – Overview

Taking due account of the connections between the scientific objectives and observation requirements addressed in Chapters 3 and 4 and the mission elements, an overview of the latter is provided in this chapter. The various mission elements are described in further detail in Chapters 6, 7 and 8.

Due to the nature of the mission, all satellite sensors and control elements form part of the overall measurement system. The principle of this overall scheme is shown in Figure 5.1.

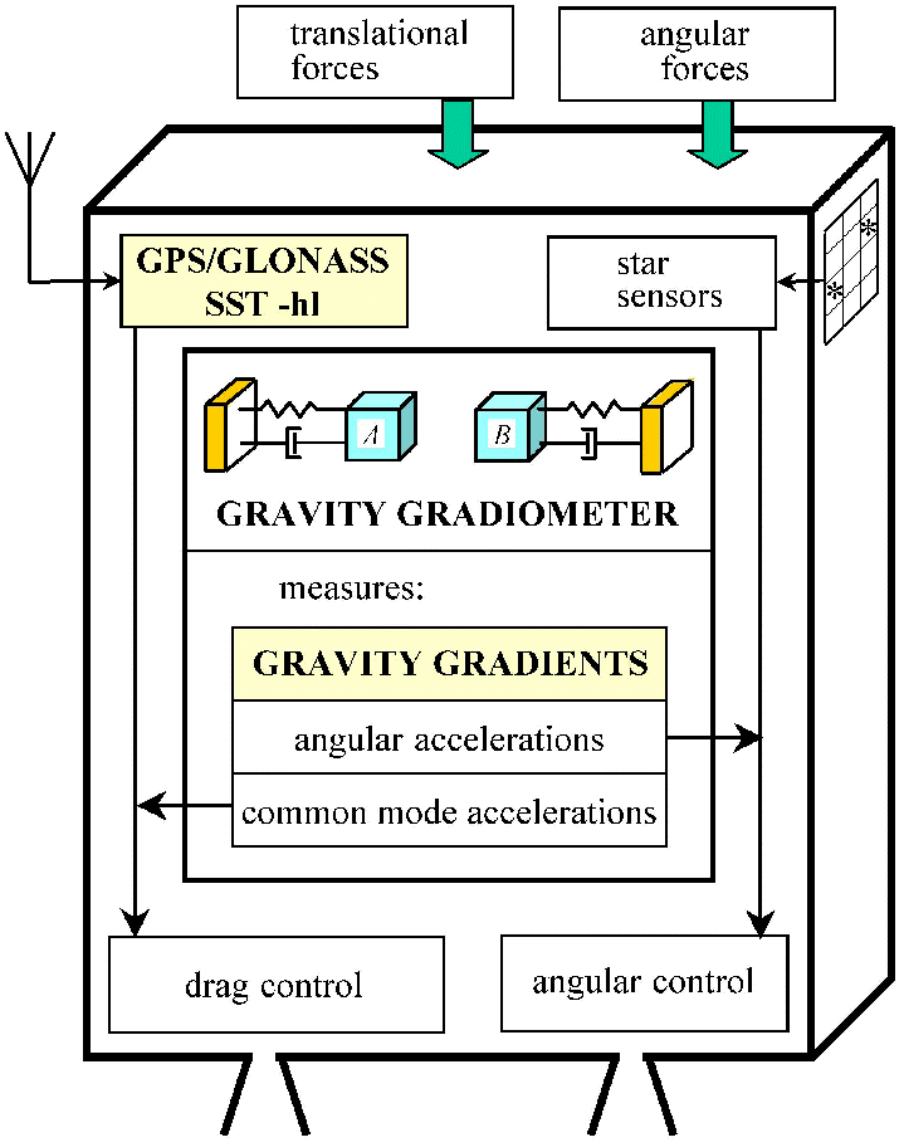

Figure 5.1. GOCE mission concept with drag and angular control and the two fundamental quantities SST-hl and gravity gradiometry, the former providing a precision orbit and the long-wavelength scales of the gravity field and the latter measuring its medium to short-scales.

To build up this system requires a close and systematic interaction between the scientists and the engineers during all phases of the satellite and mission design in order to achieve optimisation of the overall system concept.

5.1 Space Segment

Chapter 6 describes in detail the space segment briefly summarised below. It should be noted that:

- The satellite has been designed to minimise atmospheric drag. Some of its subsystems are conventional, but others have new designs reflecting the special needs of the mission.
- GOCE will carry two key instruments: a three-axis gradiometer and a GPS/GLONASS receiver.
- The baseline mission duration is 20 months. The reference orbit is a dawn-dusk Sun-synchronous orbit at a mean altitude of 250 km during the first half of the mission, and approximately 240 km during the second half.

A 3-D view of the gradiometer assembly is shown in Figure 5.2. It consists of three identical gradiometer axis units and a mounting structure. The latter is composed of a structural bench to support the gradiometer units, a central stiffener, and three isostatic mounts that support the instrument and de-couple the accelerometer units from any instabilities occurring at the gradiometer/spacecraft interface. For stability purposes, the gradiometer is divided into two thermal domains.

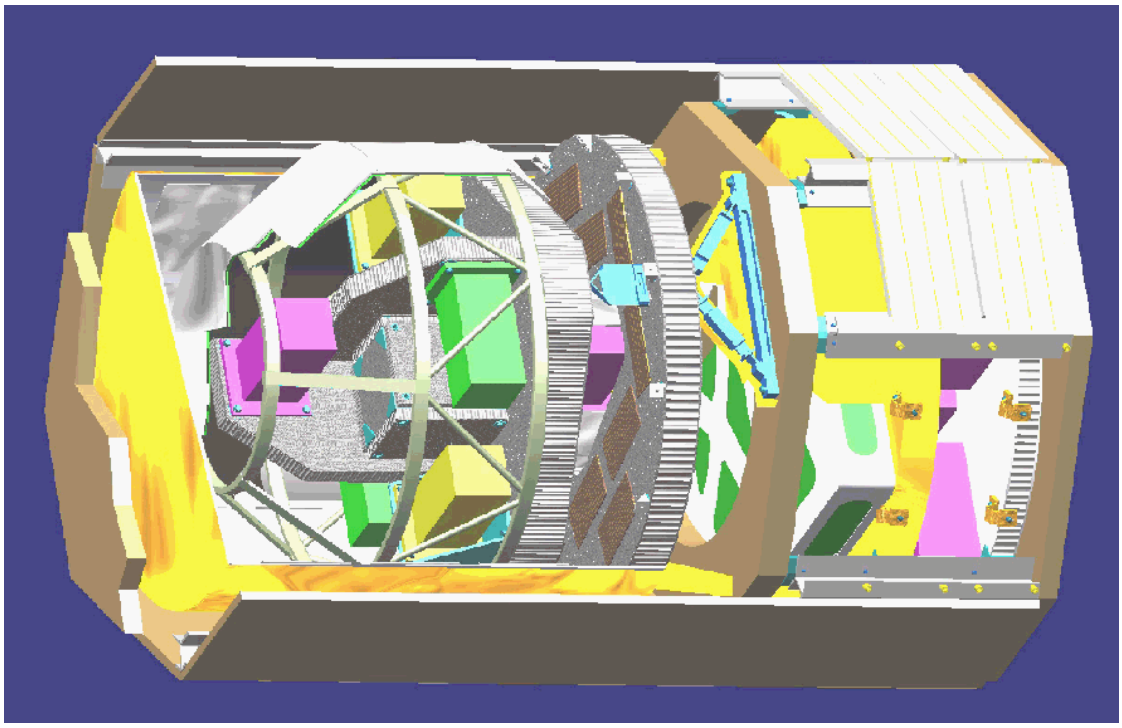

Figure 5.2. *Gradiometer assembly.*

The satellite configuration envelope is a long and slender prism, with a cross-section of 0.8 m^2 and a length of 4 m. Figure 5.3 show the outline of the satellite, including its accommodation of sensors.

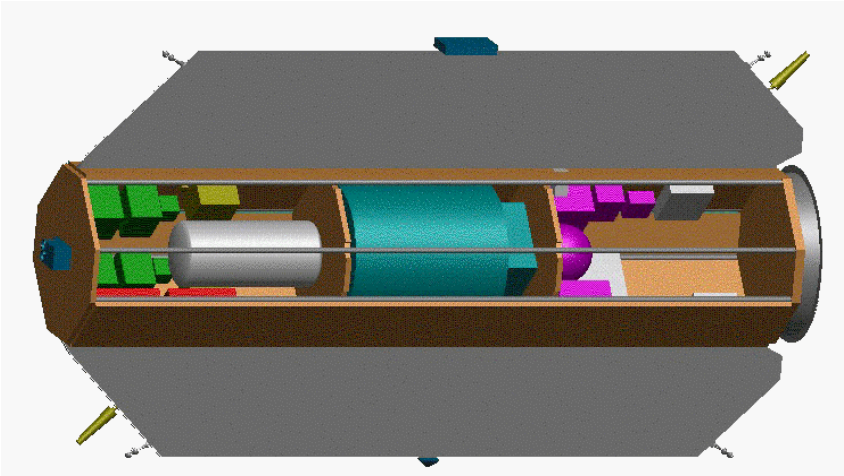

Figure 5.3. *Satellite configuration and accommodation concepts.*

5.2 Ground Segment

Section 6.6 describes the ground segment while Chapter 7 describes the data processing and mission products. The mission has a single ground station in Kiruna. ESOC will be in charge of mission and satellite control. They will also provide calibrated instrument outputs, which in turn will allow further processing of the data to the three key geophysical products for the Earth Observation science community, namely:

- gravity gradients along the orbit at satellite altitude
- geoid heights
- gravity anomalies.

5.3 Ground Observations

Ground support requirements for tracking will be satisfied by the International GPS Service (IGS), which is intending to incorporate GLONASS data in the near future. The mission performances declared in Chapters 4 and 8 do not assume the need for any ground observations. However, supplementary in-situ data could enhance the return of the mission by providing:

- external instrument calibration
- supplementary information over the Poles.

5.4 Contributions from Other Missions

GOCE does not need data from any other mission to achieve its primary goals. The complementarity with CHAMP and GRACE has been explained in detail in Chapters 2 and 4.

5.5 Mission Performances

Existing simulation tools allow the prediction of mission performance. These tools have been used extensively in the mission-definition process (section 4.2) and Chapter 8 highlights the primary results.

6 System Concept

This Chapter describes the technical implementation concept as defined at the end of the Phase-A activities. The core features underlying the concept have been outlined in Chapter 2. The baseline system parameters, which have resulted from interactions between scientific and technical analyses, have been shown in Chapter 4 next to the actual scientific requirements. Chapter 8 will show how the proposed system concept meets the established requirements. After listing in section 6.1 the main system requirements derived from the mission requirements, the Chapter moves on to describe the elements of the mission architecture.

The key issue of the orbit selection and its implications for mission performance, system design and operations are addressed in section 6.2. Though the complete satellite is the 'gravity measurement system', section 6.3 provides a detailed description of the core instruments, the gravity gradiometer and the GPS/GLONASS receiver, showing their complementary roles and the overlapping of performance around 5 MHz for cross-verification.

The satellite configuration and systems concepts are described in section 6.4 with emphasis on: drag compensation and attitude control and the associated actuation systems, the ion thrusters and the proportional cold-gas thrusters and reliability. Rockot is discussed as the reference launcher in section 6.5 and an efficient, affordable and modern concept for the ground segment is presented in section 6.6. The ground segment is based on the use of Kiruna as the command and data acquisition station, and ESOC for mission operations and satellite control. The Chapter ends with a summary of the main characteristics for the mission

6.1 From Mission to System Requirements

The GOCE scientific requirements established in Chapter 4 concern the recovery of gravity anomalies (mgal) and geoid heights (cm) over the Earth's surface. These quantities are the result of bulk processing of measurements: gravity gradients (gradiometer) and positions (GPS/GLONASS receiver) collected over a time span of months by the two satellite instruments. At constant instrument resolution, the actual measurement resolution depends on altitude, since the signal strength decreases rapidly with altitude. Equations 2.2.1 to 2.2.8 of Chapter 2 provide a rigorous definition of the observables. At the satellite altitude h, the strength of the signal associated with the harmonic of degree l of the gravity potential V decreases with $(R/R+h)^{l+1}$ and the signal associated to the gravity gradient $\nabla^2 V$ decreases with $(R/R+h)^{l+3}$. Hence, the need to fly as low as possible if high-resolution (high harmonic degree l) is sought. However, the lower the altitude the higher will be the disturbing accelerations due to atmospheric drag. Thus, the nominal altitude is determined by a trade-off between scientific performance and the satellite system's

capability for rejecting unwanted disturbing accelerations. The systems involved are principally the gradiometer itself and the drag-free control, using proportional ion thrusters. That means the altitude is mainly determined by the availability of the electrical power that will be used to compensate the aerodynamic drag. In practice, other engineering constraints also play a part in the trade-off, such as the thrusters noise and satellite safety considerations in the event of temporary failure of the orbit control system. Consideration of all of these factors has led to the selection of a nominal mission altitude around 250 km (see section 6.2.1).

The challenge in recovering the gravity is the measurement of a weak signal in a noisy environment, in which case the performance will improve proportionally with the square root of the mission duration. However, the mission duration is limited by the amount of fuel available for the orbit and attitude control, and by the life expectancy of the ion thrusters. A lifetime of about 20 months has been identified as a reasonable compromise.

GOCE requirements refer to a specified resolution. It has already been explained in section 2.5 and in Figures 2.7 and 2.8 that the contribution of the gradiometer and the GPS/GLONASS receiver provide an optimal output at specific ranges of harmonic degrees, i.e. at a specific resolution. The Earth's gravity field will be measured by the satellite in the time domain. The higher degree harmonics will be with high frequencies and the lower degree harmonics with low frequencies. Hence, the performances of the GPS/GLONASS receiver and of the gradiometer will be defined for complementary frequency ranges.

The problem of apportioning requirements to the gradiometry (Eötvös) and the SST-hl part (cm) of the mission, given altitude and mission duration as additional variables, is solved by covariance analysis. These analytical predictions of performance are later checked numerically, including all the known error sources, in end-to-end simulations. The results are processed in the same way as the satellite data will be after the mission. Covariance analysis and an end-to-end simulation capability for GOCE already exist, and show excellent agreement (Chapter 8). The simulation tools have provided a practical way of checking the scientific implications of any design change and have been used extensively to arrive to an optimal design.

Once the top-level requirements have been apportioned and flying altitude and mission duration decided, the different types of errors are further broken down. The process is continued until a full error tree is built up. Top-down and bottom-up analyses have been performed to adjust the design to the required scientific performances. Explanations of error types and error budget structure are provided in section 8.1.

The gradiometer is the tool that provides the high-resolution measurements which are the justification for GOCE. Thus, the gradiometric error budget has been the essential tool for mission design. The final allocations for the different error categories are shown in Table 6.1.

	$mEotvos/\sqrt{Hz}$
Instrument errors (mainly accelerometer intrinsic noise)	3
Instrument-Satellite coupling errors (rejection of drag induced perturbations)	1
Satellite errors (mainly satellite pointing)	2
Post flight error (recovery of the centrifugal acceleration)	1
Root sum square total	4

Table 6.1. *Error allocation for gradiometry.*

The above allocations have been used to derive requirements for the different satellite elements.

6.2 Mission Design and Operations

6.2.1 Orbit Selection

The GOCE orbit parameters are selected from a trade-off of scientific requirements and implementation constraints. The scientific requirements call for gravity field sampling for a year or more at very low, constant altitude. The ground coverage must be global and uniformly distributed. This leads to a repeat period for the ground tracks equal or larger than 2 months. In addition, the perturbations from the external environment must be made as small as possible. For a practical implementation of the above requirements, the following choices were made.

Orbit Altitude

The selected orbit is near circular, at the nominal mean spherical altitude ≈ 250 km (the actual mission profile includes variations around this altitude, as shown later in section 6.2.4). The orbit is maintained by continuous thrust in the direction of motion, of a magnitude equal to the DC component of the atmospheric drag at the given time. The mean altitude is consistent with the control authority of the thruster actuators selected for orbit and attitude control, and meets the requirement for orbit recovery after 7 days of uncontrolled flight.

Even after drag control, such a ‘nominally circular’ orbit undergoes variations in eccentricity (hence altitude) due to the Earth’s oblateness, with both short-periodic (1 orbit) and long-periodic (90 days) components. The magnitude of the eccentricity is $e \leq 4.5 \cdot 10^{-3}$ and the peak-to-peak variation of the altitude can thus be up to 50 km (Fig. 6.1). ‘Frozen’ orbits, minimising long-periodic variations, were discarded as they

would require the mean perigee to lie constantly above the North Pole, and the gravity field would be sampled, on average, at a different height at each latitude.

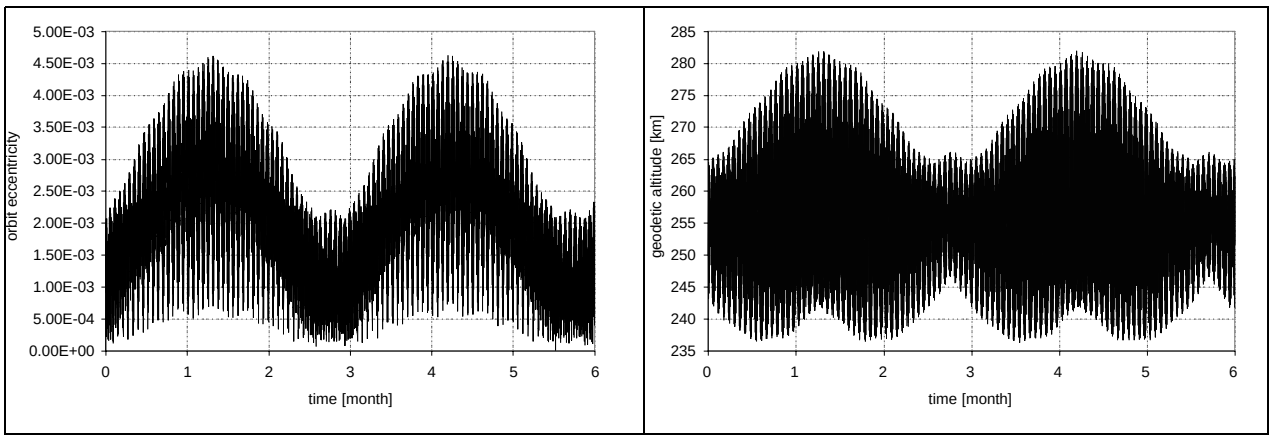

Figure 6.1. *Eccentricity (left) and geodetic altitude in km (right) variation in 6 months at 250 km mean height.*

Higher than nominal initial eccentricity can occur as a consequence of launch injection errors. To cope with this problem, and to provide adequate time margins for early operations, launch is targeted to an altitude of 270 km. During the commissioning phase, the altitude will be left to decay gently to the nominal 250 km and eccentricity errors will be corrected.

Inclination and Longitude of the Ascending Node

In order to simplify the spacecraft configuration, a Sun-synchronous orbit (SSO) is selected, and, to minimise the duration of eclipse, the orbit is oriented in space such as to face the Sun (line of nodes perpendicular to the projection of the Sun vector on the equator).

The inclination is therefore that pertaining to SSO at the given altitude, i.e. $i = 96.5°$ at 250 km. There are two seasonal launch windows for such an orbit. In the summer window, the longitude of the ascending node is at 6 hours p.m. local time (dusk-dawn), while in the winter window it is at 6 hours a.m. (dawn-dusk). Within each seasonal launch window, there is a daily window of 30 minutes during which the spacecraft can be injected into an orbit with an ascending node local time equal to 6 p.m. (or 6 a.m.) ± 0.25 h, a tolerance that does not significantly change the eclipse pattern (Fig. 6.3).

The satellite development programme is currently geared to a launch on 16 July 2004, at the beginning of the 2004 summer window, which makes the orbit dusk-dawn (Fig. 6.2).

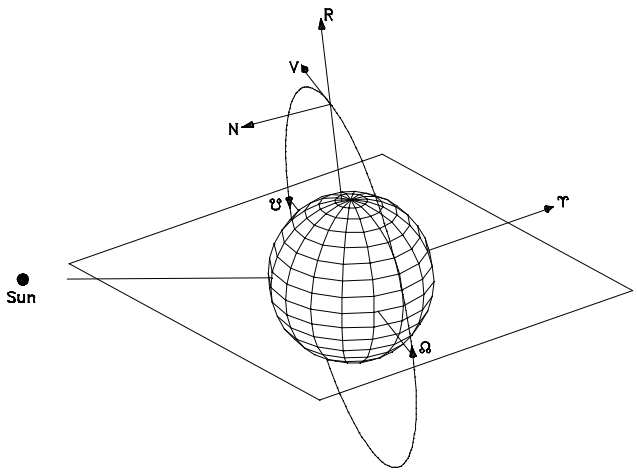

Figure 6.2. *Orbit orientation in space for summer launch window.*

Eclipse Seasons

Dawn-dusk Sun-synchronous orbits at altitudes below 300 km experience eclipses in two seasons (see Fig. 6.3), a season of short eclipses (eclipse duration per orbit T_e <10 min) and a season of long eclipses (T_e < 30 min). Eclipses are detrimental to the satellite operation because of the thermoelastic disturbances at shadow crossings and the enhanced electrical energy storage requirements of the ion propulsion. It has therefore been decided that the satellite will be designed for continued operation during the short eclipses only. By choosing the first node according to the summer or winter window, it is always possible to ensure that the season of short eclipses occurs first.

Consequent on this choice, the mission profile is as follows:

- The satellite is launched in the descending leg of a long eclipse season. Commissioning is performed in the first 1.5 months, affected by eclipse. As soon as the eclipse season is over, the payload calibration is executed, after which the first phase of the scientific operations starts. Such operations continue without interruption through the short eclipse season.
- The satellite is put in hibernation mode during the long eclipse season.
- As soon as the eclipse season is over, the calibration procedure is executed again, and second phase of scientific operations is initiated.

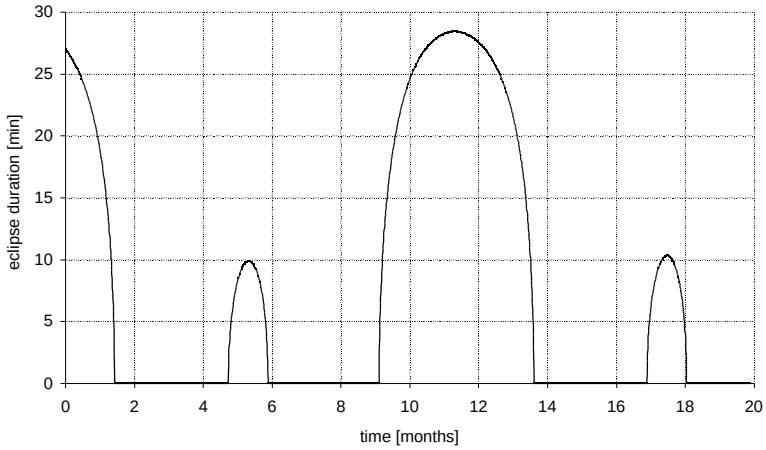

Figure 6.3. *Eclipse profile (in minutes) in the chosen orbit*

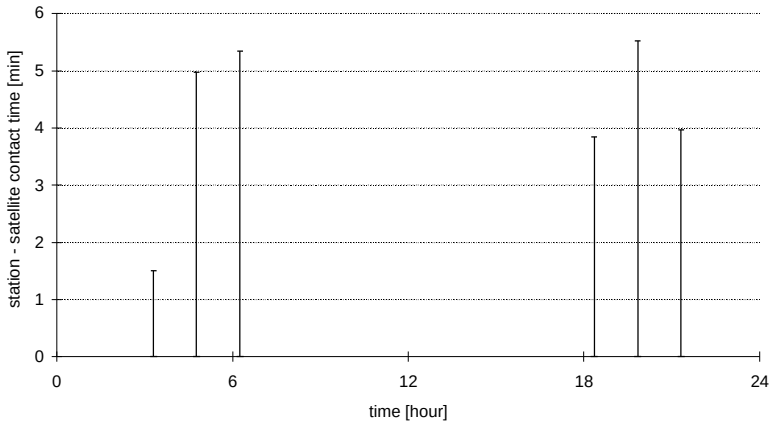

Figure 6.4. *Station-satellite contact time (min) coverage pattern.*

Ground Coverage and Ground Track

Near-polar orbits are conveniently covered by high-latitude ground stations. For GOCE, the Kiruna ground station is considered. The coverage pattern is a regular sequence of contacts during three consecutive orbits, followed by a gap of about 12 hours. The duration of typical contacts is between 1.5 and 5.5 minutes (Fig. 6.4). Given the low data rate, the sequence is sufficient for dumping the entire contents of the on-board mass memory each day, with a factor of 2 margin (section 6.4.7). The

250 km orbit meets the requirement of a ground track repeat period of at least 2 months. After this period, the maximum separation of tracks is < 40 km.

6.2.2 Orbit Environment

The orbit environment is dominated by atmospheric drag as the most important perturbation affecting the scientific measurements and consequently the satellite controls. Perturbing effects of minor magnitude are due to solar radiation pressure, the gravity gradient and the interaction with the Earth's magnetic field. The atomic oxygen at very low altitude attacks the surface of some materials. This will be taken into account in the selection of protective surfaces. Radiation doses at such low altitude are a minor effect.

Drag Force and Torque Profiles

Drag disturbances are proportional to the atmospheric density. For the spacecraft design, models of the density are employed exhibiting all the known variations with altitude, solar cycle, local solar time, and incorporating in a statistical way small-scale effects such as those due to gravity waves. When applied to a realistic orbit scenario, these models produce complex time profiles of the drag perturbations with components ranging from very long period (the solar cycle), to long period (months) to the orbit frequency and its harmonics, to short period 'fluctuations'. In particular, the position of the mission in the 11-year solar cycle determines the average value of the drag at the given altitude.

For the nominal mission of 20 months launched in July 2004, the spacecraft will experience decreasing levels of drag. For spacecraft design purposes, the NASA 95% forecast of solar activity was used, which provides a conservative estimate of the drag perturbations. Figure 6.5 shows the time profile of the drag force for a time span of four orbit periods at a mean altitude of 250 km, with the mean density associated with the epoch July 2004 at the 95% probability level. For the purposes of designing the spacecraft controls and estimating their performance, the time profiles of the perturbations have to be turned into frequency-domain information. Figure 6.6 shows the spectral density of the drag acceleration associated to the time profile of Figure 6.5.

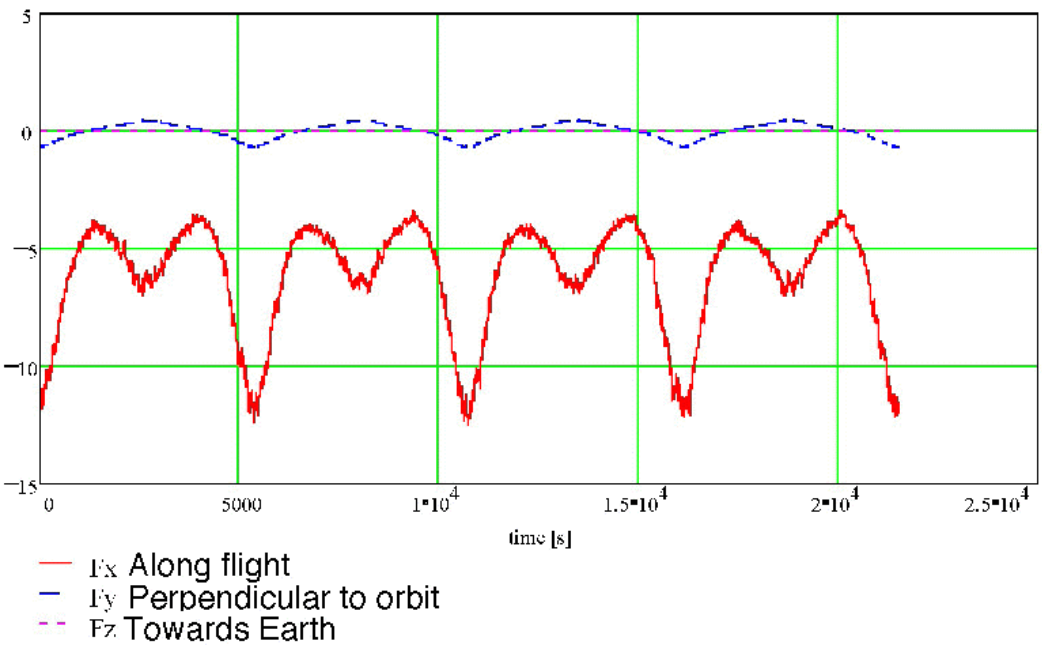

Figure 6.5. *Drag-force profile (in mN) for four orbits at 250 km mean altitude.*

6.2.3 Drag Control and Orbit Maintenance

The epoch of flight, the orbit and the spacecraft configuration (cross-section) determine the drag acceleration. In the frequency domain, this acceleration can be divided into three bands:

- average acceleration (DC)
- long periodic acceleration changes below 0.005 Hz (LF)
- short periodic components between 0.005 and 0.1 Hz, i.e. in the measurement bandwidth of the gradiometer (MBW).

The GOCE satellite is designed according to requirements specific to each frequency band. Orbit maintenance concerns itself with keeping the average altitude constant. For orbit maintenance it is sufficient that the DC component of the drag is balanced by an equal and opposite force, exerted by on-board thrusters. The dominant component of the drag is aligned with the mean direction of motion (x-axis), and it is determined on board by a suitable elaboration of the positional data from the GPS/GLONASS system. 'Drag control' is designed to reduce the perturbing accelerations in the measurement bandwidth, below it and above it, according to requirements imposed by the gradiometer instrument.

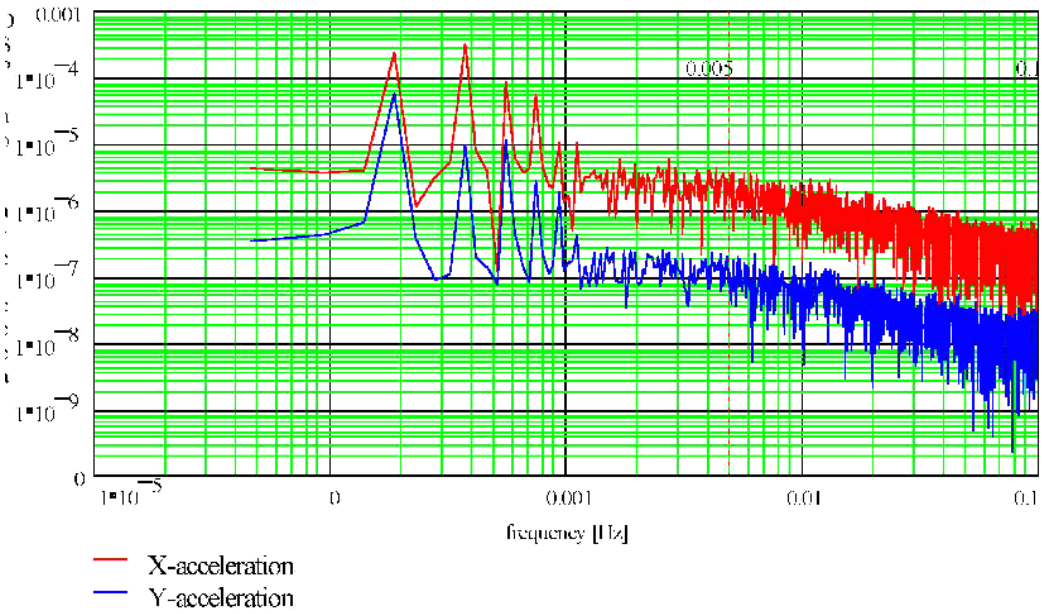

Figure 6.6. *Spectral density of the drag induced acceleration in m s^{-2} $Hz^{-1/2}$.*

Table 6.2 lists the magnitudes of the expected (95% confidence) forces in the various frequency bands during the nominal mission, and the gradiometer requirements. The magnitude of the required drag rejection is the ratio of the expected acceleration to the allowed acceleration. Such rejection is provided by an ion thruster along the x-axis, and cold-gas thrusters on the y-axis, while along the z-axis no action is required (environment always below requirement). The drag control signals are synthesised from the gradiometer common-mode acceleration measurement. The data in the Table below are used to derive, in particular, the requirements applying to the actuators, in terms of magnitude, bandwidth, and noise (see section 6.4.8).

	Linear acceleration along x-axis @ 250 km altitude			
	DC ($m\ s^{-2}$)	max LF ($m\ s^{-2}$)	max MBW ($m\ s^{-2}\ Hz^{-1/2}$)	Max all freq. ($m\ s^{-2}$)
Requirement	$1\ 10^{-7}$	$1\ 10^{-7}$	$2.5\ 10^{-8}$	$1\ 10^{-6}$
Environment	$8\ 10^{-6}$	$8\ 10^{-6}$	$3\ 10^{-6}$	$2\ 10^{-5}$
Rejection ratio (dB)	38	38	42	26

Table 6.2. *Expected and required external accelerations and resulting rejection ratio.*

Altitude Drop and Lifetime

In the GOCE mission concept, the orbital altitude will be actively controlled by thrusters such that the desired altitude is maintained through the nominal lifetime. Altitude decay can however occur unintentionally (through a spacecraft malfunction) or intentionally (to acquire a new nominal altitude).

To recover from malfunctions, the requirement is imposed that it shall be possible to recover from up to seven days of flight without orbit control. This means that the actuators must be capable of exerting the extra thrust to gradually bring back the spacecraft to the nominal altitude. During such operations, the resources available to the subsystems not involved in the manoeuvre are reduced to a minimum. At the beginning of life (BOL), the maximum 7-day altitude drop is from 250 km to 224 km, and it can be recovered in 18 days with 19 mN of continuous thrust.

The nominal mission profile also includes intentional altitude drops. As mentioned earlier, the launch is targeted to 270 km and the first scientific phase occurs at 250 km. Before the long eclipse season, the altitude will be raised to 260 km and, at the end, the second scientific phase will be performed at an altitude around 240 km. This allows the spacecraft capabilities to be matched to the prevailing drag environment (mean level decreasing with time on the downward leg of the solar cycle). Orbit drops will be executed simply by switching the ion thrust off until the new altitude is achieved.

In the nominal design, the 20-month lifetime of the mission will be limited by the on-board consumables and by the rate of decay of vital elements such as the ion thrusters. The consumables have been calculated with 50% margins with respect to the 95% drag prediction, providing more than 50% life margins. The ion thrusters guarantee a minimum lifetime of 10000 hours. By employing two thrusters in cold redundancy, a life of more than 20000 hours (2.3 years) is expected.

6.2.4 Mission Profile

Figure 6.7 outlines the nominal mission profile. Table 6.3 lists the main activities performed during the various mission phases, according to the requirements set forth in the previous sections.

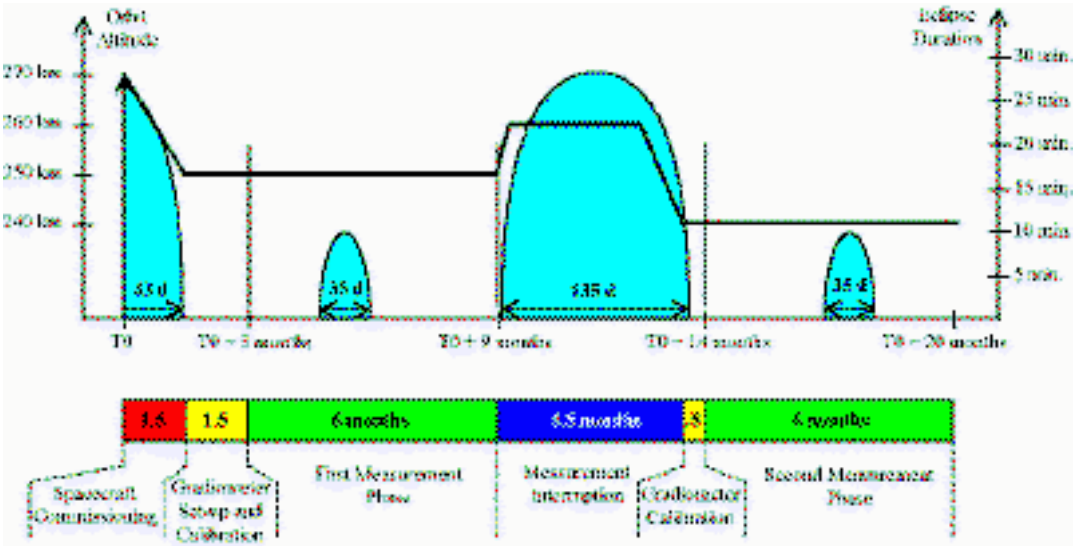

Figure 6.7. *Mission Profile.*

A list of the main mission events is provided in Table 6.3.

Launch start: day 0 end: day 0	Launch by Rockot, direct injection into operational orbit, 270 km. Duration from lift-off to spacecraft separation: ≈ 5000 s. Separation in Sun-pointing attitude, with 2°/s max residual spin rate. Start of altitude drop
Separation start: day 0 end: day 0	DHS activation by separation switch, power-on by battery, activation of RF and AOCS. Autonomous three-axis coarse attitude acquisition. Transition to solar power. First ground contact with Earth station about 2 hours after launch. Subsequent contacts with ESA LEOP ground network.
Satellite Checkout and Commissioning start: day 0 end: day 45	Initial checkout of spacecraft subsystems. Tracking by S-band network and orbit determination. Activation of attitude thrusters. Transition to Earth-pointing mode, medium accuracy, based on star sensors. Activation of ion propulsion (constant thrust). LEOP network released; control handed over to Kiruna station. Checkout of service-module functions and payload electronics. Initialisation of GPS/GLONASS receiver system. Configuration of satellite to operational mode. End of altitude drop (250 km reached).
Thruster Calibration start: day 46 end: day 60	Uplink of command sequence for thruster calibration (semi-autonomous). Firing of attitude thrusters in different combinations to determine thruster configuration matrix against measurement of attitude by star sensor. Activation of gradiometer.
Gradiometer Set-up start: day 61 end: day 90	Activation of DFC feedback control, based on gradiometer common-mode output. Generation of 'pure' translational accelerations by thrusters. Calibration of differential scale factors, misalignments, quadratic factors. Generation of 'pure' rotational motion by thrusters. Determination of common misalignments. Calibration of gradiometer absolute scale factor.
Operational Phase 1 start: day 91 end: day 270	Routine data collection and transmission.
Short Eclipse Season start: day 135 end: day 170	Continuation of routine data collection. Characterisation of spacecraft thermal deformation effects.
Long Eclipse Season start: day 271 end: day 405	Gradiometer off. Ion propulsion set to constant thrust mode, at more than orbit maintenance level, until 260 km altitude is reached. GPS/GLONASS receiver continues data collection. Non-essential equipment in survival mode. Towards the end of the LES, altitude drop to 237 km.
Gradiometer Re-calibration start: day 406 end: day 420	Gradiometer on.. Ion thrusters to proportional mode and iteration of thruster calibration. Re-activation of DFC feedback control. Re-activation and calibration of gradiometer differential mode.
Operational Phase 2 start: day 421 end: day 600	Routine data collection.

Table 6.3. *Mission events timeline*

6.3 The Instruments

It is recalled that there are two key instruments, i.e. the gradiometer and the GPS/GLONASS receiver, and two secondary instruments, i.e. the laser retro reflector and the radiation monitor. In this Chapter the instruments are described in the context of the system concept.

6.3.1 Synergy of Gradiometry and Satellite-to-Satellite Tracking

In GOCE, two measurement techniques are used to achieve the mission goals in gradiometry and satellite-to-satellite tracking (SST-hl). In gradiometry, the difference in the acceleration measured by two accelerometers placed some distance apart provides the basic observable, proportional to the gravity gradient in the direction joining the two sensors through a constant scale factor. In SST-hl, the positional data measured with reference to a constellation of reference satellites in known orbits are used to extract the gravity information through orbit perturbation analysis.

The techniques are complementary in that SST-hl works best at providing the long- and medium-wavelength part of the geopotential, while gradiometry is especially sensitive to the short-wavelength part. The cross-over frequency between the two techniques is not sharp, providing redundant measurements in a wide frequency band.

Many studies performed in the past have shown that the lower limit of the gradiometer measurement bandwidth (MBW) can be safely taken as high as 5 MHz. The upper limit of 0.1 Hz is consistent with the required spatial resolution of 100 km. With this definition of the bandwidth, the gradiometer measurements start giving a contribution at harmonic degree L = 15, while SST-hl is valid to at least L = 60. This proves the statement that both measurement types concur in the determination of the gravity field over a considerable wavelength span.

In both approaches, the lower the altitude the higher is the sensitivity, but the higher also are the disturbing effects from air drag. Here, another level of synergy comes into play. In SST-hl, independent measurements of the non-gravitational accelerations are needed to extract the gravity signal from the positional data, and such measurements are obtained as a byproduct of the gradiometer sensing (‘common mode’ accelerations). In gradiometry, the measured gravity gradients have to be linked to a precise location in space, and that is provided by the SST-hl.

6.3.2 Gravity Gradiometer

The main purpose of the gravity gradiometer is to measure the three diagonal components (V_{xx}, V_{yy}, V_{zz}) of the gravity-gradient tensor. The principles of gravity gradiometry have been explained in section 2.3. The fundamental idea is that a

gradiometer is able to measure the differences in acceleration between the points where their accelerometers are located. The accelerometers measure not only the gravity pull, but also the angular, centrifugal and Coriolis accelerations and the external (mainly drag) and internal (satellite self gravity) perturbations. A rigorous derivation of the gradiometry observables will be found in section 7.2.1. The addition of all the error sources acting on the recovery of the three gravity gradients must be compatible with the mission requirements. The gradiometric error structure is explained in section 8.1.

At the beginning of the GOCE Phase-A study, two gradiometers were considered: one working at ambient temperature and another working at 2 K. The instrument working at the cryogenic temperature could, in principle, provide much better performances. Nevertheless it was larger, heavier and its development status was less mature. On the other hand, the performances of the ambient temperature instrument are adequate to fulfil the requirements. So, the ambient temperature instrument was selected at a review that took place in December 1998. All the explanations in the rest of this Chapter refer to this ambient temperature gradiometer.

Accelerometer Characteristics

The principle of operation of the accelerometers is based on the measurement of the forces needed to maintain a proof mass at the centre of a cage. A six degree of freedom servo-controlled electrostatic suspension provides control of the proof mass in terms of translation and rotation. Figure 6.8 illustrates position sensing on one of the axes. Any movement of the proof mass will produce differences in capacitance between C1 and C2. This difference will be sensed, amplified and corrected. The correction is done by adjusting the electrical potential of electrodes S until the difference in capacitance is reduced to zero.

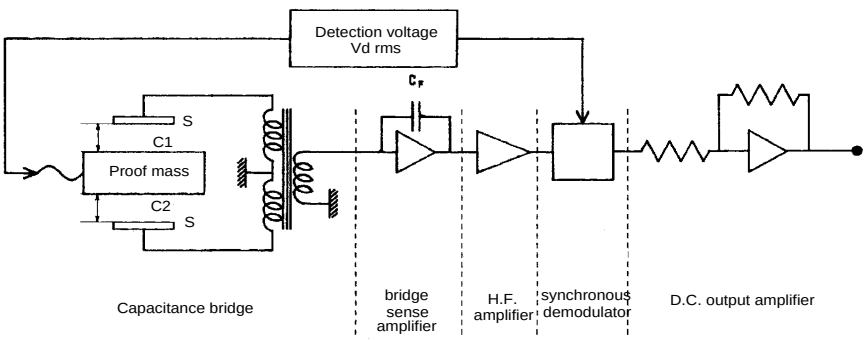

Figure 6.8. *Principle of the capacitive position sensor.*

Figure 6.9 shows an exploded view and a photograph of the accelerometer. The electrodes are titanium glass ceramic plates. The proof mass is a 4 × 4 × 1 cm cube of platinum-rhodium, and its mass is 0.32 kg. The cage around the proof mass is made of Invar. The dimensional accuracy of the accelerometers is required to be of the order of 1μm. The electrostatic forces applied in the servo loop provide the acceleration measurement, proportional to the inertial forces acting on the proof mass. In order to allow testing in the laboratory, each accelerometer has two highly sensitive axes, and one less sensitive axis designed to sustain 1g during ground tests.

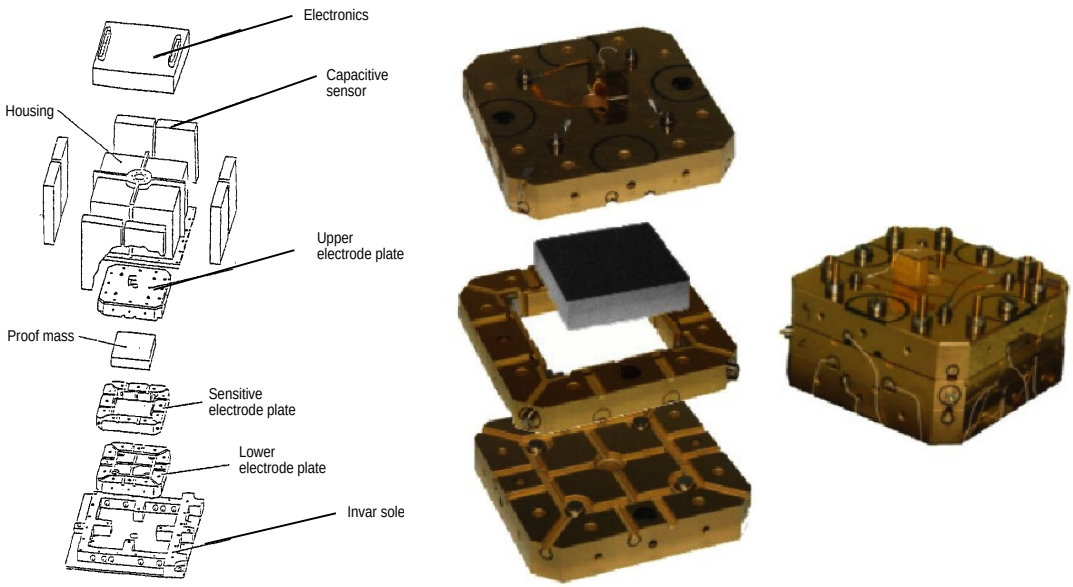

Figure 6.9. *Exploded view of the capacitive accelerometer: (Left) schematic, (Right) actual accelerometer.*

Instrument Configuration

A pair of identical accelerometers, mounted on an ultra-stable structure, 50 cm apart, form a ‘gradiometer arm’. The difference between accelerations measured by each of the two accelerometers, in the direction joining them, is the basic gradiometric datum (‘differential measurement’), while half the sum is proportional to the externally induced perturbing drag acceleration (‘common mode measurement’). Three identical arms are mounted orthogonal to one another and, in orbit, the axes so defined are nominally aligned to the along-track, cross-track and vertical directions. The three differential accelerations provide direct, independent measurements: not only of the diagonal gravity gradient components, but also of the perturbing linear and angular accelerations. Figure 6.10 shows the layout of the six accelerometers with the orientation of their highly sensitive and less sensitive axes. They have been arranged

so to recover to the highest accuracy V_{xx}, V_{yy}, V_{zz} and the centrifugal accelerations around the axis perpendicular to the orbit. This acceleration will be produced by the Earth-pointing nominal attitude of the satellite and it needs to be removed from the raw measurements. This is explained in detail in section 7.2.1. The accuracy of the 'coarse' axes is adequate for the recovery of all other external perturbing accelerations at the level required for their control.

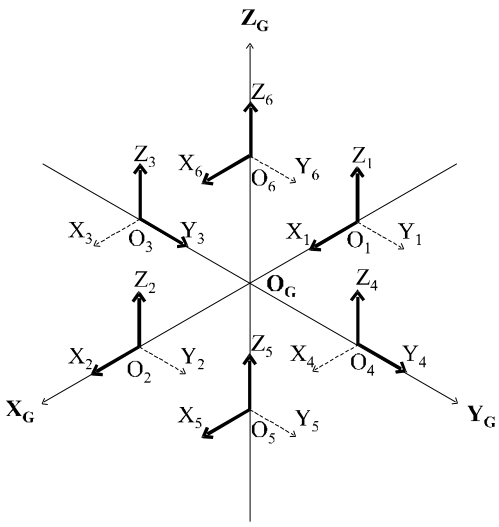

Figure 6.10. *Asymmetric diamond configuration (less sensitive axes are in dotted line)*

An integrated overall view of the gradiometer can be found in Figure 5.2 of Chapter 5. Figures 6.11 and 6.12 show exploded views of the main components. The structure assembly consists of three identical axes and a mounting structure. The latter is composed of a structural bench to support the gradiometer units, a central stiffener and isostatic mounts (TMDD) that support the instrument and decouple the accelerometers units from all instabilities occurring at the gradiometer/spacecraft interface. For thermal stability, the gradiometer is divided into two thermal domains.

The electronics units are mounted at a distance from the sensor assembly. The front-end electronics performs the functions of voltage bias supply to the capacitive sensors, signal extraction and amplification, anti-alias filtering and 24-bit analogue-to-digital conversion. The functional requirements of the downstream electronics include in-flight calibration, science data processing, provision of data to the attitude and drag control system (AOCS/DFC), health and safety control (including autonomous safeguard), commanding, power control and diagnostics. The main functional blocks are spacecraft interface, AOCS/DFC interfaces, gradiometer data and control interfaces, and the processor system. A power control unit includes a DC-DC converter to supply isolated secondary power to the instrument. The telemetry packets produced by the gradiometer include science data, housekeeping, and data provided to the attitude and drag control system. Science data will be sampled at 1 Hz, digitised

and then packetised and telemetered to the ground with no further processing. The current estimate of the science data rate is 432 bps. The housekeeping data are used to report instrument status; they amount to 516 bps. The common mode channels of the gradiometer will be sampled at up to 10 Hz and supplied to the AOCS/DFC. Special calibration packets will be created and sent to the ground during the calibration process. Engineering packets, consisting of high-resolution housekeeping data from selected channels or memory dump, will be used during commissioning or for diagnostic purposes. The redundancy concept of the gradiometer features fully redundant electronics, and a prime and redundant internal bus structure. The gradiometer support electronics are grouped by axes, so that failures will result only in a gradual degradation of performance.

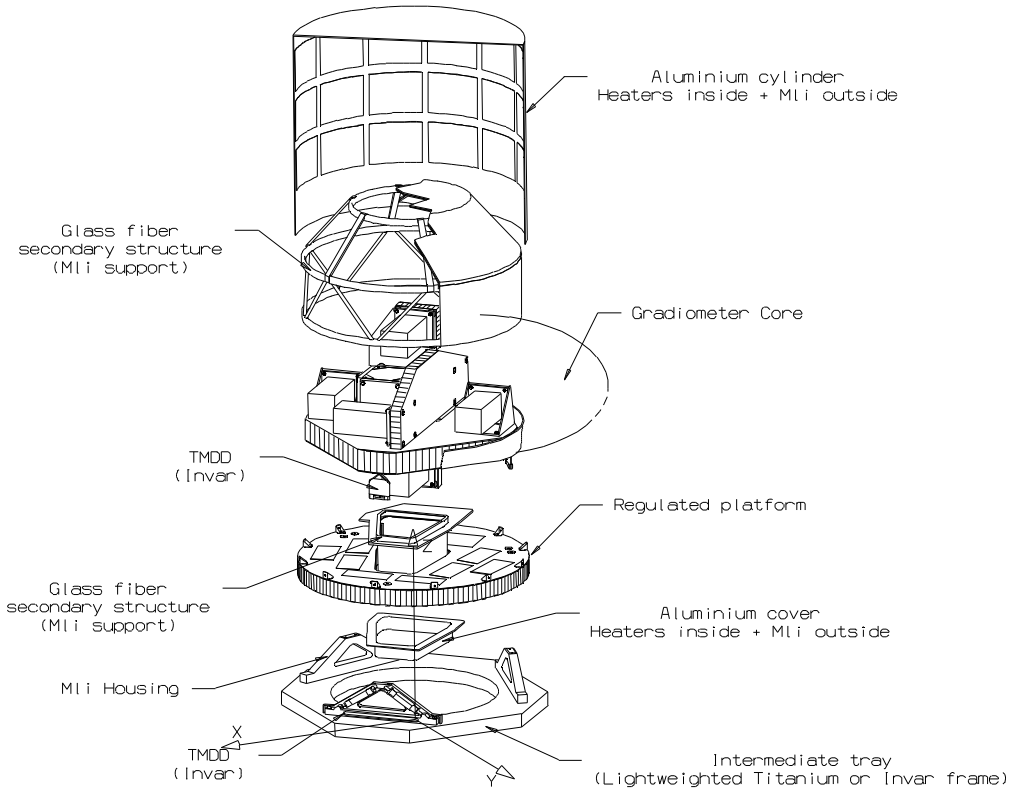

Figure 6.11*.Gradiometer configuration – exploded view*

The main interface data of the gradiometer can be seen in Table 6.4:

Instrument assembly dimensions	1320 mm length, 850 mm diameter
Instrument weight (including margins)	137 kg
Power (including margins)	47W (incl. converter efficiency) 18W (thermal control electronics)
Data rate Science (24 bit @ 1 Hz) Housekeeping (12 bit @ 0.1 Hz) To AOCS/DFC (12 bit @ 10 Hz)	 432 bps 561 bps 720 bps

Table 6.4. *Interface data for the gradiometer.*

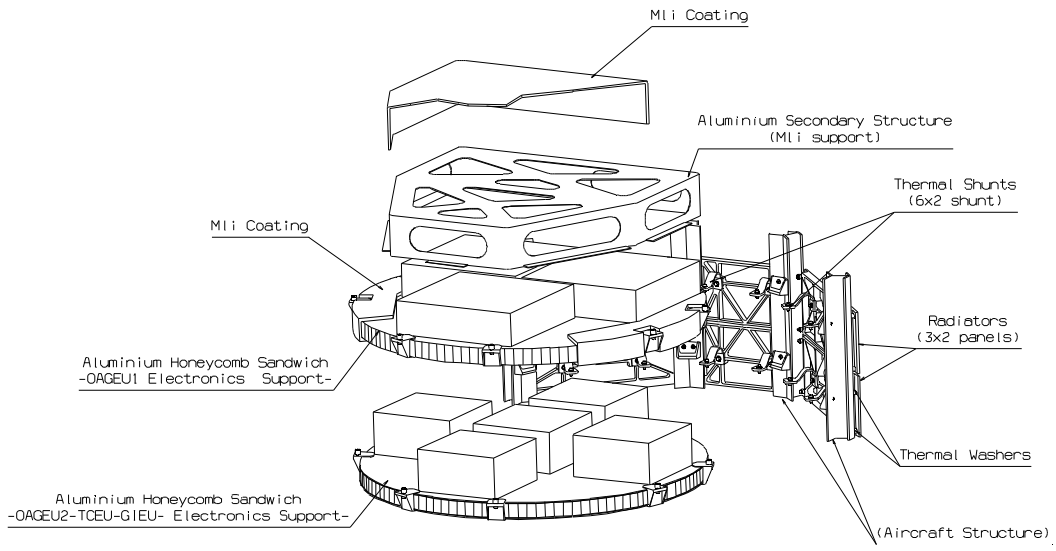

Figure 6.12. *Exploded view of the gradiometer electronics.*

Instrument Operation and Performance

The main factors that establish the performance for a single gradiometer axis, composed of two accelerometers, are:

- the accelerometer sensors noise
- the common misalignment of the accelerometers, equivalent to a position error, which limits the rejection of the satellite attitude motion
- the differential misalignment of the accelerometers, which limits the rejection of any transversal acceleration (from a translation or a rotation)
- the mismatching of the scale factors, which limits the rejection of any common mode acceleration

– the accelerometer proof mass motion with respect to the gradiometer structure
– the dimensional stability of the gradiometer structure.

A summary discussion of the most important effects is provided below.

The accelerometer sensor noise is by far the most important intrinsic instrument error source. An allocation of 3 mE $Hz^{-1/2}$ (mE=10^{-12} s^{-2}) was provided in section 6.1 to cover this error category. With a 0.5 m separation between the proof masses, the resulting objective of the accelerometer noise for each accelerometer will be: 10^{-12} m $s^{-2}Hz^{-1/2}$ – this, in a measurement bandwidth defined as lying between 5 MHz and 0.1 Hz.

Realisation of such performance requires the careful control of many parasitic effects, including spacecraft self gravity changes, magnetic forces, pressure gradients, thermal radiation due to temperature gradients, position-sensing back action, electrostatic disturbing forces (stiffness, patch effect, contact potential difference evolution, charge of the proof mass if not controlled), noise induced by damping due to the gold wire which controls the proof-mass charge, residual pressure and surface phenomena…

As already noted, the finite precision with which the sensors can be aligned and the scale factors can be matched, affects the gradiometer measurements through coupling with the external accelerations. These errors are classified inside the 'instrument-satellite coupling errors' of section 6.1. To fulfil the 2 mE allocation, it will be necessary to specify the quality of the calibration and the quality of the control of the external accelerations. A requirement of 10^{-5} for the quality of the calibration, i.e. alignment and scale factors, has been derived. The corresponding quality of the control of the external accelerations will be discussed in section 6.4.8

The principal misalignment and scale errors are presented in Figure 6.13. They are divided in two classes. The differential mode errors will couple with external linear accelerations that are identical, i.e. common, for the two accelerometers used to derive the gradiometric measurement. The common errors will couple with the external angular accelerations that will be recorded as having opposite signs by both accelerometers. In both cases an error term (equal to the alignment or scale-factor error multiplied by the external perturbations) will appear in the derivation of the gravity gradients.

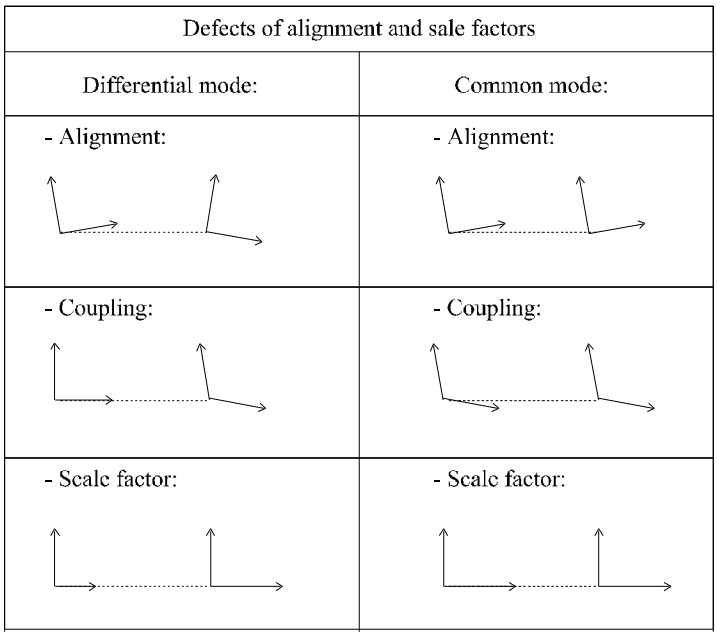

Figure 6.13. *Definition of misalignment and scale-factor effects.*

Dimensional Stability of the Structure

During the scientific measurements, another stability problem comes into play: any relative motion of the accelerometers on time scales falling in the measurement bandwidth will produce a differential acceleration that cannot be distinguished from that originating from a gravity gradient. As a consequence, major requirements apply to the dimensional stability of the structure assembly:

- high stability from on-ground operations to in-orbit conditions
- very high short-term stability under thermal variations.

The solution adopted relies on carbon/carbon (C/C) technology providing insensitivity to moisture release, high stiffness, and very low coefficient of thermal expansion (CTE < 10^{-7} K^{-1}) in all directions by means of a quasi-isotropic lay-up. C/C structures with such requirements have already been realised; Figure 6.14 shows an example.

Besides the low CTE, specific measures must be implemented to guarantee very high thermal stability in the short-term (of order 10 mK @ 5 MHz). These include high thermal inertia of the instrument, thermal decoupling between the satellite and the gradiometer core, and very small power consumption in the instrument core. The thermal-control concept selected involves dividing the instrument into two thermal domains: the area with the gradiometer itself (i.e. the structure and the accelerometers) and the area with the electronics. The temperature in the gradiometer area is kept

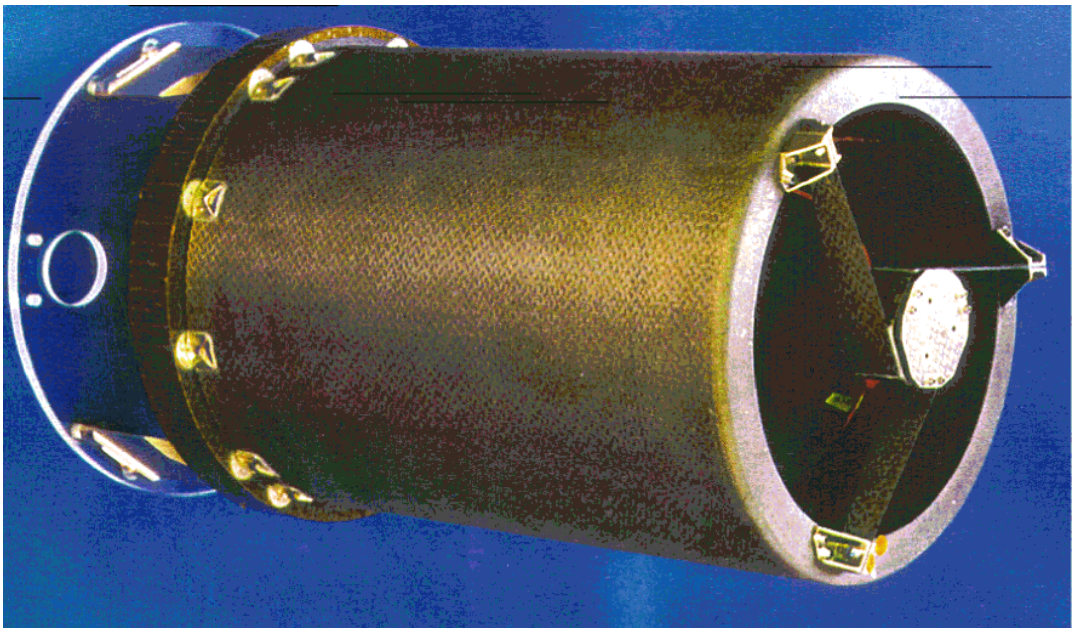

Figure 6.14. *Carbon-carbon telescope structure.*

stable by means of a two-stage control system (Fig. 6.15). The gradiometer is connected by isostatic mounts (TMDD) to a base platform and is surrounded by layers of multi-layer insulation (MLI). The temperature of the outer domain is actively controlled by heaters to reach a thermal stability better than ± 0.5 °C, so that the thermal flow to the inner area is very smooth. This outer thermal domain has a second layer of MLI to protect it from external perturbations.

The performance of the thermal-control system has been analysed by means of a detailed thermal model (70 nodes) including active control of temperature variations generated by the external environment and power instabilities inside the gradiometer enclosure. Transient analysis has been performed. The results can be seen in Figure 6.16. The thermal behaviour of the gradiometer is of 0.1 mK over 200 s. This is compatible with the temperature stability requirement of 0.8 mK over 200 s.

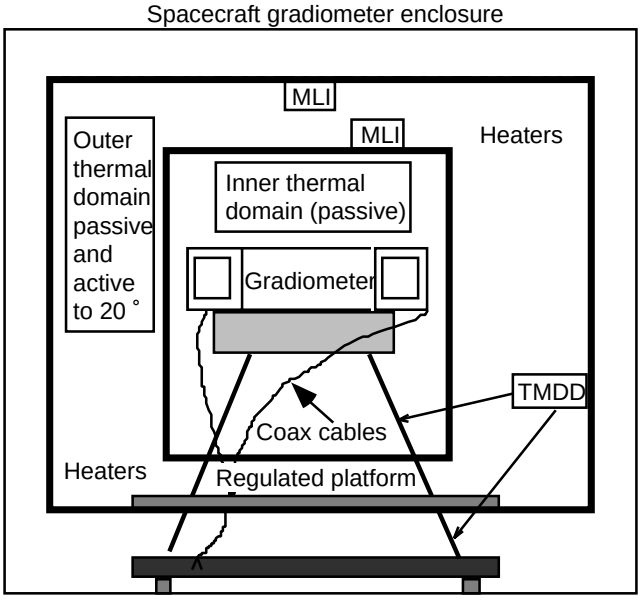

Figure 6.15. *Gradiometer thermal concept.*

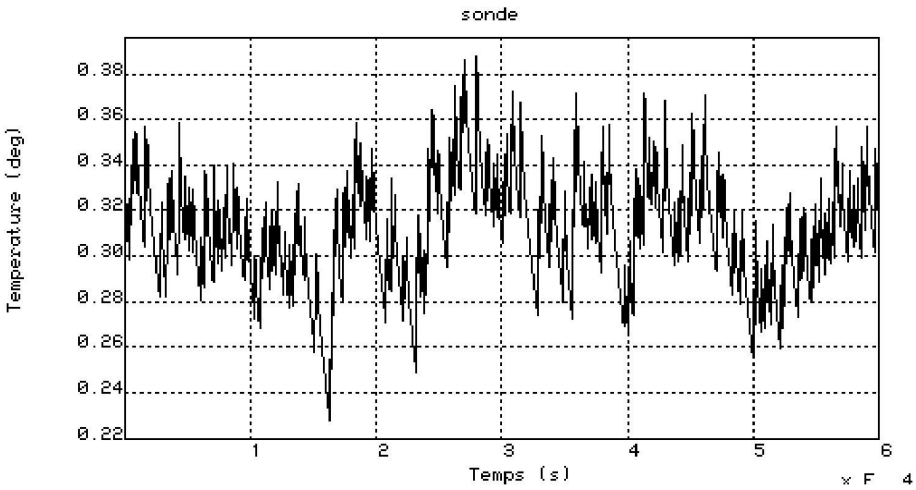

Figure 6.16. *Temperature variations on the gradiometer along 60 000 sec.*

Instrument Performances Summary

Table 6.5 provides a summary of the instrument performances.

Parameter	**Value**
Design bandwidth (MBW)	$5\ 10^{-3} \div 10^{-1}$ Hz
Baseline length	0.5 m
Sensitivity (detection noise) Measurement bandwidth Extended bandwidth ($10^{-5} \div 1$ Hz)	 $< 10^{-12}$ m s^{-2} Hz$^{-1/2}$ $< 10^{-10}$ m s^{-2} Hz$^{-1/2}$
Proof-mass positioning error	$6\ 10^{-8}$ m Hz$^{-1/2}$
Absolute / relative scale factors	10^{-3} / 10^{-5}
Absolute / relative misalignment	10^{-3} rad / 10^{-5} rad

Table 6.5. *Gradiometer performances.*

Instrument Test, In-orbit Set-up and Calibration

The gradiometer is a highly sophisticated sensor that will require extensive calibration, first on ground and then in orbit. The flight calibration, in particular, will involve carefully planned co-ordination with spacecraft manoeuvres and feedback from the gradiometer to the attitude- and drag-control system. Such calibration will be repeated once a month, to check parameter stability with respect to thermal drifts and fluctuations. On the other hand, once the set-up and calibration have been performed, the operation of the instrument will be simple, with minimal commanding in the absence of anomalies.

Ground verification will be performed in stages. The accelerometers will be tested first, then accelerometer pairs mounted on the gradiometer arms and finally the complete assembly. The ground calibration will be performed by rocking the accelerometers in a controlled direction on a pendulum bench (see Fig. 6.17). The 1-g environment, which is sustained by the vertical, less-sensitive axis, will project over the sensitive perpendicular axes and it will measured by them. The differences in these readouts will provide information about the actual alignments of the axes. By rocking in different directions, it will be possible to determine all the ground calibration parameters. For both accelerometers and gradiometer arms, the functional tests will be performed on the pendulum bench. A microgravity test in free fall (drop tower) will also be performed. In the flight-ready instrument, scale factors will have been matched to 1 part in 10^4, and misalignments and couplings will have been calibrated to 10^{-4} radians. It will be specified (and verified by test) that these ground values must not

change due to launch effects, and so these calibration parameters will still apply to the satellite in orbit.

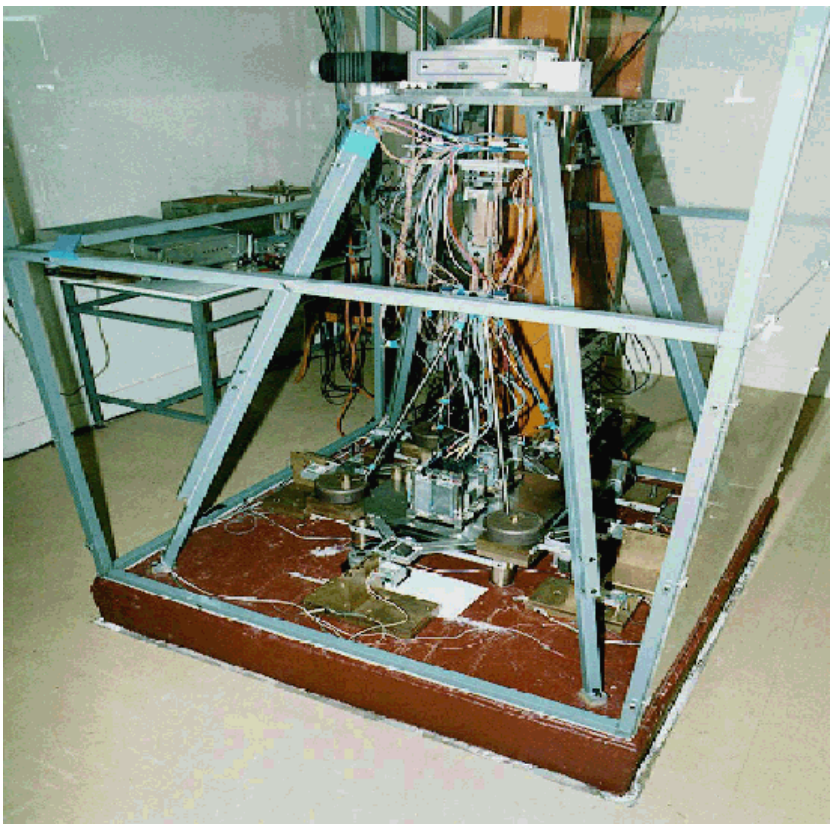

Figure 6.17. *Pendulum bench test set-up.*

In-orbit Calibration

The objective of the calibration in orbit is to enhance the level of balancing to 10^{-5} in both scale-factor matching and alignment. The method proposed involves producing reference signals (linear and angular) larger in magnitude than the environment noise, and adjusting the voltages in the bias circuits until the reference signal merges into the noise. The procedure is iterated for each degree of freedom. These accelerations are produced using the proportional cold gas propulsion (section 6.4.10).

The basic steps in the balancing procedure are:

- calibration of thrusters against star sensors
- activation of AOCS/DFC feedback control, based on ‘coarse’ (as from ground alignment) gradiometer common mode output

– generation of ‘pure’ translational accelerations
– calibration of differential scale factor, misalignment, quadratic factor
– generation of ‘pure’ rotational accelerations by the thrusters
– calibration of common misalignment.

The requirements on the external reference signals to be provided to the gradiometer are:

– linear excitation: 10^{-6} m s^{-2} at 0.03 Hz and 0.1 Hz
– angular excitation: 2 10^{-6} rad s^{-2} at 0.1 Hz
– mixing between degrees of freedom: < 1%.

Such requirements are compatible with the cold-gas micro-thrusters described in section 6.4.10, and hence no dedicated calibration device needs to be employed.

Another level of calibration concerns the ‘absolute’ scale factors of the gradiometer. One possibility is to compare the gradiometer measurements with the dominant, time-varying gravity gradient terms. These terms are due to the flattening of the Earth (J2) and the coupling between the central term of the Earth’s gravity field and radial orbit variations. The J2 gravity gradient variations have a magnitude of about 7 E, while the coupling with the central term amounts to more than 3 E. These terms are well known and can be modelled with very high accuracy.

Another possibility is to use well-surveyed areas on the Earth’s surface where the gravity field is known to high accuracy [CIGAR IV, 1996]. Gravity data for such an area can be extrapolated upward to the GOCE satellite altitude and compared with the actual observations. The gradiometer observations can also be checked by cross-comparison with SST-hl observations. An overlap in sensitivity with gravity field parameters in the medium-wavelength area exists, i.e. wavelengths of a few thousands of kilometres that can be utilised for this comparison. The linear accelerations from the common mode of the gradiometer can be checked against the low-frequency perturbations of the GOCE orbit derived from the SST-hl observations. Besides absolute calibration, the above techniques will be used to assess the data quality in an independent manner, during the mission.

Development Status

The development of ultra-precise space accelerometers at ONERA began in 1962 with the CACTUS accelerometer. Four years of in-orbit measurements (1975-79) confirmed the expected resolution of 10^{-10}g. Thereafter, they undertook the development of the GRADIO accelerometer, based on the electrostatic suspension of a proof mass, the motion of which is measured through high-resolution capacitive sensors, and controlled. For more than 20 years, original capacitive sensor designs

have been established and widely exploited in the fields of metrology and instrumentation. Since 1980, these accelerometers have been studied in the context of space gradiometry, first with CNES for the GRADIO project, and then with ESA for its Aristoteles mission.

As part of these activities, not only the development of ultra-sensitive space accelerometers, but also the development of a specific ground test bench (up to 3×10^{-10}g / $\sqrt{Hz}$ test resolution) was addressed.

This experience makes the electrostatic gradiometer a mature development for GOCE, as shown by successful in-orbit testing of the ASTRE accelerometer (a derived version of GRADIO made for ESA) on board the Space Shuttle (STS 78, STS 83, STS 94) for the monitoring of the low-frequency acceleration environment, by the STAR accelerometer delivery to CNES for the German CHAMP mission, and the production of SuperSTAR for the US-German GRACE mission.

Lately, the ground-test capabilities at ONERA have been enriched by the provision of an electrostatically suspended torsion pendulum. This allows the measurement of parasitic forces inside electrostatic devices with unprecedented resolution. In particular, it can characterise the stiffness and damping of thin wires foreseen for the charge control of gradiometer proof masses. It can also investigate the evolution of contact potential differences to a level commensurate with the GOCE objective.

6.3.3 Geodetic GPS/GLONASS Receiver

The GPS/GLONASS on-board system will supply the SST-hl contribution to the gravity field recovery, by simultaneously tracking 8 to 12 GPS/GLONASS satellite signals. Moreover, it will provide data for precise orbit determination (POD) and it will be used in real-time for on-board navigation and attitude-reference-frame determination.

Instrument Requirements

The GPS/GLONASS instrument for GOCE will be a 12-channel dual-frequency receiver with a codeless tracking capability. It will process, demodulate and decode the signals from GPS and GLONASS satellites, received through a hemispherical antenna pointing at the Zenith. Two operating frequency bands are used, L1 (centre frequency 1574.4 MHz) and L2 (centre frequency 1227.6 MHz), in order to allow the compensation of ionospheric delays by ground post-processing. On GPS satellites, encryption (anti-spoofing, AS) may be imposed on the high-resolution (P) code, which prevents straightforward processing of the L2 signals; therefore a special mechanism is provided for codeless tracking. Each channel may receive either GPS or GLONASS signals and will provide the following measurements: C/A pseudo range (L1), L1 and L2 carrier phase, P1 and P2 code pseudo range (L1 and L2), L1-L2 differential carrier

phase and P1-P2 differential pseudo range. In addition, the receiver provides the following capabilities:

- position and velocity measurements from GPS (GLONASS optional) and corresponding UTC time
- one pulse per second output synchronised with GPS time
- measurement time-tagging with respect to instrument internal time
- redundant communication interface
- ability to turn off unused measurement channels for power saving.

Geodetic quality GPS/GLONASS receiver systems have been the subject of dedicated technology development. The system will therefore be available on a standard basis by the time the GOCE enters its development phase. Potential instruments are GRAS flying on Metop and Lagrange that will fly on the Argentinean mission SAC-C.

Experiment Architecture, Configuration and Budgets

Table 6.6 shows the receiver specification for the ESA GRAS receiver, developed for stratospheric profiling applications. Sampling rates as high as 10 Hz are not required for GOCE, where 1 Hz will be sufficient.

Item	Requirement
Carrier phase GPS L1 GPS differential L2-L1 GLONASS L1 and L2	 σ = 1 mm @ 10 Hz σ = 2 mm @ 10 Hz σ = 1 mm @ 10 Hz
Pseudorange GPS C/A code GLONASS P1 and P2	σ = 50 cm @ 1 Hz

Table 6.6. *GRAS performances..*

Functionally, the equipment consists of a pre-filter and low-noise amplifier unit, a receiver processing unit, an antenna and cabling. The equipment design and interface data used in the GOCE Phase-A study are given in Table 6.7.

Item	Size (mm)	Mass (kg)	Power (W)	
			Avg.	Peak
Receiver	250 x 164 x 203	5	25	38
Antenna	132 x 132 x 40	< 0.5	--	--

Table 6.7. *GOCE GPS/GLONASS interface reference data.*

The antenna is a planar with a ground plane. Planar antennas have better performance with respect to the conical or the helical GPS antennas. Exact knowledge of the antenna phase centre is essential in cm-level accuracy measurements; in patch antennas it can be determined to 3-4 mm accuracy, but for conical or helix antennas the same levels of accuracy cannot be reached. The antenna is placed in the anti-Earth (+z) side for unobstructed hemispherical coverage of the sky.

The main instrument operational modes are:

- Stand-by Mode: allowing access to processor and memory (to upload software, etc.)
- Initialisation Mode: to initialise instrument with position knowledge accuracy better than 10 km (all directions), velocity knowledge accuracy better than 10 m/s (all directions), time knowledge accuracy better than 1 s
- Navigation Mode: providing real-time navigation measurements from all tracked satellites (only a small number of channels needed)
- Observation Mode: providing all science data from tracked satellites.

Performances

Standard requirements apply for spacecraft navigation purposes: position estimation accuracy within 100 m and velocity estimation accuracy of 0.1 m/s. The expected performance of POD for the GOCE mission, with availability of ground (IGS) receiver data associated, is about 3 cm, as required (section 8.1.2). For the purpose of post-processing of the SST-hl data, the variable non gravitational accelerations acting on the spacecraft will be known to an accuracy better than 10^{-9} m/s^2 at 1 Hz, from the gradiometer common-mode acceleration measurements.

6.3.4 Secondary Payloads

The standard radiation-environment monitor (SREM), already developed by ESTEC, will be implemented on board to provide radiation-environment measurements. Since the gravity gradiometer primary payload is sensitive to electrical charging, SREM data can be used to correlate its measurements with encountered electron and proton fluxes.

The detector unit features two heads, each with 20º half-cone field-of-view. The electronics unit comprises three particle detectors for electron and proton spectroscopy (measurement error < 1%), cosmic-ray events counting and radiation-dose measurements. The instrument has a mass of less than 2.5 kg and a power demand of less than 2 W. It is compatible with a primary bus input voltage of 20V-50V.

A laser retro reflector (LRR) will provide a supplementary data set of range observations as backup for the precise orbit determination post-processing. The LRR is a corner cube array capable of reflecting laser pulses back along the incident direction of the light path. By means of this instrument, the satellite can be tracked by the satellite laser ranging ground stations network. The total mass is 0.5 kg.

6.4 The Satellite

6.4.1 Major Requirements and Design Drivers

The satellite has been designed starting from the scientific requirements and taking into account the availability of equipment. Several top-down and bottom-up design processes have been performed. This has been made possible by the availability of tools that allow an easy translation of design features into scientific performances (Chapter 8). Finally, the following major requirements and constraints have become the key design drivers:

- The reference launch vehicle is Rockot, and the total satellite mass must not exceed about 1000 kg. Up to the 1000 kg level, high mass is an advantage (lower accelerations for a given perturbing force).
- The satellite attitude is Earth-pointing throughout the mission and the cross-section in the direction of motion (x-axis) must be on the order of 0.8 m^2 or less.
- The actuators for orbit maintenance and along-track drag control are a pair of ion thrusters, with a maximum thrust of 20 mN, working in cold redundancy. The actuators for attitude control are cold-gas proportional micro-thrusters of new design, with a maximum thrust of 1 mN.
- Given the limited thrust available, disturbance forces and torques must be minimised by the configuration, to make the total control authority sufficient down to a mean altitude of 250 km at the beginning of life.
- The power subsystem must support full operation during eclipses for up to 10 min; operation during longer eclipses is performed in survival mode.
- The gradiometer is accommodated in a special compartment. Integration of the gradiometer compartment must allow easy mounting and dismounting and must preserve the alignments.

- The gradiometer compartment must be protected from external (Sun and Earth) and internal heat inputs to realise a constant environment temperature.
- The total mission lifetime will be at least 20 months, with two data-collection periods of at least six months each.

6.4.2 Satellite Configuration and Budgets

The satellite configuration envelope is a long and slender prism, with a cross-section of 0.8 m^2 and a length of 4 m (Figs. 6.18 and 6.19 and Fig. 5.3 of Chapter 5). A high degree of symmetry is provided to minimise the external disturbance torques. The centre of mass is designed to be approximately 10 cm above the centre of pressure to provide extra stability in case of attitude loss. There are no deployable appendages. From the point of view of integration, the satellite can be divided into upper and lower modules, with the following layouts:

- Lower module, lower bay: launcher interface, AOCS/DFC and ion propulsion including xenon tank. Lower module, upper bay: gradiometer assembly and its electronics
- Upper module: electrical, data-handling and radio-frequency equipment, and Nitrogen gas tank.

This means that the centre of the gradiometer assembly will be located at the mid-point of the satellite. Moreover, it will stay within 10 cm of the centre of mass throughout the satellite's lifetime, ensured by the symmetric depletion of the fuel tanks. The upper module will be fixed to the lower module after integration of the gradiometer in its bay. The solar array is divided into one body-mounted panel and two wings. It shields the satellite and gradiometer from direct solar illumination and its back side is insulated to prevent transmission of heat into the interior. The ion thrusters are mounted on the bottom platform and the cold-gas thrusters are mounted in four clusters on the upper and lower edges of the solar-array wings. Equipment mounted externally includes the GPS/GLONASS antenna in the anti-Earth direction and the S-band communication antennas placed on opposite edges of the solar array. Table 6.8 provides the mass budget. Margins are included according to the maturity status of each subsystem; a system margin has also been added.

	Total Mass (kg)
Drag & Attitude Control System	22.3
Cold Gas Propulsion	45.6
Ion Propulsion	43.5
On Board Data Handling	33.8
Solar Array	35.0
Electrical Power System	79.8
Radio Frequency	10.5
Structure	210.1
Thermal Control	17.2
Harness	35.3
Spacecraft	**533.2**
Gradiometer	72.3
Gradiometer Electronics	24.0
GRAS	8.5
Laser Retroreflector	0.6
SREM	3.0
Payload	**108.4**
Nitrogen Propellant	36.0
Xenon Propellant	22.0
Propellant	**58.0**
10 % System Margin	**64.2**
Grand Total	**763.8**

Table 6.8. *GOCE mass budget.*

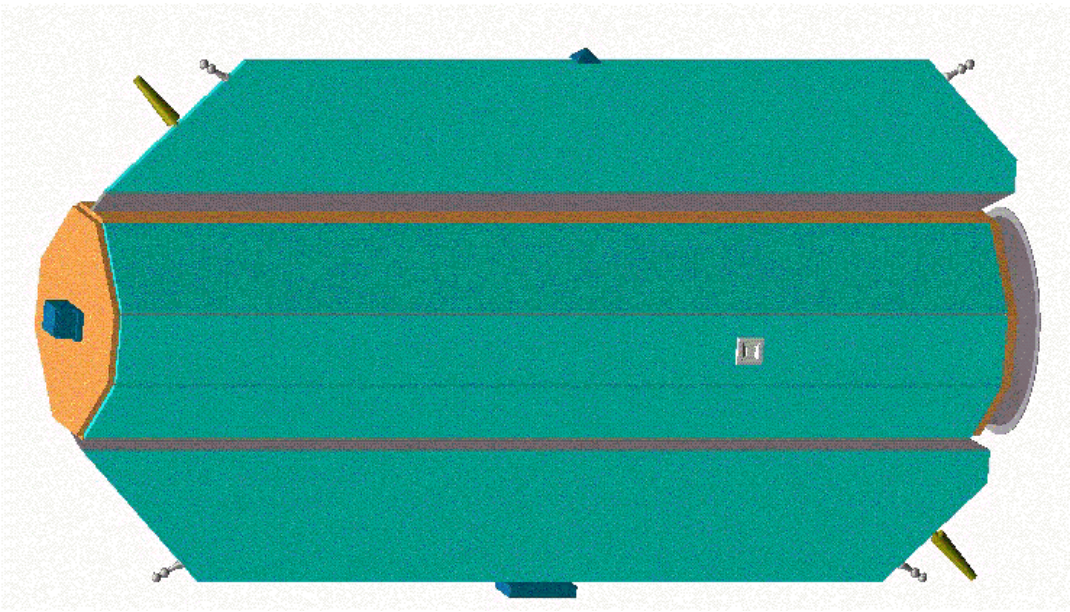

Figure 6.18. *Front view of the satellite.*

The inertia budget and an indication of the location of the centre of mass and centre of pressure are provided in Table 6.9. The reference is the intersection of the longitudinal axis with the launch separation plane.

	X		Y		Z	
	BOL	EOL	BOL	EOL	BOL	EOL
Principal Moments of Inertia (kg m^2)	113.1	112.4	1104.3	1051.7	1121.7	1069.1
Centre of Mass (mm)	2185.2	2174.2	-5.0	-5.4	-7.7	-8.3
Centre of Pressure (mm)	2080		--		--	

Table 6.9. *Inertia budget.*

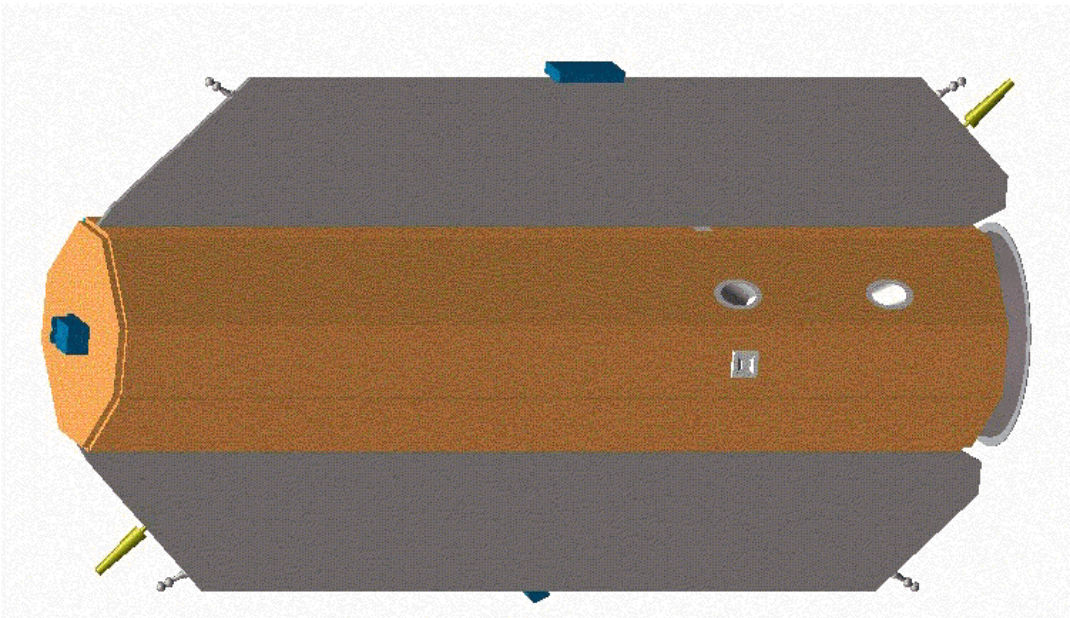

Figure 6.19. *Back view of the satellite.*

Figure 6.20 shows the avionics architecture. More details about the component elements (data handling, radio frequency and power) are given in sections 6.4.5 to 6.4.7.

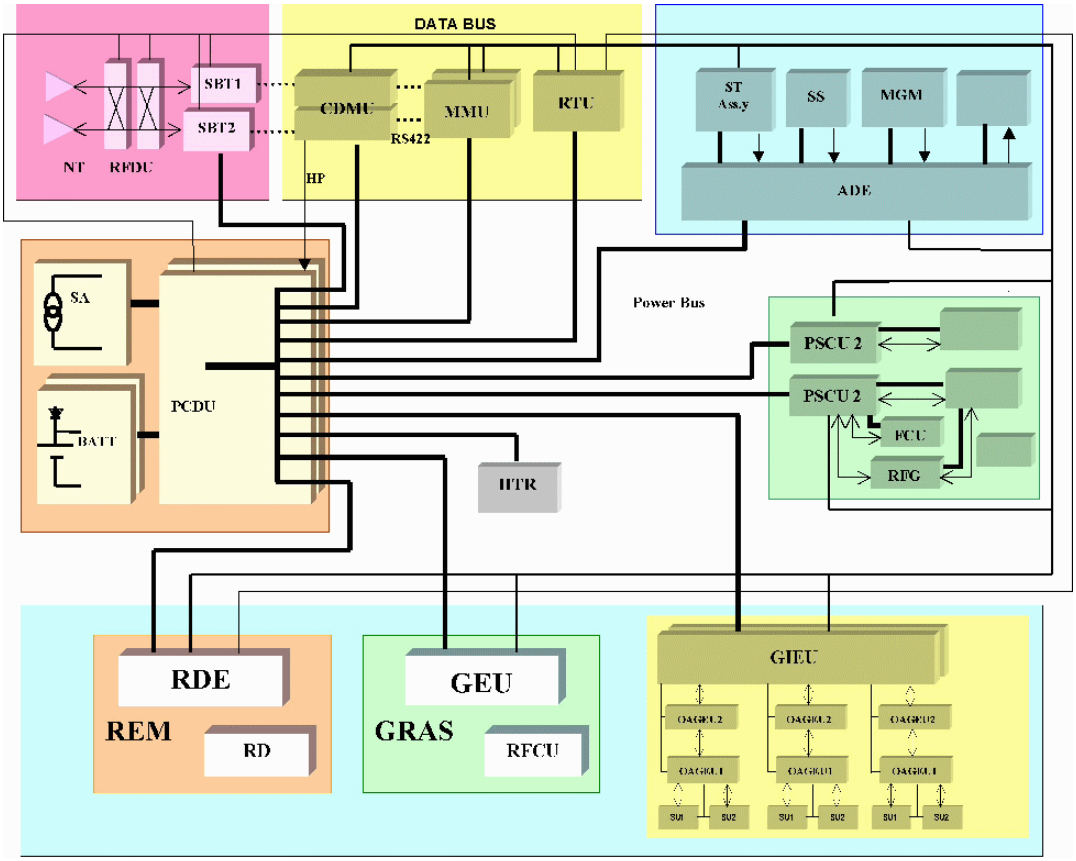

Figure 6.20. *Satellite avionics architecture.*

Table 6.10 provides the power budget per orbital condition (Sunlight, short and long eclipse). A margin of 15% is included in the subsystem power estimates. Table 6.11 gives the uplink and downlink communications budgets.

	Power (W)			
	Short Eclipse (10') Season		Long Eclipse (28.5') Season	
	Sunlit	Eclipse	Sunlit	Eclipse
Gradiometer	74.7	74.7	5.4	5.4
GRAS	41.1	41.1	41.1	41.1
REM	3.3	3.3	3.3	3.3
Total Payload	**119.1**	**119.1**	**49.8**	**49.8**
Drag-free and Attitude	30.9	30.9	30.9	30.9
Electric Propulsion	474.6	474.6	280.4	280.4
Data Handling	54.6	54.6	54.6	54.6
Radio Frequency	39.1	39.1	39.1	39.1
Thermal Control	0.0	46.0	0.0	93.0
Total Spacecraft	**599.2**	**645.2**	**405.0**	**498.0**
Total Power Demand	**718.3**	**764.3**	**454.8**	**547.8**
Eclipse demand				
Harness Loss		38.2		27.4
Power from Battery		802.5		575.2
Energy Request (Wh)		133.8		273.2
Sunlight demand				
Harness Loss	35.9		22.7	
Battery Recharging	116.9		304.7	
Power from PCDU	871.1		782.3	
PCDU Losses	130.7		117.3	
Array Power Requirement	**1001.8**		**899.6**	

Table 6.10. *Power budget*

Parameter		Nominal	mean-3σ	margin-w.c. RSS
Telecommand Data Rate	kbps	4		
Telemetry Data Rate	kbps	1000		
TX Downlink Power	W	1,00		
TX Downlink Ant. Gain (at edge of f.o.v.)	dB	-12,00		
Uplink				
Margin Basic Uplink	dB	40,64	38,80	39,23
Margin Telecommand Recovery	dB	35,17	31,54	30,95
Margin Transponder Ranging-Channel	dB	32,56		
Downlink				
S/C EIRP	dBW	-20,41		
Margin Carrier Recovery	dB	16,20	13,75	12,96
Margin Telemetry Recovery	dB	6,50	5,73	5,22
REQ E_b/No (BER=10^{-9}, PFL=10^{-6})	dB	2,70	2,70	

Table 6.11. *Link budget.*

6.4.3 Structural Design

The structure will be an octagonal prism in aluminium with bars at prism edges, panels as prism faces and platforms to create three bays (lower bay, gradiometer bay, upper bay). An additional platform will be provided to support the gradiometer assembly. A short adapter ring, with a diameter of 937 mm, supports the launcher interface. The progressive process of assembly can be seen in Figure 6.21. The design drivers are the lateral frequency requirements, and the stability of the structure and alignments during the assembly process. The satellite mass target is 800 kg, providing ample room for the structural mass to meet the frequency requirements and the centre-of-mass and inertia constraints.

For the structure sizing, frequency requirements, dimensioning loads and safety factors are all taken into account. The minimum eigenfrequencies requested by the Rockot launcher for a hard-mounted spacecraft are 17.25 Hz lateral and 37.25 Hz axial. The flight limit loads are 8.1 g (axial compressive) ± 0.8 g (lateral in any direction); the most severe combination of axial and lateral loads acting simultaneously in any direction is used to size the structure. The minimum safety factors are 1.25 (ultimate), 1.1 (yield stress) and 3.0 (buckling). The NASTRAN finite element analysis gave 17.7 Hz for the first lateral mode, 114 Hz for the first axial mode, and safety margins greater than 2 for both strength and stability. The structural mass budget amounts to 182 kg. Figure 6.21 shows the assembly concept.

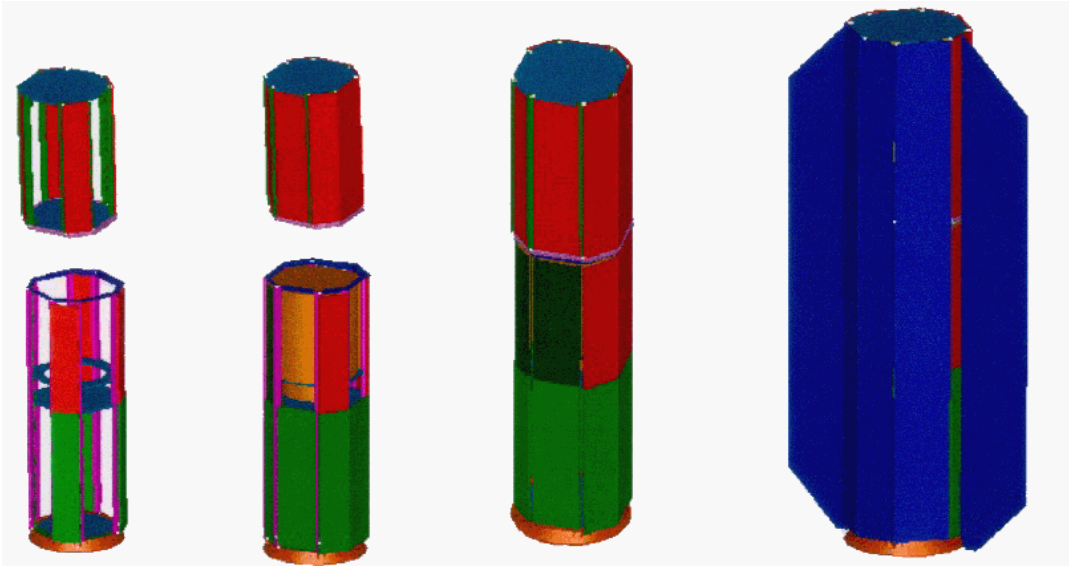

Figure 6.21. *Satellite assembly concept.*

6.4.4 Thermal and Thermoelastic Design

The major requirements applicable to the thermal control of the satellite system are:

- to provide the required interface temperatures to the gradiometer assembly and its electronics, and
- to maintain all the other satellite equipment within their operating temperature ranges through all phases of the mission, with adequate design margins.

The main temperature requirements are presented in Table 6.12:

The spacecraft thermal design and control is based on passive insulation and radiation techniques. Radiators coated with optical surface reflectors (OSRs) are located in the anti-Sun side and on the top platform according to the layout in Figure 6.22. All other external surfaces are covered with multi-layer insulation blankets. Thermal interface filler will be applied at the high-dissipation units, and insulating washers to units sensitive to temperature variations. Black coating will be applied to units and the internal radiator surfaces. Thermistor-controlled heaters will be used on the gradiometer electronics, batteries, star-tracker heads, and ion-propulsion Power and Flow Control Units. Multi-layer insulation blankets will cover the back of the body-fixed solar array, which will be further decoupled from the spacecraft by low-conductivity supports, while the rear of the wings will be white-painted.

Unit	Temperature (ºC)		Temperature Stability
	Min.	Max.	
Gradiometer Assembly	10	15	<5 K/orbit
Signal Processing Electronics	15	25	<30 mK/200s
Remote Electronics	15	25	<10 K/orbit
GPS/GLONASS Receiver	-10	50	
Power, DHS, RF, AOCS and Propulsion Electronics	-10	50	
Solar Panels	-85	95	
Battery	0	10	
Star Tracker Head	-20	40	
Ion Thrusters		160	
Xenon Tank	-60	60	

Table 6.12. *Thermal requirements.*

The analysis was carried out by means of a 280-node ESATAN model and included both steady-state and transient analysis (no eclipse, and short and long eclipse at different epochs). Gradiometer temperature variations have been found to be maintained well within the limits (< 1K/orbit for the assembly and <13 mK/200s for the most sensitive electronics). The sizing case for the radiators is the hot case with short eclipse for the upper module and the hot case without eclipse for the lower module. Heaters are sized by the long eclipse cold case. The results show adequate area margins (10%) for the radiators. The mass budget is 17.2 kg including margins and the required heater power is 93W (long eclipse cold) and 46W (short eclipse cold). 14 thermistor-controlled heater circuits are required, with an additional 45 thermistors for house-keeping.

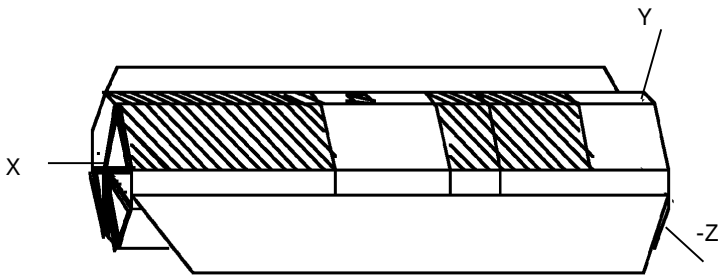

Figure 6.22. *Location of the radiators. X = velocity, Y = anti-Sun and –Z = anti-Earth.*

The basic concepts for the thermal control of the instruments have been presented in section 6.3.2. To ensure correct instrument performance, the spacecraft thermal control shall provide a temperature of 10-15ºC at the interface.

The thermoelastic stability of the GOCE structures is important on two accounts:

- To ensure the relative stability of the reference frames of the gradiometer and the star sensors. The instrument-to-star-tracker alignment requirements are of the order of 10^{-4} rad at DC and low frequency and of order $2\ 10^{-6}$ rad $Hz^{-1/2}$ in the measurement bandwidth.
- To avoid a spurious gravity gradient signal produced by the satellite gravity field variation. The differential acceleration between each pair of proof masses, due to this effect, must not exceed 0.2 mE $Hz^{-1/2}$ in the measurement bandwidth.

The procedure for checking the alignment requirements consists of: setting up a structural finite-element model of the spacecraft (including the thermal properties of the materials); applying temperature fields to the structural elements, representative of the worst-case temperature gradients occurring at the time scales of interest; and computing the displacements and rotations between the points one wants to keep under control.

For the Phase-A exercise, the temperature gradients were obtained by differencing the temperatures found at two time points before and after entry into the short eclipse. This case is then representative of the long-term (low-frequency) thermoelastic behaviour of the spacecraft in a worst case. The maximum rotation angles between the star-tracker line of sight and the gradiometer reference frame were found to be around $7\ 10^{-5}$ rad. This shows that the long-term stability requirement is met. Investigation of the stability in the measurement bandwidth would require a much more detailed exercise, in which the displacements and rotations are computed at a large number of time points (about 1000 over one orbit), in order that a Fourier analysis can be performed.

For checking the self-gravity requirements, another step in the analysis is required, in which the contribution of the mass of each spacecraft element to the gravity field at the location of each accelerometer is computed and then differences are taken between pairs of accelerometers in each gradiometer arm. For this purpose, a model of the spacecraft mass distribution (lumped masses) has been set up to obtain the gravity acceleration produced at each accelerometer location. The gravity acceleration variation has then been obtained by applying to the mass points the displacement computed from the thermo-elastic analysis.

Again, the analysis was carried out for the long-term requirement only. The results show gravity gradients of the order of 4 mE ($4\ 10^{-12}\ s^{-2}$) across the gradiometer, which

are negligible with respect to the 'nearly static' requirement (10^{-6} s^{-2}, related to the coupling with the proof mass motion). However, the magnitude of the self-gravity field is enough to cause a large effect, should it occur on time scales ≤ 200 s (i.e. inside the gradiometer measurement bandwidth). Therefore, in the study follow-on an in-depth analysis of these effects is warranted, based on a thermo-elastic analysis to be performed on about 1000 points along the orbit, and using a more high-fidelity gravity model of the spacecraft based on distributed mass modelling.

6.4.5 Power Generation and Distribution

The electrical power requirements of the spacecraft have been presented in Table 6.10. The electric propulsion is the largest power user on board. To limit power and energy storage requirements, the thrusters will be operated at constant thrust throughout the long eclipse season, and the gradiometer will be turned off. The solar array and batteries support full scientific operations in the season of short eclipses. As shown in the table, this approach results in similar demands in the two cases of long and short eclipse. The key power demands and battery and solar array requirements can be seen in Table 6.13:

	Short Eclipse Season		Long Eclipse Season	
	Sunlit	Eclipse (10')	Sunlit	Eclipse (28.5')
Power Demand	718 W	764 W	455 W	548 W
Required Array Power including Battery Charging	1002 W + 10%		900 W + 10%	
Energy Storage	134 Wh + 10%		273 Wh + 10%	

Table 6.13. *Power subsystem sizing parameters.*

The solar array consists of three body-mounted panels (total area 3.35 m^2, upper limit temperature 110ºC), and two lateral wings (total area 3.96 m^2, upper limit temperature 70ºC). Using GaAs cells (19% efficiency @ 22.5ºC), the total area meets the demand, including 10% system margin, of around 1 kW at the end of life and 31º Sun incidence angle.

Two batteries, in cold redundancy, are provided. The design-driving case is the long eclipse, with an energy demand of 265 Wh. Both Ni-Cd and Ni-H cells meet the requirements. The required cell capacity is 25 Ah for Ni-Cd (45% DOD) and 14 Ah for Ni-H (80% DOD). The batteries provide 2h survival after launcher separation.

The electrical power subsystem block diagram is shown in Figure 6.23. Power is distributed via an unregulated 24-32 VDC power bus. A power control and distribution unit (PCDU) provides the functions of array power regulation (by maximum power tracking, to optimise solar array area), battery health monitoring, charge/discharge control and reconditioning, and load power distribution and protection.

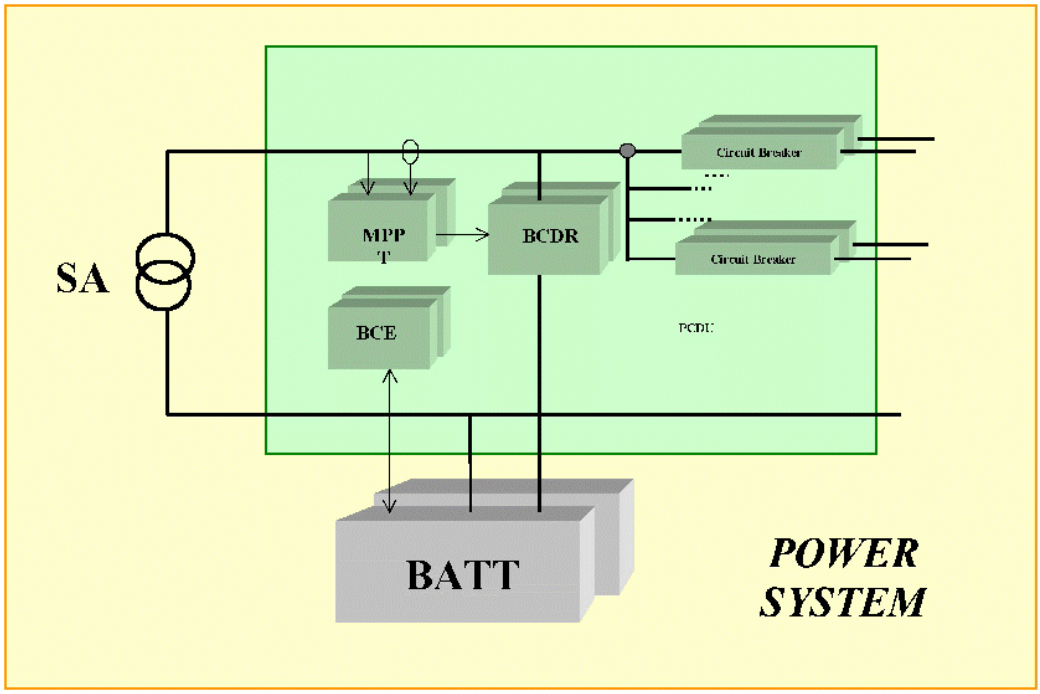

Figure 6.23. *Electrical power block diagram.*

6.4.6 Data Handling Systems and Software

The data handling subsystem (DHS) architecture envisaged for GOCE includes (see Fig. 6.24 for a functional block diagram):

- Central data management unit (CDMU), internally redundant, including encoder / decoder, DC/DC converter, central processing unit
- Mass memory unit (MMU), based on solid state technology, 1 Gbit capacity
- Remote terminal unit (RTU), internally redundant.

The required computing capability and throughput are compatible with a centralised computer architecture, including the drag-free and attitude-control data processing. Data exchange occurs via a 1553 data bus, with the exception of the transponders that use a high speed RS422 serial link with the DHS. The data exchange between the

gradiometer and the central processor for the attitude/drag control is also realised via the main data bus. Tables 6.14 and 6.15 show the data rate and the mass memory budgets.

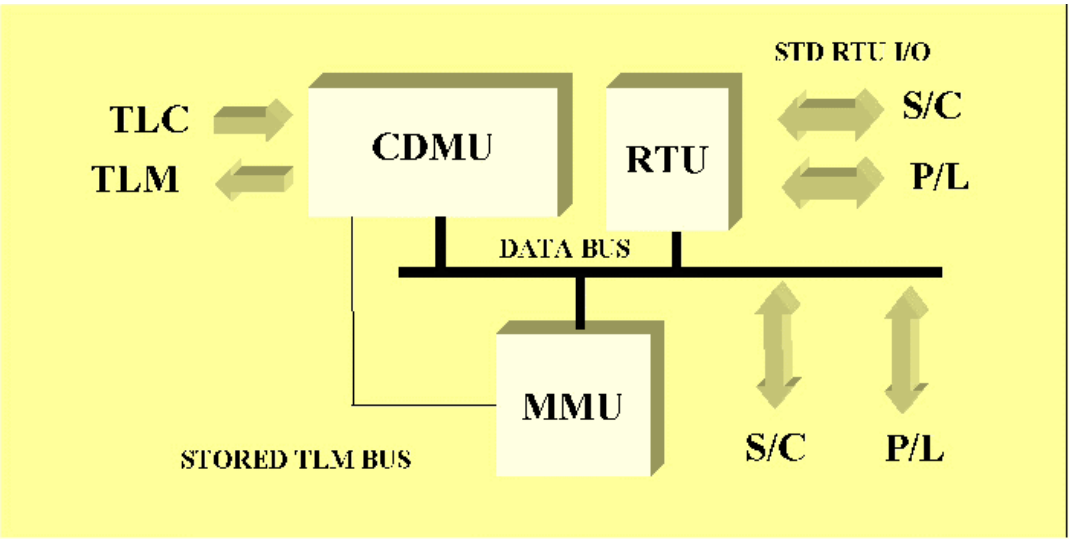

Figure 6.24. *Data handling functional block diagram.*

	Data rate (bps)	
Science data		**4292**
Gradiometer	432	
GPS / GLONASS	3840	
REM	20	
Payload Housekeeping		**526**
Gradiometer	516	
GPS / GLONASS	8	
REM	2	
Post-processing Support Data		**64**
AOCS/DFC	64	
Spacecraft Housekeeping		**134**
AOCS/DFC	14	
Electric Propulsion	24	
RF	6	
Thermal Control	16	
Power	62	
DHS	12	
Total		**5016**

Table 6.14. *Data rates.*

Item	Assumption	Mass Memory (Mbit)
Raw Data Storage	5.02 kbps × 24h	434
Margin	20%	86
Data Storage Requirement		520
Coding Overhead	EDAC 16/22, 38%	198
System Margin	50%	359
	Total	1077

Table 6.15. *Data storage.*

6.4.7 Radio-Frequency System

The radio-frequency system will be a standard implementation with two S-band coherent transponders, two antennas and a radio frequency distribution unit (see Fig. 6.25).

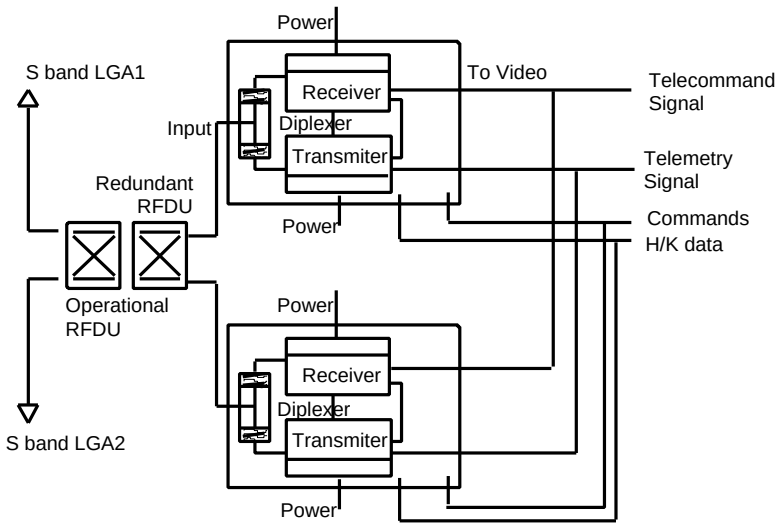

Figure 6.25. *Radio-frequency subsystem block diagram.*

The antenna will be a quadrifilar resonant helix design with hemispherical coverage and a gain of 3 dB at peak and 0dB at θ=90°. Its wide beamwidth assures hemispherical coverage and, in conjunction with another antenna, spherical coverage for any recovery situation with ample overlap margins. The telemetry data rate will be 850 kbps.

The pattern of ground contacts can be seen in Figure 6.4. It generally has three consecutive contacts followed by a 12 h gap. The accumulated contact time in three

passes is always ≥ 12 minutes. The data volume (computed assuming a worst-case blind period of 24 hours) is generally compatible with complete memory dump to Kiruna station in the next three passes of 12 minutes total duration.

6.4.8 Attitude and Drag-free Control (AOCS/DFC)

The design drivers on the AOCS/DFC are derived from the error allocation in Table 6.1 and from the definition of the external environment in Table 6.2. The allocation of 1 mE for coupling error and the 10^{-5} performance of the calibration established in 6.3.2, will allow the derivation of accuracy requirements for the control of the perturbing angular and linear accelerations. The allocation of 2 mE for satellite errors will allow the same analysis to be carried out for the absolute pointing requirements. Finally, the 1 mE allocation for the post-flight recovery of the centrifugal acceleration allows the specification of the recovery of the angular accelerations and velocities.

AOCS/DFC Requirements

The allocations above drive all the AOCS/DFC-derived requirements. They are summarised in Table 6.16 below.

Linear Acceleration	
In the measurement bandwidth	2.5 10^{-8} m s^{-2} $Hz^{-1/2}$ (all axes)
Below 5 MHz	1 10^{-7} m s^{-2} (x, z axes), 5 10^{-7} m s^{-2} (y axis)
Mean value	1 10^{-7} m s^{-2} (x, z axes), 5 10^{-7} m s^{-2} (y axis)
At all frequencies	1 10^{-6} m s^{-2} (x, y axes), 5 10^{-7} m s^{-2} (z axis)
Angular Acceleration	
In the measurement bandwidth	2.4 10^{-8} rad s^{-2} $Hz^{-1/2}$ (all axes)
Below 5 MHz	1 10^{-6} rad s^{-2} (all axes)
At all frequencies	1 10^{-6} rad s^{-2} (all axes)
Spacecraft Pointing	
Stability in the MBW	8.7 10^{-6} rad $Hz^{-1/2}$ = 1.8 arcsec $Hz^{-1/2}$(all axes)
Stability below 5 MHz	3.8 10^{-4} rad = 1.3 arcmin (all axes)
Pointing error bias	3.8 10^{-4} rad = 1.3 arcmin (all axes)
Angular Rates	(post-flight measurement accuracy requirements)
Spin mean value	3 10^{-7} rad s^{-1} (y axis)
Rate variations below 5 MHz	3 10^{-7} rad s^{-1} (all axes)
Rate variations in the MBW	4 10^{-10} rad s^{-1} $Hz^{-1/2}$ (y axis),
	4 10^{-7} rad s^{-1} $Hz^{-1/2}$ (x, z axes)

Table 6.16. *AOCS/DFC requirements*

Measurement errors are also generated by the satellite angular velocities, which give rise to differential centrifugal accelerations on each accelerometer pair. In particular, the fluctuations of the satellite spin rate about the pitch axis (nominal speed of 1.17 10^{-3} rad/s), would produce the largest error affecting the measurements of the V_{XX} and V_{ZZ} components of the gravity-gradient tensor. However, these errors are generated by a coupling of the angular rates with themselves (ω^2 terms) and therefore they can be completely reconstructed from the measurement of the angular rates only and then removed a-posteriori from raw data. The required angular rate measurement accuracy is also reported in the Table 6.16 above. The angular rates will be determined on the ground by combining the angular acceleration measurements provided by the gradiometer with the attitude measurements provided by the star sensors.

Comparison of the requirements in Table 6.16 with the natural (uncontrolled) environment provided in Table 6.2 leads to the following conclusions:

- Wideband drag control (extended to the lowest frequencies) will be required along the x-axis, and, marginally along y, where, anyway, the low frequency components of the disturbances along y caused by the coupling with x- axis through the ion-thruster tilt must be compensated. The drag along z is negligible and the major disturbances on this axis will be caused with coupling with the x-axis by thruster errors. However they will be smaller than the requirements, therefore no drag control along z is needed.
- Angular acceleration control is required at low frequency (LF, below the measurement bandwidth), about the three axes. Pointing-stability fluctuations in the measurement bandwidth (MBW) and at LF also need to be controlled.

AOCS/DFC Sensors and Actuators

The gradiometer is the principal sensor, providing both linear common mode acceleration measurements (with noise power spectral density < 10^{-9} m s^{-2} $Hz^{-1/2}$), and angular accelerations (with noise power spectral density < 10^{-9} rad s^{-2} $Hz^{-1/2}$). Linear acceleration measurements used for x-axis drag control need to be sampled at 10 Hz while other gradiometer measurements are only acquired at 1 Hz. To integrate the angular measurements into rates and angles, supplementary information at low frequency is required, which is provided by a star sensor.

The attitude of the axes of the gradiometer reference frame (GRF) in the Earth pointing reference frame (EPRF) is described by a rotation matrix that implements the following transformations:

- from the GRF to the AOCS frame
- from that to an inertial frame
- from the inertial frame to the EPRF

Reconstruction of the EPRF matrix requires knowledge of the Earth–satellite direction and the orientation of the orbit plane, which can be obtained on board in real time from successive pseudo-range measurements of the GPS/GLONASS receiver and a simple orbit propagator. The reconstruction of the inertial frame can be implemented by the star sensor to provide the inertial orientation of the satellite. Finally, the AOCS frame is affected by calibration errors and thermo-elastic deformation.

The actuators are ion thrusters for the in-line (x-axis) drag control, and cold-gas proportional thrusters for the y-axis drag control and the attitude control. The thruster performance parameters are discussed in sections 6.4.9 and 6.4.10.

AOCS/DFC Estimation and Control Approach

The drag control (DFC) must compensate drag fluctuations, along the x and y directions, both in the gradiometer measurement bandwidth and below, so as to reduce the satellite common-mode accelerations according to the requirements of Table 6.16. The major disturbance of the DFC loop is the drag force. The envelope spectrum of the drag disturbance is used to derive the DFC rejection requirements in the MBW, above it and below it, according to the gradiometer requirements. The frequency template of the DFC rejection needs, complemented by constraints on bandwidth (set by sampling rate and loop delay budget) are used to specify the DFC controller as a low-pass filter providing high rejection (20 to 40 dB) in the MBW. The order of the controller is high (5) to ensure steep roll-off above the MBW, so as to minimise the bandwidth. Given the large ratio of x to y disturbances (a factor of 20), single-axis analysis can be performed. Classical frequency-domain methods are used to synthesise the controller for the reference case at 250 km altitude. Figure 6.26 shows the open-loop x-controller performance (0.5 Hz open-loop cut-off) with respect to the rejection requirements.

Closed-loop performances are first evaluated in the frequency domain, as the product of the drag spectrum with the closed-loop transfer functions. This makes it possible to verify that the spectrum of the residual accelerations is consistent with the performance requirements, and to evaluate control-force requirements. In a final stage, the performance of the design is validated by time simulations (closed-loop drag-free and attitude control). This allows the verification of the design and the consistency with the frequency-domain predictions. Figure 6.27 shows the x-axis residuals after control. All requirements are fulfilled. The high noise level in the HF band (0.1-2 Hz) is mainly due to ion-thruster noise, specified as 5 mN below 2 MHz and 50 μN above 0.2 Hz (with 1/f slope in between). This means that aliasing has to be carefully cancelled in order to avoid any impact on the gradiometer measurements.

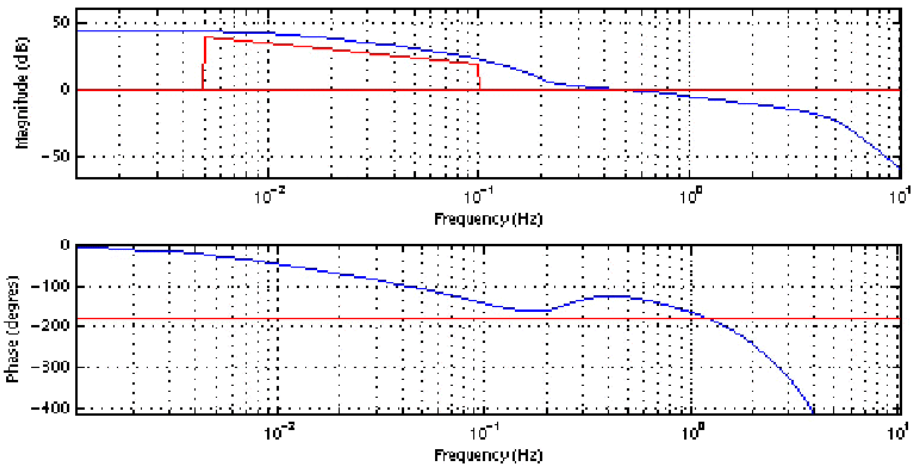

Figure 6.26. *Bode diagram of the X-DFC controller.*

Y-axis DFC controller design is easier because of reduced rejection requirements, the major design driver being the minimisation of the required control demand to the cold gas thrusters. The resulting design is a third-order bandpass controller active between 0.1 MHz and 0.1 Hz. The main impact is on cold-gas consumption, due to the large LF components of the perturbations. The mean gas flow rate is found to be around 0.46 mg/s, leading to a nitrogen budget of 24 kg for 20 months (no margins included).

The angular measurements provided by the star sensor are suitable for controlling the satellite within the 1.3 arcmin absolute pointing requirement, but are too noisy to drive the control of angular rates as demanded in Table 6.16. On the other hand, the gradiometer provides excellent measurements of angular rates, though it is not capable of any measurement of the absolute orientation in an inertial frame. The logical solution is to combine the two types of measurements in an attitude estimator. Angular-acceleration measurements are of such good quality that they can be used 'raw'.

The estimator chosen is a constant-gain Kalman filter, derived from the classical gyro-stellar scheme (the gradiometer replaces the gyros) with an hybridisation frequency of 1 MHz allowing to rely mainly on the accurate gradiometer reference. The control design is performed for the most demanding degree of freedom, rotation, i.e. about z-axis. The same controller is applied to x and y-axes, providing 'free-of-charge' improvement of the pointing performance for these axes. The controller is quite simple (second-order), with a proportional term with double-phase lead filter to ensure good phase margins. Figure 6.28 shows the open-loop z-axis attitude controller performance with respect to the rejection requirements. The design of this controller allows the sampling frequency to be established (1 Hz), the specifications on the cold-gas thruster noise and the star tracker to be defined, and the hybridisation frequency (1 MHz) to be specified.

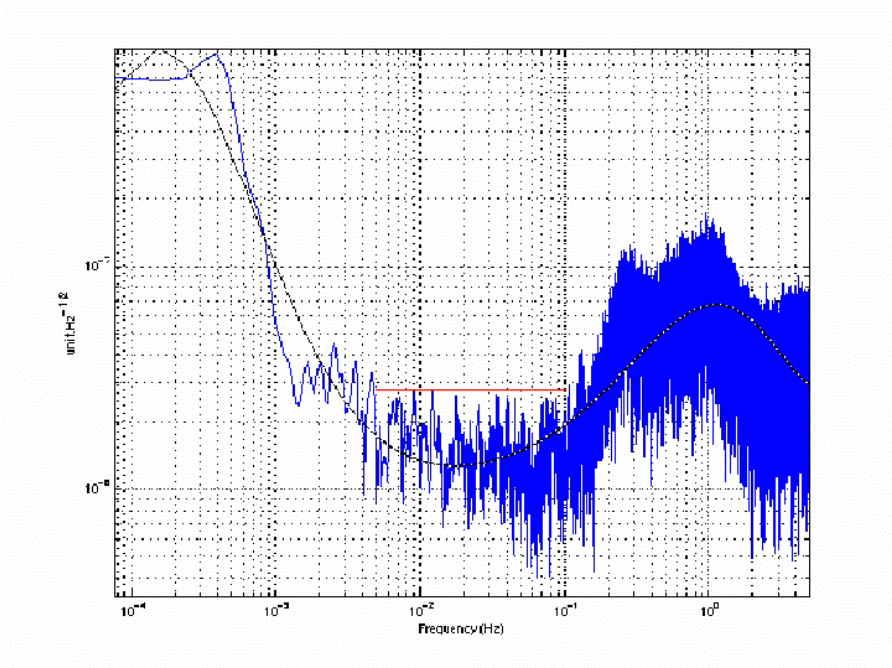

Figure 6.27*. Residual acceleration along x as a function of frequency (ms^{-2} $Hz^{-1/2}$). The requirement within the gradiometer measurement bandwidth can be seen as a flat line in red.*

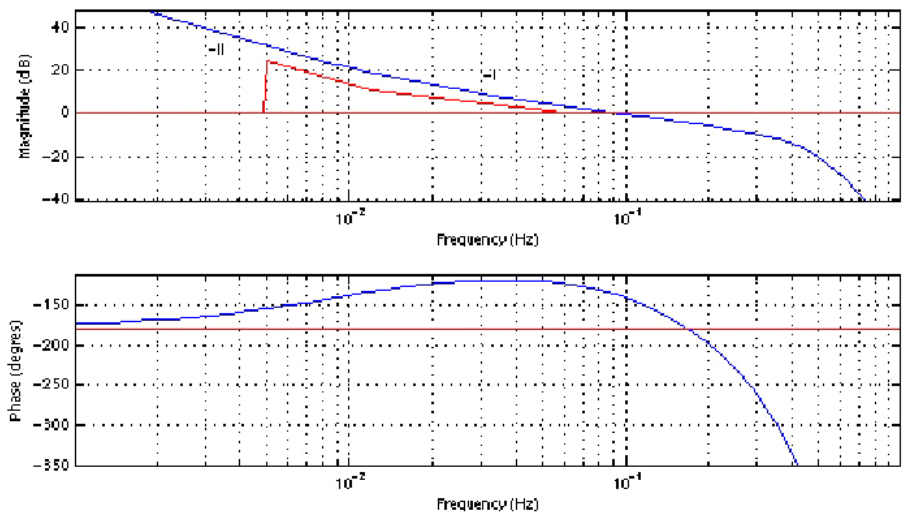

Figure 6.28. *Bode representation of open loop z-axis attitude controller performance. The amplitude rejection requirement is indicated in the upper diagram by the red slope.*

Figure 6.29 shows the performance of the closed-loop z-attitude controller. All requirements are fulfilled. Similar or better performance is obtained for the other axes. In the same way as for translation control, thruster noise is the main factor affecting

performance. The cold-gas thruster noise spectrum is therefore specified as 0.6μN $Hz^{1/2}$ above 25 MHz and 0.5 mN $Hz^{-1/2}$ below 5 MHz with $1/f^2$ slope in between.

An AOCS/DFC simulator, incorporating all the features of the design, has been developed to validate the performance, including coupling between axes. Figure 6.30 shows the block diagram of the global simulator.

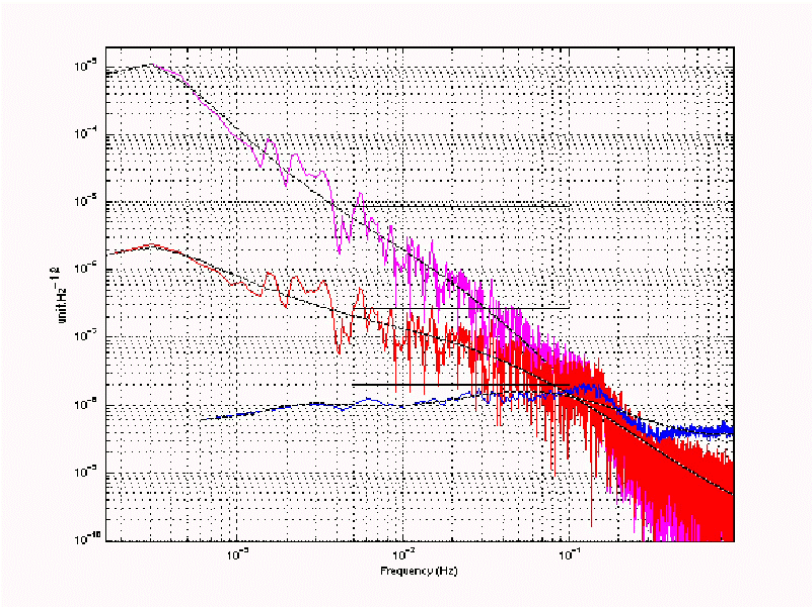

Figure 6.29. *Residual attitude (rad $Hz^{-1/2}$), velocity (rad s^{-1} $Hz^{-1/2}$), and acceleration (rad s^{-2} $Hz^{-1/2}$), on the z-axis. The specified values within the gradiometer measurement bandwidth are indicated by black horizontal lines.*

AOCS / DFC Modes, Architecture and Budgets

Figure 6.31 shows the AOCS/DFC modes and mode transitions. The acquisition sequence starts with the coarse attitude acquisition mode (CAAM). This mode is designed to damp the angular motions and stabilise the satellite with coarse Sun pointing. The CAAM exploits the fact that the satellite is to some extent passively stabilised by the aerodynamic restoring torque. The actuators are the cold-gas thrusters, supplemented by magnetic torquers to shorten the acquisition time. As soon as the rates have stabilised below a threshold, the fine attitude acquisition mode (FAAM) is initiated, to acquire the nominal pointing accuracy by means of the star sensor. After fine attitude acquisition, the ion thrusters are switched on at constant thrust to perform the orbit maintenance. Then the gradiometer data are acquired, and the drag-free initialisation and gradiometer calibration are performed according to the steps described in section 6.3.2 (calibration mode). The normal mode is dedicated to science data collection. An intermediate step, the eclipse and reconfiguration mode, is

entered during the long eclipse, where relaxed attitude requirements apply, and when anomalies are detected (autonomous failure analysis and switching to redundant equipment). The attitude safe mode will be a last resort, only entered on detection of major anomalies (processor failure, large pointing errors). It relies on dedicated sensors (magnetometer, Sun sensor), actuators (redundant cold-gas thruster branch and magnetic torquers) and processor (part of the ADE, Attitude Drive Electronics). It is a very robust mode, designed to maintain the Earth-pointing attitude (same as normal mode) with 10° accuracy. It relies also on aerodynamic stiffness for the yaw axis, but active pitch and roll control will be provided. It is independent of the ion propulsion, which is initially switched off to ensure robust convergence, and then re-instated, either automatically after 24 hours, or by ground command. Exit from the safe mode is via the CAAM, after which the whole initialisation sequence has to be re-run.

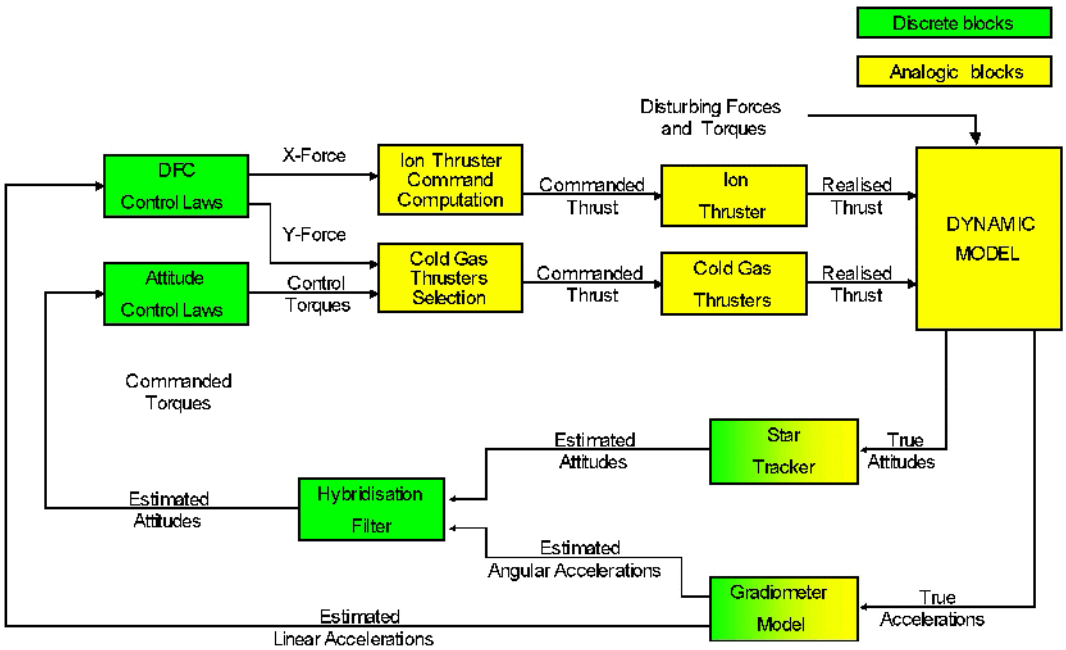

Figure 6.30. *AOCS/DFC simulator block diagram.*

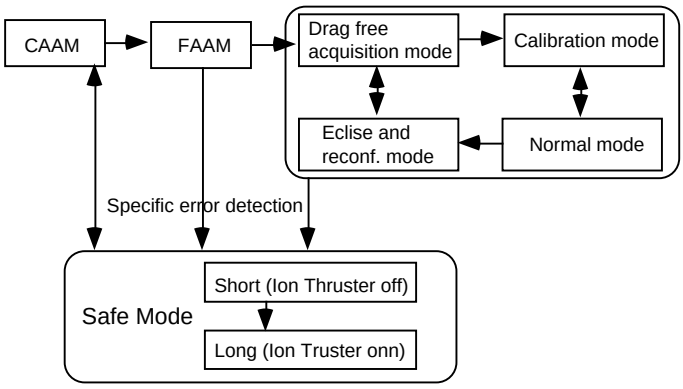

Figure 6.31. *AOCS/DCF modes.*

Table 6.17 and Figure 6.32 summarise the AOCS/DFC components and their use in the various modes.

Sensors Acquisition and safe mode measurement phase	coarse analogue Sun sensor (1 + 1) 3-axis magnetometer (1 + 1) star sensor (1 + 1) gradiometer + GPS/GLONASS receiver
Actuators Acquisition and safe mode measurement phase	3 magnetic torquers + cold-gas thrusters (4+4 pods) 16 + 16 micro-thrusters (attitude control) 1+ 1 ion thrusters (drag control)
Software	Magnetic-field model Star catalogue (Mv $\leq$ 6.5) Orbital navigator (Kepler+J2)

Table 6.17. *Sensor acting in the different modes.*

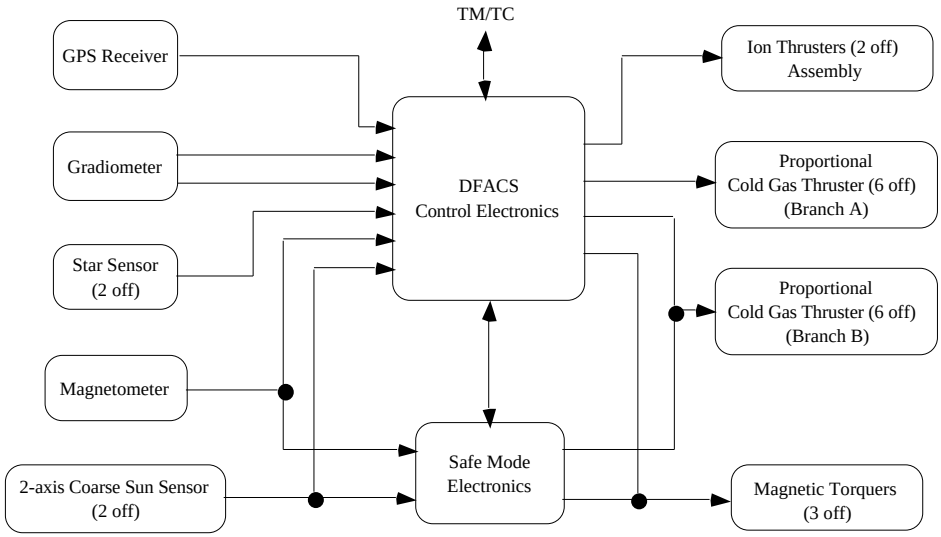

Figure 6.32. *AOCS/DFC subsystem block diagram.*

6.4.9 Ion Propulsion

The ion propulsion must provide continuous thrust to counteract the air drag force in a wide frequency band from DC (orbit maintenance) to low frequency (orbit frequency and its harmonics) to high frequency (up to 0.1 Hz). It must meet stringent accuracy requirements and provide a lifetime compatible with the mission. The requirements on the ion propulsion derive directly from the general requirements on the AOCS/DFC listed in Table 6.16. The derived performance requirements for the ion thrusters are summarised in Table 6.18.

Requirement	Value		Remarks
Drag control thrust range Orbit recovery thrust setting	1-12 20	mN mN	
Thrust variation Long-term (> 1000s) Short-term (0.1 s)	 ± 5 200	 mN μN	
Bandwidth	10	Hz	
Thrust vector direction Misalignment Stability	 ±0.5 0.5	 deg deg	 3σ 3σ
Thrust noise	5 mN $Hz^{-1/2}$, f < 2 MHz 50 μN $Hz^{-1/2}$, f > 0.2 Hz 1/f slope in between		PSD level
Thrust quantisation	18	μN	
Thrust scale factor uncertainty	<10	%	Closed-loop control
Hysteresis	<5	%	of full thrust

Table 6.18. *Ion- thruster requirements.*

The reference design is a radio-frequency ion-thruster assembly (RITA), a schematic of which can be seen in Figure 6.33. It consists of a quartz discharge chamber around which an RF field coil is wrapped, which induces the internal ionising electric field. Separate xenon propellant flows feed the discharge chamber and a hollow-cathode neutraliser. A positive voltage on the screen grid attracts electrons into the discharge chamber from the neutraliser plasma, to initiate the discharge. A flat triple-grid system is used to extract the ion beam, with the thruster grid at +1200V, the acceleration grid at -500 V, and a grounded deceleration grid. To minimise erosion, the acceleration grid is made from graphite.

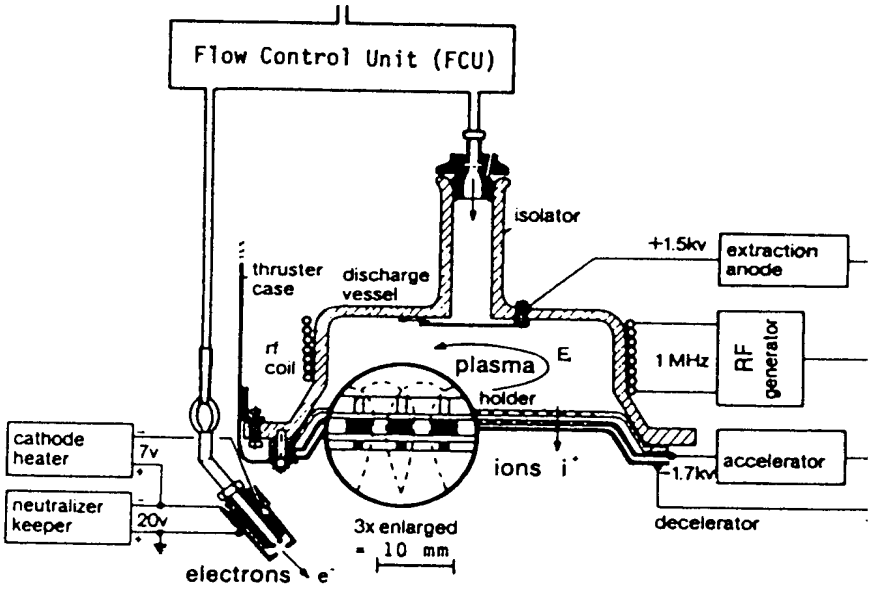

Figure 6.33. *Ion thruster cross-section.*

The thruster has been exhaustively characterised (with encouraging results) and has undergone all space-qualification tests. Currently it is undergoing a 15 000 hour life test. It has flown on Eureca and will soon fly on Artemis, in fixed-point operation at 15 mN. It has been demonstrated by test performed under GOCE, that the thruster can be throttled widely and quickly by varying the discharge power only. Test results can be seen in Figure 6.34. The measured reaction speed fulfils the AOCS/DFC requirements. The matching of the high-amplitude but low-speed variations in atmospheric drag (see Figure 6.5) is better counteracted by adaptation of the xenon mass flow. This double control approach allows a perfect and continuous matching of the drag forces and optimises mass flow. The ion thruster is shown in its test chamber setp-up in Figure 6.35.

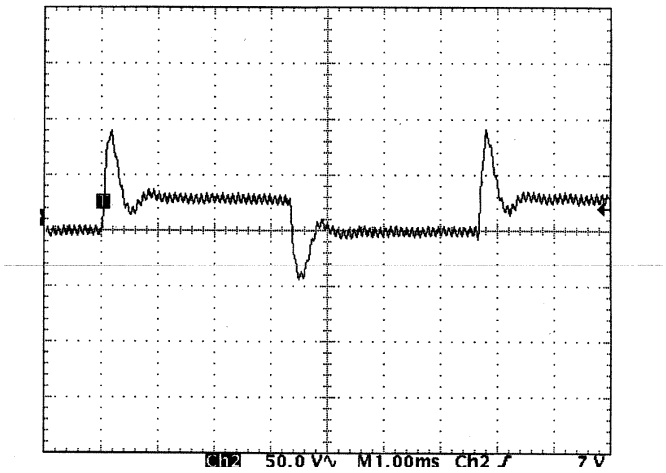

Figure 6.34. *Quick step thrust change command. The vertical divisions are 50 V and the horizontal 1 ms.*

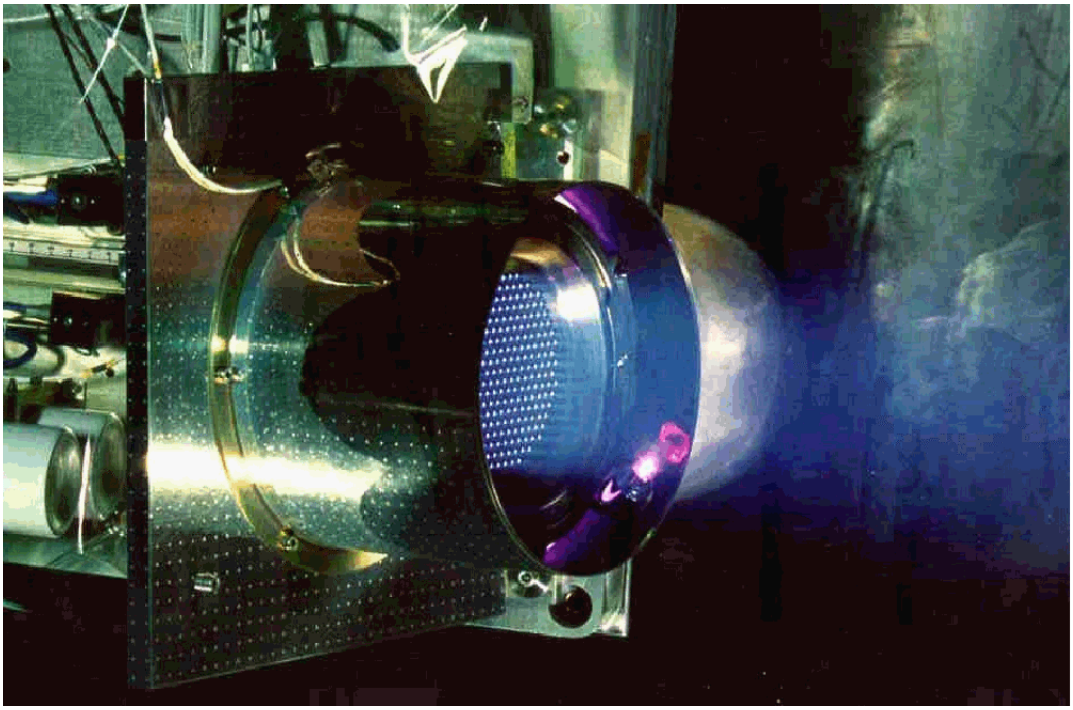

Figure 6.35. *Ion thruster on its test bench.*

The configuration of the ion thrusters on GOCE is driven by the orbit maintenance needs and by fault tolerance. The preferred solution uses two thrusters on the -x side, canted by about 2° such that their lines of action converge at the position of the estimated centre of mass. In the nominal operation, one thruster is active and the other in cold redundancy. This configuration is preferred for electrical efficiency, although a small lateral torque is generated, which is balanced by the attitude thrusters. Figure 6.36 shows the propulsion block diagram.

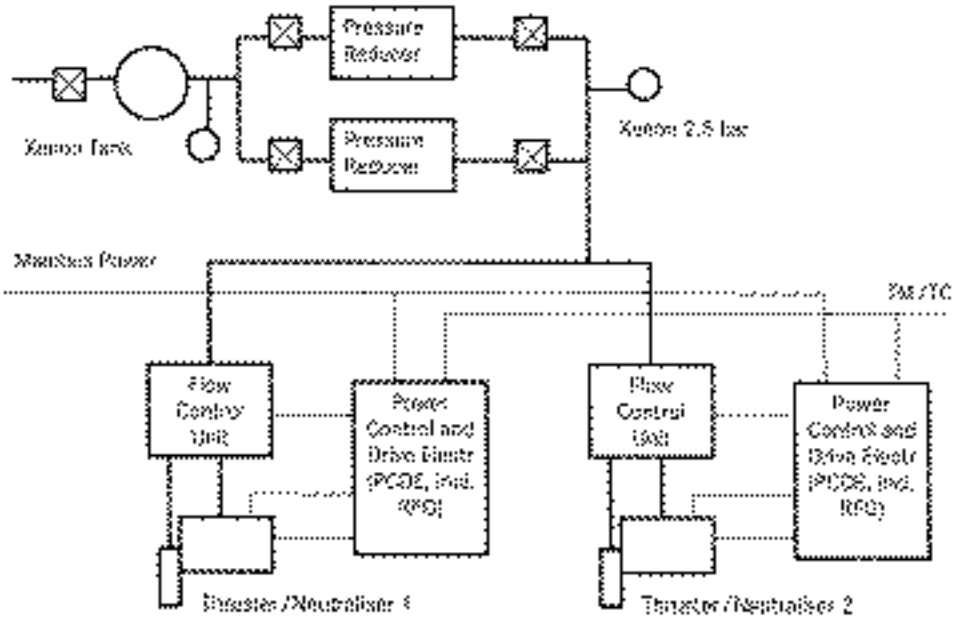

Figure 6.36. *Ion-propulsion block diagram.*

The ion thruster has the largest power demand on board the satellite. The total power increases with the thrust demanded. In the drag control range, it goes from 100 W for 1 mN to 500 W for 12 mN. The 20 mN required for orbit reboost require 625 W. The mass budget of the electric propulsion elements is given in Table 6.19.

Equipment Item	Unit Mass (kg)	No. of Units	Total Mass (kg)
Thruster and Neutraliser	1.8	2	3.6
Thruster Mounting Bracket	1.0	1	1.0
Power Control and Drive Electr. incl. RFG	9.8	2	19.6
Flow Control Unit incl. Oxygen Absorber	2.0	2	4.0
Pressure Reducer and Valves	0.6	2	1.2
Fill and Vent Valves	0.8	1	0.8
Harness	1.0	1	1.0
Piping	0.5	1	0.5
Xenon Tank (20% of propellant mass)	4.4	1	4.4
Total Electric Propulsion			**36.1**

Table 6.19. *Electric-propulsion mass budget.*

6.4.10 Proportional Cold-Gas Propulsion

To match the performance of the gradiometer, the GOCE attitude control requires smooth, low noise, low thrust actuators with a high bandwidth. These actuators will be used not only for attitude and drag control, but also for calibration (section 6.3.2). Table 6.20 provides the consolidated requirements.

Requirement	Value		Remarks
Thrust Range	0.15-700	μN	12-bit A/D conversion @300 K
Bandwidth	10	Hz	
Thrust Vector Direction			
Misalignment	±0.5	deg	1σ
Stability	1	deg	1σ
Thrust Noise PSD			
> 25 MHz	0.6	μN $Hz^{-1/2}$	3σ
< 5 MHz	0.5	mN $Hz^{-1/2}$	

Table 6.20. *Requirements on the cold gas proportional micro-thrusters.*

The proposed implementation uses the micro-machined cold-gas thruster technology under development under ESTEC contract. These devices feature a totally integrated design with four thrusters integrated onto three silicon wafers (with three-dimensional micro-machining methods) and a fourth wafer, with the control electronics, also bonded to the gas-handling wafer stack. To generate very small thrust levels, the dimensions need to be quite small. The nozzle throat diameter is on the order of 10 μm and the internal channels or pipes have a diameter of 100 μm. A laser-activated chemically-etched conical nozzle has been successfully micro-machined (see Fig. 6.37).

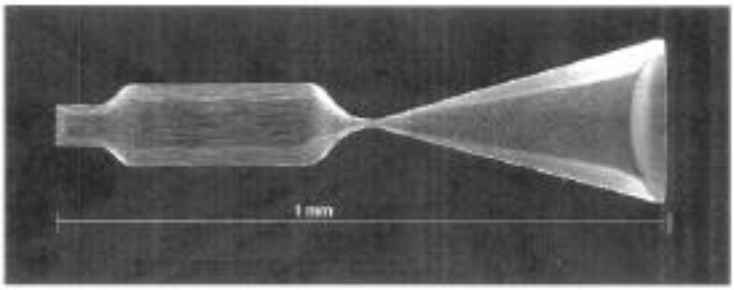

Figure 6.37. *Etched micro-thruster nozzle.*

In the proposed design, the thruster module is a 40 mm diameter disc and contains input filter, five valves, five differential pressure sensors, a plenum chamber, four nozzles with particle filters and heaters and the control-electronics wafer with interface circuits and four closed-loop circuits to control the thruster force. The ongoing development encompasses the development of critical components and theory verification on a number of prototypes. The complete development programme for the flight-standard version with integrated electronics is estimated to take three years, and is compatible with the GOCE development programme.

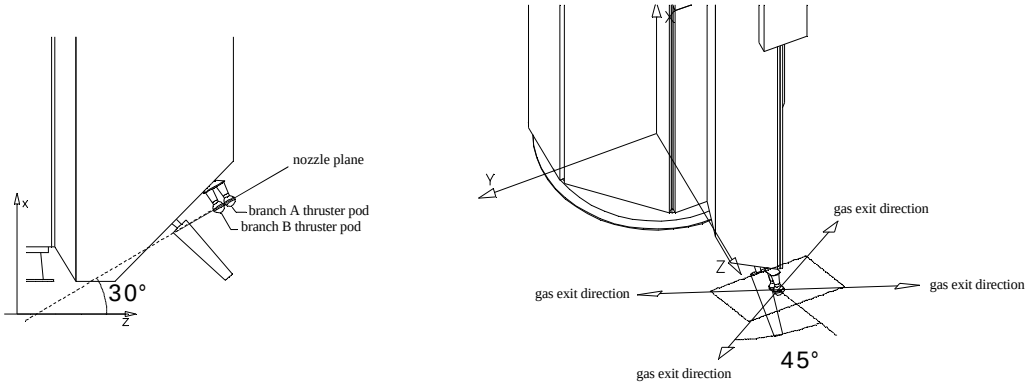

Figure 6.38. *Micro-thruster accommodation.*

The GOCE application will use two redundant branches of four pods each. The pods (each with four nozzles) are placed at the edges of the solar panels, 90° apart in two planes (Fig. 6.38). The propellant gas is nitrogen with a specific impulse of 60 s at 300 K. The gas will be stored at 400 bar and the pressure will be reduced to 4 bar by pressure regulators. The flow rate will be regulated according to the needs, with maximum rates of 0.5 mg/s during normal operation and 2 mg/s during calibration, giving a maximum control authority of, respectively, 0.35 mN and 1.4 mN. The block diagram can be seen in Figure 6.39.

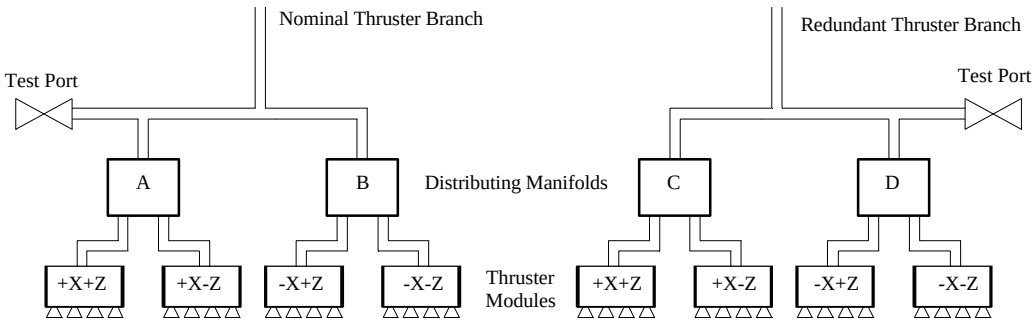

Figure 6.39. *Micro-thruster system block diagram.*

6.4.11 Failure Tolerance of On-Board System and Mission Products

Tolerance to single failures leading to loss of system performances critical to mission success is one of the most demanding GOCE objectives. In particular, the spacecraft and instruments are required to implement a single Failure Tolerance (1FT) design policy against total loss of mission critical functions, while a 0FT approach is acceptable against performance degradation.

The majority of the system functions are mission-critical. The current design concept shows a failure-tolerance policy implementation fully compatible with the above-mentioned objective. This is achieved by duplication of equipment items and equipment parts, as well as functional redundancy or design-embedded provisions including:

- Internally redundant CDMU, MMU and RTU (DHS)
- Main and redundant transponders and RFDUs (RF)
- Main and redundant battery packages and PCDU internally redundant (EPS)
- The AOCS/DFC subsystem foresees duplication of star trackers and magnetometers, redundant Sun sensors (considering the anomaly detector as a functional backup). The driving electronics is internally redundant.
- The electrical propulsion is 1FT against loss of operations by two pressure reducers in parallel and two separate RF-ion thruster/neutraliser branches, working in cold redundancy. Inadvertent expulsion of propellant is prevented by at least two inhibits (valves) in series along each thruster path.
- The cold-gas propulsion is 1FT oriented by two latch valves in parallel downstream the tank, main and redundant thruster branches (4 pods each) with independent pressure regulation. The current number of thruster pods can be optimised by appropriate coupling with magneto-torquers. Inadvertent expulsion through thrusters during flight is prevented by two barriers in series.

– Main and redundant heater circuits are provided with a failure tolerance scheme consistent with the requirements.

Two single-point failures have currently been identified: the single Earth-pointed antenna, whose calculated risk level is very low (2.0×10^{-4} failure probability over 20 months) and the pressure relief valve in the cold-gas propulsion, whose potential open failure (8.0×10^{-4} probability) would lead to loss of propellant. The risk level is sufficiently low to meet the system-availability objective (0.98 obtained by preliminary analysis versus 0.95 specified). This figure needs to be confirmed in detailed design, but the current assessment indicates that the system objective is achievable over 20 months.

Physical and/or functional redundancy is also provided in the gradiometer to ensure that the mission returns a significant science product even in the case of multiple failures including:

– loss of one axis in each of the six accelerometers making up the gravity gradiometer can be tolerated without impairment of the scientific performance
– the accelerometer configuration allows measurement redundancy in the case of loss of one accelerometer out of six (full recovery for x and z-axes; recovery but loss of required accuracy for y-axis, which is still acceptable for AOCS/DFC)
– each accelerometer pair is acquired by dedicated electronics and complete loss of one gradiometric arm is tolerated by the intrinsic redundancy of the measurement scheme (the trace of the gravity gradient tensor must equal zero)
– the gradiometer electronic unit (common to three axes) is internally redundant.

The FT policy implementation for the GPS/GLONASS receiver is currently open (pending subcontractor selection). A 1FT policy can be achieved by measurements redundancy, electronic unit duplication or internal redundancy.

Additional levels of protection are provided by the short-term safe mode (without electrical propulsion, activated by anomaly detectors when large depointing or a main failure occur), and by long-term safe mode (with electrical propulsion, automatically activated after a predefined period in short-term safe mode).

None of the on-board systems seems currently to have intrinsic time limitations, while the consumables are designed with 50% margins.

6.5 The Launcher

The requirements call for a low-cost launch vehicle able to inject up to 1000 kg into very low, circular, Sun-synchronous orbit. Furthermore, because of the low control authority of the on-board actuators, highly accurate injection and low attitude rates at

separation are sought. A number of ‘small’ launch vehicles are available or in an advanced stage of development. Table 6.21 shows a comparison of the launcher characteristics, based on the information available to date. The ability to launch into near-polar orbit is strongly constrained by the range of launch azimuth available to each vehicle at the respective launch site.

Launch Vehicle	Performance SSO @270 km	Fairing		P/L I/F	Quasi -Static Loads		Min. Dynamic Requirements		C.O.G. Max. Height
		φ [mm]	h [mm]	φ [mm]	Lateral [g's]	Axial [g's]	Lateral [Hz]	Axial [Hz]	[mm]
Rockot	1000	2420	5925	937	±0.8	8.1	15	33	>4000
Cosmos	975 TBC	2200	4728	1060	±1.6	6.8	10	25	1400
Long March CZ-2C	1600	3070	5000	937	±1.2	5.8	10	26	TBD
Athena 2	1300	1984	3639	944	±2.5	8.0	12	30	TBD
Taurus 92” XL	1025	2051	5738	944	±3.0	8.5	20	35	700

Table 6.21. *Launchers characteristics.*

The design parameters for GOCE, to be compared with the data in the above table, are a 2400 mm diameter, 4000 mm height, and 800 kg launch mass. On that basis, the fairings of Taurus, Athena and Cosmos are too small. For Cosmos, moreover, the ability to launch into very low altitude Sun-synchronous orbit (SSO) is not confirmed. This appears to restrict the choice to Long March or Rockot. The latter was taken as the reference launcher for the purposes of the Phase-A study. The datum on payload performance for the GOCE Sun-synchronous orbit (from Plesetsk, at 345° launch azimuth), shown in Table 6.21 is to be confirmed after mission analysis by the launch provider.

The Rockot Users’ Guide provides the following information:

- Launch site: Plesetsk, Russia (62.7°N, 40.3°E)
- Launch azimuth: 345°
- Mass into orbit (270 km, 96.8˚): 1000 kg
- Duration of ascent phase: 4000 s (stage 1 + stage 2 + upper-stage boost)
- Circular orbit altitude error: < ± 2% (3σ)
- Inclination error: < 0.05° (3σ).

Rockot can provide both spin and three-axis stabilised satellite release, in any pre-defined orientation. For three-axis stabilised release, the typical performance after separation is as follows:

- angular rate about longitudinal axis: < 1 °/s
- transverse angular rates: < 0.5 °/s.

The above residual rates have been taken into account in the design of the GOCE AOCS.

6.6 The Ground Segment

Chapter 7 provides a detailed description of the steps needed to transform the satellite output into mission products. This section provides a description of the ground facilities needed to do that.

The GOCE ground segment (Fig. 6.40) is composed of three main elements: the command and data acquisition element (CDAE), the mission and satellite control element (MSCE) and the processing and archiving element (PAE).

Command and Data Acquisition Element

The CDAE handles all direct interactions between the ground and the satellite, under the control of the MSCE. It is responsible for telemetry reception, checking and temporary storage, satellite health status monitoring, and telecommand validation and uplinking. The CDAE comprises the ground antenna with acquisition and tracking modules, facilities for data storage and pre-processing, and operations and data distribution interfaces.

The CDAE selected for GOCE is the Kiruna S-band ground station. It is optimally located for a near-polar orbit, it has good operational maturity (ERS, Envisat), sufficient telemetry-rate capability at S-band (1.2 Mbps by 2004), sophisticated antenna-pointing devices with scanning capabilities, high-performance-link quality control and range/range-rate tracking systems, and an on-line communications link with ESOC. The launch window selected ensures that all ground contacts occur in the daytime. The nominal operations schedule uses four ground passes per day (out of six available), three of them in the morning, at a maximum telemetry rate of 850 kbps.

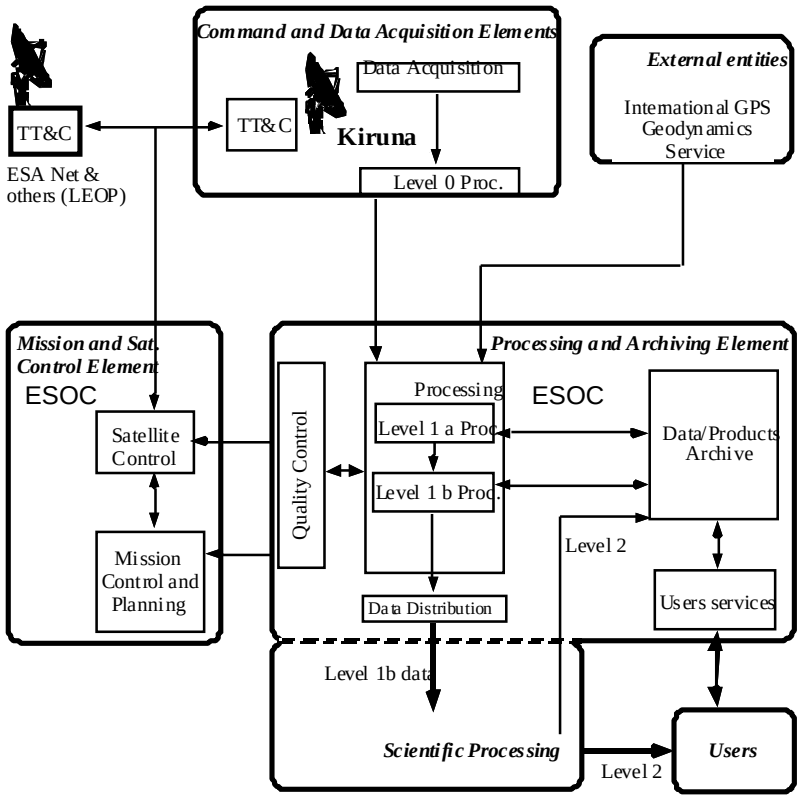

Figure 6.40. *Ground control architecture (data-level definition in section 7.1).*

The fourth, afternoon pass is the one used, when needed, for telecommanding. This is a simple and robust strategy that ensures that the on board memory is completely empty after the morning passes, and leaves two complete passes available for contingencies. The whole operations sequence can be run on a schedule provided by the MSCE one day in advance, and implementing all information of the orbital dynamics elaborated at the MSCE. The possibility of on-line direct remote control from the MSCE also exists.

The CDAE provides immediate storage of the received telemetry stream and near real-time pre-processing to prepare the telemetry data for further use. Given the very limited data rate produced by GOCE (6 kbps), a storage capacity of 4 Gb is sufficient for one-week of data, providing wide margins for any contingency.

The Level 0 products are sent to the MSCE for satellite-monitoring and flight-dynamics support, and to the PAE for gradiometer and SST-hl receiver data processing. Transmission to the MSCE for operational purposes occurs via the electronic link on a near real-time basis. Transmission to the PAE can occur on a more relaxed schedule, for example by using the file transfer protocol (FTP) service during the night hours.

Mission and Satellite Control Element

The mission and satellite control element (MSCE) at ESOC is responsible for the management, monitoring and control of all operations, on the ground as well as on the satellite. It creates the operations plan, manages and co-ordinates the operations, and manages, monitors and controls the satellite and the payload instruments. Moreover, the MSCE provides data quality assessment, control of the instrument behaviour, and generates auxiliary data for use by the PAE together with the scientific data. It has operational and data interfaces with the CDAE and PAE, and links with the ESA ground station network for early-orbit and contingency-phases support.

In addition to ESOC's great experience in mission and satellite control, the entire infrastructure for communications and control via the Kiruna station is already in place. For operations planning, satellite management and ground-segment monitoring, use of the SCOS2000 system, developed for Envisat, is considered. This system also provides the capabilities for on-line management of the Kiruna station. For flight-dynamics support, the ORATOS system will be used, also provided with a direct interface with SCOS2000. A GOCE dynamics and control software simulator, derived from that developed for the end-to-end simulations (see section 8.1) will also be installed at ESOC, for instrument and control systems health checking, operational procedure validation, and troubleshooting.

During the launch and early-operations phase (LEOP), round-the-clock service will be provided (and supplementary ESA ground stations will be available as needed). The 24 hours per day service will be also provided during the first three months of the mission dedicated to commissioning and payload calibration. For the rest of the mission, a single shift of 8 hours a day will be provided, with engineering support on-call.

The normal satellite operations will consist of a regular routine of measurements by the on-board instruments, supported by operation of the attitude and drag-free control. No attitude or orbit manoeuvres are needed, and neither are changes to the operational status of the instruments. Therefore, mission planning will basically be limited to the selection and scheduling of ground passes for telemetry and telecommand, satellite and instrument health checks, and data transmission, processing and delivery.

Different procedures will apply during the instrument set-up and calibration phases, and in case of contingencies. The iterative calibration procedures will be autonomous, based on dedicated operations schedules which will be validated prior to uplinking by means of the spacecraft software simulator. Severe contingencies will require quick reaction times, because of the very low operational altitude of the satellite. The most critical problem would be an orbit-control failure during the blind orbits. Knowledge of such a failure may be available up to 12 hours after the event, during which the orbit will have evolved differently from the predictions, and the visibility periods will

have shifted away from the nominal pattern. Countermeasures for such cases are to be taken both at satellite level and at mission-control level. The first include robust control strategies and different levels of autonomous spacecraft safe modes, including autonomous spacecraft navigation based on GPS/GLONASS and on-board orbit propagation algorithms. On the ground-control side, contingency actions include increasing the frequency of satellite interrogation (by making use of all contact opportunities), search scans performed by the ground antenna, satellite-initiated ground contacts, and calling on support from other ESA network stations.

Processing and Archiving Elements

The PAE performs data collection, processing to Level 1, archiving and delivery to the scientific consortia responsible for the production of the Level 2 geophysical products. As part of the generation of Level 1b data products, precise orbit determination based on the payload data will be performed.

The PAE has data interfaces with the CDAE (to receive Level 0 data), and operational and data interfaces with the MSCE (for receiving operational status information and transmitting samples of Level 1 data for operational use). In addition, the PAE has interfaces with the scientific consortia (for delivery of Level 1 data and reception of Level 2 data for archiving) and with the IGS for reception of GPS/GLONASS station data. None of these links requires real-time action, and therefore transmission via normal commercial links is adequate.

Since Level 1 data processing is closely related with the flight dynamics and operational activities, co-location of the PAE with the MSCE at ESOC appears to be an efficient solution. ESOC already possesses an IGS data-retrieval system and the small volume of data (400 Gbit accumulated over the whole mission) means that archiving is not a design driver.

The ultimate scientific output of GOCE is a map of the gravity anomalies and geoid, needing extensive data processing and analysis by specialists. This analysis will be performed by the scientific consortia and requires large data sets (encompassing at least two months of observations). Smaller data sets will be used on shorter time scales to check the consistency of the data (e.g. by comparing gravity gradients over areas where good-quality information already exists). Procedures for data validation for operational purposes will be prepared by the scientific consortia and implemented as standard routines to be run at the PAE on a daily basis.

6.7 Technical Concept Summary

Table 6.22 provides a general overview of the mission elements and the most important features of both the spacecraft subsystems and payload.

Mission and Orbit	
Orbit	250 km altitude, Sun-synchronous, dawn-dusk
Launch window	spring/autumn windows
Launcher	Rockot or similar (1000 kg payload in SSO)
Lifetime	20 months
Operation	Continuous data take in two eclipse-free cycles of 6 months each hibernation in long-eclipse season
Ground Contact	Cycles of 3 contacts spaced by 12 hours with Kiruna station
Payload	
Gravity Gradiometry	Three-axis diagonal gradiometer, based on three pairs of electrostatic servo-controlled accelerometers on 50 cm baselines (5 MHz ÷0.1 Hz)
Sat-to-Sat Tracking	Geodetic quality 12-channel GPS/GLONASS receiver and zenith antenna
Spacecraft	
Configuration	Minimum cross-section in the direction of motion (0.8 m^2) 7.3 m^2 solar array lying in the orbit plane 800 kg launch mass
Structure	Two structural compartments; load-carrying external structure structural dynamics: 110 Hz axial, 18 Hz lateral
Thermal Control	Passive with heaters High-thermal-stability gradiometer compartment (10 Mk @ 5 MHz)
Electrical Power	24-32Vdc unregulated bus; protected and redundant lines Fixed GaAs cell solar array,1kW EOL 270 Wh battery energy, 25 Ah cell capacity
Attitude Control	Nadir pointing Wide-field star trackers hybridised with gradiometer angular acceleration measurement Coarse Sun sensors and magnetometer for acquisition and safe mode Proportional nitrogen thrusters for actuators augmented with magnetic torque rods in acquisition and safe mode AOCS/DFC application software run in central computer
Drag Control	Ion thrusters commanded in closed loop, based on gradiometer common-mode acceleration measurements
RCS	20 mN RF-ion thrusters (2x) 1 mN nitrogen proportional micro-thrusters (2x4 pods)
Data Handling	Packet telemetry Flexible and reallocatable packet sizes High-rate (10 Hz) gradiometer-to-computer link via 1553 bus for drag control command synthesis
RF	S-band up- and down-link and ranging Two hemispherical antennas on solar array edges TC: 2 kbps TM: up to 850 kbps 1W RF power

Table 6.22. *Technical concept summary.*

7 Data Processing

The ground segment is described in Chapter 6, including consideration of data archiving and distribution approach. This chapter provides an overview of the different steps required to recover the gravity field information from the GOCE observations and to put this information in formats suitable for further scientific data processing and analysis.

7.1 Introduction

The gradiometer and the GPS/GLONASS navigation receiver will provide the main measurements for the gravity field recovery: the satellite gravity gradient (SGG) and satellite-to-satellite high-low (SST-hl) observations. Ancillary data will be provided by the attitude and orbit control system (AOCS) and the on-board calibration procedure.

The different levels of data products are:

Level 0: Consists of the time-ordered raw data as measured by GOCE. The satellite will downlink the data during contact with a dedicated ground station.

Level 1a: Consists of the instrument time series with the calibration data attached. It is realistic to expect that they will be available from several days to one-week after they are produced. This target will be a reasonable compromise between ease of implementation and the need for a relatively quick check on the quality of the output.

Level 1b: Consists of time series along the orbit, which can be divided into different data sets.

These latter Level 1b data sets include instrument data:

- Calibrated and corrected data on gravity gradients in three directions. They will be provided in Earth-fixed and local satellite reference frames.
- Calibrated and corrected SST-hl observations and GOCE satellite position in an Earth-fixed reference frame.

and other satellite data:

- Satellite linear and angular acceleration vectors
- Thrust history of the AOCS/DFC actuators
- Satellite attitude, angular velocities and centrifugal acceleration.

Note also that the calibrated gravity gradients along the orbit are an important geophysical data product.

Level 2:

- Global gravity potential modelled as harmonic coefficients
- Global ground-referenced gridded values of geoid heights (Earth geoid map)
- Global ground-referenced gridded values of gravity anomalies (Earth gravity map).

Supplementary outputs are:

- Quality assessment of gravity field products
- Regional gravity field models.

Level 3 data will be scientific value-added products that are derived for studies of solid-Earth physics, absolute ocean circulation, ice-sheet dynamics, geodesy and sea-level change. Examples of such products were extensively discussed in Chapter 3.

The overall procedure of data processing, i.e. from Level 0 to Level 2, is complicated and requires many steps (see Fig.7.1). The raw data will contain the readouts from the instruments, together with calibration, time, attitude and orbit control system (AOCS) and drag-free control (DFC) data and other housekeeping information such as temperatures. The data will be pre-processed and stored as Level 1a data on appropriate media. Calibration data will be included in the Level 1a data products. These will be used to derive the Level 1b data, which will consist of calibrated and corrected gravity gradients, linear accelerations, thruster activity parameters and attitude information. The attitude information will contain the history profiles of not only the attitude of the GOCE satellite itself, but also the angular velocities and accelerations. This, together with a first estimate of the GOCE orbit, will make it possible to refer the gravity gradients to an Earth-fixed reference frame.

Use will also be made of external data (e.g. accurately defined reference systems), a-priori reference models and the precise ephemerises of the GPS and GLONASS satellites. GPS and GLONASS information will be computed on a routine basis in the framework of the International GPS Service (IGS). Once processed, the Level 1a and 1b data will be further transformed and processed to a Level 2 product (i.e. the global gravity field model and its quality assessment). This Level 2 product will be used as starting point for further scientific analysis (Level 3). The mature algorithms and tools required to convert the data from Level 1 to 2 exploit the work of the CIGAR consortium (CIGAR, 1989, 1990, 1993, 1995, 1996).

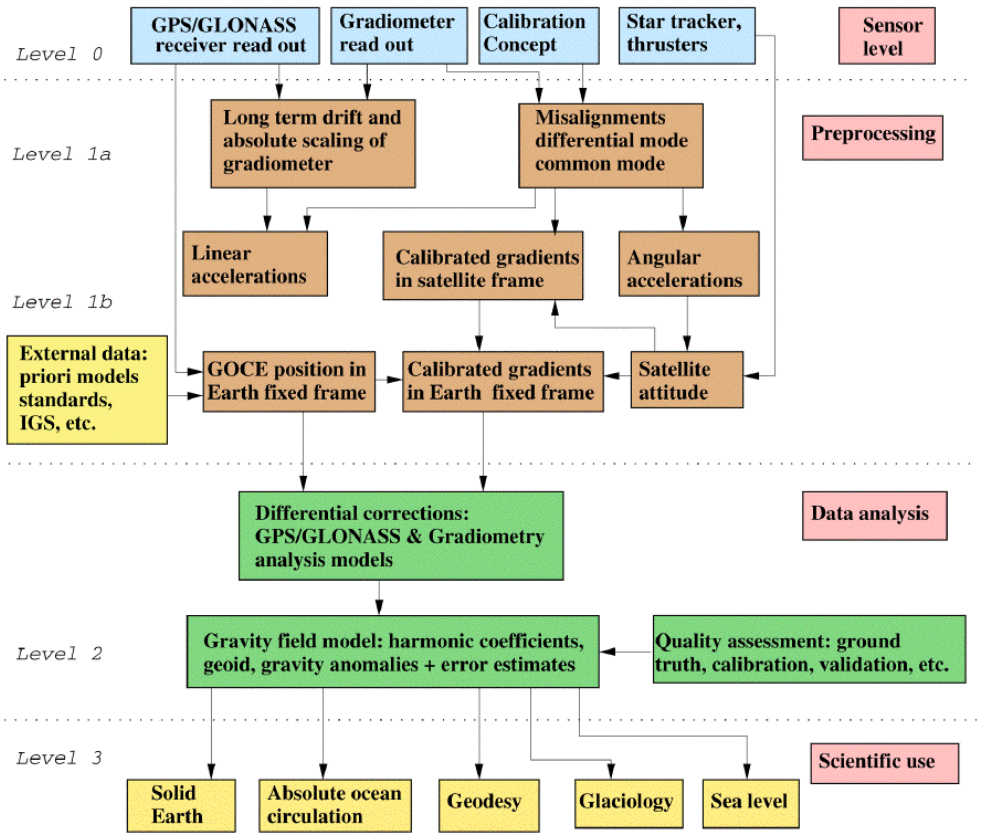

Figure 7.1. *Scheme for GOCE data reduction.*

7.2 Pre-processing (Level 0 and Level 1 Processing)

The raw payload data collected by the instruments on-board GOCE will be analysed and converted to observables in a proper format for data analysis in a well-defined reference system.

7.2.1 Gradiometry

The raw gradiometer data consist of output voltages as measured by the accelerometers (six three-axes accelerometers). A transfer function transforms these voltages to accelerations. For further processing, ancillary data are required, such as:

- in-orbit calibration parameters
- satellite attitude, angular velocities and accelerations
- linear accelerations.

Derivation of Observables

The gradiometer and its calibration have been described in section 6.3.2 and the configuration of the accelerometer axes is shown in Figure 6.10. To a good approximation, the following relation can be used to link a measurement by the *n*th accelerometer along one of its axes *i* with the real accelerations:

$$\gamma_{n,i} = (1+\varepsilon_i)a_i + \varepsilon_i^j a_j + \varepsilon_i^k a_k + \varepsilon_i^{jk} a_j a_k \qquad (7.2.1)$$

where a_i, a_j and a_k are the sum of all the accelerations projected on the *i*, *j* and *k* axes; ε_i is a scale factor error, e.g. due to an electronic or mechanical bias in the accelerometer; $\varepsilon_i^j, \varepsilon_i^k$ and ε_i^{jk} are the coupling terms between the *i*, *j* and the *k* axes, due to misalignment of the sensitive axis of the accelerometer and due to obliqueness of axes. The onboard calibration procedure will deliver the scale factors and coupling terms to be included in the Level 1a data. Application of these terms to the raw observations yields calibrated acceleration measurements. The general expression to extract the gravity gradient from the calibrated accelerations can be written as:

$$\gamma_i = {}^2V\ L_i + \dot{\omega} \times L_i + \omega \times (\omega \times L_i) + 2\omega \times \dot{L}_i + \gamma_c + \gamma_{sg} \qquad (7.2.2)$$

where γ_i represents the acceleration of the i-th accelerometer. The location of this accelerometer with respect to the satellite's centre of mass is denoted by the vector L_i, ω represents the angular velocity of the satellite, γ_c is the common non-conservative external acceleration, and γ_{sg} is the self-gravity component of the satellite. The local gravity gradient tensor is denoted by $\nabla^2 V$, where V is the gravity field potential. The well-known centrifugal and Coriolis terms can also be distinguished in this equation. Assuming that the norm L is constant and the same for all axes, the differential acceleration measurements can be expressed as:

$$\frac{1}{L}\begin{bmatrix} \gamma_{x2}-\gamma_{x1} & \gamma_{y2}-\gamma_{y1} & \gamma_{z2}-\gamma_{z1} \\ \gamma_{x4}-\gamma_{x3} & \gamma_{y4}-\gamma_{y3} & \gamma_{z4}-\gamma_{z3} \\ \gamma_{x6}-\gamma_{x5} & \gamma_{y6}-\gamma_{y5} & \gamma_{z6}-\gamma_{z5} \end{bmatrix} = \begin{pmatrix} V_{xx} & V_{xy} & V_{xz} \\ & V_{yy} & V_{yz} \\ sym & & V_{zz} \end{pmatrix} + \begin{pmatrix} 0 & \dot{\omega}_z & -\dot{\omega}_y \\ -\dot{\omega}_z & 0 & \dot{\omega}_x \\ \dot{\omega}_y & -\dot{\omega}_x & 0 \end{pmatrix} + \begin{pmatrix} -\omega_y^2-\omega_z^2 & \omega_x\omega_y & \omega_x\omega_z \\ & -\omega_y^2-\omega_z^2 & \omega_y\omega_z \\ sym & & -\omega_y^2-\omega_z^2 \end{pmatrix} \qquad (7.2.3)$$

where the subscript *x2*, for example, denotes the measurement in the *x*-direction of the second accelerometer (see Fig. 6.10).

The nominal frequency range of the accelerometers is from 0.005 to 0.1 Hz, referred to as the measurement bandwidth (indicated by the superscript '*w*'). Outside this bandwidth, the accelerometers still provide information, but with reduced sensitivity.

For a calibrated gradiometer with constant arms *L*, the equation above shows that the angular acceleration terms are anti-symmetric and can thus be separated from the gravity gradient tensor:

$$
\begin{aligned}
L\ \dot{\omega}_x^w &= (\gamma_{z4}^w - \gamma_{z3}^w) - (\gamma_{y6}^w - \gamma_{y5}^w) \\
L\ \dot{\omega}_y^w &= (\gamma_{x6}^w - \gamma_{x5}^w) - (\gamma_{z2}^w - \gamma_{z1}^w) \\
L\ \dot{\omega}_z^w &= (\gamma_{y2}^w - \gamma_{y1}^w) - (\gamma_{x4}^w - \gamma_{x3}^w)
\end{aligned}
\qquad (7.2.4)
$$

The centrifugal accelerations and the gravity-gradient tensor are both symmetric and cannot be separated. The satellite is Earth-pointing, and so the centrifugal accelerations around the y-axis (perpendicular to the orbit) will be much larger than the terms around the x and z-axes. The dominant centrifugal term around the y-axis can be recovered to very high accuracy by integrating the angular accelerations in combination with star-sensor data (Aguirre-Martinez, 1999). The gradiometer instrument will also provide observations of the linear accelerations that act on the satellite.

These observations are a measure of the residual non-gravitational accelerations, which will be kept small by the drag-free control (DFC) described in section 6.4.8. By observing these accelerations, non-gravitational accelerations can be separated from gravitational accelerations in the processing of the SST data. The accuracy of the recovery of the linear accelerations is limited by the accuracy of the coarse axis of the accelerometers, but is sufficient to meet the requirements.

Transformation to Earth-fixed Reference Frame and Time-Tagging

After calibration and elimination of the centrifugal terms, the gravity gradients that are measured in a local satellite frame will be transferred to gravity gradients in an Earth-fixed reference frame. To this end, use will be made of the measured and derived satellite attitude angles φ, θ, and ψ. To keep the error of this transformation small, it is not only necessary to measure the actual pointing, but also to control it. The position of the satellite in the Earth-fixed reference frame can be determined using the SST data. The time-tagging information can also be provided by the GPS/GLONASS receiver.

7.2.2 Satellite-to-Satellite Tracking (high-low)

The GPS/GLONASS receiver will provide coarse acquisition (C/A) code (pseudo-range) observations and carrier phase observations of the GPS and GLONASS signals

at the L1 and L2 frequencies from GOCE. For GPS, the measurement noise of the C/A code observations will be 25 cm at a data rate of 1 Hz. The accuracy for the L1 carrier phase measurements will be better than 0.4 mm at this data rate. In fact, the second phase measurement is differential, i.e. L2-L1 code-less measurement with an accuracy of better than 2 mm. Concerning GLONASS, both carrier and code measurements can be taken in two bands L1' and L2'. The measurement noise for the code measurements will be 50 cm and for the carrier phase measurements 0.4 mm, both at a sampling rate of 1 Hz. All performance figures can be tested with a high degree of confidence on the ground using simulated signals before launch.

Much experience has already been built up using GPS observations for orbit determination. The objective of the pre-processing is to obtain fully corrected SST-hl observations and to compute the GOCE orbit on an operational basis. Corrections that are applied to the SST observations include those required to account for ionospheric propagation. The tropospheric correction can be obtained by making use of observations at the two frequencies L1 and L2.

The operational orbit is required for orbit maintenance and a first checkout of the SGG observations. An orbit accuracy of a few decimetres is acceptable. For this accuracy, it is not necessary to fix the so-called cycle ambiguities of the phase measurements, which are in principle measurements of the change in distance between GOCE and the GPS/GLONASS satellites and not measurements of the absolute distance. High-quality orbits of the GPS and GLONASS satellites are made available by the IGS in addition to precise information on ground station co-ordinates and the GPS/GLONASS observations made from them. These external data can be used to obtain a fast orbit GOCE solution in combination with the SST observations. An accuracy of a few decimetres is easily achievable with current processing and analysis tools. For the final data analysis, the accuracy requirements for the orbit determination are more stringent and a level of a few centimetres is required (section 7.3). This has been demonstrated sufficiently by existing satellites carrying a GPS receiver, especially the TOPEX/Poseidon mission (Bertiger et al., 1994; Perosanz et al, 1997).

A laser retro-reflector is included in the baseline design of GOCE as a back up to GPS/GLONASS tracking (Tapley et al., 1993; Noomen et al., 1993; Degnan, 1985). This will enable satellite laser ranging (SLR) of GOCE by a worldwide network of ground stations. SLR stations are irregularly distributed over the Earth, and because of the very low altitude of GOCE, the observational coverage will be limited to a few minutes above each station. However, it is expected that acceptable operational GOCE orbits in the metre-class can be computed based on SLR observations.

The Level 1b data, including calibrated and corrected gravity gradients in three directions and SST-hl observations and GOCE satellite position in an Earth-fixed reference frame, form the basis for the derivation of the Level 2 products.

7.3 Level 2 Processing

The three main Level 2 products include global gravity potential modelled as harmonic coefficients, global ground-referenced gridded values of geoid heights (map of geoid), and global ground-referenced gridded values of gravity anomalies (gravity map).

The number of unknown gravity parameters (harmonic coefficients) is proportional to the square of the maximum degree L of spherical harmonic expansion (see Chapter 2). A field with a half-wavelength or resolution of 80 km requires the estimation of all parameters up to degree and order 250 or $250^2 = 62\ 500$ unknowns. Gravitational field observations (orbit and gravity gradiometer data) are required to estimate these parameters. In order to assess (and to considerably improve) the quality of the estimated parameters (and also to assess the quality of the original observations), it is customary that the number of observations significantly exceeds the number of estimated parameters.

Each observation has to be linked to the gravity parameters and thus gives rise to one observation equation. A typical figure for the number of observations that the GOCE mission will produce is 60 million. For the estimation of 62 500 parameters this would result in a linear system of 60 million equations with 62 500 unknowns. It goes without saying that the solution of such an enormously large and full system of equations requires the use of both the most powerful, optimally tuned and tailored solution techniques and computer systems, including vector- and parallel-processing units. It is a major challenge not just because of the size of the problem, but also because of the need to take realistic coloured measurement noise into account and because of sophisticated solution stabilisation requirements. It is a computationally demanding task, but a possible one with existing (parallel) computer hardware and software technology.

The first step in the data analysis of both the SGG and SST observations is the computation of a precise orbit. This will result in precise knowledge of the GOCE satellite position. An orbit-recovery accuracy at the centimetre level seems feasible and has been demonstrated by the TOPEX/Poseidon mission (Tapley et al., 1994). The expected performance of the GPS/GLONASS receiver on board GOCE will be significantly better than the TOPEX/Poseidon GPS receiver. The satellite position enters both the SGG and orbit observation equations. A linear relation can be derived linking the SGG observations to the gravity parameters by knowing the position of the satellite. In addition, the history of satellite's positions is also a function of the gravity parameters. However, the observation equations for the orbit are non-linear and so an iterative procedure will be applied with successive linearisations. In this procedure, a-priori models have to be used to ensure the convergence to the correct solution. An overall scheme of the steps needed for the derivation of the unknown gravity parameters is displayed in Figure 7.2.

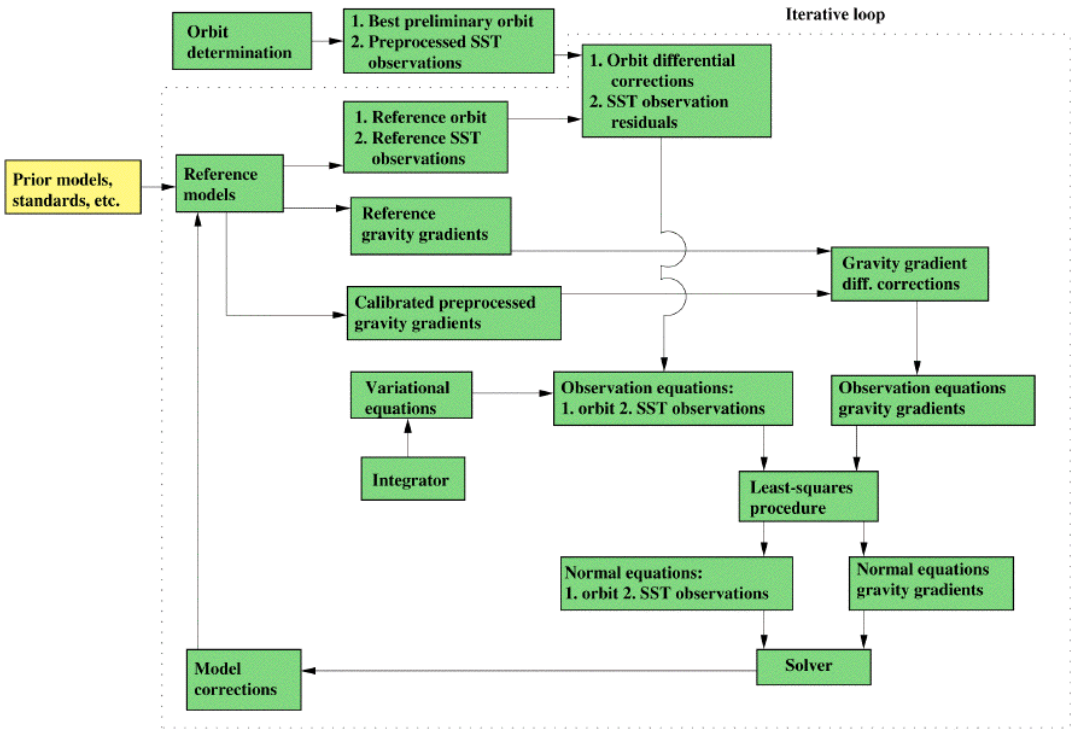

Figure 7.2. *Overall scheme of the data analysis procedure*

The a-priori models define a reference (or baseline) for the computation of reference orbit and gravity gradients as shown in Table 7.1.

Dynamic models	Elements of the Reference system and time variations	Measurement corrections	IGS
A-priori gravity field model Solid-Earth tides Ocean tides Third bodies (Moon, planets) Relativistic effects	ITRF ICRF Precession Nutation Earth rotating parameters Pole tide Ocean loading Tectonic motion	GOCE centre of masses Atmospheric models	GPS/GLONASS ephemeris Station co-ordinates Ground stations GPS/GLONASS observations

Table 7.1. *Overview of models and reference systems needed to compute the reference orbit.*

These a-priori models will be subtracted from the precise orbit or SST-hl observations and pre-processed calibrated gravity gradients to obtain orbit and gravity-gradient differential corrections. These corrections contain the high-accuracy and high-resolution gravity field information that will be added to the reference gravity field model. The orbit differential corrections are linked to the gravity parameters by numerically integrating the so-called variational equations around the reference orbit defined by the reference models, forming the observation equations for the orbit. Aliasing of non-gravitational forces is prevented by including the linear accelerations (as measured by the gradiometer) in the reference model. Linear relations can be used to compute the observation equations for the gravity gradients. Different approaches can be used to set up and solve the observation equations. For example, the SGG observations can be considered as a series in time ('time-wise') or as observations at a certain location ('space-wise'), leading to different methods for setting up the observation equations for the gravity unknowns. Separate solutions can be derived from SGG or SST-hl observations, or combined solutions can be derived. In addition, global and/or regional gravity field recovery methods have been developed. As an example, in Figure 7.2, a least-squares procedure was selected to derive the normal equations that will be solved to obtain the unknown gravity parameters. With these corrections, new reference models can be derived and the above procedure can be repeated until convergence.

Certain methods suffer from instability because of the non-polar orbit of GOCE. The inclination of the GOCE orbit will be about 97°, leading to small areas over the poles that will not be covered – less than 1% of the total Earth's surface. Using the representation form introduced in Chapter 2 with global harmonic coefficients results in an unstable set of equations. However, it can be shown that this problem can be solved by applying appropriate stabilisation methods. This has been already demonstrated by several studies (CIGAR, 1996). In addition, use can be made of different representation forms, for example making use of so-called Slepian functions that do not cover the entire globe. In these cases, the gravity field can be recovered with high accuracy over the entire globe, apart from the small polar caps. It can be shown that the GOCE observations do provide information on the gravity field over the polar caps, only with reduced sensitivity (see Fig. 8.6). Also, some prior information about the gravity field over the poles is available.

The large amount of preparatory work conducted during the CIGAR studies (CIGAR, 1995) has resulted in the development of mature algorithms and software tools. A simulation has already been carried out setting-up and solving the observation equations for a gravity field model complete to degree and order 250 using a 48-day data set of simulated SGG observations (Fig. 7.3). A least-squares procedure was used to establish the normal equations for the unknown gravity parameters. It can be shown that this procedure leads to a full system of equations that can be solved by an efficient iterative process. The red line indicates Kaula's rule of thumb, the green line an estimate of the expected GOCE performance. The black curves denote successive solutions by the iterative process referred to as preconditioned conjugate gradient

multiple adjustment (PCGMA). The recovery error after convergence towards the lower black curve is well below the green line, suggesting that no errors are expected to be advected into the solutions by the algorithms and tools.

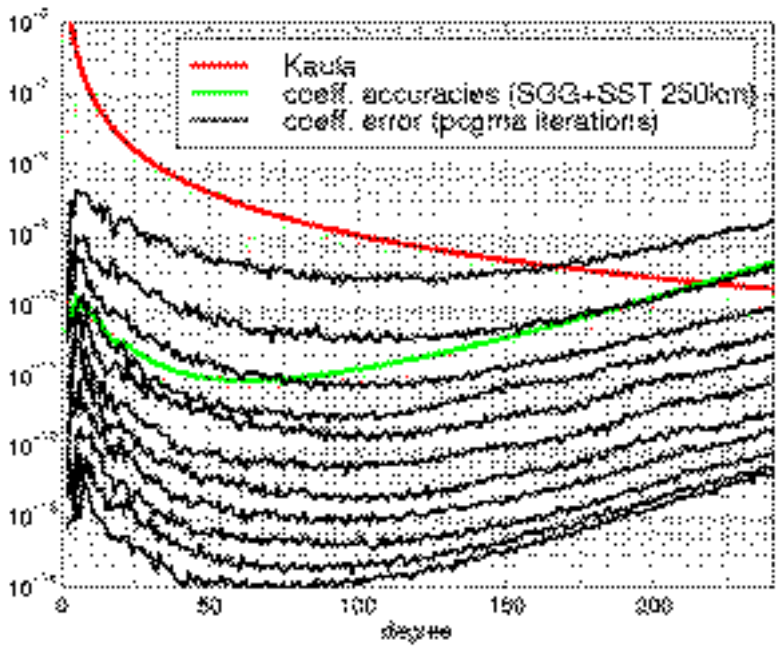

Figure 7.3. *Result of a gravity field model recovery experiment complete to degree and order 250 based on a 48-day simulated data set of error-free SGG observations.*

7.4 Validation

The accuracy and reliability of the different levels of GOCE products have to be validated and assessed. A basis for this is provided by the several calibration procedures (Chapter 6). Concerning the SGG observations, a further check on the calibrated and corrected gravity gradients (Level 1b) can be performed by making use of the traceless property of the gravitational gradient tensor (i.e. the sum of the three diagonal gravity gradients is equal to zero). In addition, SGG observations at crossing tracks can be compared with each other after transforming to a common altitude. The GPS/GLONASS SST-hl observations can be checked by comparing GOCE orbit solutions with SLR observations.

A number of possibilities exist to validate the gravity field model products (Level 2):

- comparison with existing state-of-the-art long-wavelength gravity field models
- comparison with in-situ data

– inter-comparison between SGG-only and GPS/GLONASS solutions in some common bandwidth where both solutions seem to be reliable from statistical comparisons (computed covariance).

Existing global models give an accurate description of the long-wavelength features of the Earth, i.e. features with wavelengths longer than a few thousand kilometres are well represented. The long-wavelength part of the GOCE gravity solutions can be validated by a comparison with these models. By the time GOCE flies, our knowledge of the long-wavelength features may even have been improved by an analysis of CHAMP data providing more validation data. In addition, a comparison with possible GRACE data will enable further validation especially of the long- to medium-wavelength gravity field results.

High accuracy surface gravity information is also available for a few well-surveyed land areas. Besides application for calibration purposes, this information can be used to validate the high-resolution part of the GOCE gravity field solution. Algorithms and tools to achieve this are well understood and are quite mature (CIGAR, 1996). The comparisons with existing data will also facilitate a proper quality assessment and calibration of the gravity field product.

Although the SST observations are particularly sensitive to long wavelengths and the SGG observations to short-wavelengths of the gravity field, there is a certain overlap at medium wavelength, i.e. wavelengths of one thousand to a few thousands of kilometres, where the sensitivity to the gravity field is of the same order of magnitude. In this wavelength range, SST-hl only and SGG-only solutions can be derived and the performance of the GPS/GLONASS and gradiometer instruments for gravity field recovery can be compared and validated with respect to each other.

7.5 Summary

The different steps that are required in the data processing have been identified and described. The derivation of the observables (Level 0 and Level 1 processing) that form the basis for the recovery of the gravity field products (Level 2) is well understood. It has been demonstrated how the various subsystems of GOCE, including the gradiometer instrument, the GRAS receiver, the thrusters, the star trackers, etc. (Chapter 6) provide the necessary data for this derivation, including ancillary data such as calibration parameters. It has also been demonstrated by means of a full-scale simulation experiment that already mature algorithms and software exist for the production of the gravity field products.

The outcome of the data analysis, the Level 2 products, are made available in proper formats for further use by the scientific user community as schematically illustrated in Figure 7.4. The transformation from a gravity field model given in the form of spherical harmonic coefficients to a grid of geoid values involves little difficulty.

These values can, in turn, be used in combination with altimeter data to analyse, monitor and model ocean circulation. Similarly, gravity anomalies can be computed that can be used in solid-Earth geophysical modelling. The associated error estimates can be derived from a well-calibrated variance/covariance matrix of the gravity field solution. The scientific use of the Level 2 products was outlined in detail in Chapter 3. A summary of several assessment studies of this use is given in section 8.3.

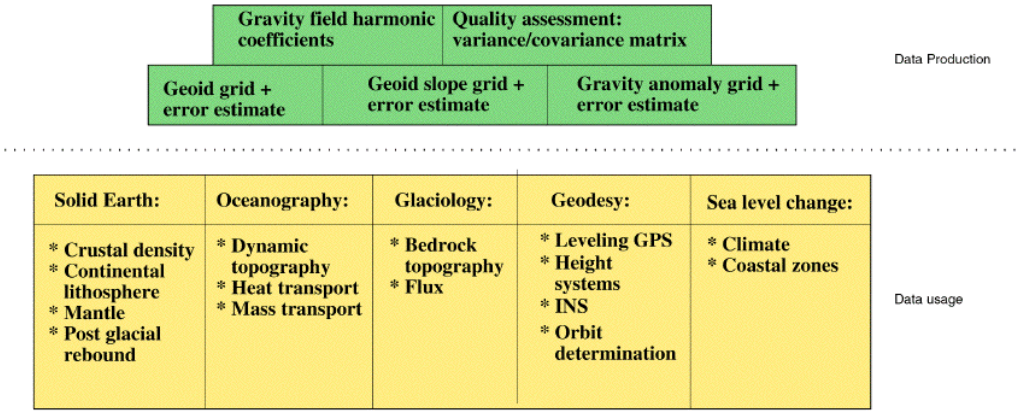

Figure 7.4. *Schematic of possible scientific uses of gravity field products.*

8 Mission Performance and Mission Requirements

The success of the mission will depend on the impact that the new and advanced gravity and geoid models will have on the fields of scientific research and applications in solid-Earth physics, absolute ocean circulation, ice sheet studies, geodesy, and sea-level change. The analysis of the mission performance consists of three stages:

- Firstly, the performance of the satellite measurement system is established. This is achieved by a comprehensive analysis and simulation of the gradiometer and SST-hl receiver characteristics themselves, and of their interaction with the satellite and the satellite environment. A short description is given in section 8.1.

- Secondly, based on this assessment, the determination of the about 100 000 gravity field and geoid model parameters, the stability of this computation and the propagation of the sensor error characteristics from the data along the orbit at altitude to the gravity field parameters on the Earth's surface are investigated. Section 8.2 gives the main elements of this process.

- Thirdly, with good knowledge about the quality of the determined gravity and geoid models, a series of impact studies have been performed for the various areas of scientific research and application. Their results are described in Chapter 3, and a summary of the overall impact is given in section 8.3.

Based on these investigations, a very complete picture is derived of the great potential impact that the GOCE Mission would have for Earth sciences, including solid-Earth physics, oceanography, ice studies, geodesy and sea-level change investigations.

8.1 Error Analysis and End-to-End Simulator

8.1.1 Error Budget for Gravity Gradiometry

The fundamental elements that will be used for the reconstruction of the gravity field by means of the gravity gradiometry technique, are the three diagonal components of the gravity gradient tensor (V_{xx}, V_{yy}, V_{zz}). Their measurement will be affected by several errors that can be grouped into four main classes:

- Instrument Errors (I)
- Instrument-Satellite Coupling Errors (C)
- Satellite Errors (S)
- Post-Flight Centrifugal Acceleration Errors (P).

The error tree is shown in Figure 8.1.

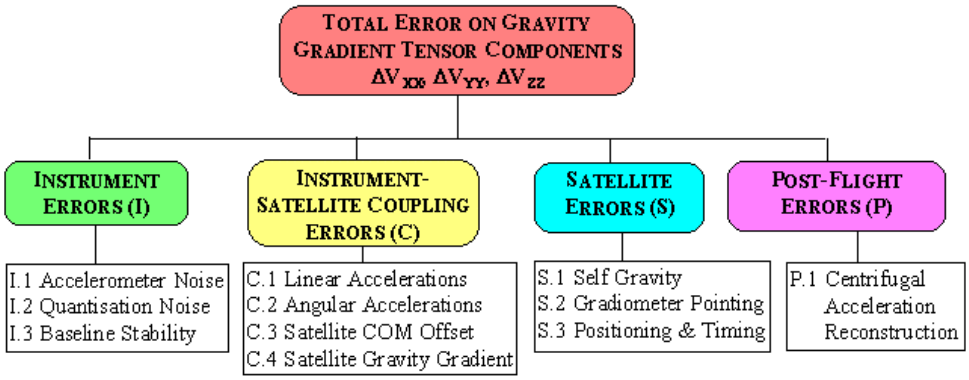

Figure 8.1. Gravity gradiometry error tree.

The Instrument Errors depend, for the assigned reference orbit and attitude of the satellite, only on the performances of the gradiometer. They include:

- The accelerometer noise, taking its main contributions from the drive voltage amplifier noise, the contact potential difference fluctuations, the position sensor noise and the DC bias relative stability.
- The measurement quantisation noise, introduced by the 24-bit analogue-to-digital conversion of the measured acceleration at 1 Hz frequency.
- The gradiometer baseline stability related to the thermal stability in the gradiometer enclosure and to the coefficient of thermal expansion of the structure connecting the accelerometer pairs.

The Instrument-Satellite Coupling Errors depend on the performances of the gradiometer and the spacecraft together. They include:

- The coupling of the gradiometer with the residual non-gravitational linear accelerations of the satellite (attenuated by the action of the drag-control system), through the differential scale factor, misalignment and quadratic factor in the in-line axes of each accelerometer pair.
- The coupling of the gradiometer with the residual angular accelerations of the satellite (attenuated by the action of the angular control system), through the common misalignment of the in-line axes of each accelerometer pair with respect to the baseline.

– The coupling of the gradiometer with the residual angular acceleration and the satellite COM offset (and its displacements) with respect to the gradiometer centre, through the differential scale factor and misalignment of the in-line axes of each accelerometer pair.
– The coupling of the proof mass motion with the static gradient of the satellite self-gravity field in the region of the gradiometer.

The Satellite Errors depend only on the performance of the satellite. They include:

– The variation of the self-gravity field at the location of the accelerometer test masses, produced by the displacement of the spacecraft equipment caused by the thermo-elastic deformations of the structure.
– The mixing of the diagonal component of the gravity gradient tensor nominally measured by a gradiometer arm with the components that are not supposed to be measured by that arm, caused by the gradiometer pointing errors.
– The inaccuracy in the localisation of the gradiometric measurements relative to an Earth-fixed frame, due to the errors in satellite position measurement and in the time-tagging of the collected data.

Finally, the Post-Flight Errors concern the on-ground reconstruction of the variation of the centrifugal acceleration in the measurement bandwidth (MBW) caused by the fluctuations of the satellite spin rate, using the angular accelerations measured by the gradiometer itself and the attitude angles measured by the star sensors. This centrifugal acceleration has the largest effect on the measurements of the along-track and radial components of the gravity gradient tensor and must be estimated and removed from the data, before the determination of the Earth's gravity field. However, some residual errors will still remain.

Both the gradiometer and the spacecraft performances have been optimised to minimise the error on V_{xx}, V_{yy}, V_{zz} in the gradiometry MBW from 5 MHz to 100 MHz.

An error budget has been established during the Phase-A study, and analyses and numerical simulations have been carried out in order to estimate the contributions associated with each item in the error tree. Most of the gradiometer performance parameters were assigned error estimates that take into account the results of the laboratory tests carried out so far.

The spectral densities of the total error of the four main classes are given in the plots of Figure 8.2. These densities have then been added quadratically to get the total error of ΔV_{xx}, ΔV_{yy}, ΔV_{zz}, also shown in Figure 8.2. A summary of the total measurement errors is given in Table 8.1.

	Mean value in MBW	Max value in MBW	Error standard deviation in MBW
ΔV_{xx}	1.6 mE/Hz$^{1/2}$	3.0 mE/Hz$^{1/2}$	0.69 mE
ΔV_{yy}	1.6 mE/Hz$^{1/2}$	3.0 mE/Hz$^{1/2}$	0.69 mE
ΔV_{zz}	1.8 mE/Hz$^{1/2}$	3.1 mE/Hz$^{1/2}$	0.72 mE

Table 8.1. *Gradiometry error budget summary.*

The gravimetry measurement errors resulting from this budget have then been utilised to obtain, by covariance analysis, the errors on the gravity field coefficients, the geoid height and the gravity anomaly, which thus represent the expected scientific performance of the GOCE mission.

8.1.2 Error Budget for Satellite-to-Satellite Tracking

The reconstruction of the gravity field from the effects that it produces on the satellite trajectory utilises as input the precise orbit determination (POD) obtained from the SST-hl.

The precise orbit determination process will be 'initialised' at the beginning of the mission by a reduced-dynamic technique, in order to obtain a first 'reference trajectory' for the spacecraft, accurate to some decimetres. Then, using the GPS/GLONASS measurements together with this reference trajectory, the kinematic technique will provide an orbit accurate to the centimetre level. From this first precise orbit (and from the gradiometry data), a first improvement of the gravity field model will be obtained.

This model, in turn, will allow the precise orbit determination to be initiated using the dynamic technique. The result will be more accurate than the one obtained kinematically (at least after some iterations). This, in turn, will allow further improvement of the model of the gravity field.

The kinematic POD does not need as input a dynamic model of the satellite. The achievable accuracy in the determination of the satellite centre of mass (COM) position depends mainly on:

- the GPS/GLONASS receiver measurement noise
- the GPS/GLONASS ground station co-ordinates error
- the GPS/GLONASS ephemeris error
- the troposphere correction error

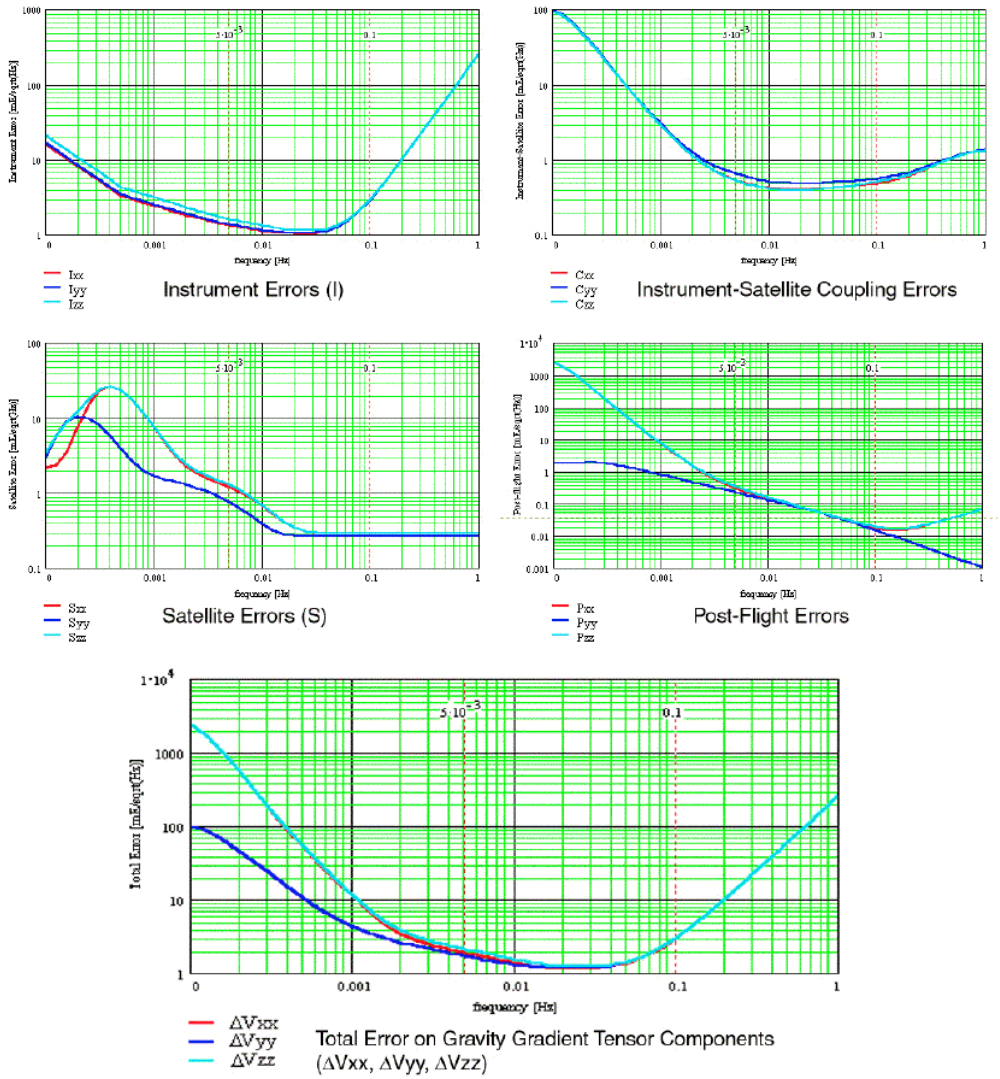

Figure 8.2. *Spectra of the gravity-gradient measurement error budget for the components V_{xx}, V_{yy}, and V_{zz}. It can be seen that the error level is below 3 mE/Hz in the measurement bandwidth between 5×10^{-3} Hz and 0.1 Hz.*

– the error in the phase centre location of the GPS/GLONASS antenna
– the error in the location of the spacecraft COM relative to the GPS/GLONASS antenna.

For the dynamic POD, the error in the measurement of the non-conservative linear accelerations of the satellite centre of mass (COM) and the error in knowledge of the gravity field model knowledge must be added to this list.

The multipath effect (due to the GPS/GLONASS signal rebound against the satellite structure before arriving at the antenna) can be neglected, provided that signals from the GPS/GLONASS satellites seen under a low elevation angle (< 5°) are not taken into account.

From the assessment of the error sources listed above (based on the characteristics of the GPS constellation and of the IGS ground stations, the expected performance of the candidate GPS/GLONASS receivers, the antenna characteristics, the accelerometer performances, and a detailed geometric theory of diffraction analysis to establish the effect of the satellite surfaces in the carrier phase error), an error budget for the satellite position determination at 1 Hz frequency by SST-hl has been determined (see Tables 8.2 and 8.3). Note that the ionospheric path length delay can be retrieved with high precision from the dual-frequency GPS/GLONASS measurements. Although the troposphere does not affect the SST-hl measurements, it enters the GOCE orbit indirectly via the GPS/GLONASS measurements to the ground stations.

The SST-hl measurement errors resulting from these budgets have then been utilised, together with the gradiometry error-budget results, to obtain the expected scientific performance of the GOCE mission.

	Radial [cm]	Along-track [cm]	Cross-track [cm]
GPS measurement noise (9 mm)	1.9	0.9	0.7
GPS station co-ordinates (1 cm)	0.6	0.5	0.3
GPS ephemeris error (4 cm)	1.1	0.6	0.5
Tropospheric correction error (0.5%)	0.6	0.3	0.3
Phase centre location error	0.5	0.5	0.5
COM location error	0.2	0.2	0.2
Total error on single position determination	2.5	1.4	1.1

Table 8.2. *Satellite-to-satellite tracking error budget summary (kinematic POD).*

	Radial [cm]	Along-track [cm]	Cross-track [cm]
GPS measurement noise (9 mm)	0.6	0.5	0.5
Linear acceleration measurement error (10^{-9} m s^{-2} 1σ)	0.1	0.1	0.1
GPS station co-ordinates (1 cm)	0.2	0.2	0.2
GPS ephemeris error (4 cm)	1.0	0.5	0.5
Tropospheric correction error (0.5%)	0.3	0.3	0.3
Phase centre location error	0.5	0.5	0.5
COM location error	0.2	0.2	0.2
Remaining dynamic model errors	0.8	0.5	1.0
Total error on single position determination	2.1	1.2	1.5

Table 8.3. *Satellite-to-satellite tracking error budget summary (dynamic POD).*

8.1.3 GOCE End-to-End Simulator

In parallel with the Phase-A, the development of a software tool dedicated to the end-to-end simulation of the system performance is under study.

The purpose of this tool is to build a virtual (simulated) mission, including realistic software models of the gradiometer, of all the spacecraft elements affecting the scientific measurement accuracy (attitude sensors, drag and attitude control laws, thrusters, etc.), of the external environment (gravity field model, atmospheric model), of the environmental disturbances on the spacecraft, of the dynamics of the spacecraft (orbit and attitude) and of the gradiometer proof masses.

The GOCE end-to-end simulator block diagram is shown in Figure 8.3. A reference orbit is generated for the computation of the environmental disturbances and of the gravity-gradient signal experienced by the satellite and the gradiometer. The spacecraft dynamic block computes the residual linear accelerations of the COM and the attitude motion about the COM (angular accelerations, angular rates, attitude angles). This task is performed in the presence of the external disturbances and of the reaction forces and torques computed by the controllers on the basis of the information provided by the sensors and supplied to the actuators (ion-thruster, cold-gas thruster). The linear and angular accelerations of the COM are utilised, together with the angular rates, to integrate the dynamics of the proof masses of the gradiometer. The attitude angles are utilised to transform the gravity-gradient tensor into the spacecraft reference frame; the resulting gravity-gradient forces are also applied to the proof masses.

A gradiometer measurement model is used to transform the proof-mass dynamics into common-mode accelerations, angular accelerations, and differential acceleration readout. The effects of the instrument noise, scale-factor mismatching, sensitivity-axis misalignment and other factors, are included here. The common-mode accelerations

are utilised to feed the drag control system. The angular accelerations are introduced, together with the measurements of the star sensor, into an estimator providing an optimal reconstruction of the complete attitude state vector, which is then utilised to feed the attitude control and to derive the centrifugal accelerations acting on each pair of test masses of the gradiometer. Finally these accelerations are removed from the measured differential accelerations to obtain the measured components of the gravity-gradient tensor, which represents the end-product of the simulator.

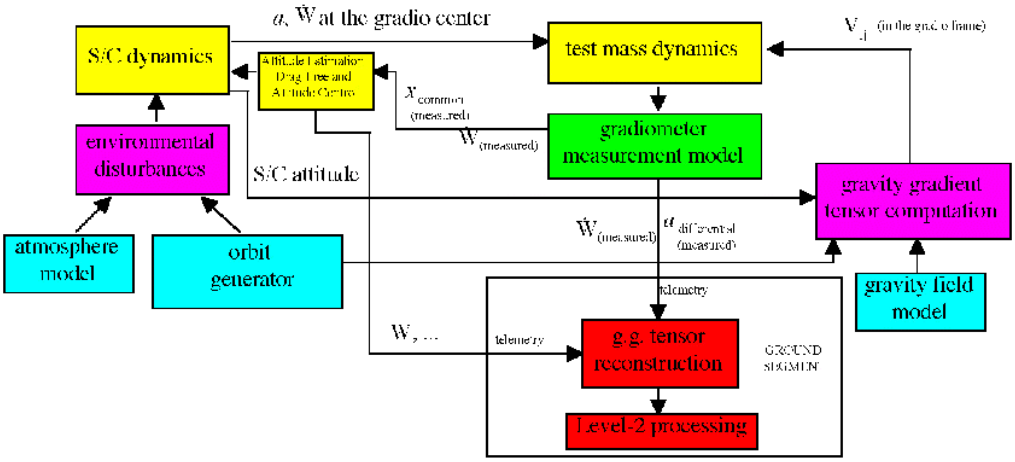

Figure 8.3. *GOCE end-to-end simulator block diagram. The left side of the diagram accounts for the perturbation exerted on the satellite by the environment whereas the right side accounts for the impact of the gravity field and its variations on the gradiometer.*

The GOCE end-to-end simulator plays a fundamental role in the following mission planning and execution phases:

- during the mission design phase, as a means for determining the expected scientific performance and for validating the error budget (and thus the specifications that are derived from it for all system elements)
- in parallel, to set up realistic procedures for scientific data reduction, based on representative ‘raw’ data

– during the mission implementation phase, to consolidate the expected scientific performances, given the measured performance of all the elements, tested separately and together, as far as possible
– during the mission operation planning, as a means to test the in-flight operation sequences, with particular regard to the gradiometer set-up and calibration
– during the mission itself, as a means for interpretation of the flight data.

A first version of the end-to-end simulator has been implemented and utilised to generate time series of the gravity-gradient-tensor components as they are expected to be measured by GOCE.

Figure 8.4 shows an example of the end-to-end simulation. The upper panel shows a time series of the gravity-gradient component V_{xx} as obtained from the simulator. The signal varies from -1381 E to -1361 E. The middle panel displays the corresponding time series of the measurement error. It is derived by combining the value obtained from a model of the gravity field with the simulated measured value. The large noise level (of up to 300 mE) is due to the high-frequency error behaviour outside the MBW. The lower panel shows the measurement error spectrum. Again, inside the MBW (i.e. between 5×10^{-3}Hz and 0.1 Hz) the error level stays below 3 mE/Hz.

8.2 Expected GOCE Performance

From the investigations described in section 6.2 and section 8.1, a baseline mission profile and an overall error budget have been identified. Its main parameters are summarised in Table 4.3. With the parameters of section 8.1, a full mission error propagation simulation has been carried out (section 4.4). The maximum spherical degree and order that has been resolved is L = 300. This corresponds to a half-wavelength of D = 65 km. The full triangular error spectrum of spherical harmonic coefficients is displayed in Figure 8.5.

It can be seen that all coefficients up to degree and order 300 can be resolved. Also apparent is the weakness in the determination of the coefficient band with order m close to zero. This effect is caused by the orbit not exactly covering the poles. It will be shown that this effect in the spectrum is confined to the polar areas when transforming the errors back from the spectrum to the sphere.

Based on these simulations, the capabilities of GOCE can be summarised, up to a certain wavelength, in terms of geoid and gravity anomaly field recovery as given in Table 8.4.

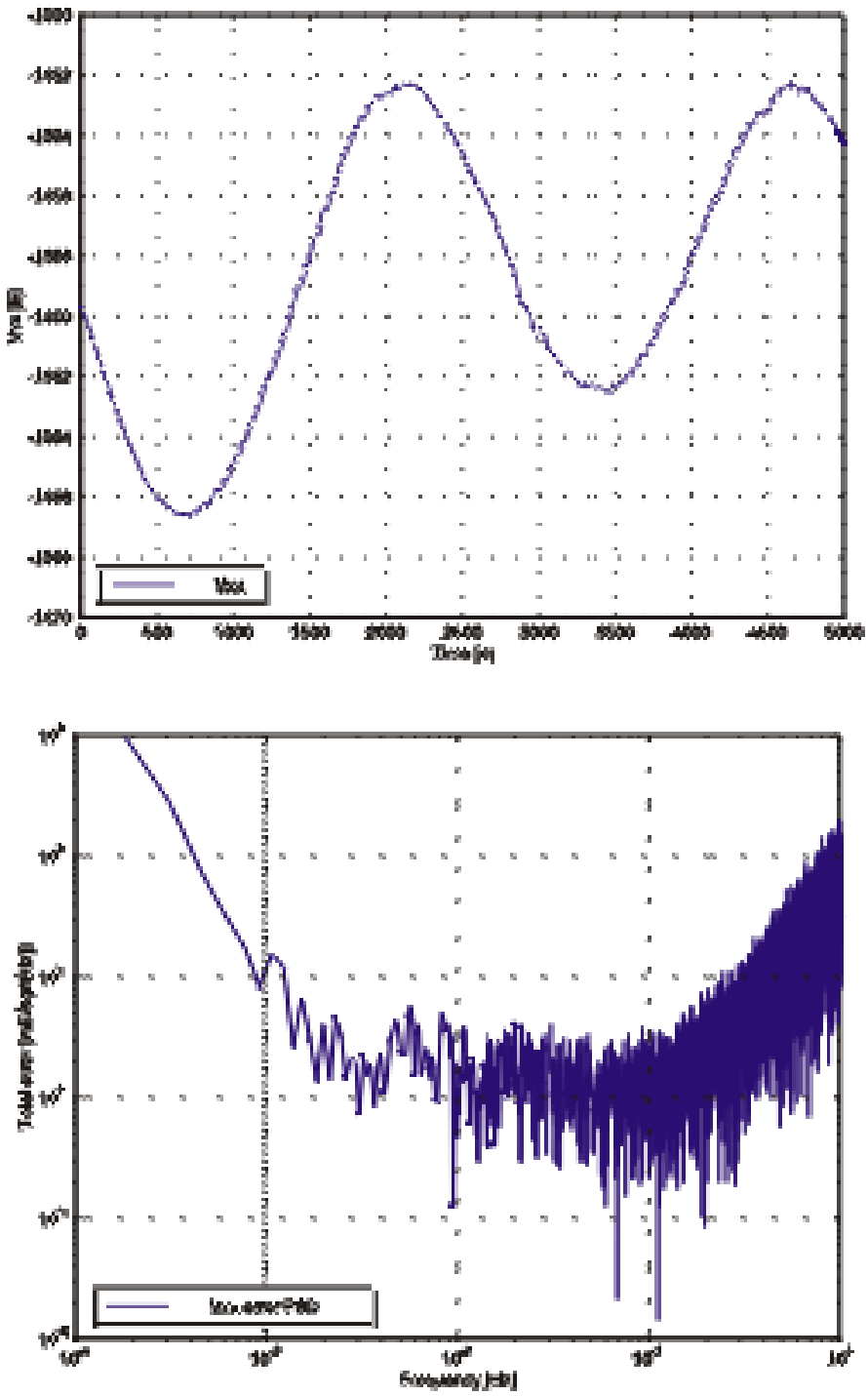

Figure 8.4. *Simulated signal (upper) and error spectrum (lower) of the gradient component V_{xx} as obtained from the GOCE end-to-end simulator discussed in section 8.2.*

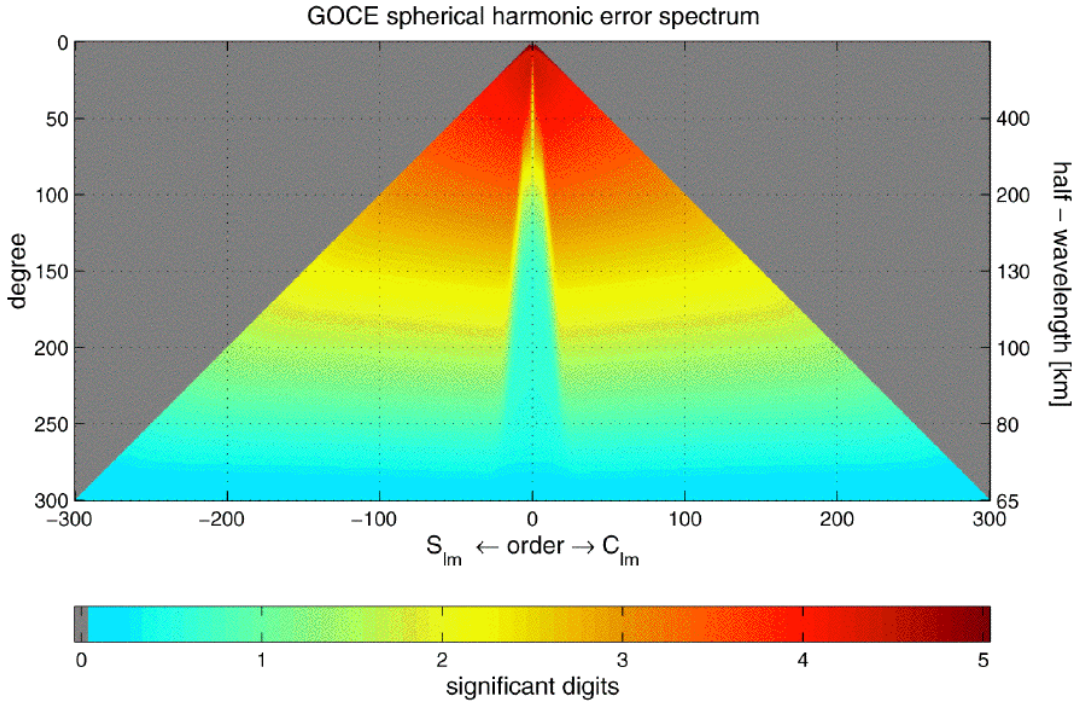

Figure 8.5. *GOCE spherical harmonic error spectrum. The vertical axis of the triangle refers to the spherical harmonic degree l (or to the corresponding spatial resolution D), the horizontal axis refers to the order m of the coefficients, with the* C_{lm} *coefficients on the right and the* S_{lm} *coefficients on the left. Thus the coefficient* C_{00} *would be located at the top of the triangle, whereas the coefficients with increasing degree and order refer to smaller and smaller scales of the gravity field. The colour code refers to the number of decimal digits (significant digits) to which the individual coefficients can be resolved. For example, two significant digits mean a determination of coefficients with only 1% uncertainty.*

Spatial resolution *D* (half-wavelength)	Maximum degree *L* (corresponds to *D*)	Geoid height [mm]	Gravity anomaly [mgal]
1 000 km	20	0.4	0.0006
400 km	50	0.5	0.001
200 km	100	0.6	0.03
100 km	200	2.5	0.08
65 km	300	~ 45	~ 2

Table 8.4. *Expected RMS. errors on the geoid height and gravity anomalies at given resolutions, as derived from the GOCE baseline mission simulations. At resolutions where the regularisation of the inverse problem plays a role, numbers are approximate.*

Another way of looking at the performance is to map the errors as a function of latitude by propagating the covariance error characteristics onto the sphere for the geoid and gravity anomaly. This is shown in Figure 8.6. The errors are homogeneous except for the polar gaps (~ 7° radius) where the errors increase by up to about one order of magnitude. Elsewhere, the level of the RMS curves is consistent with the cumulative errors up to the specified maximum degree *L* (see Fig. 4.2b,c) or with Table 8.4. For instance, up to degree 200 (100 km resolution) GOCE yields a geoid error at 2.5 mm level, and a gravity anomaly error just below 0.08 mgal, for the static field.

The distortions in the spherical harmonic error spectrum caused by a non-polar orbit are of little concern because it is clear from Figure 8.6 that these distortions are perfectly mapped back to the polar regions. A strict lack of data over the pole would therefore not degrade the use of the GOCE results for the main applications. On the other hand, this situation may be improved by including results brought by more aero-gravimetric campaigns over the Arctic and Antarctic areas, which are planned in the years to come and which will help to close the gap. In any event, the gravity anomaly error at, for instance, 100 km length scale (curve with maximum degree L = 200 in Fig. 8.6) remains below 7 mgal close to the poles and below 1 mgal at five degrees from them, which is quite an astonishing and useful result over those remote areas.

Finally, it should be remembered that the gradiometer is three-dimensional, i.e. it simultaneously measures the gravitational field in all three spatial directions. Consequently the errors of the resulting gravity parameters (gravity anomalies or geoid heights) exhibit no preferred direction. Apart from the redundancy, the errors are independent and isotropic. This isotropy of the error structure is of great advantage, in particular when the directional structure of the gravitational field is of importance, as is the case in oceanography where slopes of dynamic topography are to be derived.

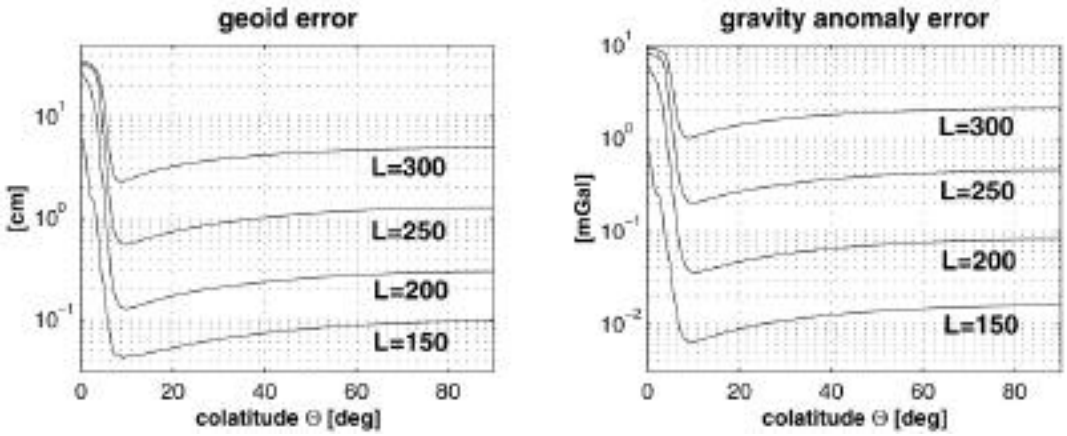

Figure 8.6. *Accumulated point error on geoid* [*a*] *and gravity anomaly* [*b*], *for series expansions up to degree and order L = 150 (D = 135 km), L = 200 (D = 100 km), L = 250 (D = 80 km), L = 300 (D = 65 km), as function of co-latitude for the northern hemisphere (results are symmetrical with respect to equator), from the GOCE baseline mission simulation. Note that the errors decrease when going towards the pole due to the accumulation of satellite ground tracks, and then increase due to the polar gap.*

8.3 Summary of Expected Science Performance

The GOCE mission will produce a new model of the gravity field of unprecedented accuracy and spatial resolution. Its main products will consist of sets of spherical harmonic coefficients up to maximum degree and order *L* which will describe the global gravity field and geoid. In addition, a range of detailed global and regional gravity anomaly, geoid and geoid slope maps or gridded data sets will become available to the community. All of these primary products will be accompanied by estimates of their error standard deviations. Although the products themselves will clearly become available only after the mission, it is already foreseen that the error estimates will be very similar to those given in section 8.2. Therefore, based on these error estimates, it is possible to reliably assess the degree of impact of GOCE on the fields of science and applications discussed in Chapter 3.

The quantification of the effect of GOCE gravity information is straightforward in those fields where the GOCE models can be directly converted into a science or application product. For example, this is the case for all applications in geodesy and for the direct determination of absolute ocean circulation in combination with satellite altimetry. A more complicated situation is met when GOCE data are included in assimilation schemes in combination with other data types. This is the case in some areas of solid-Earth physics and oceanography (sections 3.2 and 3.3). Finally, there are

fields of application where the benefits of GOCE enter via several directions. For example, the study of sea-level changes spans research into changes in ocean circulation, steric changes and changes in ocean volume, vertical land movements, ice mass changes, height systems and satellite orbits. GOCE data will facilitate more comprehensive investigation of such a complex topic. Chapter 3 discusses a range of scientific research in which GOCE data will enter at different levels of complication.

8.3.1 Solid Earth

In solid-Earth physics the GOCE gravity model is not in itself the primary goal; rather it is a detailed three-dimensional image of the density variations in the lithosphere and upper mantle, derived from a combination of gravity, seismic tomography, lithospheric magnetic-anomaly information and topographic models (Achache, 1994 and section 3.2). This density image is well constrained by knowledge of the gravity field, since gravity anomalies result directly from a convolution with the density fluctuations. The knowledge of density then allows precise quantitative modelling of sedimentary basins, rifts, tectonic motions and sea/land vertical changes. Also it contributes significantly to the understanding of the occurrence of subcrustal earthquakes, a long-standing geophysical modelling objective which will lead to the quantification of seismic hazard risks. The expectations from this area of work are reviewed in section 3.1 and schematically illustrated in Figure 8.7.

8.3.2 Absolute Ocean Circulation

With the mean dynamic ocean topography derived from the GOCE geoid in combination with precise altimetry, practically all ocean current systems from the strongest (Gulf Stream, Kuroshio, Antarctic Circumpolar Current) through to weaker deep-ocean and coastal current systems can be determined in terms of location and amplitude (section 3.3 and Fig. 8.8).

In a series of detailed assimilation studies for a number of ocean sections, it has been shown that the uncertainties of mass and heat transport can be reduced by a factor of 2 in the upper-layers and with significant reductions throughout the water column (e.g. 40% in the ACC as shown in Fig. 3.15). The high-spatial-resolution afforded by GOCE has been found to be essential for such an achievement. Clear benefits are also expected in high-resolution ocean forecasting.

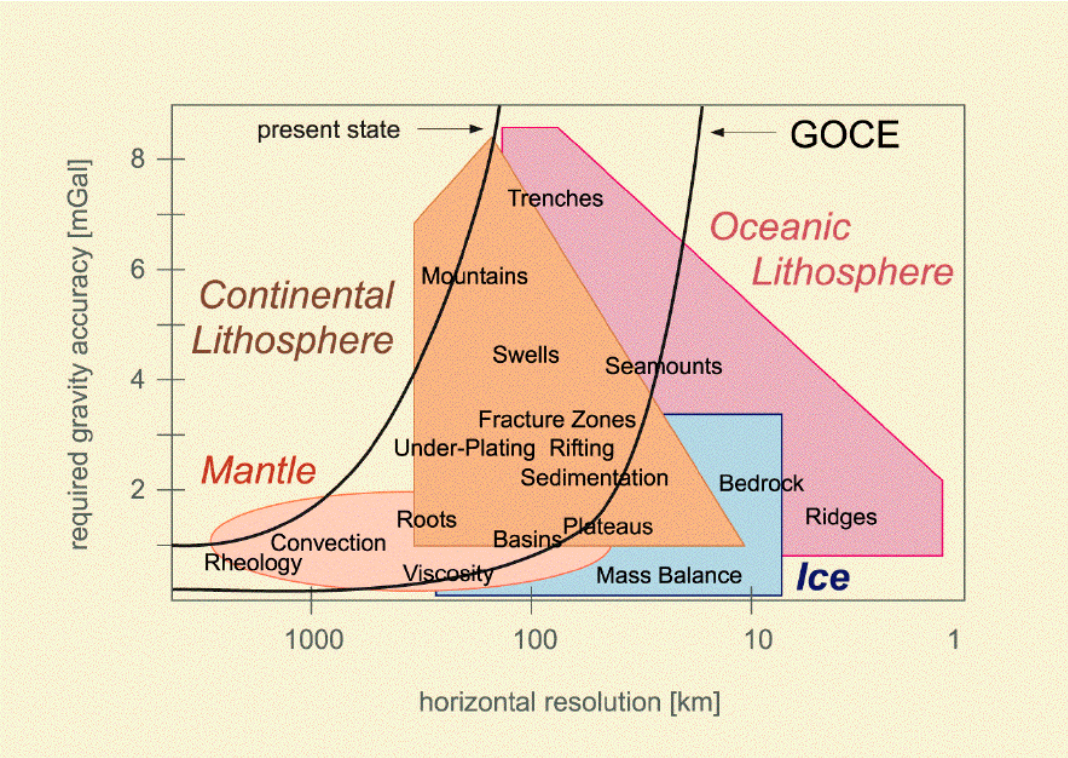

Figure 8.7. *Schematic of the required accuracy (estimated at approximately 10% of the gravity signal) as a function of spatial-scales necessary to resolve the quoted geodynamical and tectonic features. The two curves represent the present and the potential accuracy from GOCE.*

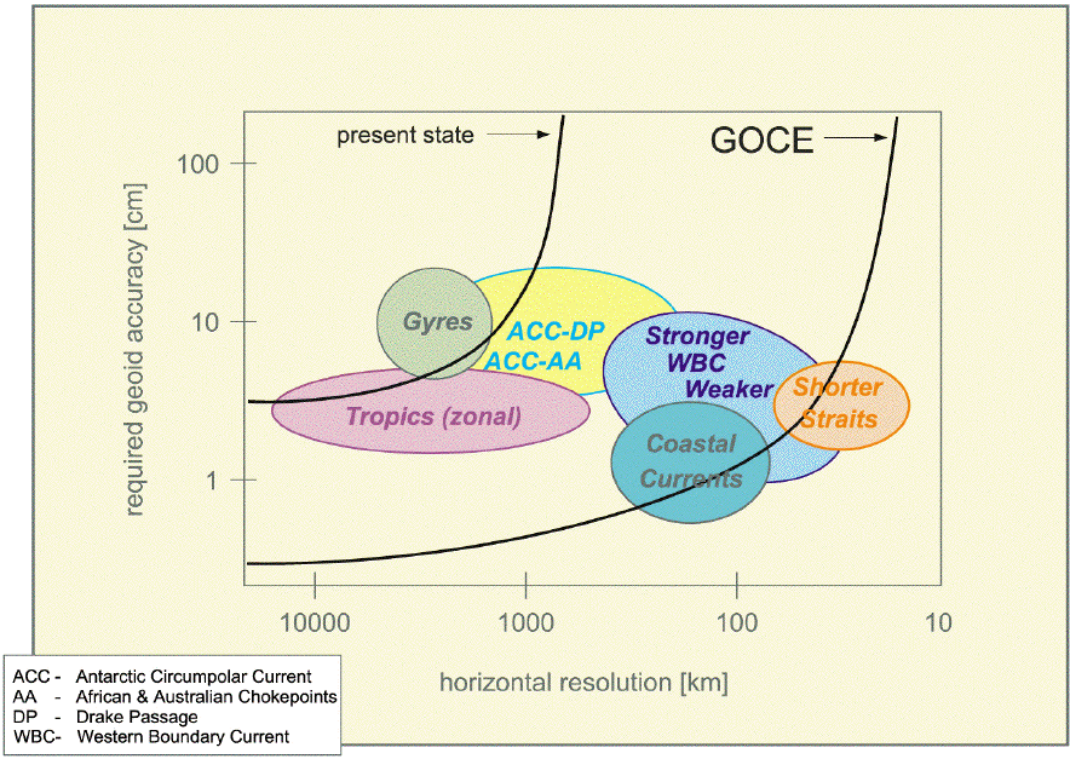

Figure 8.8*. Schematic of 10% of the dynamic topography signals of selected ocean circulation features (10% representing order of magnitude knowledge of the mean flows) and geoid accuracy as a function of spatial-scales obtainable from present models and after GOCE.*

8.3.3 Ice Sheets

Section 3.4 summarises how a precise gravity field over the Greenland and Antarctic ice sheets, such as is achievable by GOCE, will provide improved knowledge of bedrock topography for inclusion in models of ice dynamics, especially benefiting undulations with half-wavelengths of 50-100 km. It is envisaged that techniques for bedrock determination will first be developed in Greenland, where more copious in-situ information already exists for validation, and then applied to Antarctica. A precise geoid will be a major benefit to modern geodetic surveys of the ice sheets (particularly within 'GPS levelling'), while improved gravity fields in polar regions will aid altimetric orbit determination. Ice topographic data from missions such as ICESAT and CRYOSAT, which will be available before GOCE, will be exploitable to greater effect.

8.3.4 Geodesy

In geodesy, one has to distinguish regions such as Europe, North America, Japan and Australia, where high-resolution local geoid, gravity and height information is available which will complement perfectly the gravity field data to be obtained from GOCE, from those regions where such local information is either not available or is erroneous or biased. For the former regions, one can claim that with GOCE all objectives in terms of 'levelling by GPS', unification of height systems, and gravity support of inertial navigation can be met perfectly. For the latter regions, these goals can be met to a large extent, and in addition it will be possible to remove most of the systematic distortions in presently available information. Objectives for orbit determination will be met completely, implying that in future gravity-induced orbit errors will be negligible. These findings are summarised in section 3.5 and Figure 8.9.

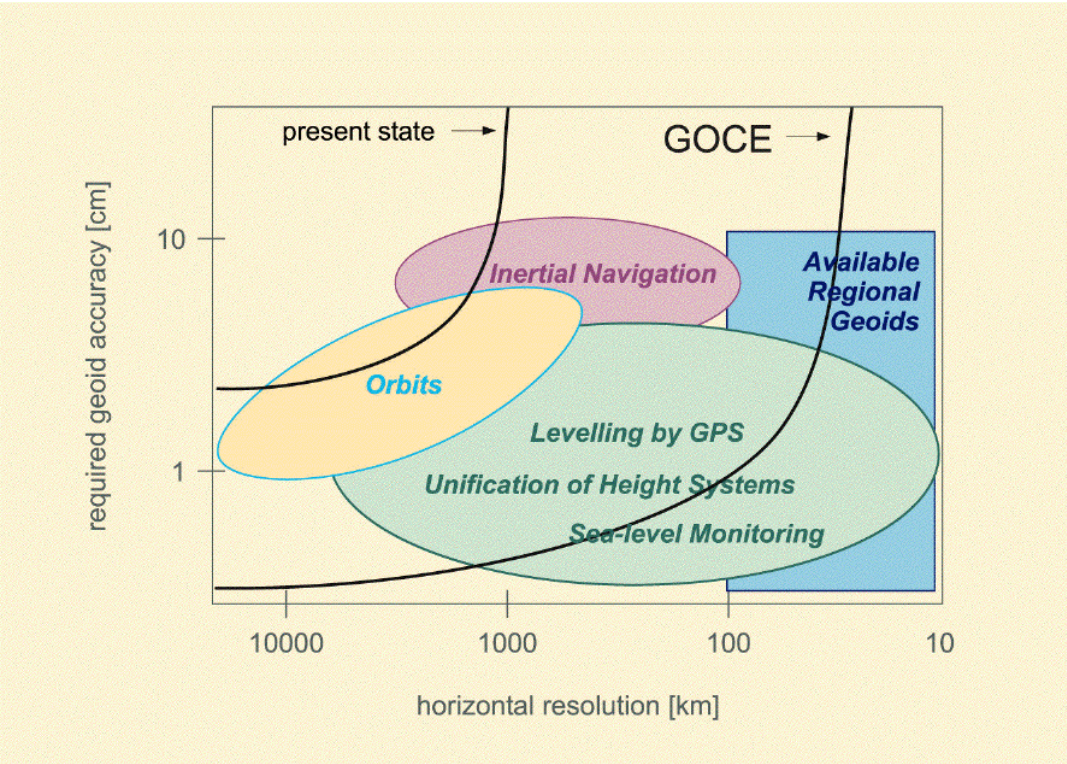

Figure 8.9. *Schematic of the required accuracy (estimated at approximately 10% of signal strength and all expressed in terms of geoid requirement) as a function of spatial-scales necessary to resolve the specific geodesy areas of application. The two curves represent the present and the potential accuracy from GOCE.*

8.3.5 Sea-Level Studies

The development of advanced GCMs for sea-level-related climate studies, in combination with increased knowledge of solid-Earth and glacial processes, will result in a better understanding of observed sea-level changes in the past, and the potential for more accurate prediction of future changes, both at the global level, and also at regional and local levels, where spatial variations in ocean processes, or variations in rates of vertical land movements are especially significant. The various contributions of GOCE to sea-level studies are summarised in section 3.6.

9 Programmatics

9.1 Development Approach

The development schedule as proposed by the industrial team at the end of Phase-A is shown in Figure 9.1. The ground-segment development is not explicitly shown, but it would run in parallel to the space-segment development. The proposed launch date is in the summer window of 2004.

It is particularly important to meet the schedule because if the launch window is missed, there is a one-year delay until the summer window next year. For the schedule to be met, it is necessary to continue the technology developments already started and to strengthen them already in Phase-B. The ongoing activities on AOCS/DFC, the electrical and cold-gas thrusters, and on gradiometer characterisation will have to be continued and expanded.

The development flow is shown in Figure 9.2. It recognises the two main lines of concern, the thermo-mechanical design, essential to guarantee gradiometer performance, and the AOCS/DFC which involves the spacecraft avionics and the onboard software.

As far as the thermo-mechanical issues are concerned, it is proposed to develop a structural-thermal model (STM) of the satellite. It will consist of the gradiometer bay, including the gradiometer, STM, mass dummies of other units and instruments and for the platform the proto-flight model of the structure. On this model, the alignment and stability issues particularly will be addressed.

Before final integration of the satellite proto-flight model and in parallel with the mechanical verification activities carried out on the STM, a partial satellite engineering model will be developed for testing on a system test bench. This model will include engineering/qualification models of the electric propulsion and cold-gas thrusters and a functional model of the EGG. For all other units and payload elements, only the prototype flight model (PFM) will be procured. The onboard software will be validated in a software validation facility (SVF) prior to integration on the system test bench. The latter will allow integration and testing of the AOCS / DFC elements, including the gradiometer, AOCS sensors and actuators and the onboard software.

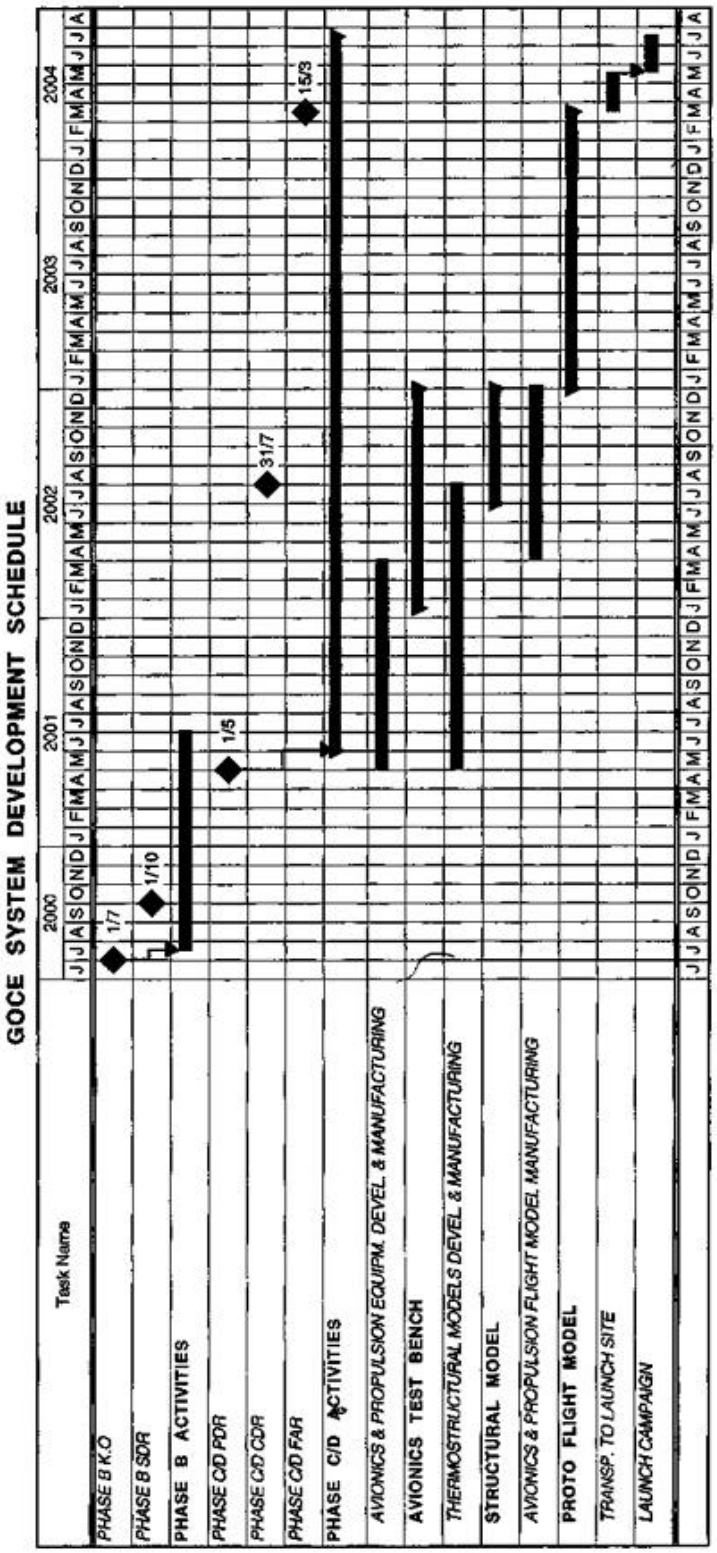

Figure 9.1. *Development schedule.*

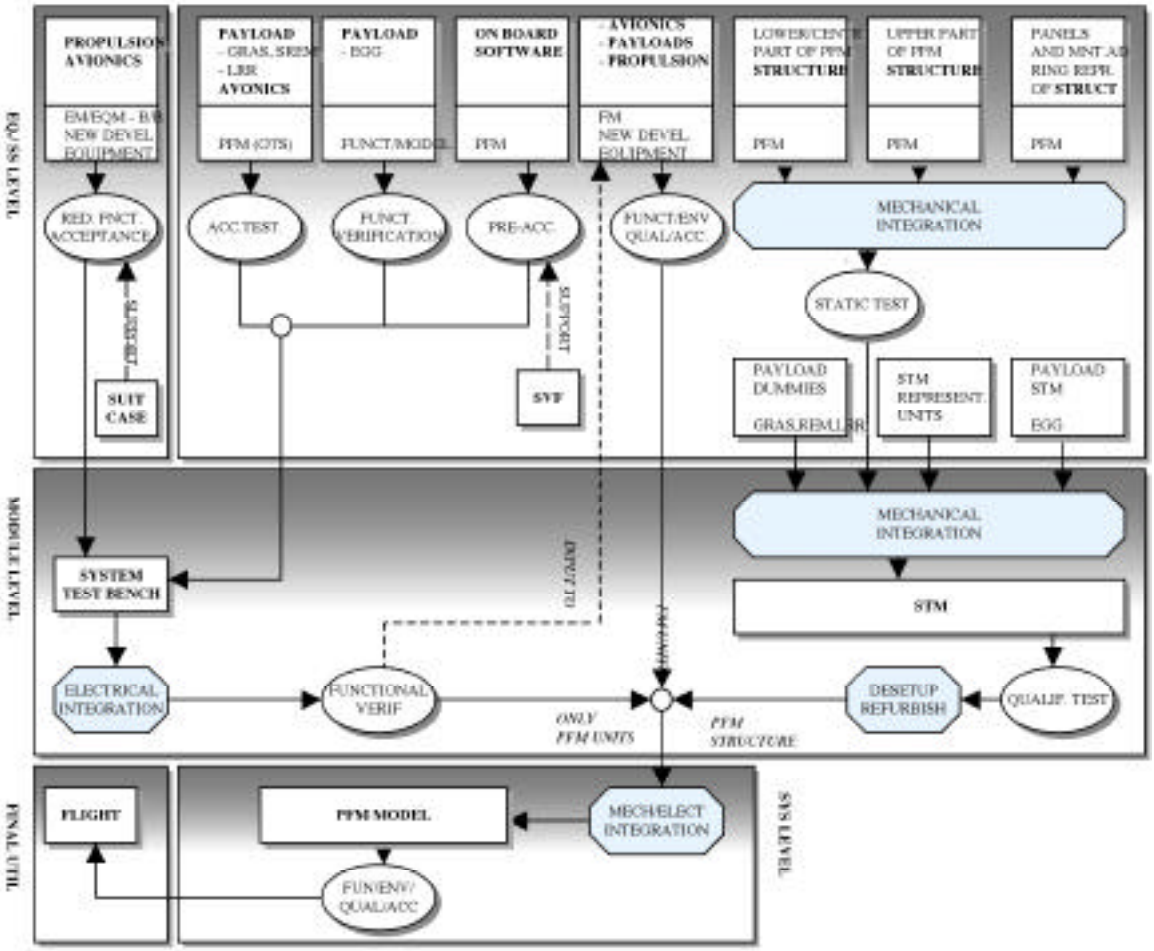

Figure 9.2. *Development flow.*

9.2 Heritage, Critical Areas and Risks

Table 9.1 summarises the implementation of the space and ground segments and indicates the relevant heritages. The novelties are in the gradiometer, though considerable heritage exists for the accelerometer, and the AOCS/DFC including the utilisation of the gradiometer as attitude sensor and of electric propulsion and proportional cold-gas thrusters as actuators.

Table 9.2 shows the critical areas identified for each element and the proposed risk-reduction measures. The critical areas affect the elements with lower heritage in Table 9.1. At system level, the key concerns are the performance of the proposed

gradiometer calibration strategy, the safety at the low orbit altitude and the tight power budgets. For the gradiometer calibration, a concept has been established that should provide the required performance. The safety and tight power budget concerns can be alleviated by raising the orbital altitude while still keeping it compatible with the required mission performance. The risk-reduction measures identified lead to the need for the early breadboarding activities and the model philosophy proposed in section 9.1.

It can be concluded at this stage that the GOCE's technical implementation is feasible and mature. Only a few critical areas have been identified and risk-reduction measures are already in hand and are also addressed in the development plan.

9.3 Related Missions, International Co-operation Possibilities and Timeliness

The uniqueness of GOCE has been demonstrated in previous chapters. From the technical/programmatic point of view, the CHAMP and GRACE missions should be mentioned as they provide complementary developments.

Concerning CHAMP, GOCE would benefit from the exploitation of satellite-to-satellite tracking and from the experience with the STAR accelerometer. The US-German mission GRACE will further promote the advances in data processing and provide more experience with the SUPERSTAR accelerometer. International co-operation is being pursued at scientific level and contacts have been already established between the GRACE and GOCE science teams.

From the technical/programmatic point of view, the proposed launch in 2004 is very timely. It allows benefit to be drawn from the European advances for missions like CHAMP and GRACE, with the associated positive impact in terms of implementation cost and readiness of the scientific community. It is also very timely in terms of relations with other missions that are targeting the same research areas as GOCE (Chapter 2). In the solid Earth domain the magnetometry missions such as ØERSTED, CHAMP and SAC-C will have produced several years worth of data. In oceanography, the conventional altimetry missions such as ERS-2, Envisat and Jason will have finished or be approaching completion. It is important to note the relation with the first Earth Explorer Opportunity Missions, CRYOSAT (2003-2006).

Finally, 2004 is already well into the low-activity part of the solar cycle and certainly late enough in the cycle that postponement of the mission would not bring significant simplification to the satellite in terms of easier drag-compensation requirements.

		Implementation	Heritage
Instruments			
GPS / GLONASS receiver		Geodetic GPS/GLONASS receiver	GRAS (Metop and GPSOS), LAGRANCE (SAC-C)
Gradiometer			
Accelerometers		3 axis, 6 DOF servo-controlled, capacitive accelerometer	CHAMP, GRACE (one order of magnitude better performance needed)
Gradiometer		Full tensor	Revised Aristoteles concept
Structure		Carbon-carbon	Military, TRP/EOPP development
Thermal		Two domain control, inner domain very low dissipation, excellent isolation	Classical
Calibration		Initial ground calibration and onboard adjustment with DFACS, ground truth and overlapping with SST	New
Platform			
Configuration		Slender, 0.8 m^2 cross-section + 2 fixed solar wings, 4 m length, no deployables	
Structure		Aluminium, separated Gradiometer bay	Very large heritage
Thermal Control		Decoupling gradiometer – rest of satellite, passive and heaters	Very large heritage
Propulsion	Electric propulsion	Ion thrusters, 0-12 mN modulated with 25 μN steps, 20 mN maximum thrust, Control and Drive Electronics Flow Controller, Xenon tank 22 kg fuel, valves and lines	RIT ion thrusters used on Eureca and Artemis, Electronics adapted under EOPP, Flow controller new UK national development with EOPP support.
	Cold gas	Proportional micro-thrusters	New, development started under GSTP
Power		1 kW by body-mounted and fixed solar arrays with GaAs cells, 25 Ah NiCd or 14 Ah NiH batteries, unregulated voltage power bus	Large heritage
Communications		S-band for TC and housekeeping and science telemetry (850 kbps)	Proteus
AOCS / DFC	Position Guidance	GNSS receiver and gradiometer common mode acceleration measurements	New
	Drag Control	Electric propulsion and cold-gas thrusters	New
	Attitude estimation	Gradiometer, star sensors and GNSS receiver in nominal mode Magnetometer and Sun sensors in acquisition and safe mode Anomaly detector	New implementation Large heritage
	Attitude control	1 arcmin, cold- gas thrusters in nominal mode	Strict requirement, new implementation
Data Handling		Data-handling computer, AOCS/DFC electronics, MIL 1553 bus	Large for data handling, AOCS/DFC new
Launcher		Rockot	SS19 and Proton. Demo flights in 1999
Ground segment			
Ground Segment Facilities	**CDAE**	Kiruna	ERS, Envisat
	MSCE	Mission operations and satellite control	Large
	PAE	Processing to Level 1b and archiving	Large

Table 9.1. *Implementation solutions and heritage.*

		Critical areas	Risk reduction
Instruments			
GPS / GLONASS receiver		No particular critical area	
Gradiometer			
Accelerometer		Order of magnitude better than previous developments	Breadboarding in Phase-B, functional model in development plan
Gradiometer		New, not even a single axis gradiometer has been built yet	Breadboarding in Phase-B, functional model in development plan
Calibration		New, based on DFACS, ground calibration. Ground calibration at best 10 worse than onboard requirements.	Testing ground calibration capabilities Analysis
Platform			
Configuration		Location of centre of mass, alignment	Analysis
Structure		Alignment and stability	Analysis, STM
Thermal Control		Atomic oxygen	Choice of materials
Propulsion	Electric propulsion	Performance, low noise, high stability in direction and module	Tests in Phase-B. Part system test bench in development flow
	Cold gas proportional thrusters	Performance / cost	Phase-B testing, part of system test bench in development flow Alternatives: FEEP, non-European
Power		Tight margins, impact on performance and / or cost	Higher orbit altitude possible
Communications		No issue	
AOCS / DFC	Position guidance	Performance / cost	Simulation Phase-B. Functional model in development flow
	Drag control	Performance / cost / safety	Simulation Phase-B. Functional model in development flow. Higher orbit altitude
	Attitude estimation	Performance / cost	Simulation Phase-B. Functional model in development flow
	Attitude control	Performance / cost	Simulation Phase-B. Functional model in development flow
Data Handling		Allocation AOCS/DFC functions	Normal work
Launcher		Launcher market evolution	Alternative launchers available
Ground segment			
Ground Segment Facilities	CDAE	12 h without contact	Simplicity, autonomy
	MSCE	No issue	
	PAE	No issue	

Table 9.2. *Critical areas and risk-reduction measures.*

9.4 Enhancement of Capabilities and Applications Potential

The preparations for the GOCE mission have already provided advances in Earth observation capabilities with important spin-off results. Thus the geodetic-quality GPS/GLONASS receiver that started to be developed for gravity missions has been modified for use as atmospheric sensor in radio-occultation techniques. It will be implemented, for instance, on the Metop satellites. Derivatives of the Aristoteles/GOCE accelerometers have been selected for CHAMP (STAR) and GRACE (SUPERSTAR) and are being considered for new more demanding space-science missions. GOCE also means a new approach for Earth-observation missions with integrated science-engineering teams. GOCE has raised interest in very low Earth-orbiting satellites, which may enable new research.

The GOCE mission is mainly scientific. Its applications are not in the direct utilisation of the techniques for operational / commercial missions. Though in some areas such as geodesy the usefulness of GOCE will be perceived directly, this would not be but a fraction of its application potential. The data provided by GOCE are fundamental to expanding our knowledge in key research areas that have important applications in our daily life.

Annex: Gravity Field Quantities/Terminology

Gravitational potential (*V*)	:	potential generated by the attraction of masses.
Gravity potential (*W*)	:	sum of the gravitational potential (*V*) and of the centrifugal potential (*C*) of the rotating Earth. Differences between two points may be observed by levelling.
Equipotential surface	:	a surface where *W* is equal to a constant. Points on one such surface may be determined regionally with tide-gauges, which define *regional* **mean sea-level**.
Height datum	:	defined by the equipotential surface which best agrees with *local* **mean sea-level** calculated from tide-gauges for a specific time period.
Geoid	:	equipotential surface which approximates the *global* **mean sea-level**, i.e. a global set of tide-gauges and levelling bench-marks, after subtraction of the dynamic components. It can be considered as the hypothetical ocean at rest.
Mean Earth ellipsoid	:	it is an ellipsoid of revolution, rotating with the Earth around its z-axis, and centred at the Earth's centre of mass. It is determined as the surface which gives *best fit* in some sense *to mean sea-level*. **The height above this ellipsoid**, *h*, is measured along the normal to the ellipsoid. It is observed indirectly by satellite positioning (such as GPS) from the determined cartesian co-ordinates (*x*, *y*, *z*).
Geoid height	:	it is the height, *N*, of a point on the geoid with respect to the ellipsoid (it is positive above).
Orthometric height	:	it is the height, *H*, measured from the geoid along the *plumbline*; it is commonly called the **height above mean sea-level**. It is observed by levelling: the measurements (level differences and gravity) yield the *geopotential number* which is converted to metric units by dividing by the mean gravity along the plumbline. This is how the **height system** of most countries is established.

Gravity	:	it is the magnitude, *g*, of the *gradient* of *W* at the Earth's surface and of *V* in space. It may be observed by an absolute technique (e.g. in a free fall experiment) or relatively (as a difference) by a spring gravimeter.
Gravity gradients	:	they are *derivatives* of the gravity vector, i.e. *second-order derivatives* of *W* at the Earth's surface and of *V* in space. Certain linear combinations may be measured by a *torsion-balance* at Earth's surface, and by forming *differences of adjacent accelerometer measurements* in space.
Normal gravity potential	:	it is a *model* gravity potential, *U*, with the ellipsoid as an equipotential surface. It is used to calculate *normal gravity*, γ.
Anomalous potential	:	it is the difference $T = W - U$. it is small and allows linearisation, such as the Bruns equation $N = T/\gamma$, which directly relates *potential* and *geoid height*. Measured quantities are frequently expressed as derivatives of *T*, such as the gravity gradients.
Gravity anomaly	:	at any point of given latitude and orthometric height, **the gravity anomaly** Δg is the value derived by subtracting measured and normal gravity $(\Delta g = g - \gamma)$. The gravity γ is calculated at a point with the ellipsoidal height put equal to the orthometric height.
Spherical harmonic coefficients	:	the potential *V* (or *T*) may be expanded as an infinite *series of spherical harmonic functions* which are the *spherical equivalent of Fourier series in a plane*. The coefficients of the series are numbered according to *degree* and *order*, *l* and *m* respectively $(m \le l)$, which corresponds to wave numbers in the plane. The **zonal harmonics** are those coefficients of **order zero** and correspond to averages of the potential in longitude. The other coefficients are called **tesseral harmonics** (sectorial when $l = m$).
Kaula's rule	:	for a given degree, the quadratic mean (over all orders) of the harmonic coefficients for the Earth decreases approximately like $10^{-5}/l^2$; the square of this quantity is called *degree variance* and corresponds to the signal power spectrum density.
Global (geopotential) model	:	it is a model of the Earth's gravitational potential in the form of a set of *spherical harmonic coefficients, truncated* at a maximum degree and order *L*.

Spatial resolution of a global model in spherical harmonics	:	for a truncation at degree and order *L*, this is the maximum resolved half-wavelength, *D = 20 000 km/L*.

Units and Orders of Magnitude

Gravity is expressed in m/s^2 or in *milligal* (1 *mgal* = $10^{-5}\ m/s^2$; from the *gal* : 1 *gal* = $10^{-2}\ m/s^2$) ; the mean Earth gravity is about 981 000 mgal (the well-known $9.81\ m/s^2$), varies from 978 100 mgal to 983 200 mgal from Equator to pole due to the Earth's flattening and rotation. Excursions, i.e. *gravity anomalies* due to density inhomogeneities, mountain ridges, etc., range from *tens to hundreds of milligals.*

Geoid : its excursions (*geoid height), N*, measured from the mean Earth ellipsoid, amount to about + 90 and - 105 metres in the extremes. These are long-wavelength features (several thousand kilometres). Variations of shorter extensions (tens to hundreds of kilometres) have a magnitude of centimetres to one or a few metres.

Gravity gradients are expressed in the *Eötvös* unit $\left(1\ E = 10^{-9}\ s^{-2}\right)$. The largest component is the vertical gravity gradient, being about 3000 *E* on Earth (*gravity changes by* $3.10^{-6}\ m/s^2$ *per metre of elevation*). The horizontal components are approximately half this size; mixed gradients are below 100 *E* for the normal field. Gravity-gradient anomalies can be much larger and reach 1000 *E* in mountainous area.

References

Achache, J. (1994): Magnetic field,: ESA (1994) *Report of the ESA Earth Observation User Consultation Meeting* , ESA SP-186, Noordwijk.

Aguirre-Martinez, M. and S. Cesare (1999): GOCE mission concept, error derivation and performances, *Proceedings, 2nd Joint Meeting of the IGC and IGeC commissions,* Trieste, Sept. 1998 – in press.

Aguirre-Martinez, M. Derivation of the satellite gravity gradient observables and recovery of the centrifugal terms in GOCE, *ESA-ESTEC working paper EWP-2033*, July 1999.

Albertella, A., F. Migliaccio and F. Sanso (1999): New simulations for the spaceborne gravimetry inversion, *Proceedings, 2nd Joint Meeting of the IGC and IGeC commissions,* Trieste, Sept. 1998 – in press.

Arabelos, D. and C.C. Tscherning (1995): Regional recovery of the gravity field from SGG and gravity vector using collocation, *J. Geophys. Res.*, **100**, B11, 22009-22015.

Arabelos, D., and C.C. Tscherning (1999) Vertical datum control using GOCE mission error model, E.G.S., *Geophysical Research Abstracts,* 1, 1, 236.

Balmino, G., F. Perosanz, R. Rummel, N. Sneeuw, H. Sünkel and P. Woodworth, European Views on dedicated gravity field missions: GRACE and GOCE, *Earth Sciences Division Report*, Con.-001, ESTEC, Noordwijk, The Netherlands, May 1998.

Balmino, G. and F. Perosanz (1994): Comparison of geopotential recovery capabilities of some future satellite missions, *Proc., IAG symposium, Gravity and Geoid*, Graz, 403-412.

Balmino, G., F. Perosanz, R. Rummel, N. Sneeuw and H. Sünkel (1999): CHAMP, GRACE and GOCE: Mission Concepts and Simulations, *Proceedings, 2nd Joint Meeting of the IGC and IGeC commissions,* Trieste, Sept. 1998 – in press.

Berge-Nguyen, M., Colmant, S. and Cazenave, A. 1999. A new global bathymetric map from ERS-1, GEOSAT and ship track data based on generalised least squares inversion. (In preparation).

Bertiger, W.I., Y.E. Bar-Sever, E.J. Christensen, E.S. Davis, J.R. Guinn, B.J. Haines, R.W. Ibanez-Meier, J.R. Lee, S.M. Lichten, W.G. Melbourne, R.J. Muellerschoen, T.N. Munson, Y. Vigue, S.C. Wu, T.P. Yunck, B.E. Schutz, P.A.M. Abusali, H.J. Rim, M.M. Watkins, and P.Willis (1994), GPS precise tracking of

TOPEX/Poseidon: Results and implications, *J. Geophys. Res*., 99/(C12), 24449--24464.

Best, S.E., Ivchenko, V.O., Richards, K.J., Smith, R.D. and Malone, R.C. 1999. Eddies in numerical models of the Antarctic Circumpolar Current and their influence on the mean flows. *Journal of Physical Oceanography*, 29, 328-350.

Bijlsma, L. (and 18 others). 1996. Chapter 9 (Coastal zones and small islands) of, Climate Change 1995: Impacts, adaptations and mitigation of climate change: scientific-technical analysis. Contribution of working group II to the second assessment report of the Intergovernmental Panel on Climate Change, eds. R.T. Watson, M.C. Zinyowera and R.H. Moss. Cambridge: *Cambridge University Press*. 879pp.

Blaser J.-P., J. Cornelisse, A.M. Cruise, T. Damour, F. Hechler, M. Hechler, Y. Jafry, B. Kent, N. Lockerbie, H.J. Paik, A. Ravex, R. Reinhard, R. Rummel, C. Speake, T. Summer, P. Touboul, S. Vitale (1996): STEP Satellite test of the equivalence principle, *Report on the Phase-A Study*, ESA, SCI(96)5.

Brozena, J.M., M.F. Peters (1994): State-of-the-art airborne gravimetry, in: Gravity and Geoid (eds. H. Sünkel and I. Marson), IAG Symposia 113, 187-197, Springer, Berlin.

Brozena, J.M., M.F. Peters, R. Salman (1997) Arctic airborne gravity measurement Programme, in: Gravity, Geoid and Marine Geodesy, eds. J. Segawa, H. Fujimoto, S. Okubo, IAG-Symposia, 117, 131-138, Springer, Heidelberg.

Bryan, K. 1996. The steric component of sea-level rise associated with enhanced greenhouse warming: a model study. *Climate Dynamics*, 12, 545-555.

Chassignet, E.P., Garrafo, Z. and Paiva, A.M. 1999. Fine mesh (1/12 degree) modelling of the North Atlantic: The spin up phase. (In preparation).

CIGAR I (1989): Study on precise gravity field determination methods and mission requirements. Part 1: Final Report, *ESA contract 7521/87/F/FL*.

CIGAR II (1990): Study on precise gravity field determination methods and mission requirements. Part 2: Final Report, *ESA contract 8153/88/F/FL*.

CIGAR III (1993): Study on precise gravity field using gradiometry and GPS, Phase 1, Final Report, *ESA contract 9877/92/F/FL*.

CIGAR III (1995): Study on precise gravity field using gradiometry and GPS, Phase 2, Final Report, *ESA contract 10713/93/F/FL*.

CIGAR IV (1996): Study of advanced reduction methods for spaceborne gravimetry data, and of data combination with geophysical parameters, Final Report, *ESA contract 152 163, Study ESTEC/JP/95-4-137/MS/nr*.

Coles, S.G and Tawn, J.A. 1990. Statistics of coastal flood prevention. *Philosophical Transactions of the Royal Society of London*, A332, 457-476.

Colombo, O. (1989): Advanced techniques for high-resolution mapping of the gravitational field, *Lecture Notes in Earth Sciences*, Vol. **25**, Springer Verlag.

Degnan, J.J. (1985), Satellite Laser Ranging: Current status and future prospects, *IEEE Trans. Geosci. Remote Sens*., GE-32, 398--413.

Di Donato G., A.M. Negredo, R. Sabadini and L.L.A. Vermeersen (1999): Multiple Processes causing Sea-level Rise in the central Mediterranean, *Geophys. Res. Letters* – in press.

Dombrowsky, E., Giraud, S. and Dibarboure, G. 1999. Impact of a precise mean dynamic topography on the assimilation of altimeter data in an eddy resolving quasi-geostrophic model. *CLS Space Oceanography Division*. Unpublished manuscript.

Douglas, B.C. 1997. Global sea-level rise: a redetermination. *Surveys in Geophysics*, 18, 279-292.

Dziewonski, A.M. and D.L. Anderson (1981): Preliminary Reference Earth Model, *Phys. Earth Planet. Int*., **25**, 297-356.

Emery, K.O. and Aubrey, D.G. 1991. Sea-levels, land levels, and tide gauges. New York: Springer-Verlag. 237pp.

ESA (1978) European workshop on space oceanography, navigation and geodynamics, ESA SP-137, Paris.

ESA (1986): Solid Earth Science and Application Mission for Europe, *ESA special workshop in Ising*, ESA SP-1080, Paris.

ESA (1991): The Solid-Earth mission Aristoteles, *Proceedings of an international workshop in Anacapri*, ESA publication division, ESTEC, Noordwijk.

ESA (1994): Report of the ESA Earth Observation User Consultation Meeting, ESTEC, ESA SP-1186, Noordwijk.

ESA SP-1196 (1) Report for Assessment: Gravity Field and Steady-State Ocean Circulation Mission, ESA Publication Division, ESTEC, Noordwijk, The Netherlands, April, 1996.

ESA SP-1227, The Earth Explorer: The Science and Research Element of ESA's Future Earth Observation Programme, *ESA Publication Division*, ESTEC, Noordwijk, The Netherlands, September, 1998.

Forsberg, R. (1985) Gravity-induced position errors in inertial surveying, in: *proc. Inertial Technology for Surveying and Geodesy*. Banff.

Ganachaud, A., Wunsch, C., Kim, M-C. and Tapley, B. 1997. Combination of TOPEX/Poseidon data with a hydrographic inversion for determination of the oceanic general circulation. *Geophysical Journal International*, 128, 708-722.

Gill, A.E. 1982. Atmosphere - ocean dynamics. *New York: Academic Press*, 662pp.

Gordon, A.L. 1986. Interocean exchange of thermocline water. *Journal of Geophysical Research*, 91(C4), 5037-5046.

GRACE (1998) – Gravity Recovery and Climate Experiment: Science and Mission Requirements Document, revision A, JPLD-15928, NASA's Earth System Science Pathfinder Program.

Hager, B.H., M.A. Richards (1989) Long-wavelength variations in Earth's geoid: physical models and dynamical implications, *Phil.Trans.R.Soc.Lond.* A 328, 209-327.

Heck, B., and R. Rummel (1990) Strategies for solving the vertical datum problem using terrestrial and satellite geodetic data, in: *Sea-surface Topography and Geoid*, eds. H. Sünkel, T. Baker 116-128, Springer, Berlin.

Heiskanen, W.A., Moritz, H. (1967): Physical Geodesy, Freeman, San Francisco.

Hughes, C.W. and Ash, E. 1999. Eddy forcing of the mean flow in the Southern Ocean. (Paper in preparation).

Hughes, T. 1981. The weak underbelly of the West Antarctic Ice Sheet. *Journal of Glaciology*, 27, 518-525.

Kaula W.M. (1966): Theory of Satellite Geodesy, Waltham, Blaisdell.

Khafid (1998) On the Unification of Indonesian Local Heights, DGK, C-488, München.

Knudsen, P. and Andersen, O. 1996. Ocean bottom topography from ERS-1 altimeter data. *Earth Observation Quarterly*, 51, 16-18. (Published by the European Space Agency).

Kooi, H., S. Cloetingh and J. Burrus (1992): Lithospheric Necking and Regional Isostasy at Extensional Basins, Part 1, *J. Geophys. Res.*, **97**, B12, 17553-17571.

LeGrand, P. and Minster, J-F. 1999. Impact of the GOCE gravity mission on ocean circulation estimates. *Geophysical Research Letters* (in press).

Lemoine, F.G., Kenyon, S.C., Factor, J.K., Trimmer, R.G., Pavlis, N.K., Chinn, D.S., Cox, C.M., Klosko, S.M., Luthcke, S.B., Torrence, M.H., Wang, Y.M., Williamson, R.G., Pavlis, E.C., Rapp, R.H. and Olson, T.R. 1998. The Development of the Joint NASA GSFC and the National Imagery and Mapping Agency (NIMA) Geopotential Model EGM96. *National Aeronautics and Space Administration Report*, NASA/TP-1998-206861, Goddard Space Flight Center, Greenbelt, Maryland, July, 1998.

Macdonald, A. 1995. Oceanic fluxes of mass, heat and freshwater: a global estimate and perspective. *Ph.D thesis*, Department of Earth, Atmospheric and Planetary Sciences, Massachusetts Institute of Technology, Cambridge, USA.

Maltrud, M.E., Smith, R.D., Semtner, A.J. and Malone, R.C. 1998. Global eddy-resolving ocean simulations driven by 1985-1995 atmospheric winds. *Journal of Geophysical Research*, 103(C13), 30825-30853.

McKenzie, D. (1994): Relationship between topography and gravity on Earth and Venus, Icarus, 112, 55-88.

Mueller, I.I., S. Zerbini (eds.) (1989): The Interdisciplinary Role of Space Geodesy, in: Earth Sciences, 22, Springer, Berlin.

NASA (1987): Geophysical and Geodetic Requirements of Global Gravity Field Measurements, 1987 – 2000 Report of a Gravity Workshop at Colorado Springs, NASA-Geodynamics Branch.

Negredo, A.M., E. Carminati, S. Barba and R. Sabadini (1999): Dynamic Modelling of Stress Accumulation in Central Italy, *Geophys. Res. Letters* – in press.

Neilan, R., Van Scoy, P.A. and Woodworth, P.L. (eds). 1998. Proceedings of the workshop on methods for monitoring sea-level: GPS and tide gauge benchmark monitoring and GPS altimeter calibration. Workshop organised by the IGS and PSMSL, Jet Propulsion Laboratory, 17-18 March 1997. 202pp.

Nerem, R.S. et al. 1994. Gravity model developments for TOPEX/Poseidon: joint gravity models 1 and 2. *Journal of Geophysical Research*, 99(C12), 24421-24447.

Noomen, R., B.A.C. Ambrosius, and K.F. Wakker (1993), Crustal motions in the mediterranean region determined from laser ranging to LAGEOS, in Contributions of

Space Geodesy to Geodynamics: Crustal dynamics, vol. Geodynamics series, v. 23, edited by D.E. Smith and D.L. Turcotte, *American Geophysical Union*, Washington D.,C.

NRC (1997): Satellite Gravity and Geosphere. *National Academy Press*, Washington D.C.

Oberndorfer, H., R. Dorobantu, C. Gerlach, J. Müller, R. Rummel, N. Sneeuw, R. Koop, P. Visser, P. Hoyng, A. Selig and M. Smit (1999): GOCE sensor combination and error analysis, *Proceedings, 2nd Joint Meeting of the IGC and IGeC commissions*, Trieste, Sept. 1998 – in press.

Paiva, A.M., Hargrove, J.T., Chassignet, E.P. and Bleck, R. 1999. Turbulent behaviour of a fine mesh (1/12 degree) numerical simulation of the North Atlantic. *Journal of Marine Systems* (in press).

Peltier, W.R. 1998. Postglacial variations in the level of the sea: implications for climate dynamics and solid-Earth geophysics. *Reviews of Geophysics*, 36(4), 603-689.

Perosanz, F., J.C. Marty and G. Balmino, Dynamic orbit determination and gravity field model improvement from GPS, DORIS and laser measurements on TOPEX/Poseidon satellite, *Journal of Geodesy*, 71, 3, 160-170, Feb., 1997.

Ramillien, G. and Cazenave, A. 1997. Global bathymetry derived from altimeter data of the ERS-1 geodetic mission. *Journal of Geodynamics*, 23, 129-143.

Reigber Ch., R. Bock, Ch. Forste, L. Grunwaldt, N. Jakowski, H. Lühr, P. Schwintzer and C. Tilgner, CHAMP Phase-B Executive Summary, *G.F.Z., STR96/13*, 1996.

Ricard, Y., C. Froidevaux (1990) Seismic Imaging, plate velocities and geoid: the direct and inverse problem, in: *Glacial Isostasy and Mantle Rheology*, eds: R. Sabadini, K. Lambeck, E. Boschi 533-569, Kluwer, Dordrecht.

Rintoul, S.R. 1991. South Atlantic interbasin exchange. *Journal of Geophysical Research*, 96(C2), 2675-2692

Roman, D.R., B. Csatho, K.C.Jezek, R.H.Thomas, W.B.Krabill, R. von Frese, R.Forsberg: A comparison of geoid undulations for west central Greenland. *J.Geophys. res*., Vol. 102, B2, pp. 2807 - 2814, 1997.

Rummel, R. (1992) GPS, heights and the role of the geoid, *Geodetical Info Magazine*, 6, 8, 52-56.

Rummel, R., F. Sanso, M. Van Gelderen, M. Brovelli, R. Koop, F. Migliaccio, E.J.O. Schrama and F. Sacerdote (1993): Spherical Harmonic Analysis of Satellite Gradiometry, *Neth. Geodetic Commission*, N. 39 (New Series).

Rummel, R., N. Sneeuw and J. Mueller (1995): Geodetic requirements and prospects. Study of Gravity Explorer Mission requirements. (A simulation study). DASA, Dornier SatSyst GmbH.

Rummel, R. (1997) Spherical spectral properties of the Earth's gravitational potential and its first and second derivatives, in: Lecture Notes in Earth Sciences, 65, 359-405, Springer, Heidelberg.

Schrama, E.J.O. (1991): Gravity field error analysis: applications of GPS receivers and gradiometers of low orbiting platforms, *J. Geophys. Res.*, **96**, B12.

Schwarz, K.P. (1981) Gravity induced position errors in airborne inertial navigation, The Ohio State University, 326, Columbus, Ohio.

Schwarz, K.P., M.G. Sideris (1987) Orthometric heights without levelling, Journ. Surv. Engineering, 113, 1, pp. 28.

Schwintzer, P., Ch. Reigber, A. Bode, Z. Kang, S.Y. Zhu, F.H. Massmann, J.C. Raimondo, R. Biancale, G. Balmino, J.M. Lemoine, B. Moynot, J.C. Marty, F. Barlier, Y. Boudon (1997): Long-wavelength global gravity field models: GRIM4-S4, GRIM-C4, *Journal of geodesy*, 71/4, 189-208.

Smith, W.H.F. and Sandwell, D.T. 1994. Bathymetric prediction from dense satellite altimetry and sparse shipboard bathymetry. Journal of Geophysical Research, 99(B11), 21803-21824.

Smith, W.H.F. and Sandwell, D.T. 1997. Global sea floor topography from satellite altimetry and ship depth soundings. *Science*, 277, 1956-1962.

Smith, R.D., Maltrud, E.M., Bryan, O.F. and Hetcht, M.W. 1999. Numerical simulation of the North Atlantic Ocean at 1/10 degree. *Journal of Physical Oceanography* (in press).

Sneeuw, N (1994) Global spherical harmonic analysis by least-squares and numerical quadrature methods in historical perspective, *Geophys.J.Int*., 118, 707-716.

Tapley, B.D., J.C. Ries, G.W. Davis, R.J. Eanes, B.E. Schutz, C.K. Shum, M.M. Watkins, J.A. Marshall, R.S. Nerem, B.H. Putney, S.M. Klosko, S.B. Luthcke, D.Pavlis, R.G. Williamson, and N.P. Zelensky (1994), Precision orbit determination for TOPEX/Poseidon, *J. Geophys. Res*., 99(C12), 24383--24404.

Tapley, B.D., B.E. Schuts, R.J. Eanes, J.C. Ries, and M.M. Watkins (1993), Lageos laser ranging contributions to geodynamics, geodesy, and orbital dynamics, in Contributions of Space Geodesy to Geodynamics: Earth dynamics, vol. Geodynamics series, v. 24, edited by D.E. Smith and D.L. Turcotte, American Geophysical Union, Washington D.C.

The International Geosphere-Biosphere Programme (IGBP): A Study of Global Change (1990). The Initial Core Projects, 12, ICSU, Stockholm.

Thomas, R.H., Sanderson, T.J.D. and Rose, K.E. 1979. Effects of a climate warming on the West Antarctic Ice Sheet. *Nature*, 227, 355-358.

Touboul, P., E. Willemenot, B. Foulon and V. Josselin (1999): Accelerometers for CHAMP, GRACE and GOCE : synergy and evolution, *Proceedings, 2nd Joint Meeting of the IGC and IGeC commissions*, Trieste, Sept. 1998 – in press.

Tushingham, A.M., and W.R. Peltier, ICE-3G: A new global model of late Pleistocene deglaziation based upon geo-physical predictions of post-glacial relative sea-level change, *J. Geophys. Res., 96* 4497-4523, 1991.

Warrick, R.A., Le Provost, C., Meier, M.F., Oerlemans, J. and Woodworth, P.L. 1996. Chapter 7 (Changes in sea-level) of, Climate Change 1995: The science of climate change. Contribution of working group I to the second assessment report of the Intergovernmental Panel on Climate Change, eds. J.T.Houghton, L.G.Meira Filho, B.A.Callander, N.Harris, A.Kattenberg and K.Maskell. Cambridge: Cambridge University Press. 572pp.

Webb, D.J., Coward, A.C., de Cuevas, B.A. and Gwilliam, C.S. 1997. A multiprocessor ocean general circulation model using message passing. Journal of Atmospheric and Oceanic Technology, 14, 175-183.

Wei, M., K.-P. Schwarz (1997) Comparison of different approaches to airborne gravimetry by strapdown INS/DGPS, in: Gravity, Geoid and Marine Geodesy, eds. J. Segawa, H. Fujimoto, S. Okubo, IAG-Symposia, 117, 155-162, Springer, Heidelberg.

Williamstown Report (1969): The Terrestrial Environment. Solid-Earth and Ocean Physics, Application of Space and Astronomic Techniques. Report of a Study at Williamstown, Mass., to the NASA, Cambridge, Mass.

Woodworth, P. J.A. Johannessen, P. Le Grand, C. Le Provost, G. Balmino, R. Rummel, R. Sabadini, H. Sünkel, C.C. Tscherning and P. Visser. Impact of GOCE for ocean circulation studies. WOCE Newsletter, 1998.

Wunsch, C., and E.M. Gaposchkin, 1980: On using satellite altimetry to determine the general circulation of the oceans with application to geoid improvement. Reviews of Geophysics and Space Physics, 18, 725-745.

Wunsch, C. and Stammer, D. 1998. Satellite altimetry, the marine geoid, and the oceanic general circulation. Annual Reviews of Earth and Planetary Sciences, 26, 219-253.

Xu, P., R.Rummel (1991) A quality investigation of global vertical datum connection, Netherl. Geodetic Commision, 34, Delft.

Zerbini, S., J. Achache, A.J. Anderson, F. Arnet, A. Geiger, E. Klingelé, R. Sabadini and S. Tinti (1992): Study of the geophysical impact of high-resolution Earth potential fields information, *ESA study*, Final Report.

GLOSSARY

AACC	the short section across the ACC near to the Greenwich Meridian
ACC	Antarctic Circumpolar Current
ADE	Attitude Drive Electronics
AOCS	Attitude and Orbit Control System
AS	Anti Spoofing
ATSR	Along-Track Scanning Radiometer
BGI	Bureau Gravimétrique International
BOL	Beginning of Life
C/A	Coarse Acquisition
CAAM	Coarse Attitude Acquisition Mode
CD	Compensated Depth
CDAE	Command and Data Acquisition Element
CDMU	Central Data Management Unit
CHAMP	Challenging Mini-Satellite Payload for Geophysical Research and Application (GFZ)
CIGAR	Consortium for Investigations in Gravity Anomalies Research
CLIVAR	Climate Variability and Predictability
CMR	Common Mode Rejection
CNES	Centre Nationale d'Etude Spatiale
COM	Centre of Mass
CTE	Coefficient of Thermal Expansion
DC	Direct Current
DFACS	Drag-free and Attitude Control System
DFC	Drag-free Control
DHS	Data Handling System
DORIS	Doppler Orbitography and Repositioning Integrated by Satellite
DTM	Digital Terrain Model
EGM	Earth Gravity Model
EIRP	Equivalent Isotropic Radiated Power
Envisat	Environmental Satellite
EOL	End of Life
EPRF	Earth Pointing Reference Frame
EPS	Electrical Power System
ERS	European Remote-sensing Satellite
ESATAN	ESA Thermal Analyser
EURECA	European Retrieval Carrier
FAAM	Fine Attitude Acquisition Mode
f.o.v	Field of View
FTP	File Transfer Protocol

GCM	General Circulation Model
GEOSAT	Geodetic Satellite
GFO	GEOSAT follow-on
GIA	Glacial Isostatic Adjustment
GLONASS	Global Navigation Satellite System (Russian concept)
GNSS	Global Navigation Satellite System
GOCE	Gravity and steady-state Ocean Circulation Explorer
GODAE	Global Ocean Data Assimilation Experiment
GOOS	Global Ocean Observing System
GPS	Global Positioning System
GPSOS	GPS Occultation Sensor
GRACE	Gravity Recovery and Climate Experiment (NASA)
GRAS	GNSS Receiver for Atmospheric Sounding
GRF	Gradiometer Reference Frame
GRIM-4S	European gravity model
IAG	International Association of Geodesy
IAPSO	International Association for the Physical Sciences of the Oceans
ICE4G	Global geophysical model
ICESAT	Ice Cloud and Land Elevation Satellite
ICRF	International Celestial Reference Frame
IGS	International GPS Service
IMU	Inertial Measuring Unit
INSAR	SAR Interferometry
IOC	Intergovernmental Oceanographic Commission
IPCC	Intergovernmental Panel on Climate Change
ITRF	IERS (International Earth Rotation Service) Terrestrial Reference Frame
IUGG	International Union of Geodesy and Geophysics
LEO	Low Earth Orbiter
LEOP	Launch and Early Operations Phase
LES	Long Eclipse Season
LF	Low Frequency
LRR	Laser Retro Reflector
MBW	Measurement Bandwidth
MDT	Mean Dynamic Topography
Metop	Meteorological Operational Satellite
MICOM	Miami Isopycnic Coordinate Ocean Model
MIL	Military
MLI	Multi-Layer Insulation
MMU	Mass Memory Unit
MSCE	Mission and Satellite Control Element
MSS	Mean-sea-surface
NASTRAN	NASA Structural Analyser
NIMA	National Imaging and Mapping Agency

OCCAM	Ocean Circulation Climate Advanced Modelling
ØERSTED	Danish-led aeronomy/astronomy satellite (given name)
ORATOS	Orbit and Attitude Operating System
OSR	Optical Surface Reflector
PAE	Processing and Archiving Element
PCDU	Power Control Distribution Unit
PCGMA	Preconditioned Conjugate Gradient Multiple Adjustment
PGR	Post Glacial Rebound
POD	Precise Orbit Determination
POP	Parallel Ocean Program
PREM	seismic model
PSD	Power Spectral Density
REM	Radiation Environmental Monitor
RFDU	Radio Frequency Distribution
RITA	Radio-frequency Ion Thruster Assembly
RMS	Root Mean Square
RTU	Remote Terminal Unit
SAC-C	Satelite de Aplicaciones Cientificas - C
SAR	Synthetic Aperture Radar
SCOS2000	Satellite Control Operating System 2000
SGG	Satellite Gravity Gradiometry
SLR	Satellite Laser Ranging
SREM	Standard Radiation Environment Monitor
SSO	Sun-Synchronous Orbit
SST-hl	Satellite-to-Satellite High-Low Tracking
SST-ll	Satellite-to-Satellite Low-Low Tracking
STM	Structural and Thermal Model
TMDD	Thermal and Mechanical De-coupling Device
TOPEX/Poseidon	Joint French-US altimeter satellite
T/P	Topex/Poseidon
TRP	Technology Research Project
UTC	Universal Time Coordinated
VLBI	Very Long Baseline Interferometry
WCRP	World Climate Research Programme
WMO	World Meteorological Organisation
WOCE	Word Ocean Circulation Experiment

Acknowledgements

We are very grateful for the valuable contributions from O.B. Andersen, A. Anselmi, H. Bassuer, S. Cesare, C. Gerlach, P. Hoyng, C. Hughes, J. van der Ijssel, R. Klees, P. Knudsen, D. Lamarre, P. LeGrand, P-Y. Le Traon, R. Licata, J. Mueller, H. Oberndorfer F. Perosanz, F. Ponchaut, H. Rebhan, J. Schroeter, A. Selig, M. Smit, N. Sneeuw, L. Vaillon, E. Willemenot and D. Wingham.

Thanks are also extended to C.J. Readings, M.L. Reynolds and A. Tobias for their time and effort in reviewing the document, and to D. Wishart for preparing the document for publication.